MINISTRY OF EDUCATION AND RESEARCH

THE ANNALS OF "DUNAREA DE JOS" UNIVERSITY OF GALATI

Fascicle IX
METALLURGY AND MATERIALS SCIENCE

YEAR XXV (XXX),
November 2007, no. 2

ISSN 1453-083X

2007
GALATI UNIVERSITY PRESS

EDITING MANAGEMENT

RESPONSIBLE EDITOR: **Prof. Dr. Eng. Viorel MINZU**

ASSISTANT EDITORS: **Prof. Dr. Eng. Iulian BIRSAN**
Conf. Dr. Ec. Daniela ŞARPE
Conf. Dr. Anca GÂŢĂ
SECRETARY: **Assoc. Prof. Dr. Eng. Ion ALEXANDRU**

EDITING BOARD

Fascicle IX

METALLURGY AND MATERIALS SCIENCE

EDITOR IN CHIEF: **Prof. Dr. Chim. Olga MITOŞERIU**

SECRETARY and EDITOR: **Prof. Dr. Eng. Marian BORDEI**

MEMBERS:

Acad.Prof.Dr.Hab. **Iurie Nicolaevich Shevcenko**–Director of the Thermoplasticity Department, National Academy of Science of Ukraine
Acad.Prof.Dr.Hab. **Valeriu Kantser**–Coordinator of the Technical and Scientific Section of the Academy of Moldova Republic
Acad.Prof.Dr.Hab. **Ion Bostan**–Rector of Technical University of Moldova, member of the Academy of Moldova Republic
Prof.Dr. **Rodrigo Martins**–President of the Department of Materials Science, Faculty of Science and Technology, NOVA University of Lisbon, Portugal
Prof.Dr.Hab. **Vasile Marina**–Director of Department, State Technical University of Moldova, Chisinau, Moldova Republic
Prof.Dr. **Jean Pierre Celis**–Department of Metallurgy and Materials Engineering, Katholieke Universiteit Leuven, Belgium
Prof.Dr. **François Wenger**–Laboratoire Génie des Procédés et Matériaux, Ecole Centrale Paris, France
Prof.Dr. **Pierre Ponthiaux**–Laboratoire Génie des Procédés et Matériaux, Ecole Centrale Paris, France
Asoc.Prof.Dr.**Valeriu Dulgheru**–Department of Mechanisms Theory and Parts of Machine, Technical University of Moldova, Chisinau, Moldova Republic
Prof. Dr. Eng. **Elena Drugescu**
Prof. Dr. Eng. **Nicolae Cănănău**
Prof. Dr. Eng. **Anisoara Ciocan**
Prof. Dr. Eng. **Maria Vlad**
Prof. Dr. Eng. **Petre Stelian Niţă**
Prof. Dr. Eng. **Alexandru Ivănescu**
Prof. Dr. Chim. **Viorica Muşat**
Prof. Dr. Chim. **Lidia Benea**
Asoc. Prof. Dr. Eng. **Sanda Levcovici**

TABLE OF CONTENT

THE ANNALS OF “DUNAREA DE JOS” UNIVERSITY OF GALATI.
FASCICLE IX. METALLURGY AND MATERIALS SCIENCE
N^0. 2 – 2007, ISSN 1453 – 083X

STUDY ON SOME COPPER - MOLYBDENUM BASED COMPOSITE MATERIALS CONDENSED FROM THE VAPOUR PHASE

N.GRECHANYUK[1]**, Gheorghe CROITORU**[2]
[1] National Academy of Sciences, Kiev, Ukraine,
[2] “Dunarea de Jos “ University of Galati
e-mail: e-mail: gekont@ukr.net

ABSTRACT

Design features of equipment are given for realizing high-speed process of electron beam evaporation and condensation. Peculiarities of phase composition and structure of a crystallized pool (melt) on copper base are studied. Assumption was made about interrelation of structure-phase state of the melt and rate of evaporation-condensation. Specifics of surface structure and volume of condensate in different sections (before and after etching) are investigated. Technological defects, their influence on strength and ductility of the condensate at tensile test are considered. Interrelation of temperature dependence of energy of deformation activation, specifics of condensate fracture and technological defects of structure, different by origin, are studied.

KEYWORDS: installation for vacuum condensation, technology of electron beam evaporation, condensate, structure, properties.

1. Introduction

This paper presents the basis for obtaining the Cu-Mo based –alloy using electron technology and the study of structure and characteristics.

In order to obtain this alloy, condensed from the vapour phase, the UE-189 electron beam industrial installation has been used, which was modernized by „Gekont”. The image of this installation is presented in figure 1. It has a technological chamber ***1*** and another chamber, ***2***, laterally, with the electron guns ***3-6***.

The vacuum system is designed for creating dynamic vacuum in chambers of the UE-189 installation for the purpose of ensuring the process of evaporation and condensation of initial materials. The technological chamber and the gun chamber have separate vacuum pump-out systems, which ensure stability of EB heater operation.

The vacuum system consists of two roughing-down pumps, two booster pumps, and two high-vacuum units (one per the gun chamber and the technological chamber). On upper flange of the technological chamber ***1*** substrate ***14*** rotation mechanism ***15,*** designed and manufactured in «Gekont», it is installed [1].

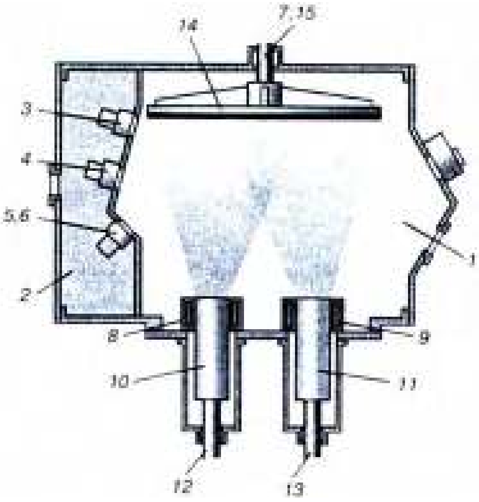

Figure 1. Principal scheme of EB installation: 1 — working chamber; 2 — gun chamber; 3-6 — EB guns; 7 — substrate rotation rod; 8, 9 — crucibles for evaporation of copper and molybdenum, respectively; 10, 11 — ingots for evaporation; 12, 13 — mechanisms for feeding ingots into evaporation zone; 14 — substrate; 15 — substrate rotation mechanism.

A peculiar feature of the design of this mechanism is the possibility of its long operation (10-12 months) without violation of vacuum when rotating a substrate of up to 50 kg mass at speed up to 40 rpm at the temperature (600 ± 50) °C. Heating of the substrate (fixed on the rotation rod 7) up to the mentioned temperature [2] is performed by EB guns ***5, 6*** of 40 kW power. Heating of the initial material for evaporation is performed by means of EB guns ***3, 4*** of 100 kW power. All guns have independent filament of cathodes and autonomous control of EB. The evaporation unit consists of two crucibles of 100 and 70 mm in diameter ***(8*** and ***9,*** respectively), designed for evaporation of copper ***10*** and molybdenum ***11***, and mechanisms ***12*** and ***13,*** which ensure their feeding into the evaporation zone.

Initial (being evaporated) materials. For producing of condensed electric contact materials the copper, molybdenum, and alloying elements (yttrium and zirconium) were used as initial elements. Calcium fluoride was used for creation of a separating layer on the substrate. Substrates for deposition of 800-1000 mm in diameter and (20 ± 2) mm thick were manufactured from steel OL-37. Surface of the substrate, on which deposition was performed, was subjected to milling and grinding till roughness not less than $\boldsymbol{R_a}$ = 0.63 (GOST 2769-73).

Preparation of ingots for evaporation. Copper ingots were turned and drilled for placement of alloying element weights. These ingots and turned ingots of molybdenum were subjected to cleaning, de-greasing, and weighing. Alloying elements were used in the form of degreased and dried chips of zirconium and yttrium. Weights of mentioned metals at the ratio 7:3 in amount (100 ± 3) g per 10 kg of copper were placed into special channels, drilled in copper ingot being evaporated, and on the surface. For creation of a separating layer a weight of fluoric calcium (2.0 ± 0.3 g) was placed on the surface heated of the molybdenum ingot.

After charging of the substrate and initial materials the installation was vacuumized**.** When vacuum 1-10 Pa was achieved, EB guns were switched on and technological process of vacuum deposition was started.

Deposition of the separating layer CaF2 was performed in vacuum not less than 1-10 Pa after heating of the rotating substrate up to the temperature (873 ± 50) K. Duration of the separating layer application was 120-180 s.

After termination of the separating layer deposition process, alloyed pool was formed on the copper ingot face. At the same time molybdenum ingot was heated. The conditions were considered achieved when evaporation currents of copper equaled 3.0-3.4 A, molybdenum 1.2-16 A at acceleration voltage of 20 kV. Change of the beam power in evaporation of molybdenum in different experiments allowed producing composite materials Cu-Mo-Zr-Y of three grades with molybdenum concentration equal to 2.5-5.0, 5.1-8.0, 8.0-12.0 wt.%, respectively [3].

Evaporator, rate of evaporation, composition, structure. The selecting of the methods for variation of the copper evaporation intensity is based on known data. Most frequently, the evaporation rate is increased by increasing size of the evaporator and power of EB [4-6]. However, when 50 kW power and specific rate of copper evaporation from the water-cooled crucible 4 10^3 g/(cm^2 s) is exceeded, stability of the pool is violated: splattering of metal from the crucible takes place. Outburst of the metal may be partially avoided by introduction of alloying additives and arrangement of a multi-component pool on surface of the melt being evaporated (an intermediate pool) [8, 9]. In [9] the intermediate pool is called melt of the additive-metal, which restrictedly interacts with the base metal, occupies ≈ 10 % of the whole melt volume, and preserves on its surface. The main requirement to the additive-metal is lower density than in the metal-base, and vapors pressure within technological range of temperatures should be lower than that of the metal-base. From chosen by us alloying elements, zirconium completely and yttrium partially met these requirements. Density values of zirconium − 6.49 10^{-3} and yttrium − 4.55 10^{-3} are lower than those of copper − 8.92 10^{-3} kg/m^3. As far as vapors pressure is concerned, for copper and zirconium required difference is preserved, while for copper and yttrium it is not so significant (Figure 2) [10]. However, according to [9], zirconium and yttrium increase specific rate of copper evaporation. From analysis of Figure 3, presented in [9], one can see that alloying elements in copper melt accelerate evaporation of copper: zirconium − 2 times, vanadium − almost 6 times. There is no satisfactory explanation of evaporation rate increase in case of using an intermediate pool. It is assumed that increase of evaporation rate may be caused by surface tension and heat diffusivity of the melt being evaporated, which change during alloying [11].

However, peculiarities of phase equilibriums in binary systems Cu-Zr, Cu-Y, Cu-Nb, Cu-Fe and Cu-V may influence specific rate of the melt evaporation. Four intermetallic compounds (YCu_6, YCu_4, YCu_2, YCu) were detected in binary system Cu-Y, three of which melt congruently within temperature range of (935 ± 15)−(985 ± 15) °C. In the system Cu-Y also four eutectic transformations were registered, which proceeded within temperature range (890 ± 10)−(760 ± 15) °C and yttrium concentrations 12.5 - 74 wt.% [12]. There are six intermetallic compounds in binary system Cu-Zr, four of which melt congruently. All compounds participate in eutectic reactions within concentration range of zirconium content 8.85-55 wt.% and temperature range 971-885 °C [12].

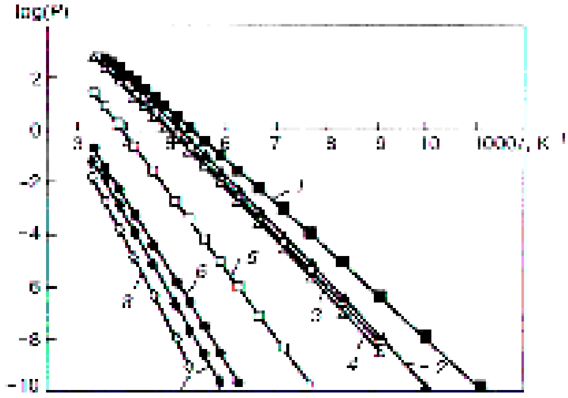

Figure 2. Dependence of vapor pressure of some metals on inverse temperature [10]:
1 – molybdenum; 2 – zirconium;
3 — niobium; 4 — vanadium; 5 — yttrium;
6 — iron; 7 - copper; 8 — chromium.

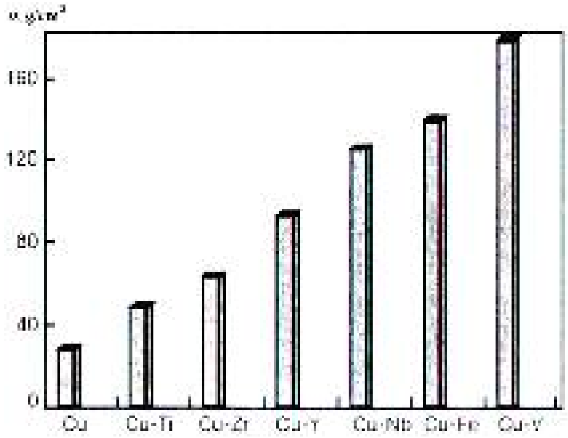

Figure 3. Change of specific copper evaporation rate v during alloying depending upon melt composition

So, the interaction of elements in each mentioned binary system exists within wide range of concentrations probability of formation of eutectic type melts with significantly lower melting point than that of initial metals. For binary systems Cu-V, Cu-Nb and Cu-Fe presence of areas of immiscibility and lamination (with the maximum, approximately, in equimolar area) is characteristic, and monotectic reaction, for example, in system Cu-V at temperature 1530 °C, and in system Cu-Nb at temperature 1550 °C [12].

This allows assuming possibility of morphology change of structural components of the system and properties of its capillarity and increase of evaporation rate at the temperature, which significantly exceeds copper melting temperature, which does not contradict data of [9] that prove increase of copper melt evaporation rate in presence of vanadium, niobium and iron additives.

In the process of development of technology for manufacturing massive Cu-Mo-Zr-Y condensed materials, samples of three alloyed pools were investigated, which ensured three rates of condensation that made up 16-20, 8-10, 4-5 μm/min, respectively. For investigation of pool materials optic and electron scanning microscopy, X-ray spectral microanalysis, and method of micro hardness were used.

Despite different values of density of alloying elements of yttrium and base metal (copper), lamination of components in the pool was not detected. Active interaction of these elements with copper, each other, and interstitial impurities was noted.

Phase composition of the pools, after solidification, corresponded mainly to binary diagram Cu-Zr, according to which in equilibrium with copper-base solid solution exists intermetallide $ZrCu_5$, which forms due to peritectic reaction, and intermetallide $ZrCu_4$, which represents a congruently melting compound.

Different mass shares of zirconium in these phases (in $ZrCu_5$ approximately 22 %, in $ZrCu_4$ – 26 %) and morphology of the latter (Figure 4) allow assuming that crystals of intermetallide $ZrCu_4$ of various shape form during solidification of the pool.

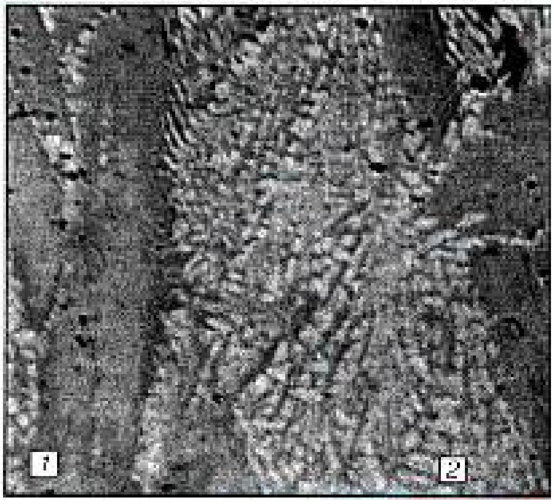

Figure 4. Morphology peculiarities of phases $ZrCu_4$ (1) and $ZrCu_5$ (2), ×200.

Intermetallide $ZrCu_5$ in the form of thin fibers precipitates in solid solution at the temperature below solidus, i.e. as a result of aging.

In solidified pool 1, which ensures maximum rate of copper evaporation, big anisotropic particles prevailed (Figure 5, ***a)*** with sizes sometimes equal to the pool depth (approximately 12 mm). It proves the fact that alloyed melt occupies the whole volume of the pool.

In pool 2, where average rate of copper evaporation was 8-10 μm/min, mainly anisotropic particles of intermetallide $ZrCu_4$ were registered having a shape of somewhat elongated hexahedron (Figure 5, ***b).***

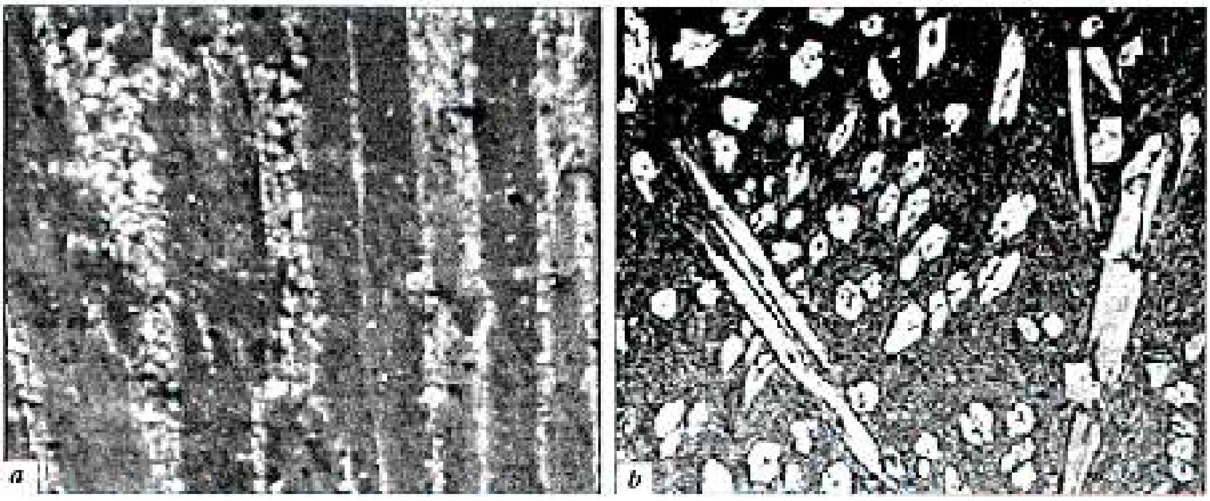

Figure 5. Melt structure of pools 1 (a − ×100) and 2 (b − ×50) after cooling.

In pool 3, for which minimum rate of copper evaporation is characteristic (4 − 5 μm/min), size of isotropic particles in dominant areas sharply reduced (Figure 6***, a).***

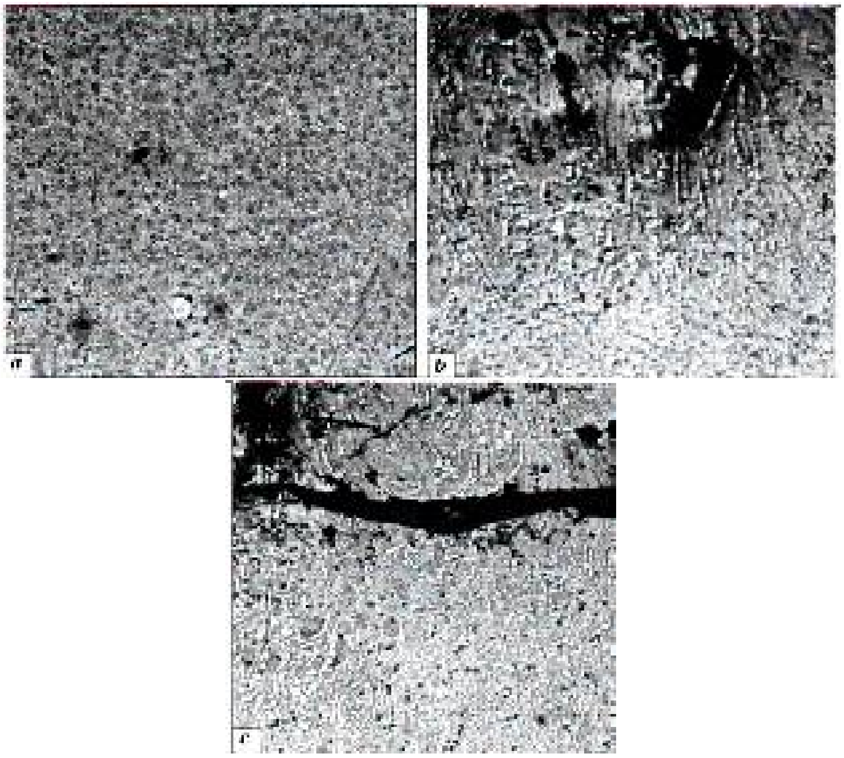

Figure 6. Pool 3 (a), structure in homogeneity (b) and slag inclusions (c) near its surface (×200).

Structure of the pool was inhomogeneous. Near surface of the pool accumulation of anisotropic particles $ZrCu_4$ was detected, as well as porosity (Figure 6, ***b)*** and slag inclusions in system Zr-Y-O (Figure 6, ***c***). Disperse (anisotropic or isotropic) phase $ZrCu_5$ (Figure 4) was present in investigated pools between particles of intermetallide $ZrCu_4$. In the near-bottom zone this very phase formed branched structure (Figure 7).

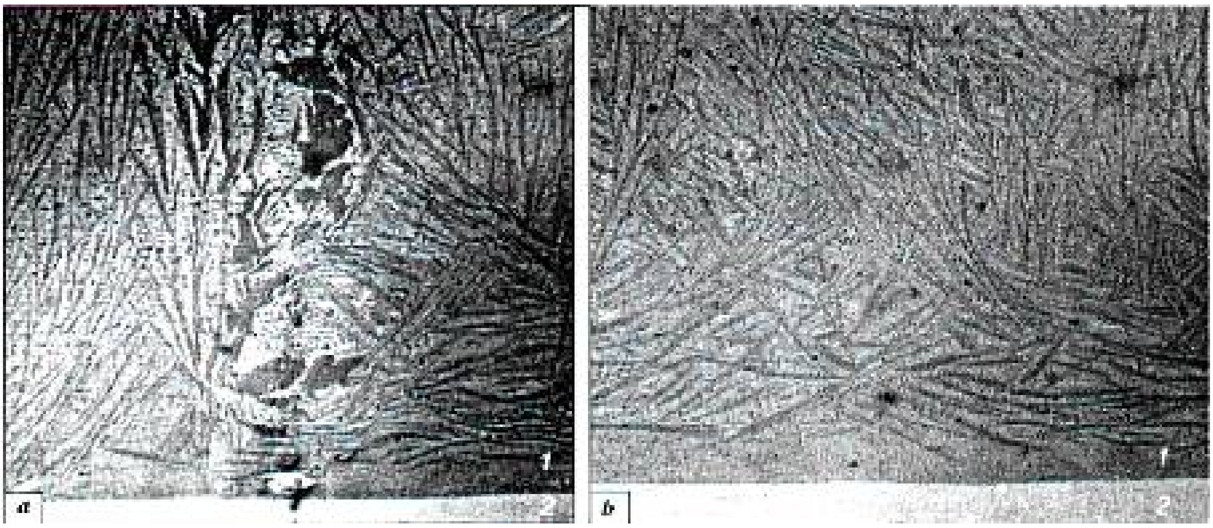

Figure 7. Structure of solidified melt (1) near boundary with copper ingot (2) irrespective of pool structure (×100): a − high; b − medium rate of evaporation

So, it was experimentally established that content and distribution of elements in the alloy Cu-Zr-Y with high rate of evaporation during solidification ensure formation of anisotropic structure, which is stipulated by directed growth of intermetallide $ZrCu_5$. Absence of sufficient knowledge about mechanism of melting and solidification does not allow authentic judging of the nature of detected interrelation. However, data of [13, 14] prove that the melt has to be considered as a crystal dispersed into clusters of 0.5-3.0 nm size. That's why one may assume existence of hereditary connection between structures of copper-base alloys in liquid and solid state and influence of ordering on the melt evaporation rate.

On the basis of established peculiarities of the structure, phase, and chemical compositions of the pools one may draw conclusion that phase equilibriums in copper-, zirconium- and yttrium-base systems, complicated by presence of impurities in commercially clean materials, have to be considered as some of the main factors which control rate of evaporation-condensation.

Efficiency of alloying elements is, probably, stipulated by their ability to change structure of the melt and its capillary properties. This assumption fits established in [9] two-fold increase of the copper-base melt evaporation rate in presence of zirconium and yttrium, which form intermetallic compounds and low-melting eutectics in correspondence with similar equilibrium diagrams.

Evidently the same analogy of equilibrium diagrams in systems Cu-Fe and Cu-V (presence of areas of immiscibility in liquid state and possibility of monotectic reaction proceeding at reduced temperature of the ingot, which determine structure of the melt) allows achieving even higher (4-6−fold) increase of evaporation rate in the presence of additives of iron and vanadium.

Condensate, its composition, structure and properties. Ratio of values of metal vapors pressure at various temperatures, composition and structure of the pool melt determine peculiarities of the condensate mass transfer and chemical composition.

As follows from presented data and results of mass-spectral analysis of copper condensate, containing alloying elements zirconium and yttrium used during its production, zirconium is mainly accumulated in the melt, while yttrium participates more actively in mass transfer. According to the results of this analysis, weight share of alloying elements varies in zirconium within 0.01-0.08 and in yttrium within 0.02 - 0.012 %.

The parameter, which allows qualitative estimating possibility of increasing intensity of the alloying element mass transfer, may be the temperature, at which pressure of saturated vapor, 133.3 Pa, is achieved [15]. For example, for iron, yttrium and zirconium it increases at 1923, 2128, and 2883 K, respectively. In the same sequence the content of elements in condensates Cu-Fe, Cu-Y, Cu-

Zr (6.08-9.43; 0.13-0.18; 0.02-0.08 wt.%, respectively) reduces [9]. These data don't contradict peculiarities of temperature dependence of vapor pressure of iron, yttrium, and zirconium (see Figure 2) [10].

The alloying elements into condensate, notably affect its mechanical properties (Table 1) [9].

Table 1. Influence of alloying elements on mechanical properties of copper-base condensate

Material	Mechanical properties of condensates at ***T***, **°**C			
	20		300	
	δ_t, MPa	δ, %	δ_t, MPa	δ, %
Cu	188	62	98	33
Cu-Y	213	53	79	34
Cu-Zr	192	56	115	50
Cu-Fe	318	33	118	25

The morphology of additive and its content affect properties of the initial condensate and intensity of its strength at the temperature 573 K. Maximum worsening of properties was registered when copper condensate was alloyed with iron. Tensile strength of the condensate reduces by 63 % and relative elongation **δ –** by 24 %. The lower reduction of property parameters by 40 and 11 % **–** takes place, when the condensate is alloyed by zirconium, whereby it should be noted that tensile strength and ductility of pure copper reduce at 573 K by 48%, in comparison with room temperature. Taking into account structural sensitivity of mechanical properties, one may assume that strength reduction is stipulated by the processes of recovery and ability of alloying elements to hinder these processes by means of action on phase composition, morphology, and dispensability of new phases. However, mechanical properties are affected, in addition to mentioned factors, by other factors as well. They are stipulated by application in technological processes of commercially pure initial materials and residual mediums. In this work, the influence of impurities on structure and properties was investigated on samples of composite material Cu-Mo-Zr-Y proceeding from the need of increasing the level, reproducibility of the condensate properties, and optimization of technological conditions of their manufacturing. As test specimens, samples of copper and molybdenum based materials have been taken from different lots, containing up to 12 mass % of Mo, 0,08 mass % of Zr and Y (for each of them) and for the rest, copper [3].

Samples were cut out from condensate sheets of 800 mm in diameter. Size of samples allowed sequential performing macro structural analysis of the surface, measuring thickness, density, electric resistance, hardness, and determining tensile mechanical properties. Surface and sections of the samples parallel and perpendicular to the vapor flow (before and after etching), and fractures were subjected to micro structural investigations [16]. Thickness measurement of the samples showed that condensate, formed during rotation of the substrate, may be represented in the form of a truncated toroid. Cuneiform shape is characteristic of the periphery. Here the thickness, in comparison with maximum for the toroid, reduces by (45 ± 3) %. Ion etching of section, perpendicular to the surface, allowed establishing that disperse-strengthened copper consists, as a gradient material, from micro-layers of different composition and morphology (Figure 8). For the layers, enriched with molybdenum, anisotropic (columnar) structure is characteristic (Figure 8, ***a),*** which, according to [17], forms as a result of connection of atoms from a volumetric diffusion field (VDF) of the condensed flow with 2D insular layers by diffusion coalescence. Different thickness of the layers occurs in this case as a result of formation of more efficient VDF and increase of rate and time of condensation of the fed vapors. For layers enriched with copper mainly isotropic structure is characteristic, which consists either of disoriented polygonal grains (Figure 8, ***b***), or from particles of spherical and (or) lenticular form dispersed in the matrix (Figures 8, ***c*** and 9, ***a).***

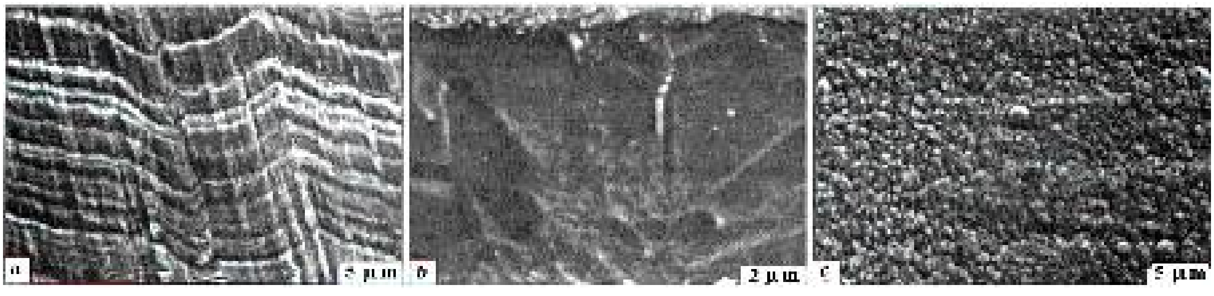

Figure 8. Condensate layers with columnar (a), polygonal (b) and spherical (c) shape of particles.

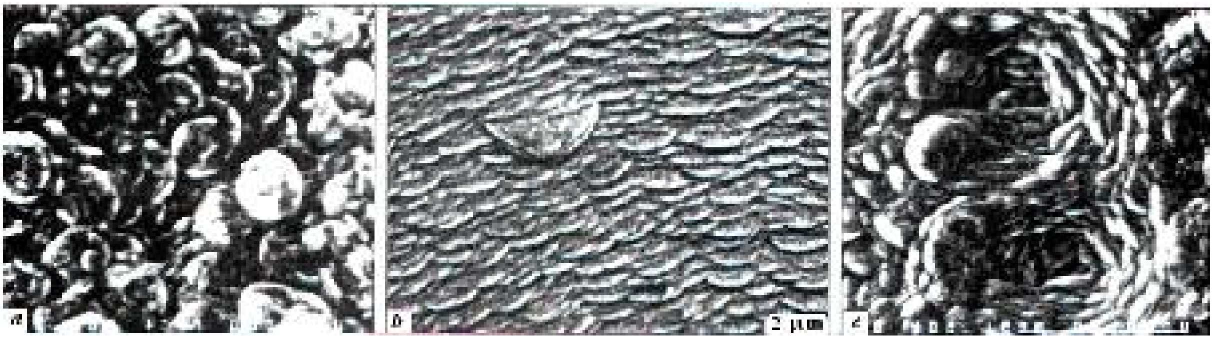

Figure 9. Mixed (a) and lenticular (b) structures of condensate and conglomerate from these particles (c) of this shape

Such analysis of sections of these condensate samples allows assuming that correct spherical shape of particles and respective morphology of layers are connected with aggregated transformation in copper in the direction vapor → liquid phase.

Lenticular shape of particles forms, evidently, as a result of coalescence of solid-liquid clusters of composite material Cu-Mo and origination of spherical particles during their approach to the substrate and deformation of these particles during their collision with the substrate and under action of the next portions of the «drop» vapor. This is proved by the shape of particles in Figure 9, ***a*** and ***b.***

Turbulence of vapor flow may be the reason of formation of different forms of conglomerates during consolidation of particles in micro layers (Figure 9, ***c***). Chemical etching of the section perpendicular to the condensate surface proves that in case of lower content of molybdenum, refractory component forms separated grains with $d \ll 1$ μm and conglomerates of these grains in the copper-base matrix (Figure 10). When content of molybdenum increases, chains of grains and anisotropic colonies form in the matrix.

Change of structure and chemical composition of micro layers fits peculiarities of the micro hardness change. Micro hardness increases together with increase of the share of columnar structure and molybdenum content in the layers. In the process of mechanical tensile tests of condensed composite material dependence of sample properties upon molybdenum content was also detected (Table 2).

In case of annealing of the samples (1173 K, 3h, vacuum), their strength reduces, ductility increases, but mean value of dispersion does not reduce. Ductility of samples, which correspond to periphery of the sheet, reduces because of lamination first of all along boundaries of macro layers enriched with carbon and other impurities.

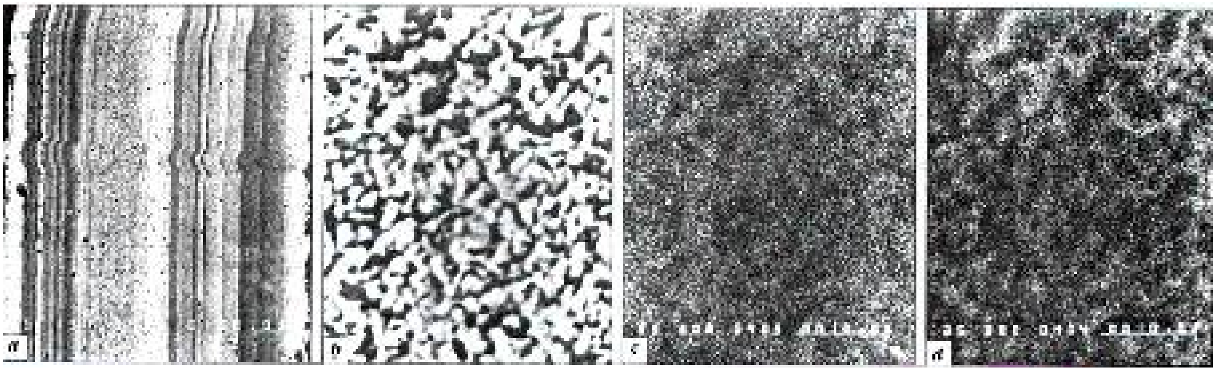

Figure 10. The grains in the copper-base matrix.

Table 2. Influence of annealing on mechanical properties of condensates

Composite materials with Mo concentration, wt. %	Initial state of composite material		Annealing of composite material at 900 °C for 3 h	
	δ_t, MPa	δ, %	δ_t, MPa	δ, %
2,5 … 5,0	518 ± 118	0,69 ± 0,53	543,0 ± 60,9	2,4 ± 1,1
8,0 … 12,0	659 ± 106	0	629,3 ± 61,3	0,79 ± 0,57

The mechanical characteristics of the condensed composite material with 8,0... 12,0 Mo content have been studied function of temperature.

Processing of the test results according to methodology of [18], which was carried out by us with determination of gross errors (blunders) in small samplings, allowed establishing step-wise character of strain activation energy change (Figure 11).

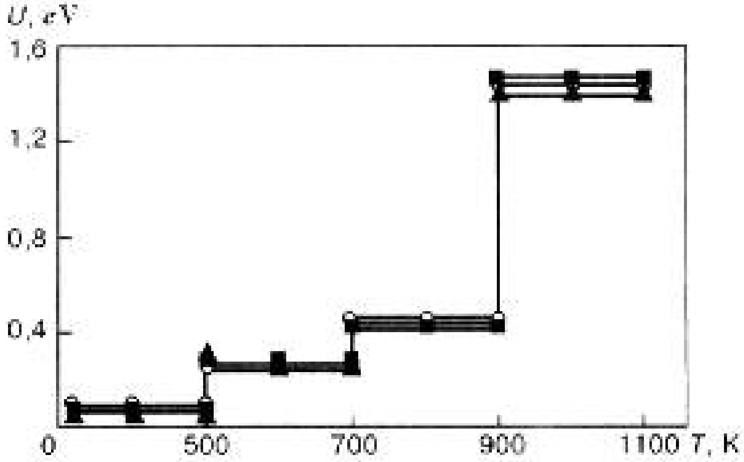

Figure 11. Temperature dependence of strain activation energy of composite material with Mo concentration 8,0 … 12,0 wt. % samples in tensile tests.

Comparative analysis of these data and peculiarities of fracture of samples of two lots allow assuming that strain activation energy is minimal and makes up 0.061-0.062 eV within temperature range 300-500 K and corresponds to strain localization near the notches on the surface. Maximum strain activation energy 1.467-1.462 eV within temperature range 900-1100 K for the same lots is connected with fracture toughness of the material with isotropic and columnar structure.

The results obtained don't contradict assumption made in [18] about change of strain mechanisms (dislocation slippage for dislocation creep age) during tensile tests of copper within the same temperature range. Data of fractographic studies expand our idea about peculiarities and role of structure defects of condensed composite materials as places of localization of plastic strain, origination and development of cracks, and failure.

Conclusions

Main technological factors (combination of conditions – preparation of a substrate, its rotation, alloying of the pool, conditions of the pool heating, etc.) which affect process of evaporation and structure formation of condensed composite materials are established.

It is shown that in case of copper alloying by the elements, which may affect rate of the melt evaporation, peculiarities of phase transformations in binary and more complex systems and possibility of morphology control of structural components and capillarity of a system in liquid-solid state have to be taken into account.

It is established that condensate surface at the condensation front is of block character with periodic and arbitrary striation according to roughness of the substrate. Behind condensation front lamellar structure with hierarchy of layers was detected, which had columnar, polygonal disoriented, composite (with spherical, lenticular or mixed shape) structure, varieties of which corresponded to the condensation mechanisms.

It is shown that in tensile tests of copper- and molybdenum-base condensates, which contained defects of structure, reduction and instability of mechanical properties were registered stipulated by combined or separate influence of defects on peculiarities of deformation and failure. In case of the tensile test temperature increase and change of the nature of structure defects, which determine localization of plastic strain, origination, development of cracks and failure match well stepwise change of strain activation energy.

References

[1]. M.I. Grechanyuk, V.O. Osokin, I.B. Afanasiev, I.M. Grechanyuk - ***Pat. 34875*** Ukraina. MPK C23C/20. Compozitionnai material dlia elecriceskih contactov i sposob ih proizvodstva, Opubl. 30.12.2002; Bul. Nr.12.

[2]. N.I. Grechanyuk, V.A. Osokin, I.B. Afanasiev, I.N. Grechanyuk ***Electronno-lucevaia*** tehnologhia polucenia materialov dlia electriceskih contactov, Electriceskie contacta i electrode: Sb. Tr. – Kiev: IMP NANU, 1998. – S. 51-66.

[3]. ***TU U 201/3410.001-98***. Materiala dispersno-uprocinennae dlia electriceskih contactov. – Vved. 01.05.98.

[4]. Movcian B.F., Malasenko I.S. - ***Jarostoikie pocratia, osajdaemae v vacuume.*** – Kiev: Nauk. dumka, 1983. – 230 s.

[5]. **Badilenko G.F., Osokin V.A., Krivasov A.K**. - ***Electonno-lucevoe isparenie i condensatia dvoinah splavov medi-itrii*** / Probl. spet. electrometallurgii. – 1989. – Nr. 1. – 230 s.

[6]. **Zuev I.V.** - ***Obrabotca materialov contentrirovannami potocami energhii***. – M.: MEI, 1998. – 162 s.

[7]. **C.d`A Hunt** - ***Pat. 335487*** USA, 1C3C23C. Prevention of splattering during vaporization processing. – Publ. 05.12.67.

[8]. **H.G. Cock, P.A. Zavrar., R.L. Hollen**. - ***Pat. 2156005*** France, 1C3C23C 13/00 HOIJ 19/00. Source de vapeur et procede de depot sous vide /– Opubl. 2709.72.

[9]. B.A. Movcian, V.A. Osokin, L.V. Pusecinicova, N.I. Grechanyuk ***Electronno-lucevoe isparenie*** i condensatia medi cerez vannu-posrednic, Probl. spet. electrometallurghii. – 1991. – Nr. 3 – S. 58-61.

[10]. **Nesmeianov A.N**. Davlenie para himiceskih elementov. – M.: Izd-vo AN SSSR, 1961. – 396 s.

[11]. Nijenco V.I., Floka L.I. - Poverhnostnoe natiajenie jidkih metallov i splavov. – M.: Metallurghia, 1981. – 208 s.

[12]. N.H. Abrocosova - ***Dvoinae*** i mnogocomponentnae sistema na osnove medi: Spravocinik, Pod. Red.. – M.: Nauka, 1979.

[13]. Maiboroda V.P., Spak A.P., Kunitkii Y.A. - Structurnae aspecta teorii plavlenia i zatverdevania. – Kiev: Academperiodica, 2002. – 124 s.

[14]. A.P. Spak, B.A. Melnik, V.D. Kralea i dr - ***Opredelenie*** rastvotov microoblastei v jidkih splavah, Protessa litya. – 1996. – Nr. 1. – S. 20-23.

[15]. L. Maissen, R. Gleng. - ***Tehnologhia*** tonkih plionok: Spravocinic, Pod. Red. – M.: Sov. radio, 1997. – S. 25.

[16]. R.V. Minakova, V.O. Osokin. M.I. Grechanyuk ta ins - ***Pro structurni*** apecta formuvania ta ruinuvannya condensovanogo compoziinogo materialu na osnovi midi, Electronnaya microscopia i procinisti materialov: Tr. IPM NANU. – Kiev, 2001. –

[17]. Perepletov V.I., Kosminskaya D.A., Kravcenko S.A. Z***aconomernosti structuroobrazovania condensatov slaboperesashennah parov Cu, Ti, Al si Cr*** // Tr. IMF NANU. – 2003. – 25, Nr. 6. – S. 725-735.

[18]. Krascenco V.P. Stetenco V.E. ***Vliyanie temperatura i scorosti deformirovania na osnovnae protessa, controliruyscie procinosti medi*** // Probl. procinosti. – 1981. – Nr. 4. – S. 78-83.

THE ANNALS OF “DUNAREA DE JOS” UNIVERSITY OF GALATI.
FASCICLE IX. METALLURGY AND MATERIALS SCIENCE
N^0. 2 – 2007, ISSN 1453 – 083X

EXPERIMENTAL RESEARCH REGARDING THE EVOLUTION OF SOME PARAMETERS OF THE SUPERFICIAL LAYER IN LOW CYCLE FATIGUE PROCESS

Silviu MĂCUȚĂ
“Dunarea de Jos” University of Galati
email: silviu.macuta@ugal.ro

ABSTRACT

The development of some mechanic engineering systems in, feasible to pressure vessels, aeronautics, ship building technology, requires a full investigation of the material features that are to be examined under a low cycles fatigue to strains close to the limit of the material elasticity. In this paper we present a testing machine at variable stresses in oligocyclic range. An own testing stand was patented by Romanian Standard Office, some results concerning the evolution of inner second order tensions, microhardness in superficial layer during low cycles fatigue process and the microscopic images of cracks, some results concerning the evolution of the crystalline lattice parameter, level of the texture were realised in steps of each two thousand cycles until a limit of 10^4 cycles. Two types of steel are tested.

KEYWORDS: low, cyclic fatigue, structure, superficial, layer, dislocation, density, texture

1. General considerations

The low cyclic fatigue of materials is a damage process that appears in various domain of engineering. This process can be finding during exploitation of some machines or aggregates subjected to a periodical or no just periodical action [2], [2], [13].

The boats during their going on sea or ocean are subjected to low cyclic fatigue. Similar process occurs during get off or landing of plane. Some vessels from chemical industry due to modification of pressure during charging or discharging are subjected to low cyclic process. During of this process the superficial layer of material suffers certain structural changes and their monitoring allow to establish the mechanism that leads at damage process. The structural changes in superficial layer are usefully in order to establish the history of material, as well as the next behavior of material. A systematic study of the structural changes is performed in frame of testing program of materials used in engineering where appear and develop the low cyclic fatigue process. Using an original testing machine some materials have been subjected to low cyclic fatigue process and by X-ray diffraction method the superficial layer of tested sampled was investigated. It was obtained information on fine structure of the superficial layer, namely: stress state, dislocation density, texture onto superficial layer as well as other mechanic characteristics as micro-hardness [4], [15].

2. Experimental methodology

In order to perform a complete study of the behaviour of the superficial layer during fatigue test and to evince the main factors, which determine the damage process, the structural cybernetic model was introduced. In Figure1 this model is presented and it allows to a systematic study of the input parameter changes under action of the commanding ones (Crudu & Macuţă 1991) [3].

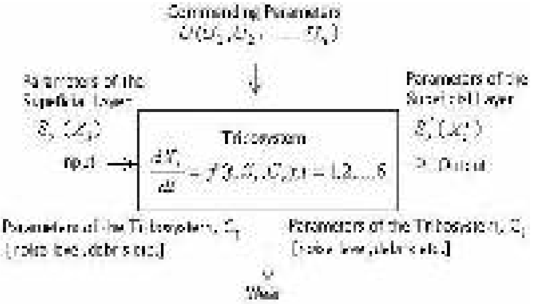

Fig.1. A cybernetic model used in study of friction process adapted in study of the low cycle fatigue process [15].

The input/out parameters are: superficial layer parameters (s_s-s'_s) [x_1- macro and micro-geometry, x_2 - microhardness and hardness, x_3 – tension state, x_4 – chemical composition, x_5 – structure, x_6 – purity] and tribosystem parameters (c_s) [noise, debris]. Some of the mentioned parameters, as x_2, x_3, x_5, can be changed from exterior such the durability of the material to be in a certain interval.

The commanding parameters (u) [u_1 – nature of material, u_2 – shape of the sample, u_3 – dimension of the sample, u_4 – working medium, u_5 – kinematics, u_6 – energetics] called external factors, by their action can change some superficial layer parameters x_i, i=1 – 6. In our experimental program the evolution of the x_2, x_3 and x_5 was showed by changing u_1 (type of steel: ol 52) and u_5 (testing frequency: ν_1=20 cycles/min, ν_2=40 cycles/min., testing deformation: ε_1=2000 μm/m, ε_2=2500 μm/m, ε_3=3500 μm/). In order to estimate the dislocation density the x-ray diffraction method was used.

3. Experimental

We have conducted the examination of material features in fatigue process for two steels used in pressure vessel engineering: OL 52 and 10TiNiCr180. Using laminate samples, the investigations have been realized at variable solicitations of pure bending on a patented machine (Buzdugan & Blumenfeld 1979). The tests have developed in a symmetrical alternative regime at two frequencies: f_1=20 Hz, f_2=40 Hz.

The deformation domain was established in an experimental program of tests using the resistive tensometry. The deformations of samples were imposed at the superior limit of elastic domain, evaluated from characteristic curves. The deformations imposed in case of OL52 were: ε_1=2000 μm/m, ε_2=2500 μm/m, ε_3=3500 μm/m and in case of 10TiNiCr180: ε_1=1500 μm/m, ε_2=2000 μm/m, ε_3=2500 μm/m, respectively.

In the present paper we presented the experimental results only for OL52 steel. The experiments were performed in steps of two thousand cycles until a limit of 10^4 cycles. In every step, we investigated the lattice parameter and texture level (Bogatet & Budaci 1980, Crudu & Macuta 1991). For this investigation we used an X rays diffractometer, DRON-3.

3.1. Results and discussions

In Figures 2 and 3 the evolution of the lattice parameter for OL 52 steel tested to fatigue process for three imposed strains, ε_1, ε_2 and ε_3 at two frequencies are respectively presented.

Analyzing those two figures, a general tendency of decreasing of the ferrite phase lattice parameter, is evinced, when the number of the testing fatigue cycles increases. This occurs for the all imposed strains. A strong decreasing is revealed for small strains and frequencies, respectively for high strains and frequencies. The change of the lattice parameter can be explained by supposing of a migration process of some alloyed elements during fatigue tests. This fact presents validity by a soft increasing of the lattice parameter during the fatigue test for an established testing cycle number.

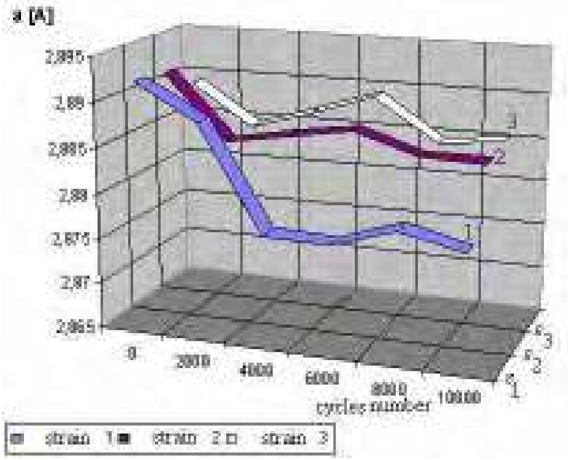

Fig. 2. Evolution of lattice parameter for f = 20 cycles/min [15].

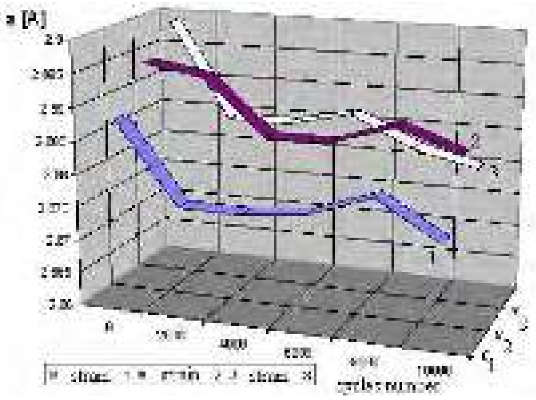

Fig. 3. Evolution of the lattice parameter for f = 40 cycles/min [15].

This increase appears more early when the strain is bigger. The migration process of atoms in and from elementary cell of the ferrite phase shows the existence of a high kinetic of atoms in the superficial layer during fatigue tests.

This kinetic can have negative effects if the material is tested in corroding media.

The migration process is more slowly in case of the small strain and more intensive at high frequencies and big strains; at small strain the process is more intensive at small frequencies. The presented data show that there is the possibility to command from exterior the durability of tested material by changes of the imposed strain and testing frequencies in a certain range. In Figure 4 and 5, for 20 cycles/min and 40 cycles/min, the evolution of the texture parameter, measured by ratio I_{max}/I_0, where I_{max} and I_0 are, respectively, the maximum intensities of the X-ray diffraction line (220) of the ferritic phase, for tested and non-tested samples, are presented.

From figures, an inverse texture (IT) process of material is evinced. The higher degree of the IT occurs in the case of the bigger strain, ε_3 [4]. This IT can be associated to some mechanical micro-processes that lead to a preferential orientation of the crystalline planes in [220] direction in relation to laminated state of material, when $I_{max}/I_0 = 1$.

From the view of presented histograms, can be analyzed the distribution of the texture degree of steel during fatigue tests and a relationship with plasticity properties can be established. At small frequencies the material presents a normal hysteresis, but at high value the inertial properties of material are smaller.

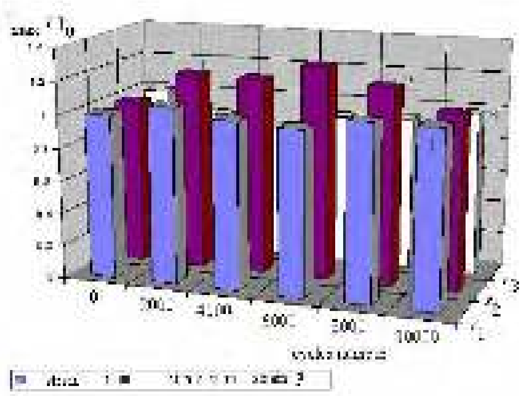

Fig. 4. Evolution of texture level for f = 20 cycles/min [15].

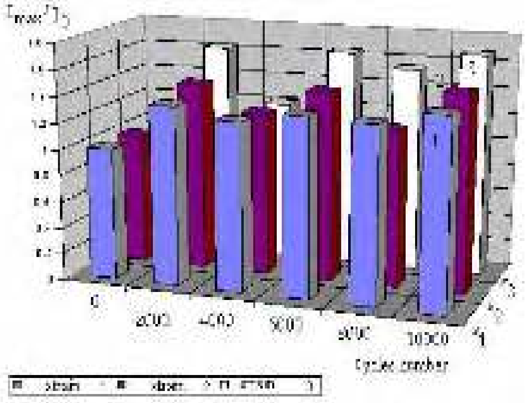

Fig. 5. Evolution of texture level for f = 40 cycles/min[15].

3.2. Conclusions

During fatigue tests, the lattice parameter presents a general tendency of decreasing when the number of the cycles increases, for those three strains and those two frequencies. The decreasing occurs in jumps and can be associated to a migration of alloying elements from steel. The migration process is strongly influenced by number of fatigue cycles and level of strain [4].

During fatigue tests, a texture process of ferrite phase occurs and it is influenced by level of strain and frequencies. The texture process, evinced by X-ray diffraction method, shows data about inertial properties of fatigue tested material. The steel looses the elastic properties when it is tested at high frequencies, the influence of strain being not very important.

3.3. Dislocation density

In our experimental is presented the evolutions of the $\left(I_f / I_{\max}\right)_{220}$ ratio (Buzdugan & Blumenfeld 1979) against of the testing cycles number for two frequencies are presented (20 and 40 cycles). For example this evolution is done for: OL52 steel, three imposed deformations, **ε**1, **ε**2, **ε**3, and a frequency of **ν**1=20 cycles /min (fig.6).

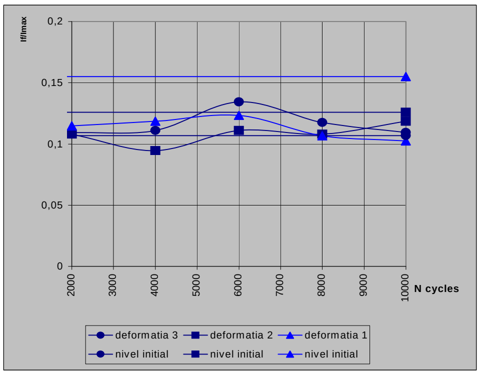

Fig. 6. Variation of the 220 on number of testing cycles for frequency ν1=20 cycles/min[15].

3.4. Analyses of the superficial layer microhardness

In Figure 7 and 8 the variation of the, HV, microhardness (Bogatet & Budaci 1980) on number of testing cycles, for ε_3=3500 **μ**m/m and the two testing frequencies are presented.

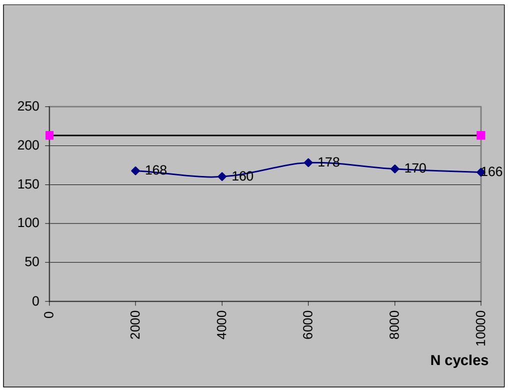

Fig. 8. Variation of microhardness vs testing cycles for v = 40 cycles/min[15].

There is a jumps decreasing of the HV by hardening and softening processes.

At low frequency this decreasing is lesser like in case of high frequency for the **SAME** imposed deformation. This shows that the hardening and softening process occur with different speeds.

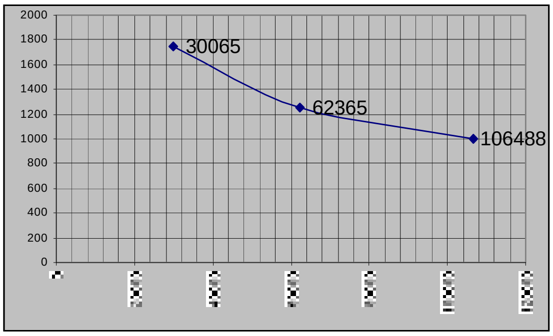

Fig. 9. Experimental Wöhler curve[15].

4. Aspect of wöhler curve

The tests have developed in a symmetrical alternative at two frequencies. The testing frequency of the samples was of 20 and 40 cycles/ min. In paper the results refer to testing frequency of 40 cycles/min. During fatigue test the temperature measurements showed a variation small 2^{o}C, the temperature effects being without importance. In Figure 9 the experimental Wöhler curve is presented.

4.1.Macroscopic aspects of the cracks

Like general aspect, in each case, Figures 10, 11 and 12 the damage process by fatigue test is initiated at sample surface in places where the microscopic flows are presented.

The tested samples present in damaged surface a smooth aspect and an area characteristic to damage.

In Figure 6a, the aspect of tested sample is presented. It can see the presence of sliding bands near crack. This appears due to relative big propagation speed of deformations into crystalline grains having favorable orientation and small relative intensity of total deformation. In deformation process in elastic-plastic range the weigh of plastic deformation is relatively big in a small time testing (N_r = 30065 cycles until damage) at deformation ε_3 = 3500 μm/m (ε_3 real = ε_3/2). The weigh of damage surface by fatigue process is small and located in vicinity damaging initiator. This is showed in Figures 10b, 10c.

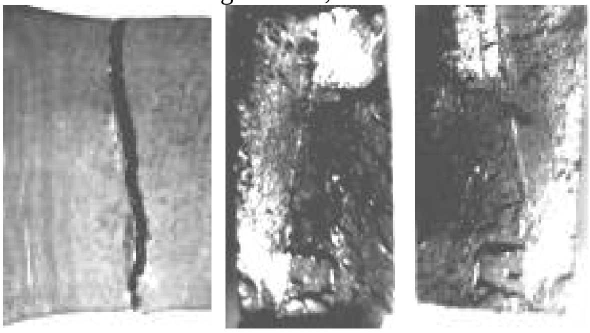
a b c

Fig. 10. Macroscopic aspects of crack for ε_3 = 3500 μm/m[15].

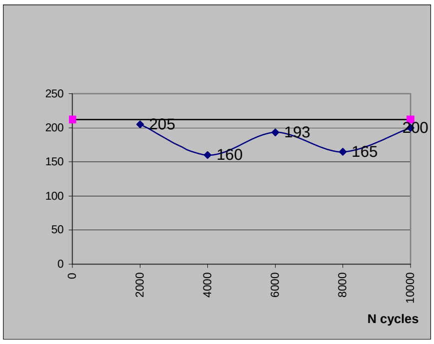

Fig. 7. Variation of microhardness vs. testing cycles for v = 20 cycles/min[15].

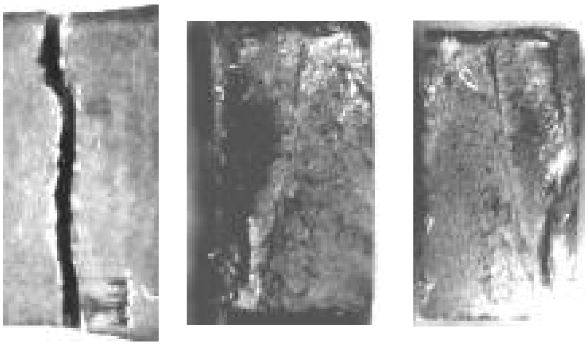
a b b

Fig. 11. Macroscopic aspects of crack for ε_2 =2500 μm/m[15].

In Figure 11a it is presented, for a deformation of ε_2 = 2500 µm/m, the shape of the sliding bands in vicinity of the damage area. The sliding bands have a high fines degree due to extension of elastic- plastic range into more time interval and a big number of cycles (N_r = 62635 cycles until damage). It is considered that the weigh of the plastic deformation in the whole elastic-plastic range is smaller comparatively with previous case. In Figures 11b, 11c the damage surface presents a large smooth area in vicinity of the damage initiator and it is developed on the whole of width of sample. The damage surface appeared in a located area well established.

In Figure 12a on the smooth surface, sliding bands appears for a very big number of fatigue cycles (N_r = 106488 cycles until damage) at a big distance of damage zone. The explanation consists in the fact that the deformation speed is relatively reduced and the plastic deformations will be taken at next fatigue cycles in neighbor zones with smaller deformation resistance. The extension of the plastic deformations in vicinity of damage zone is explained by propagation of the plastic deformations to grains situated in deformed zones [8].

In Figures 12b, 12c a large damaged zone is evinced that is developed on the whole of width of sample, having a bilateral aspect. This can be explained by fact that the propagation speed of the failure surface is small and allowed the initiation of the failure by fatigue from a zone located in opposed side.

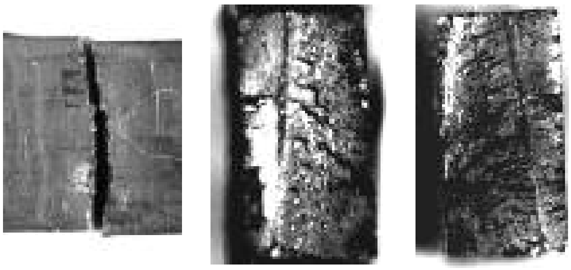

a b c

Fig. 12. Macroscopic aspects of crack for ε_2 =2000 µm/m[15].

5. Conclusions

By extension of the tribolayer and tribosystem concepts to the study low cycle fatigue process of the steel, the structural changes in the superficial layer are shown. It was evinced a microfatigue process that is strongly influenced of frequency testing, deformation level, and number of the fatigue tests.

.

The general releasing process occurs by microproceses of tensioning and releasing of the crystalline lattice. Their amplitude and periods depend of frequencies and imposed deformations [1].

Evolution of the second order tensions can be correlated with evolution of the microhardness in ferrite grains as well as with the density sliding bands (Fouquet 1979). Our results can be used in order to explain the damage mechanism of the tested samples subjected to low frequency fatigue test and high tensions.

The researches concerning micro and macro aspects of the fatigue failures at big tensions and low fatigue cycles will be continued in order to establish the relationships with structural changes occurring at lattice level.

References

[1]. Heuler, P.ş.a. , 1986, ***A criterion for omission of Variable Amplitude Loading Histories***, Int., Journal of Fatigue, 8, nr.4.

[2]. Bogatet, K. & Budaci, T., 1980. ***Sovremennie sredstva dlia ispîtanii na maloticlovaia ustalosti***, Laboratoria nr. 7/1980, pp. 654-658.

[3]. Crudu, I., Măcuţă, S., ***Universal machine for testing materials***, Invention No 102714/1991, registered in Romania.

[4]. Gheorghies, C., 1990. ***Control of fine structure of metal by X-rays***, Technical Publishing House Bucharest .

[5]. Karpenko, G., Katov, K.B., Kokotailo, I.V. & Rudenko, V.P., 1977. ***Maloticlovaia ustalosti stali v rabocih sredah,*** Kiev.

[6]. Lieurade, M.P. 1987. ***La rupture par fatigue des aciers***, Collection IRSID OTUA- Propriétés d’emploui des aciers- études de base, Paris.

[7]. Măcuţă S., Gheorghieş C. , 1998, ***The Evolution of some Parameters of Superficial Layer in Fatigue Process***, 15-th Symposion “ Danubia-Adria “, Bertinoro, Italy.

[8]. Măcuţă S., Gheorghieş C. , 2001, ***Experimental researches regarding structural changes during low cycles fatigue process for some steels used in machines construction***, International Conference on Advanced in material and processing Technologies AMPT’01, Leganes-Madrid, Spania.

[9]. Mocanu, D.S., 1982. ***Materials testing,*** Vol I-II, Technical Publishing House Bucharest.

[10]. Puskar, A., 1989. ***Microplasticity and failure of metalic materials*** Bratislava.

[11]. Strijala, V.A., 1987. Malotiklovaia ustalosti pri nizkih temperaturah, Kiev.

[12]. Troscenoko, V.T., 1985. ***Ticliceschie deformatii I ustalosti metalov***, vol I, Kiev.

[13]. Stanzl S.E., ***Lifetime Measurement For Random Loading In Very High Fatigue.*** Int. Journal of Fatigue, Oct 1986.

[14]. Suresh S., ***Fatigue of materials***, Cambridge University Press, 1991, Great Britain, Cambridge

[15]. Măcuţă S., ***Studiul comportării unor oţeluri la solicitări variabile la tensiuni mari şi număr mic de cicluri*** Universitatea „Dunărea de Jos” din Galaţi, cond. ştiinţific Prof.univ.dr.ing. Ion CRUDU, 1999.

[16]. Măcuţă S. , 2007, ***Oboseala oligociclică a materialelor***, Editura Academiei Române, Bucureşti.

THE ANNALS OF “DUNAREA DE JOS” UNIVERSITY OF GALATI.
FASCICLE IX. METALLURGY AND MATERIALS SCIENCE
N^0. 2 – 2007, ISSN 1453 – 083X

STRUCTURAL AND TRIBOLOGICAL ASPECTS ON Ti(C,O,N) MAGNETRON REACTIVE SPUTTERED THIN-FILMS

Daniel MUNTEANU[1], Camelia OLTEANU[1], Cristian IONESCU[1], Alexandru MUNTEANU[1], Filipe VAZ[2], Luis CUNHA[2]
[1]Transilvania University of Brasov, Romania
[2]Universidade do Minho, Guimaraes, Portugal
email: muntean.d@unitbv.ro

ABSTRACT

Magnetron sputtering is a flexible technique and allows producing a significant amount of types of coatings. Within the frame of present work, Ti-C-O-N thin films were deposited onto high-speed steel (AISI M2), substrates by reactive dc magnetron sputtering in a laboratory-size deposition system. It consisted of two vertically opposed rectangular magnetrons, in a closed field configuration. The films were prepared using dc power source on a titanium target (99.6 at.%). A gas atmosphere composed of argon (working gas), acetylene and nitrogen/oxygen (17:3) reactive mixture was used for the depositions. In terms of structure, the samples produced only with ethylene and argon flow reveal a TiC structure (NaCl type). The decrease of $\Phi(C_2H_2)/\Phi(O_2+N_2)$ induces amorphisation, but TiC structure, with possible N and O inclusions, is still detected. In terms of tribological aspects, the static friction coefficient and roughness (R_z) were analyzed and discussed depending of composition and structure.

KEYWORDS: magnetron, sputtering, roughness, friction

1. Introduction

During the last years, there have been several attempts to improve the properties of diamond-like carbon (DLC) films by the addition of other elements, such as silicon, nitrogen and varios metals. Many modifications have been tried and the addition of, for example, nitrogen, has shown to reduce the inner stress, electrical resistivity and friction coefficient [1]. In the same manner, oxygen has always been looked upon as an interesting element in thin film materials, not only because of its high reactivity with most metals, but also due to the changes that induces in chemical bonding states, and in the material’s electrical, optical, and mechanical characteristics.

Titanium carbonitride coatings Ti(C,N), are used mostly to improve tool life by combining the properties of TiN and TiC. The advantages of these coatings over other coatings material, stem from its superior friction behaviour in contact with steel, high hardness and residual stress [2]. Because of their low friction, the coating is durable at slow cutting speeds especially [3]. The combined effect of low friction behaviour and high residual stress help preventing cutting-edge deformation for high speed steels, and on carbides reduces the cutting-edge chipping. Moreover, it provides excellent resistance to wear due to the coating high hardness [4]. Adding oxygen to the film is a possibility to improve the coating’s characteristics. The presence of oxygen allows the tailoring of films properties between those of metallic-like carbides and those of the corresponding ion oxides, and from these a wide range of applications. It is expected that the Ti(C,N,O) films will exhibit good resistance to friction wear and corrosion due to the small atomic size of oxygen, witch creates high hardness and a compressive stress state [2,5,6].

In the present paper the Ti(C,N,O) thin films, with various compositions, were deposited in a closed field unbalanced reactive d.c. magnetron sputtering system, varying the $\Phi(C_2H_2)/\Phi(O_2+N_2)$ flow.

Sputtering is one of the most commonly used methods for the deposition of thin films. Its popularity stems from simplicity of the physical processes involved, versatility of the technique, and flexibility for alteration and customisation. It is widely used in the semiconductor, photovoltaic, recording and automotive industries. In addition, specialised applications of sputtering in the manufacturing of sensors, decorative glasses, optical devices, etc, are also very common.

High melting point materials like ceramics and refractory metals, which are hard to deposit by evaporative techniques, are easily deposited using sputtering. Sputtering techniques range from a simple dc glow discharge, which is limited to the sputtering of conductive targets, to RF sputtering where any target regardless its conductivity can be sputtered, to a more sophisticated ion beam sputtering (IBS) in which very controlled deposition of material is possible.

In terms of deposition rates, there are sputtering techniques now available, which rival evaporation or other higher deposition rate techniques. The purpose of using a magnetic field in a sputtering system is to make efficient use of the electrons and cause them to produce more ionisation [7].

Taking into account the fact that unbalanced magnetron (the magnetic field lines does not all close on the cathode surface) sputtering was used in this paper, an image is presented in figure 1.

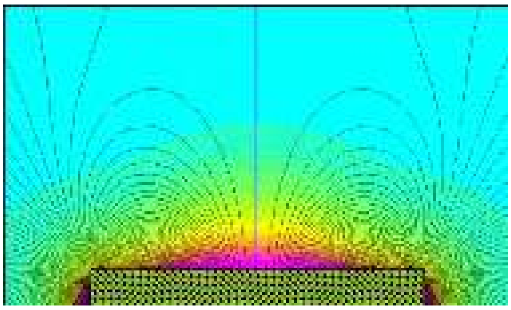

Fig. 1. Unbalanced magnetron [8].

2. Experimental details

Within the frame of present work, Ti-C-O-N thin films were deposited onto high-speed steel (AISI M2), substrates by reactive dc magnetron sputtering in a laboratory-size deposition system. It consisted of two vertically opposed rectangular magnetrons, in a closed field configuration.

The films were prepared using dc power source on a titanium target (99.6 at.%). A gas atmosphere composed of argon (working gas), acetylene and nitrogen/oxygen (17:3) reactive mixture was used for the depositions (as shown in table 1).

The deposition was carried out using a laboratory-size deposition system. During deposition the working pressure was approximately constant at 0.4 Pa and the bias voltage was -70V. In all the cases the deposition time was kept at 3600s.

Table 1. Gas flows (experimental variants)

Samples	Gas flow [%]		
	C_2H_2	O+N	Ar
TiCON 1	3	11	12
TiCON 2	5	8	12
TiCON 3	2	16	12
TiCON 4	2	8	15
TiCON 5	2	20	15
TiCON 6	1.5	6	15
TiCON 7	1.5	10	15
TiCON 8	1.5	18	15
TiCON 9	1.5	25	12
TiCON 10	1.5	0	15

The atomic composition of the as deposited samples was measured by electron probe microanalysis (EPMA) in a Cameca SX-50 apparatus. The crystallographic structure was investigated by X-ray diffraction (XRD) in the Bragg-Bretano configuration, using monochromatic Cu Kα radiation. Atomic Force Microscopy (AFM) - 5x5 μm line scans was used for roughness characterization. The static friction coefficient values were established, for each sample, in different-friction condition, using a plane fixed half-couple manufactured by heat treatable steel (AISI B7), in annealing heat-treatment conditions. The friction plane fixed half-couple had a lot of roughness R_z values, comprised between 0.4 and 2.5 µm. The work with different roughness values of fixed plane half-couple is important in order to could take into consideration the possible influence of sliding – plane roughness on friction process and to have finally an average value of static friction coefficient.

Before the tribological tests, the samples were first degaussed and then alkaline cleaned and wiped. The fixed half-couple was also degaussed and periodically alkaline cleaned and wiped. According to the method description, 10 friction tests were performed for each sample on each half-couple: 5 in one direction and 5 abeam, such as the one-way roughness would not influence the moving of the samples. In each case, the utmost values were eliminated. The environmental conditions of tribological tests were: T = 23.5^{o}C and 63% humidity.

3. Results and discussion

The measured values of the friction coefficient vary between 0.2 and 0.39, while the roughness values range from 0.13µm to a maximum of 0.21µm. The results showed a correlation between the friction coefficient and roughness evolution with the growth of the C_2H_2/(O+N) flows ratio (figure 2).

A simultaneous growth of the friction coefficient and roughness can be observed up to a 0.25 value of the $C_2H_2/(O+N)$ ratio, then the parameters register an abrupt decrease on the flow value interval from 0.25 to 0.3. After this critical value of the $C_2H_2/(O+N)$ flows ratio, the two parameters evolution is stable.

As a conclusion we could underline the existing dependence between static friction coefficient (μ) and roughness (R_z); these parameters are both increasing or decreasing on a certain interval of flow values.

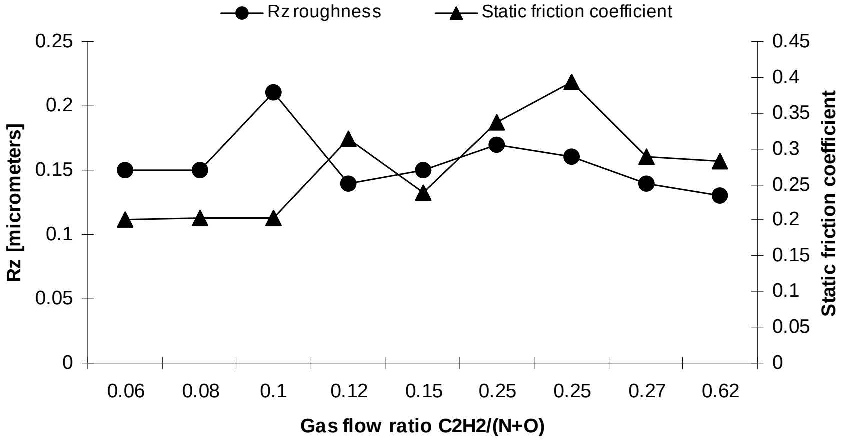

Fig. 2. Influence of gas flow ratio on friction coefficient and roughness.

In terms of the chemical composition, the results showed that, at 0.25 gas flow ratio the carbon percentage moves from an abrupt growth to a slower growth. The amount of titanium present an emphatically decrease around 0.25 gas flows ratio, while the oxygen starts growing and the nitrogen percentage is changeless (steady) for a short interval and starts a slow decrease around 0.3 gas flow ratio (figure 3).

From a tribological point of view, we can say that the growth of the oxygen percentage it is linked to the decrease of the roughness and friction coefficient values. Also, a decrease in the titanium percentage leads to a decrease of roughness and friction coefficient.

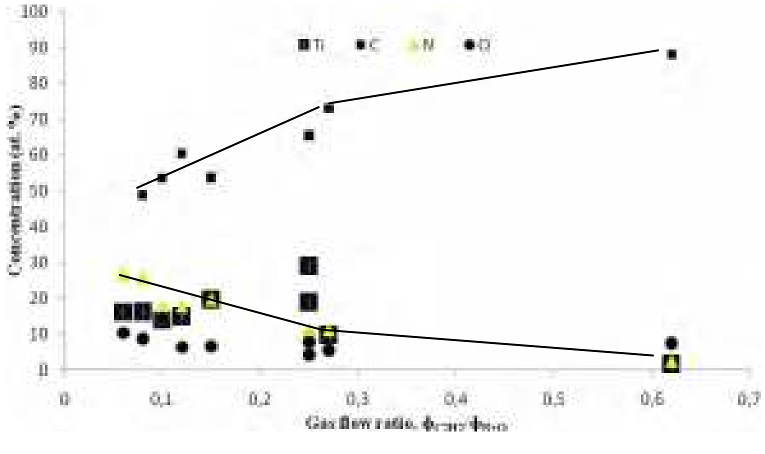

Fig. 3. Corelation between concentration and gas flow ratio.

4. Conclusions

TiCON thin-films were prepared by reactive magnetron sputtering on high-speed steel (AISI M2) substrate, using a mixture of C_2H_2 and (N_2+O_2) as reactive gases. The static friction coefficient and Rz roughness seams to have the same behaviour with the increasing of carbon percentage in the film. The maximum values for friction coefficient were registered at about a value of 0.25 for $C_2H_2/(O+N)$

flows ratio, zone where is supose that the TiC cubic lattice begins to dezorganize. In terms of concentrations, this point (0.25) marks a tendency for keeping almost constant the C and N concentrations in the films with the increasing of C_2H_2/(O+N) flows ratio.

References

[1] **Fernandes A., Carvalho P., Vaz F., S. Lanceros-Méndez A.V. Machado, N.M.G. Parreira , J.F. Pierson , N. Martin**, ***Property change in multifunctional TiCxOy thin films: Effect of the O/Ti ratio,*** Thin Solid Films 515 (2006) 866–871, www.sciencedirect.com, 2006;

[2] J.**H. Hsieh , W. Wu , C. Li , C.H. Yu , B.H. Tan**, ***Deposition and characterization of Ti(C,N,O) coatings by unbalanced magnetron sputtering***, Surface and Coatings Technology 163 –164 (2003) 233–237, www.elsevier.com/locate/surfcoat, 2003;

[3] **Baravian G., Sultan G., Damond E., Detour H**., Surf. Coat.Technol. 76/77 (1995) 687.

[4] Knotek O., Loffler F., Kramer G., Surf. Coat. Technol. 61(1993) 320.

[5] Y. Shi, H. Peng, Y. Xie, G. Xie, C. Zhao, Surf. Coat. Technol.132 (1998) 26.

[6] Stanishevsky A., Lappalainen R., Surf. Coat. Technol. 123(2000) 101.

[7] Munteanu D., Vaz F.,.Munteanu A, Schreiner A.,.Ionescu C,.Olteanu C,.Borcea B, ***Straturi subţiri de tip Ti-Si-C şi Ti-O-C obţinute prin pulverizare reactivă în sistem magnetron,*** Editura Universităţii Transilvania, Brasov, 2007***;***

[8] www.pvd-coatings.co.uk

THE ANNALS OF “DUNAREA DE JOS” UNIVERSITY OF GALATI.
FASCICLE IX. METALLURGY AND MATERIALS SCIENCE
N^0. 2 – 2007, ISSN 1453 – 083X

ELECTROMAGNETIC STRIP MILLS' DRIVING ROLLERS METALLISATION ADVANCED TECHNICS

Petra MOTOIU[1], Daniela DUMITRESCU[1],
Cornel FRATILA[1], Dacia TRUSCA[2]
[1]*National R&D Institute for Nonfferrous and Rare Metals, IMNR. – Bucharest, Romania
[2]SC PLASMAJET SRL, Măgurele, Romania
email: petramototiu@yahoo.com

ABSTRACT

The continuous increase of the applications of thermal sprayed coatings together with the demand for layers having always more and more enhanced performances and properties stimulates the research activity toward the development of new coating materials and alloys.

To meet this goal, new complex alloys, based on the Fe, Si, B, Mo, Cu, W system, are here considered, through the development of new and innovative powders to be used, as powders directly or as a wire form, for thermal sprayed coatings to improve wear and corrosion resistance, as well as thermal fatigue properties of the electromagnetic strip mills' driving rollers, highlighting the materials performances and attaining economical and environmental advantages.

KEYWORDS: thermal spraying coating, plasma jet, hard facing, surface engineering

1. Introduction

The optimal performance of a component is to a great extent determined by the state of the surface, because every work piece is exposed to several strains, namely mechanical, thermal, chemical or electro-chemical, radiation stresses, which often have their maximum in the surface area. Owing to the presence of this complex strain most failures of machine components start within or close to the surface. The high importance of the surface in regard to the lifetime of a component justifies the term “surface engineering”, which combines the knowledge of different scientific disciplines and deals with the design of a composite system which has properties, that cannot be achieved by either the surface layer or the bulk component alone [1].

Surface engineering can be seen as one of the key technologies of the present days, permitting to lengthen the lifetime of the products, simultaneously reducing costs and saving natural resources.

The surface of a component can be changed through a various amount of surface treatments.

2. Experimental researches and results

The processing powder experiments from the FeCrSiNiMnC system were realized using an atomization device of the metallic melt with water at high pressure.

The chemical composition of the obtained powders is presented in ***Table 1***.

Table 1. Chemical composition of powders

Powder type	**Chemical composition, %**										
	Fe	**Co**	**C**	**Cu**	**Al**	**Cr**	**Mn**	**B**	**Si**	**Sn**	**Zn**	**Ti**
Charge I	base	0.012	0.026	0.38	0.082	0.92	1.20	1.12	2.00	0.034	0.042	<0.005
Charge II	base	0.018	0.65	0.09	<0.005	11.53	0.98	2.09	2.04	<0.005	0.016	0.012
Charge III	base	0.017	0.87	0.06	0.020	15.80	1.86	2.66	3.90	<0.005	0.016	0.040

The experimentations continued with the coating of an OL 37 metallic surface (unalloyed steel) by plasma spraying of the complex alloys, based on the Fe, Si, B, Mo, Cu, W system powder. The applied complex alloys coating will allow its usage into industrial processes where special materials are needed. [5,7].

The coating experimentations were made with the help of a METCO 7 M plasmatron, the obtained spraying parameters being presented in the ***Table 2.***

Table 2. Optimum Coating Parameters

Argon and hydrogen flow [$m^3.h^{-1}$]	**Power plasma flame [kW]**	**Spraying distance [mm]**	**Spraying speed [$m.s^{-1}$]**	**Temperature of base material [^oC]**	**Thickness of coating [mm]**	**Powder flow [$kg.h^{-1}$]**
Ar+20 vol.%H_2 37	80	60, 80, 120	0,3	140 ± 5	0,5	0,7

The technological operations of the complex alloys, based on the Fe, Si, B, Mo, Cu, W system powder plasma spraying process underlines its main steps. It must be taken into consideration the fact that respecting the operational parameters is determining for suitable coatings.

The preliminary thermal plasma coating experimentations were made upon numerous probes, taking into account a lot of factors which influence the final structural and physical-mechanical characteristics of the experimental samples.

There are two coating aspects which must be taken into consideration:

- The contact with the metallic surface
- The internal interactions

Due to the fact that each separated particle strikes the surface and it is flattened by the powerful shock, the result is a local contraction of each particle which is somehow compensated by the material yield [1, 4, 5].

The correct choice of the plasma gas represents an important factor regarding the reactions type which can be generated at the metal-base interphase, finally a suitable surface resulting.

In order to achieve minimum expenses and a maximum heat transfer, argon is used with a 10 to 20 % H_2 addition, [7].

For pure theoretical operations, in order to avoid any possible reaction with the plasma gas, pure argon is used.

Generally, the process must take place so that the plasma gas shouldn’t react with the metallic base which has to be coated.

Macro structural studies allow examining the obtained surfaces. Samples with special prepared surfaces are used, in order to underline the present phases and the metallographic constituents.

The sample was prepared with solution attack. A HNO_3 and CH_3COOH solution mixture was used. From metallographic analysis we can see a good density of the layer and a very good adherence to under layer.

Figure1 show the metallographic aspect of layer obtained through spraying method.

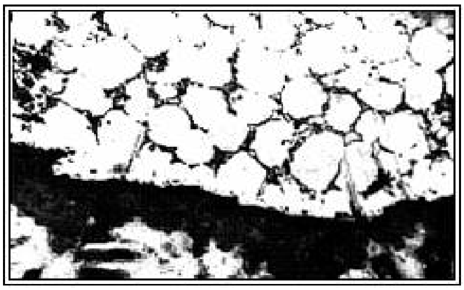

Fig.1. Metallographic of the new coat (x500).

Also we can see the beginning of diffusion phenomenon at the interface layer/under layer.

From place to place there are mini-hollows in the mass of the new layer, [7].

The structure, density and composition of the layers have been modified in order to be able to give the wished technological function to the new layers.

Among all these, the modification of the density of the new formed layer is the main use of these operations.

Warming and melting of the coverings have been used throughout heat application, after covering, using lasers, electrons flows, heating through induction, plasma jets or flames.

The existing barriers in using these technologies include the processing supplementary costs, the control of the thermal tensions which appear during remitting and solidification and ultimately the apparition of new unwanted phases in the fusion zones.

The melting may occur on the surface, in the middle or deep inside the contact zone with the under layer.

It is necessary that the used powders should have an extremely fine granular structure, the porosity being maintained at a 0.5 % maximum. A low porosity has positive consequences upon the final layer, increasing adherence between the particles and the traction strength of the layer itself.

Most of the industrial applications need very thin layers. As a consequence it is important as the adherence between the cover layer and the base one should be obtained without a middle coating layer.

First of all the nature of the adherence is due to: the high temperatures of the materials used, the fine structure of the particles and the very high speed of spraying in oxygen or helium atmosphere, the result being an extremely high resistance of the layer adherence, [2, 3].

From the details presented above about the powder fineness of grain and density it is obvious that the sprayed industrial coatings can endure the most complicated finishing techniques in order to obtain a perfect smooth surface.

The processing of the new formed layer after coating is used in certain applications in order to modify and improve the coating characteristics.

Sub missed to ultra – finishing techniques, the layers obtained by plasma spraying (industrial coatings) may reach a 2 – 5 RMS finishing degree, which represents a very satisfactory value even for the most pretentious industries, [8].

The advantages of a chosen bulk-surface system can be related to reduced production costs, failure of the part without damaging the whole machine or even risking human lives, possibility of local repair of damaged machine parts, minimal variation of the original design, energy and resource saving as well as environmental protection.

In this contest the perspective of the coating industry is a very good one. Besides the combination of new or known processes, coating engineering gains interest towards multi-layer coating. The internal layer is responsible for a good adhesion to the substrate, there is a gradually change of the properties with each additional layer so that the outer layers have the optimal properties to fulfil the functions they are designated for.

3. Conclusions

The data from this paper confirm the fact that the powder obtained by high pressure water atomisation of studying alloy has a good behaviour when flame sprayed.

The properties of the surface of a component greatly influence its performance and lifetime, among the numerous and different surface treatments useful to improve the properties of a surface, thermal spray processes gained great interest and allow many advantages, being able to produce large assortment of wear and corrosion resistant protective layers.

Moreover, the presence of porosity may constitute an optimal base, providing adhesion between substrate and applied coating, without the requirement of additional operations, like grit blasting, to roughen the substrate surface.

The contact between the implicated components in the thermal spraying process presents rugose surfaces; there are large contact surfaces between the coated layer matrix powder based on Fe and the basic layer.

We have to underline that an important contribution in achieving this goal is due to this kind of powder, which responds to the required conditions by this kind of coating during the exploitation time of the electromagnetic strip mills' driving rollers.

References

[1]. D. Ugues, M. Rosso, M. Albertinazzi, F. Raimondi, A. Silipigni, Proc. 2nd Int. Conf. High Tech Die Casting, Brescia, Italy (2004), p. 155.

[2]. D. Ugues, M. Rosso, M. Albertinazzi, Metall. Sci. and Tech., 22 No.1, (2004), Teksid, Carmagnola (I), p. 22.

[3]. A. Chowdhury, D. Cameron, M. Hashmi, Surf. and Coat. Tech., 116-119, (1999), 46.

[4]. T. Michler, M. Grischke, K. Bewilogua, A. Hieke, Surf. and Coat. Tech., 111, (1999), p. 41

[5]. H. Prengel, W. Pfouts, A. Santhanam, Surf. and Coat. Tech., 102, (1998), p. 183-190

[6]. D. Heim a, F. Holler, C. Mitterer, Surf. and Coat. Tech., 116-119, (1999), p.530-536

[7]. P. Moţoiu, G. Popescu, P. Moldovan, “***Influence of NiSiB/WC-Co components ratio on the tribologic properties of thermal spraying NiSiB/WC-Co type powder layer***”, EURO PM 2006, Congress&Exhibition –23-25 october 2006, Ghent, Belgium, Proceedings Volume 1, Hard Materials, pg. 247-252

[8]. P. Motoiu, D. Dumitrescu, G. Popescu , H. Binchiciu , C. Munteanu, *„Study of composite material for hardfacing to counteract the tooling damage”*, Bulletin of the Polytechnic Institute of Iaşi, Tomul LIII, (LVII), Fascicola 1, Iaşi 2007, ISSN 1453-1690, pag.105-112.

THE ANNALS OF “DUNAREA DE JOS” UNIVERSITY OF GALATI.
FASCICLE IX. METALLURGY AND MATERIALS SCIENCE
N^0. 2 – 2007, ISSN 1453 – 083X

ELECTRIC AND ELECTROMAGNETIC PROPERTIES OF FIBER FABRIC BASED FILLED EPOXY COMPOSITES

Adrian CÎRCIUMARU, Gabriel ANDREI,
Iulian-Gabriel BÎRSAN, Dumitru DIMA
”Dunărea de Jos” University of Galaţi
email: adrian.circiumaru@ugal.ro

ABSTRACT

Electric and magnetic properties of laminate fiber fabric based epoxy composites are investigated through experimental techniques. Various concentrations of powder fillers were used in order to change the basic properties of standard composite. Two types of fiber fabric were used in order to evaluate the effect of reinforcement. Various types of filled epoxy were also used in order to identify the effects

KEYWORDS: Laminate Composite, Ferrite, CNT, Electric Properties, Electromagnetic properties.

1. Introduction

It is known that properties of a composite are depending on properties of its parts. There are many models purposed for mathematical description of those properties but frequently they are designed for two components composites [1], [2], [3]. It is not the aim of this work to establish a mathematical model but, at least, it is possible to qualitatively measure the effects of a reinforcement or another, the effects of a filler or another.

It is the goal of this study to identify the effects of reinforcement type and of the matrix type. It was one of the problems that the epoxy resin is not adherent to the carbon fiber so the composite’s integrity is affected. One solution was to prepare the carbon fiber fabric by deposing a thin film of PNB rubber [4]. Another solution is to use a mixed aramide-carbon fabric which presents the advantage of lower price and because of kevlar’s presence the mechanical properties are improved [5], [6].

Kevlar fibers are dielectric while carbon fibers have high electric conductivity so the mixed fabric is actually a superposition of two nets. In such conditions the composite’s properties have to be effect of two behaviors. Nowadays the bi- component composites are mostly studied especially the filled polymer composites [7]. The cited paper is an excellent review of actual orientations and results in the domain of filled polymer composites and emphasizes the importance of filler dimensions and shapes bringing in attention the importance of interface.

The design of a composite is a very difficult task if just mechanical properties are emphasized [8], [9], [10]. When the electromagnetic or thermal properties are taken into account the problem is practically unsolvable. It is the aim of this work to empirically determine electric and electromagnetic parameters which characterize the composite.

One answer seek in this work is about if it is possible to establish the electromagnetic properties of composites by using various reinforcements and various filled epoxy resin layers at various depths in the composite.

2. Samples

The samples were realized by a technique described in [11]. In order to identify the effects of reinforcement over composite’s electric and electromagnetic properties two types of samples were formed. Both types of samples have reinforcements of 13 sheets of simple type of fiber fabric. The mixed fabric is realized of alternate Kevlar and carbon fibers.

For each type of reinforcement four types of matrix were realized by using filled epoxy resin in various setups. As was described in above mentioned study, the samples were realized through layer-by-layer method. In this case the matrix was realized, each time, by using the same concentration of various fillers (CNT, Ferrite, Talc) but even the filled resin was used in layers. In fact, the samples are named with four characters the first one denoting the type of reinforcement (K for Kevlar-carbon fiber fabric and C for carbon fiber fabric). The other three characters are denoting the epoxy’s filler (C for CNT, F for ferrite, T for talc). Assuming the symmetry of reinforcement reported to medial plane there were used, for example, three layers of Ferrite filled epoxy (external layers), three layers of CNT filled epoxy (middle layers) and two of Talc filled epoxy (intermediate layers). So, the structure of the sample from the matrix point of view is 3F-2T-3C-2T-3F and for carbon fiber fabric reinforcement the sample is CFTC. In the C-type samples there are alternate 0 degrees 45 degrees sheets of reinforcements wile in K-type of samples all sheets are placed such as fill and yarn are parallel.

3. Measurements

Measurements were performed in order to determine the electric conductivity across and along reinforcement and at the surface of samples [12]. Also measurements were carried out for electromagnetic properties determination [13]. The experimental arrangements were described in [11].

4. Results

It is expected that alternating the filled epoxy layers used for formatting the composite surface and bulk the electromagnetic properties to be modified.

The across resistivity $\rho_V\,[\Omega m]$ is determined by measuring the electric resistance at low frequency.

The across resistivity is evaluated in orthogonal direction to reinforcement and is depending on the type of reinforcement and on the type of filler. It is expected that small amounts of CNT to improve the electric conductivity. Figure 1 shows the across resistivity and it can be noticed that the two types of reinforcement are leading to almost the same resistivity of composite when CNT is used as filler. Also it can be seen the effect of carbon fiber reinforcement over the across conductivity.

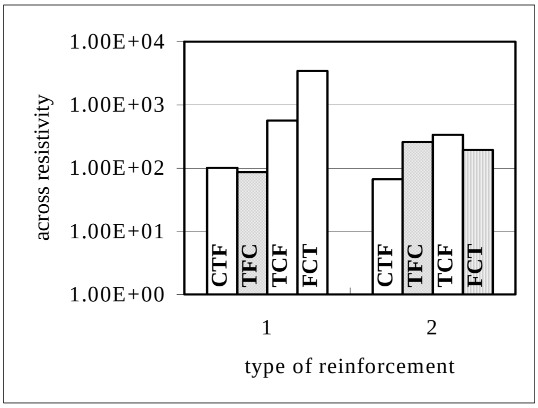

Figure 1. The across resistivity of samples 1. K-Type; 2. C-Type.

Figure 2 shows the surface resistivity $\rho_S\,[\Omega]$ of the samples evaluated through measurement of a circular sector at the surface of sample. The surface resistivity has to depend on the type of filler and can be noticed that the smallest value is reached when CNT is used as filler.

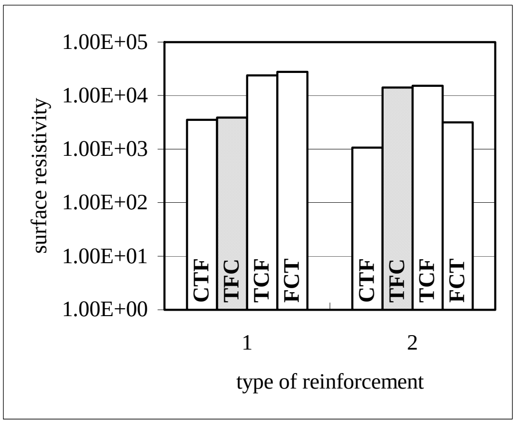

Figure 2. The surface resistivity of samples 1 – K – Type; 2 – C – Type.

Figure 3 represents the along resistivity $\rho_L\,[\Omega m]$ evaluated through the van der Pauw method and is strongly dependent on the reinforcement’s type and position. It can be noticed that in the case of carbon fiber fabric all the four values are respectively smaller than the values in the case of kevlar-carbon fiber fabric. An explanation for this situation is not only the presence of carbon fibers but also the geometry of reinforcement. In the case of C-Type samples the anisotropy is reduced.

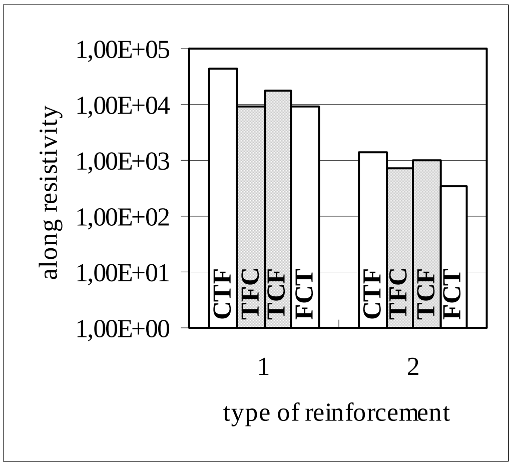

Figure 3. The along resistivity of samples 1. K-Type; 2. C-Type.

The concentration of fillers is also important to final properties of the composite. It is known that relatively high concentrations of CNT are producing an increasing of resistivity [14]. Maybe the optimal solution is to fill the epoxy with a mixture of powders in certain concentrations in order to obtain certain macroscopic electric properties. From this point of view it is necessary to analyze the electric properties through other more sensitive methods. Because the dimensions of the filler’s particles it is expected that electric and electromagnetic properties to be field dependent so all the measurements has to be carried out at more then one frequency. Regarding the electromagnetic properties of a composite there is important to specify the electric permittivity and the magnetic permeability. However measurement of electric permittivity is a much easier task than measuring magnetic permeability.

Figure 4 shows the electric permittivities $\boldsymbol{\varepsilon}[\boldsymbol{F}/\boldsymbol{m}]$ of the samples and it can be seen that the talc transforms the epoxy in a high dielectric. It is also important to notice that the position of resin layers determines the electromagnetic properties.

Another aspect of high interest is the electromagnetic shielding of a material. From this point of view in this study measurements were carried out for electric capacitance and magnetic inductance of the samples.

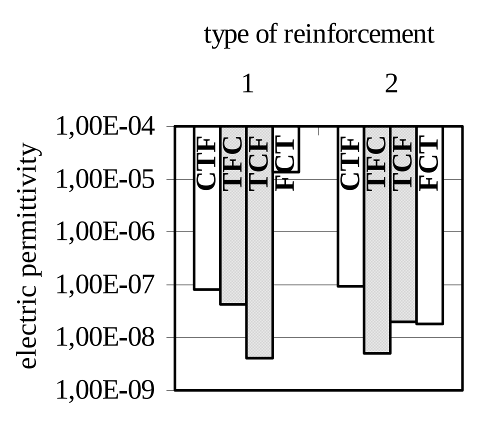

Figure 4. The electric permittivity of samples 1. K-Type; 2. C-Type.

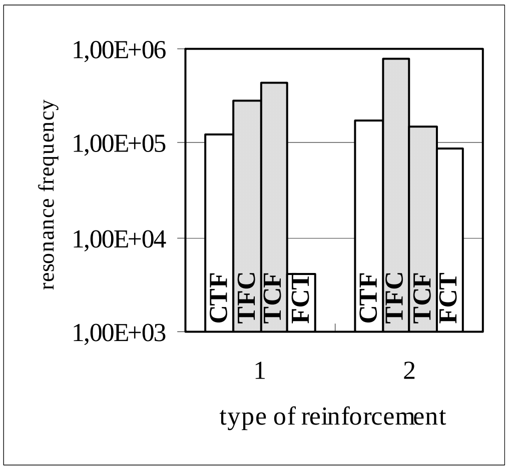

Figure 5. The resonance frequencies of samples 1. K-Type; 2. C-Type.

Figure 5 shows the resonance frequencies of the samples. The measurements for bulk capacitance and bulk inductance were performed at low frequency so, there is possible that at high frequency the results to be different because of the field sensitivity of the samples.

5. Conclusions

For special applications seems to be possible to arrange the filled resin such as the external layers of the composite to have high conductivity while the core of it to have strong dielectric or magnetic properties. The resistivities of K-type samples are susceptible to be improved in the case of the same architecture as C-type samples. It seems to be possible a combination of fillers with certain amounts which could ensure optimal electromagnetic properties for the multi-component composite material. There is a great advantage in the case of multi-component composite namely the area of interfaces is increasing if the fillers are nanosized. Mean time in the case of microsized particles’ presence the material fails.

Acknowledgments

The research was carried out inside the CNCSIS type A Grant, code 514 /theme 1/ 2006.

References

[1]. Roberts, A. P., Knackstedt, M. A., ***Structure-property correlations in model composite materials***, ***Physical Review E***, 54, 1996.

[2]. Torquato, S., ***Modeling of physical properties of composite materials, International Journal of Solids and Structures***, 37, 2000.

[3]. Liu, L., Matitsine, S. M., Gan, B. Y., Rozanov, K. N., ***Effective permittivity of planar composites with randomly or periodically distributed conducting fibers***, ***Journal of Applied Physics***, 98, 2005.

[4]. Jong-Kyo Kim, Yin-Wing Mai, ***Engineered Interfaces in Fiber Reinforced Composites***, Elsevier, 1998.

[5]. G. Hubca, H. Iovu, ***Materiale compozite***, Editura Tehnică, Bucureşti, 1999.

[6]. Elena, Alămoreanu, D. M., Constantinescu, ***Proiectarea plăcilor compozite laminate***, Editura Academiei Române, Bucureşti, 2005.

[7]. Winey, I. Karen, Vaia, A. R. (ed), ***Polymer Nanocomposites***, ***MRS Bulletin***, Vol. 32, April 2007.

[8]. Torquato, S., Hyun, S., Donev, A., ***Optimal design of manufacturable three-dimensional composites with multifunctional characteristics***, ***Journal of Applied Physics***, 94, 2003.

[9]. Kalamarkov, A. L., Kolopakov, A. G., ***Analysis, Design and Optimization of Composite Structures***, John Wiley&Sons, 1997.

[10]. M. V., Karbhori, Maria, Abanilla-Arocoli, ***Design Factors, Reliability and Durabilitry Prediction of Wet Layup Carbon/Epoxy Used in External Strengthening***, www.sciencedirect.com.

[11]. Andrei, G., Circiumaru, A., Birsan, I. G., Dima, D., ***A study of electric properties of fiber fabric based filled epoxy composites.***

[12]. Webster, J. G. (ed), ***Measurements, Instrumentations, and Sensors***, CRC Press, 1999; **Heaney, M. B.**, ***Electrical conductivity and resistivity***, 43 and **Misra, D. K.**, ***Permittivity measurement***, 46.

THE ANNALS OF “DUNAREA DE JOS” UNIVERSITY OF GALATI.
FASCICLE IX. METALLURGY AND MATERIALS SCIENCE
N^0. 2 – 2007, ISSN 1453 – 083X

MECHANICAL RESISTANCE AS A FUNCTION OF LOCAL PROPERTIES

George CHIRITA[2], Ioan STEFANESCU[1],
Delfim SOARES[2], Filipe SILVA[2]
[1] Faculty of Mechanical Engineering, Dunarea de Jos University Galati, ROMANIA
[2] Mechanical Engineering Department; School of Engineering, Minho University, PORTUGAL
email: fsamuel@dem.uminho.pt

ABSTRACT

The present study makes an estimation of an automotive engine piston mechanical properties and fatigue life based on some characteristics of metallurgical microstructure. Because it is intended to assess the properties in specific locations of the component it is made a local microstructure approach. The critical points of the engine piston were metallurgical analyzed (amount of phases and SDAS) and these were related to ultimate tensile strength and fatigue life.

The conclusion of the work is that in an engine piston the mechanical and fatigue properties are very dependent of local metallurgical properties (amount of the eutectic phase). As a consequence the component may fail in an unexpected area that may change the local assessment expected results.

KEYWORDS: Metallurgical properties, Mechanical properties, Fatigue life.

1. Introduction

Assessment of components failure is strongly dependent on failure localization. The component point where failure occurs strongly depends on local properties. And these local properties are also influenced by the processing technique. In the specific case of an engine piston local properties are influenced by the casting technique. Mechanical properties (tensile strength, tensile strain, Young modulus, etc) as well as fatigue properties (fatigue life) are very dependent on casting method. The most direct effects of casting techniques are on the metallurgical microstructure that bounds the mechanical properties. One of the important variables affected by the casting technique is the cooling rate and the cooling rate strongly restricts the microstructure. As it is known the values of the SDAS (secondary dendrite arm spacing) as well as other constituent dimensions are correlated with mechanical properties as, for example, the ultimate tensile strength. Usually, in design, it is not taken into consideration that in different parts of one cast component there are different values of constituent dimensions (SDAS, amount of constituents, etc). These differences in metallurgical properties are conducting also to different mechanical and fatigue properties in the same single component material.

The automotive engine pistons are usually cast in near eutectic aluminium-silicon alloys. The structure and properties of cast aluminium silicon eutectic alloys are very dependent on the cooling rate, composition, modification, heat treatment operations, etc [3,5,6]. That’s why to estimate the mechanical properties and fatigue life of the cast piston is not enough to know the material characteristics and properties. It is also necessary to know all the factors that are influencing the characteristics of the final casting part: type of casting, temperatures (melt and mould), cooling rate, refiners etc. [4,9,11], and to know it in the different parts of the component because they strongly change along the same component. A way to predict both mechanical properties as well as the fatigue life of the material component is based on some metallurgical characteristics of the obtained casting.

A number of papers have been published showing several relations that estimate the tensile strength with other different microstructure characteristics. For example, Bernsztejn proposed a relation to calculate the average strength as a linear function of the volume fraction of silicon [1]:

$$\sigma = \sigma_\alpha \ V_V^\alpha + \sigma_{Si} \ V_V^{Si} = \sigma_\alpha + V_V^{Si}\left(\sigma_{Si} - \sigma_\alpha\right) \quad (1)$$

where σ_α and σ_{Si} are rupture strengths in the volume unit.

This formula neglects the influence of the morphology, the average size, and the distribution of brittle particles, that is, silicon precipitates and also the volume fraction of constituents which can differentiate the properties of materials of similar value of the silicon volume fraction to an important degree.

A correlation between tensile strength (σ) and silicon particle size for aluminium-silicon alloy containing 17-27% Si, was presented by Mandal et al.[7]:

$$\sigma = 252{,}8 - 3{,}73 \cdot \text{particle size} \qquad (2)$$

Another relationship between tensile strength and secondary dendrite arm spacing and the size of silicon lamellas in interdendritic eutectic regions, was proposed (ASM Int. 2004):

$$\sigma = k + k_2 \cdot \gamma^{-\frac{1}{2}} + k_3 \cdot \lambda^{-\frac{1}{2}} \qquad (3)$$

where: σ is the tensile strength, k, k_2 and k_3 are empirical constants, γ is the size of silicon lamellas in interdendritic eutectic regions and λ is the secondary dendrite arm spacing.

Secondary dendrite arm spacing is also in attention of researcher and generates several models to estimate tensile strength [10]:

$$UTS = -1{,}4399 \cdot SDAS + 340 \text{ [MPa]} \qquad (4)$$

where: UTS is ultimate tensile strength and SDAS is secondary dendrite arm spacing.

In order to optimize the design of the cast components based on local properties it is necessary to know the local metallurgical properties which determine the mechanical properties that may help to estimate the failure of the component.

2. Experimental method

A commercial engine piston obtained by gravity casting on permanent mould was studied. The engine piston was provided for this study by Rito, Lda company from Portugal. The material used to cast the piston was a near eutectic aluminium-silicon alloy. The piston was sectioned, polished and optical analysed in order to quantify the volume fraction of phases and measuring the secondary dendrites arm spacing (SDAS). The quantification of phases (eutectic, α-Al dendrites, intermetalics) was done optically and using statistical methods. The SDAS was quantified by identifying and measuring small groups of well-defined secondary dendrite arms on the screen of the image analyzer. The value of SDAS was then determined using SDAS=d/nM, where d is the length of the line drawn from edge to edge of measured arms, M is the magnification, and n is the number of dendrite arms. The volume fractions of the constituents were quantified by image analysis. (Fig.1)

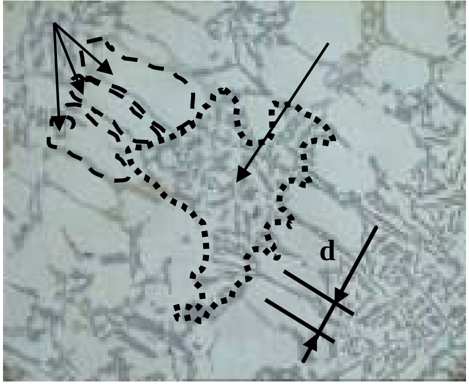

Fig.1. Microstructure analysis.

The regions of the piston that were studied are: 1. Top position, 2. Piston ring position, 3. Top pin position, 4. Down pin position, 5. Skirt position. (See fig. 2).

To verify the results obtained by analytical formulas was done an FEM analysis with Cosmos software to the piston and from the elastic stresses plot were extracted the values of stresses on the selected regions.

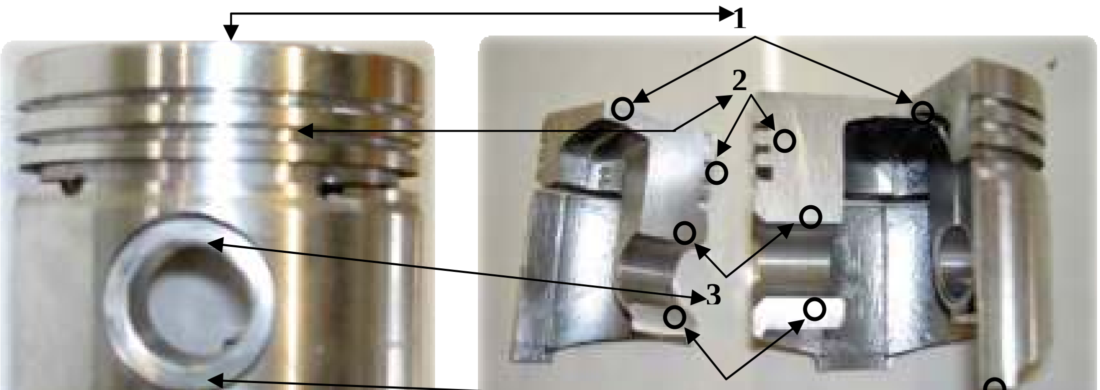

Fig. 2. Position of regions studied.

3. Results

The secondary dendrites arm spacing measured values are presented in fig. 3. The SDAS shows an increasing of about 90% from skirt position-24µm to top position-47µm.

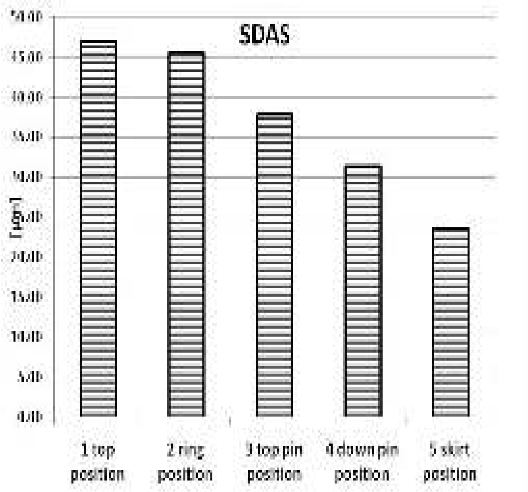

Fig. 3. Secondary dendrites arm spacing (SDAS).

From volume fraction quantification of constituent phases (Fig. 4) is noticed that the volume fraction of eutectic phase is increasing from position 1 (top position) to position 5 (skirt position) which is in opposite relation with the α-Al dendrites phase.

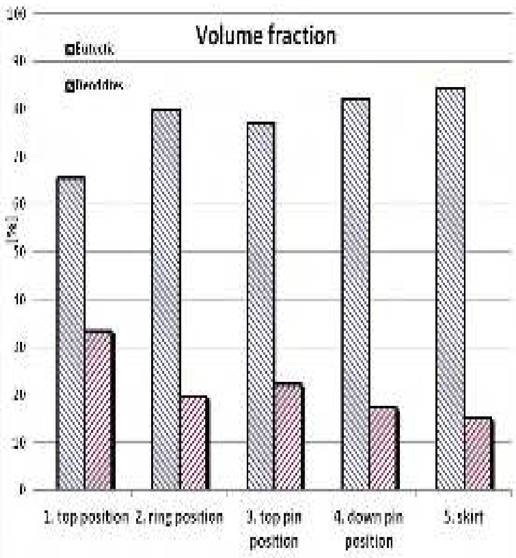

Fig. 4. Volume fraction of eutectic and α–Al dendrite phase.

Analysing together volume fraction of the eutectic phase with the SDAS results it is interesting to highlight the fact that exists a relation between them: the region with higher values of the SDAS has small amount of eutectic phase and reverse the region with smaller values of the SDAS has low values of the eutectic phase.

4. Discussion

Mechanical and mechanical fatigue failures occur in critical localizations. Critical localizations are not those where stresses are higher then in the rest of component but where the ratio of local stress vs. ultimate tensile local strength is higher. Thus, estimative prediction of the cast aluminium component properties should be made based on local material mechanical properties which makes possible calculate the ratio of stress vs. UTS. Local mechanical and fatigue properties may be obtained by local metallurgical features.

In all the casting moulds different variables such as component wall thickness, mould thickness, etc causes different cooling rates in different places of the cast component.

The decreasing tendency of SDAS could be explained by the differences of cooling rates in different places of the mould. As is already known from literature [3, 8], the secondary dendrites arm spacing, for a given alloy, is influenced mainly by the cooling rates.

Empirical equations were used to estimate the values of the ultimate tensile strength in all the specific regions described above. From several equations that exist in literature that correlate the ultimate tensile strength and the secondary dendrites arm spacing, the one developed by Takahashy and all [10] was adapted for the present studied alloy. The results of the microstructure and predicted UTS are presented in table 1.

Table 1. UTS calculated using Eq.4

Position	**SDAS** [µm]	**UTS** [MPa]
1. top position	46,98	202,36
2.ring position	45,60	204,35
3.top pin position	37,94	215,38
4.down pin position	31,47	224,69
5. skirt position	23,64	235,97

It can be seen that there is a change in SDAS of about 100%, as occurs between positions 5 and 1, and that it is equivalent to significant changes in UTS, e.g. the stress level changes from about 236 to 202 MPa (about 17%).

A previous study [2] was done by the authors of this paper to develop a relation of volume fraction with the ultimate tensile strength because in some alloys the SDAS are not easy to measure due to the fact that they are not well defined. The majority of the existing relations are able to calculate an estimative value of the ultimate tensile strength from the measured value of secondary dendrite arm spacing and only some of them were developed to correlate the amount of the eutectic phase with the UTS. This study also does a verification of the two formulas: one based on volume fraction of eutectic and the other one based on SDAS.

The previous developed equation that correlates the ultimate tensile strength with the volume fraction of the eutectic phase is: [2]

$$UTS = 100 + 1{,}55\ V_{fr.eutectic}\ \text{[MPa]} \qquad (5)$$

The values of the expected ultimate tensile strength obtained by equation 5 are shown on table 2.

Table 2. UTS calculated using Eq.5

Position	**Vol.F.eut.** [%]	**UTS** [MPa]
1. top position	65,67	201,79
2. ring position	79,96	223,94
3. top pin position	77,21	219,67
4.down pin pos.	82,11	227,26
5. skirt position	84,50	230,98

Two important notes from these results are: there is a difference in local UTS of about 15% on different locations of the same component; there is a very good approximation with the ones obtained by equation 4 (Table1).

These differences are big enough so that they should be taken in consideration in designing the component. As a fact they may strongly affect not only the local mechanical properties but also the fatigue properties. In a previous paper [2] it is shown that a difference in about 25% on UTS, in a similar near eutectic alloy, is equivalent to a change in the fatigue limit of about 50%, which means a difference in fatigue life of about two orders of magnitude. Thus a 15% difference in UTS as the one obtained in the present study may be equivalent to at least one order of magnitude difference in fatigue life, which is quite relevant in fatigue life predictions. In order to verify how these changes may affect a specific component design, an analysis of stresses obtained by FEM and real local stresses (estimated based on metallurgical eutectic volume fraction) on a piston was performed.

Example of component design

As observed in fig. 6, due to the pressure at the piston head (Fig.5), there are mainly two important critical areas: top piston pin holes and the piston head. The values of stresses, obtained by FEM in each verified position (see fig. 2) are presented in table 3. It is worth to note that on design it is used a limiting value (for example Ultimate Tensile Strength) for the material, e.g, for the whole component. If the stress value is plotted against the UTS it is obtained the predicted ratio stress/UTS (table 3). A single input value (global material) of the ultimate tensile strength is used and is equal for the whole component.

Table 3. Predicted and Real Stress/UTS ratios.

Position	**Ultimate tensile strength** [%] **Eq.4**	**Stress** [MPa] **FEM**	**Predicted Stress/UTS ratio FEM**	**Real Stress/UTS ratio**	**Real and Predicted ratios differences**
1. top	202,36	56,00	23,7	27,7%	3,9%
2. ring	204,35	78,40	33,2	38,4%	5,1%
3. top pin	215,38	96,00	40,7	44,6%	3,9%
4.down pin	224,69	44,00	18,6	19,6%	0,9%
5. skirt	235,97	21,20	9,0	9,0%	0,0%

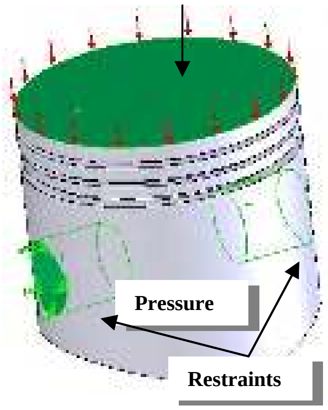

Fig. 5. Pressure and restraints applied surfaces.

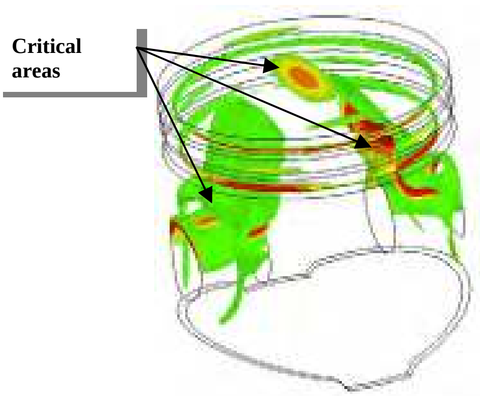

Fig. 6. Stress distribution critical zones.

However if the values of the stress (obtained by FEM) are plotted against the real ultimate tensile stress values (as obtained by the metallurgical features in different parts of the component), a new ratio is obtained (real stress/UTS ratio) (see table 3). The differences between these two ratios, the predicted and the real ones are plotted in the last column in table 3. It can be seen that there are some differences on material local resistance with a maximum difference of about 5%. It is worth to note that these differences may have a significant influence mainly on fatigue predictions and that they also may cause a shift of the critical points changing the expected failure locations and making it more difficult to obtain reliable failure assessments.

4. Conclusion

This study wants to verify if, in the case of cast components, the value of ultimate tensile strength could be different in different locations of the component. The main conclusions of the study are:

- Substantial changes of mechanical and fatigue properties may occur in different locations of the component;
- Those differences can be easily predicted by using different metallurgical features such as SDAS or phase volume fractions;
- The differences observed may have an impact on mechanical and fatigue design of the component;

Finally it should be emphasized that damage assessment can be influenced or distorted by a wrong failure location prediction.

Acknowledgement

The research presented here was carried out in Materials Testing Laboratory of the Mechanical Engineering Department of University of Minho, and was supported by "Fundação para a Ciência e Tecnologia" (Portugal) through the PhD grant with the reference SFRH / BD / 19618 / 2004.

References

[1]. Bernsztejn, L., Zajmowskij, **W.A.**, ***Struktura i własnos´ci mechaniczne metali (Structure and Mechanical Properties of Metals)***, Wyd. Naukowo-Techniczne, 1973, Warsaw.

[2]. Chirita, G., Stefanescu, I., Cruz, D., Soares, D., Silva, F.S, ***Centrifugal effect on aluminium castings mechanical properties,*** Materials and Design, in press., 2007

[3]. Goulart, P.R., Spinelli, J.E., Osorio, W.R., Garcia, **A** ***Mechanical properties as a function of microstructure and solidification thermal variables of Al-Si castings,*** Materials Science and Engineering A **,** 2006,421, p245-253.

[4]. Han, S.W., Kumai, S., Sato, **A.**, ***Effects of solidification structure on short fatigue crack growth in Al-7%Si-0,4%Mg alloy casting***, Materials Science and Engineering **,** 2002, A332, p56-63.

[5]. Haque, M.M., Maleque, **M.A.**, ***Effect of proces variables on structure and properties of aluminum-silicon alloy***, Journal of Materials Processing Technology 77, 1998, p.122–128.

[6]. Haque, M.M., Sharif, **A.**, ***Study on wear properties of aluminum-silicon piston alloy***, Journal of Materials Processing Technology 118, 2001, p. 69–73.

[7]. Mandal, P., Saha, A., Chakraborty, **M.,** ***Size of primary silicon particles and mechanical properties of as-cast high Silicon Al alloy***s, AFS Trans. 1991, p.99, 33.

[8]. Nikanorov, S.P., Volkov, M.P., Gurin, V.N., Burenkov, Yu. A., Derkachenko, L.I., Kardashev, B.K., Regel, L.L., Wilcox, **W.R.,** ***Structural and mechanical properties of Al-Si alloys obtained by fast cooling of a levitated melt***, Materials Science and Engineering 2005, A 390, p.63–69.

[9]. Shabestari, S.G., Moemeni, H., ***Effect of copper and solidification conditions on the microstructure and mechanical properties of Al-Si-Mg alloys,*** Journal of Materials Processing Technology, 153-154, 2004, p.193-198.

[10]. Takahashi, T., Sugimura, Y., Sasaki, **K.,** ***Thermal plastic-elastic analysis in consideration of metallurgical microstructure***, Journal of Manufacturing Science and Engineering, 2004, Vol.126, p.25-32.

[11]. Wang, **Q.G.,** ***Micro structural effect on the tensile and fracture behaviour of aluminium casting alloy A 356/357***", Metallurgical and Materials Transaction, 2003, Vol. 34 A, December, p.2887-2899.

THE ANNALS OF “DUNAREA DE JOS” UNIVERSITY OF GALATI.
FASCICLE IX. METALLURGY AND MATERIALS SCIENCE
N^0. 2 – 2007, ISSN 1453 – 083X

EXPERIMENTAL INVESTIGATION OF FATIGUE OF THIN-WALLED WELDED STRUCTURES OF COMMERCIAL VEHICLE FRAMES

Athanassios FOKILIDIS, Georgios SAVAIDIS
Aristotle University of Thessaloniki, Dept. of Mechanical Engineering, Greece
email: gsavaidis@meng.auth.gr

ABSTRACT

The fatigue behavior of bus frame components consisting of thin-walled tube beams joined together by fillet welding has been investigated. Numerical analysis by means of finite elements and experimental stress analysis by means of strain gages explored the failure-critical locations at the weld toe. In addition, a proposal for finite element modeling in particular of the welded area, and evaluation of hot spot stresses to be used for fatigue life calculations of such thin-walled structures has been developed. The calculation results have been verified based on experimentally determined fatigue lives of the components under constant amplitude loading. A satisfactory agreement between experimental and theoretical results has been observed.

KEYWORDS: Fatigue, welds, finite elements, hot spot stress, experimental analysis

1. Introduction

Calculation methods for the investigation of fatigue behavior of welded structures under operational loading are gaining increasing importance in many technical applications, since they contribute in decreasing developmental costs and time. Extensive research activities over the last decade especially in the fields of crane and marine construction led to various calculating procedures, which differ fundamentally in their type of evaluation (based on nominal, local or structural hot spot stresses). Radaj et al. [5] and Maddox [12] give an overview and a systematic survey of the existing methodologies and concepts dealing with fatigue evaluation of welds. Details for numerical analyses by means of finite elements are given in [13]. In addition, fracture mechanics based approaches have been also elaborated [2, 11]. A state of the art has been recently reported by Tovo and Livieri [16] and Fricke [9].

Valuable recommendations for fatigue assessment of welds engineering applications are also given in international guidelines, e.g. the one of the International Institute of Welding (IIW) [9], Eurocode [6], as well as [4] and [1]. However, all these recommendations deal mainly with quite thick structures.

In the automotive sector, there is an increasing interest for computer-aided methods to shorten the development time. In the last years developments on theoretical assessment of welded automotive components with low thicknesses have been achieved in conjunction with the hot spot stress approach, see e.g. Boven-Griffon et al. [3], Fayard et al. [7] and Fermér and Svenson [8]. Own initial experience [14, 15] revealed that fatigue analysis based on hot spot stresses might be capable for handling such thin components.

However, nowadays it still lacks of experimentally verified guidelines for the calculation of fatigue life. Therefore, the assessment of thin-walled welded components under operational loading is still dominated by experimental methods.

Taking new generation bus frame components consisting of thin-walled tube beams with thickness ***t***=2mm joined together by fillet welds as examples, the investigation focuses to:

a) the investigation of the mechanical behavior of the components, in particular of structural stresses acting at the failure critical welds

b) the determination of the fatigue live curves under bend loading

c) the development and assessment of the reliability of a finite element meshing and calculation procedure that can be applied for the fatigue life prediction based on hot spot stresses.

2. Hot spot stress approach

The so-called “structural” stress at the hot spot (HSS), i.e. at the failure-critical point of the weld, is a fictitious stress. In many applications, this point corresponds to the weld toe. The HSS value can be determined using reference points in certain distances from the weld toe by extrapolating the surface stress values measured or calculated at the reference points at the weld toe [10]. The reference points are set dependent on the thickness ***t*** of the welded components and the extrapolation method used. Depending on the shape of the stress distribution acting perpendicular to the weld toe a linear or quadratic stress extrapolation at the weld toe is recommended as depicted in fig. 1 and 2, respectively.

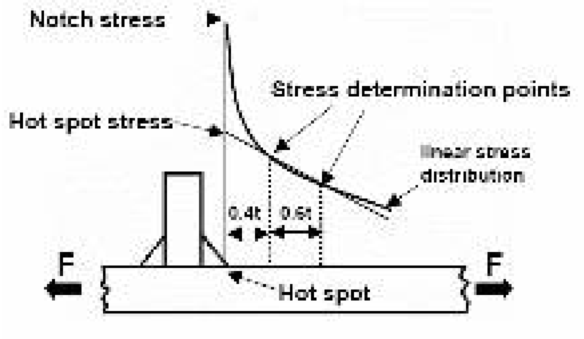

Fig. 1. Determination of HSS by linear extrapolation

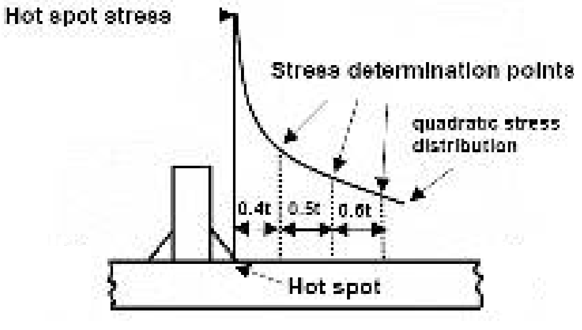

Fig. 2. Determination of HSS by quadratic extrapolation

Note that the HSS includes all stress raising effects of the structural detail except the stress concentration due to the local weld profile itself.

3. Specimens and loading

Figure 3 illustrates the geometry of the specimens and the load configuration applied in the present investigation.

Two longitudinal tube beams with dimensions 50x50x2 [mm] are jointed to a vertical tube beam with dimensions 50x50x2 [mm] by fillet welds. The thickness of the weld amounts to 4mm.The ends of the longitudinal beams are fixed while the load is introduced at the one end of the vertical beam.

The specimens were subjected to force-controlled, fully reversed loading with constant amplitudes. Therewith, mainly normal stresses due to bend loading are acting at the weld toes.

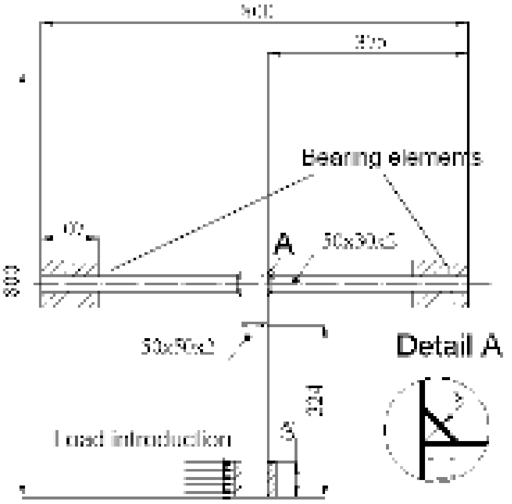

Fig. 3. Specimen’s geometry and load configuration

4. Finite element meshing

Figure 4 shows schematically the procedure followed here to model the weld and to calculate the HHS value at the weld toes in the longitudinal and the vertical beam. The origin of this procedure goes back to Fayard et al. [7].

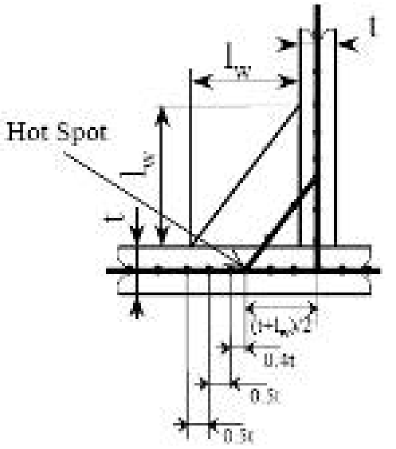

Fig. 4. Specimen’s geometry and load configuration

The vertical and longitudinal beams of the component are shown in fig. 4. Their thickness amounts to ***t***=2mm. The fillet weld triangle is illustrated with side lengths l_w. Two rectangular surfaces consisting of intermediate shell elements have been used to model the beams shown in fig. 4 with bold lines. In accordance with Fayard’s et al. [7]

suggestion, the fillet weld itself has been modeled by an additional surface of shell elements, whereby the dimensions of the rectangular sides of the fillet weld triangle amount to $(t+l_w)/2$ on both the longitudinal and the vertical beam, respectively. The stiffness of the shell elements of the fillet weld is assigned to replicate the stiffness of the real weld.

Differing from Fayard’s initial suggestion, the finite element mesh has been created to explore nodal stresses at the distances of 0.4***t***, 0.9***t*** and 1.4***t*** from the weld toe. These distances correspond to the principal recommendation of the IIW guideline [10] when a fine mesh with quadratic surface stress extrapolation is to be applied.

Figure 5 shows the finite element mesh detail of the welded area used for the theoretical analysis.

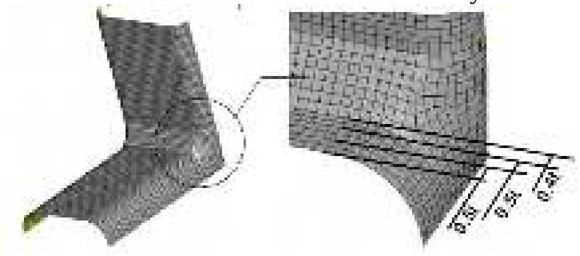

*Fig. 5. **Finite element mesh detail of the weld***

The stress values at the reference points 0.4***t***, 0.9***t*** and 1.4***t*** from the weld toe will be used to calculate the HSS values at the weld toe using Equation (1) [10]:

$$HSS = 2.52\ \sigma_{0.4t} - 2.24\ \sigma_{0.9t} + 0.72\ \sigma_{1.4t} \quad (1)$$

5. Test rig

Figure 6 shows the test rig used for the experimental investigation. Note that the adjustment of the specimen in the test rig is rotated by an angle of 90° in comparison to the illustration shown in fig. 3.

*Fig. 6. **Test rig***

A servo-hydraulic actuator introduces the load into the end of the vertical beam. The longitudinal beams are beard to the test rig traverse and the table using two bearing elements. The bearing elements are designed to compensate possible misalignments between the vertical and the longitudinal arms due to residual stresses induced by the weld-heat as well as possible deviations of the real geometrical dimensions of the beams from the nominal ones.

Three batches of specimens with equal dimensions of the beams and the welds but made up of three different constructive steels have been tested, named as T1, T2 and T3. However, the steels provide similar mechanical behavior and fatigue properties so that no influence is expecting due to the different steel material.

The specimens were tested under force-controlled, fully reversed cyclic loading (force ratio R_F=-1) with constant amplitudes vs. time. Thereby, various force amplitudes were applied in order to determine secured knowledge of the component’s Woehler curves. The specimens were tested in the as-welded condition, at room temperature with a frequency of 4 Hz.

6. Results

Fatigue cracks were initiated at the weld toe very near to the edges of the beams, where the highest stresses arise, during the applied force-time sequences.

The cracks propagated along the weld toe perpendicular to the direction of the normal stresses. Thereby, both weld toes, the one in the vertical and the one in the longitudinal beam, have been found out to be failure-critical. The initiation of fatigue cracks with lengths of approximately 3mm to 4mm at the surface of the components has been defined as failure criterion.

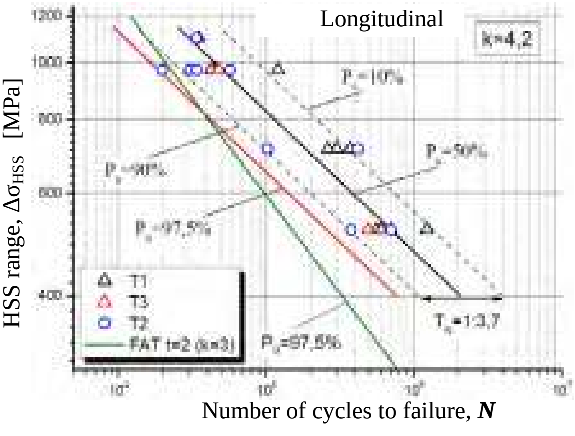

*Fig. 7. **Fatigue life results for failure at the longitudinal beam***

A crack length of this size causes a reduction of the component’s stiffness of approximately 5%, which can be measured reliably by the electronic devices of the test rig. Figures 7 and 8 contain the experimentally determined fatigue life results plotted vs. the range of the HSS, $\Delta\sigma_{HSS}$, calculated by means of finite elements for failure detected in the longitudinal and the vertical beam, respectively.

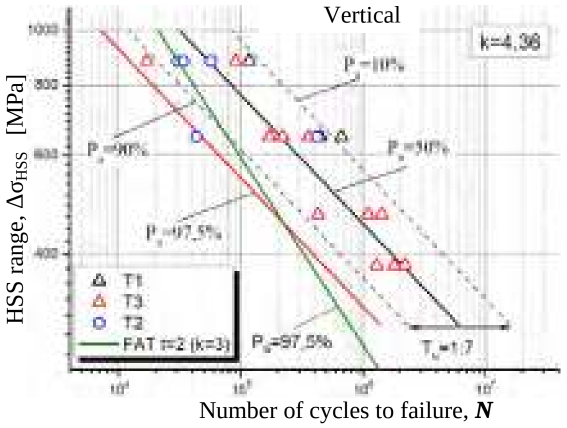

Fig. 8. Fatigue life results for failure at the vertical beam

The different marker symbols in fig. 7 and 8 stand for the different specimen batches. The Woehler lines for the various probabilities of survival $P_{Ü}$ have been determined by means of regression analysis of the corresponding results.

The characteristic scatter band T_N can be derived from the Woehler curves for the probabilities of survival of 10% and 90%. It is defined as

$$T_N = \frac{N_{P=10\%}}{N_{P=90\%}} . \qquad (2)$$

It amounts to T_N=1:3,7 for the cases with failure at the longitudinal beam, and T_N=1:7 for those with failure at the vertical beam.

The slopes of the Woehler curves for the two failure cases do not deviate significantly from each other. They amount to k=4.2 (failure at the longitudinal beam) and k=4.36 (failure at the vertical beam). These k-values are slightly higher than the one reported in the IIW-guideline (k=3).

Furthermore, a general comparison of the fatigue life results determined according to the procedure described in section 4 with the hot spot stress-life curves suggested by the IIW-guideline [10] is shown in fig. 7 and 8 for the two failure cases, respectively. The latter are to be used for the design of fillet welds in an as-welded condition if no experimental results are available.

They are based on several fatigue tests and assigned with a probability of survival of 90% within a confidence belt of 75%, which results in an overall probability of survival of $P_{Ü}$=97.5%.

To determine the Woehler curves according to the IIW guideline, the so-called FAT value for this weld configuration, i.e. the HSS range at a lifetime of 2000000 cycles, has been used as reference value. The reference FAT value for the weld configuration under investigation amounts to FAT=100 MPa. This value considers wall thicknesses of approximately 25mm and stress ratios of R>0.5. Therewith, the benign thinness effect due to the reduced thickness of the beams investigated here (t=2mm) has been taken into account explicitly, using the correction thickness factor reported in the IIW guideline. Finally, an additional correction factor due to the acting stress ratio R_σ=R_F=-1 has been considered. To determine fatigue lives at lower N-values, IIW recommends a unique Woehler curve slope of k=3 for all types of welds.

In both failure cases noticed in the present investigation, a satisfactory agreement between the Woehler curves determined according to the IIW guideline and the corresponding ones determined by the presented calculation procedure for the probability of survival 97.5% can be observed.

7. Conclusions

The fatigue behavior of thin-walled, fillet-welded components made from various ductile steels used for bus frames have been investigated theoretically and experimentally under fully reversed constant amplitude cyclic loading. The following remarks are made in conclusion:

The test results identified the weld toes at the edges of the horizontal arm to be the failure critical locations. Few specimens failed at the corresponding weld toe of the vertical arm. The finite element analysis unraveled the locations, which were identified experimentally as failure-critical.

A finite element meshing procedure according to Fayard’s et al. proposal for weld modeling by means of shell elements in conjunction with the recommendations of the IIW guideline has been applied. In addition, a quadratic surface stress extrapolation at the hot spot of the modeled weld has been proposed.

The HSS-Woehler curves determined by the suggested calculation procedure have been found out to be in satisfactory agreement with the corresponding ones determined according to the IIW guideline. These results confirm the accuracy and efficiency of the so-calculated hot spot stresses for fatigue design of thin-walled components such as the ones investigated here.

Though the experimental database used here for the verification of the calculation procedure is certainly narrow for generalizations, the results encourage to apply and verify this procedure to thin-walled structures such as the one investigated.

References

[1]. American welding society, Structural welding code – steel, ANSI/AWS D1.1-86, 1986.

[2]. **Atzori B., Lazzarin P., Tovo R.**, ***From a local stress approach to fracture mechanics: a comprehensive evaluation of the fatigue strength of welded joints***, Fatigue & Fracture Engng Mat. Struct., 22, 1999, pp. 369-381.

[3]. **Bovet-Griffon M., Ehrström J.C., Courbiere M., Bignonnet A., Thomas J.J., Puchois J.P., Rethery S., Liennard, C.**, ***Fatigue assessment of welded automotive aluminium components using the hot spot approach***. Proc. 8th INALCO, Munich, 2001.

[4]. British Standards Published Document, ***Guidance on methods for assessing the acceptability of flaws in fusion welded structures***, PD6493, BSI Standards, London, 1991.

[5]. **Radaj D., Sonsino, C.M., Fricke, W.**, ***Fatigue assessment of welded joints by Local Approaches***, 2nd edition, Abington Publ., Cambridge, 2006.

[6]. European Committee for Standardization Eurocode 3. ***Design of steel structures***. Part 1-1: General rules and rules for buildings, ENV 1993-1, 1992.

[7]. **Fayard J.L., Bignonnet A., Dang Van K.**, ***Fatigue design criterion for welded structures***. Fatigue & Fracture Engng Mat. Struct., 19, 1996, pp.723-729.

[8]. **Fermér M., Svenson H.**, ***Industrial experiences of FE-based fatigue life predictions of welded automotive structures***, Fatigue & Fracture Engng Mat. Struct., 24, 2001, pp.489-500.

[9]. **Fricke W.**, ***Fatigue analysis of welded joints: state of development, Marine structure***s, 16, 2003, pp. 185-200.

[10]. **Hobbacher A.**, ***Fatigue design of welded joints and components, recommendations of IIW***, Doc XIII-2151-07/XV-1254-07, 2007, Paris, France.

[11]. **Livieri P., Lazzarin P.**, ***Fatigue strength of steel and aluminium welded joints based on generalized stress intensity factors and local strain energy values***. Int. J. Fatigue, 26, 2004, pp. 1-29.

[12]. **Maddox S.J.**, ***Fatigue strength of welded structures***, 2nd edition, Abington Publ., Cambridge, 1991.

[13]. **Niemi E., Fricke W., Maddox, S.J.**, Fatigue ***analysis of welded components – Designer's guide to the hot spot stress approach.*** Woodhead Publ., Cambridge, 2006.

[14]. **Savaidis G., Vormwald M.**, ***Hot-spot stress evaluation of fatigue in welded structural connections supported by finite element analysis***, Int. J. Fatigue, 22, 2000, pp. 85-91.

[15]. **Savaidis G.**, ***Fatigue behavior of welded structures of bus frames***, Proc. Symposium on Structural Durability, Darmstadt, Germany, 2005, pp. 145-158.

[16]. **Tovo R., Livieri P.**, ***Local and non-local approaches to fatigue of weldments: state of the art and possible developments***, Key Engng Mat., 348/349, 2007, pp. 529-532.

THE ANNALS OF “DUNAREA DE JOS” UNIVERSITY OF GALATI.
FASCICLE IX. METALLURGY AND MATERIALS SCIENCE
N^{0}. 2 – 2007, ISSN 1453 – 083X

THE INFLUENCE OF COLD ROLLING ON THE MICROSTRUCTURE FOR DRAWING STEELS

Florentina POTECAŞU, Octavian POTECAŞU, Elena DRUGESCU, Petrică ALEXANDRU, Miltiade ISTRATE, Doru HANGANU
“Dunarea de Jos” University of Galati
email: fpotec@ugal.ro

ABSTRACT

The paper presents the structural changes that appeared in steel for deep drawing, as a result of cold rolling and of recrystallization thermal treatment. The research was conducted on samples taken from the rolled strap, treated and rerolled after the present technology in Arcelor Mittal. For comparison samples sampled from the steel strap before cold deforming (hot rolled) were used as blank tests. The thermal processing was done under industrial conditions in bell furnace. For the chosen steel the critical deformation degree was around the value of 6.5%.

KEYWORDS: deep drawing steel, critical deformation degree, microstructure.

1. Introduction

The chemical composition of the analyzed steel is presented in table 1.

Table 1. The chemical composition of the steel specimens used in experiments

C	Mn	Si	S_{max}	P_{max}	Al
[%]					
0.04	0.25	0.1	0.009	0.012	0.05

In order to establish the influence of the cold deformation degree on the steel straps’ properties, samples were sampled from a coil deformed on the continuous milling machine TANDEM with five four-high stands with the rolling cylinders’ diameter of 550 mm.

To obtain samples with different degrees of deformation the rolling process was started and when the normal running regime was reached, the mill was stopped and cut off parts of the strap between the stands. To achieve deformation degrees lower than 20%, the rolling process was continued only with the first stand. Samples were taken for different deformation degrees: ε_1 = 2.2% ; ε_2 = 6.5% ; ε_3 = 15.2%; ε_4 = 32.5% ; ε_5 = 50.0% ; ε_6 = 65.0% (the deformation degree was calculated with the formula: $\varepsilon = \Delta h/h_o x100$).

The samples obtained after the cold rolling have been heat-treated under industrial conditions in bell furnace according to the diagram in fig. 1.

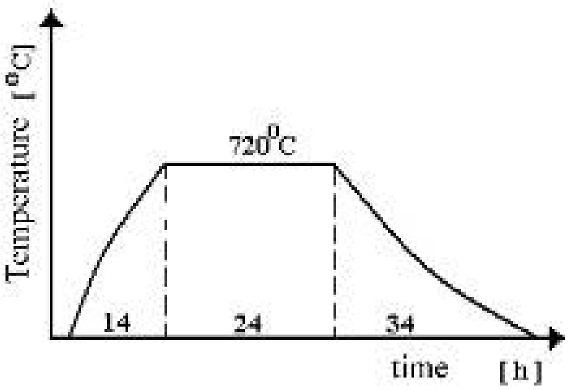

Fig. 1. The diagram of thermal treatment conducted in industrial conditions, for the cold deformed samples with different deformation degrees

2. Experiments

The microstructure of the blank tests sampled from the hot rolled strap is presented in fig. 2 (a, b) and in fig. 3 are presented the microstructures corresponding to different deformation degrees, obtained through cold rolling (without thermal treatment). The microstructural analysis of the cold deformed samples, with different deformation degrees (ε_1 = 2.2% ; ε_2 = 6.5% ; ε_3 = 15.2%; ε_4 = 32.5% ; ε_5 = 50.0% ; ε_6 = 65.0%) reveal at high deformation degrees (over 50%) the occurrence of the fibrous structure, a highly noticeable aspect especially in longitudinal sections (fig. 3j and fig. 3l).

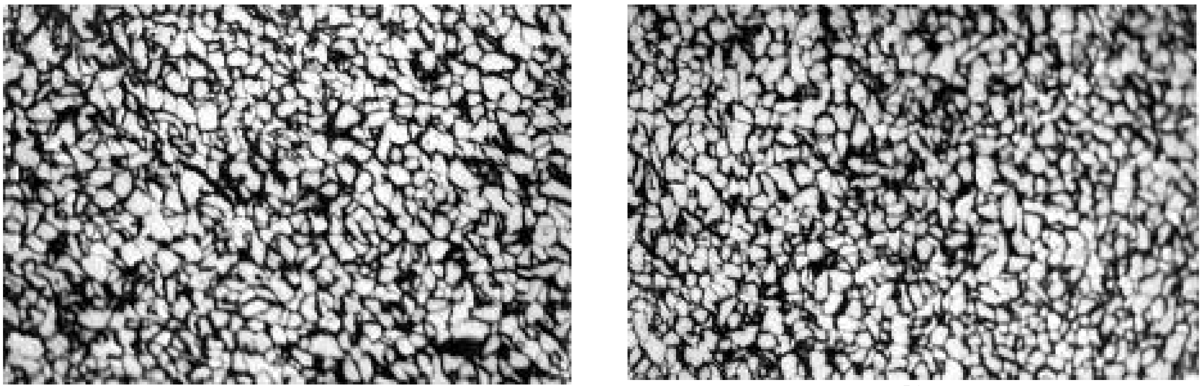

a) ***b)***

Fig. 2. The microstructure of the blank tests (hot rolled):
a – longitudinal section; b – cross section (x250).

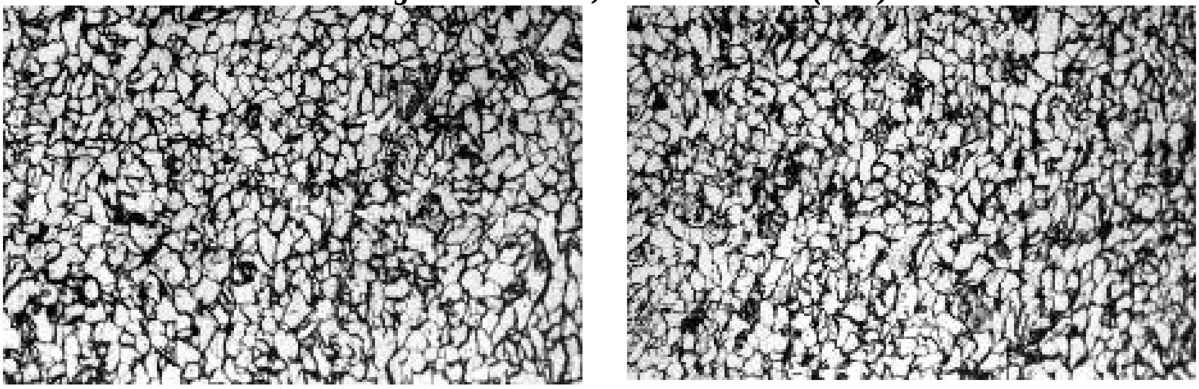

a) $\varepsilon_1 = 2.2$ ***%*** ***b)***

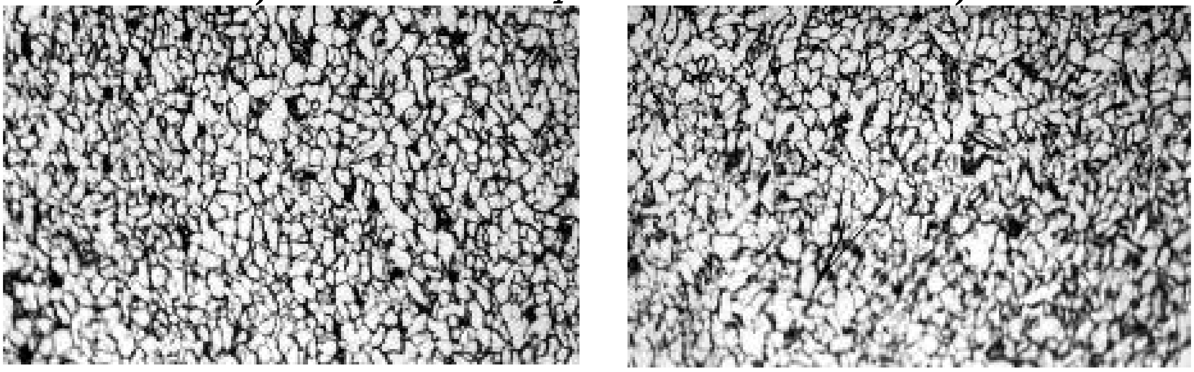

c) $\varepsilon_2 = 6.5$ ***%*** ***d)***

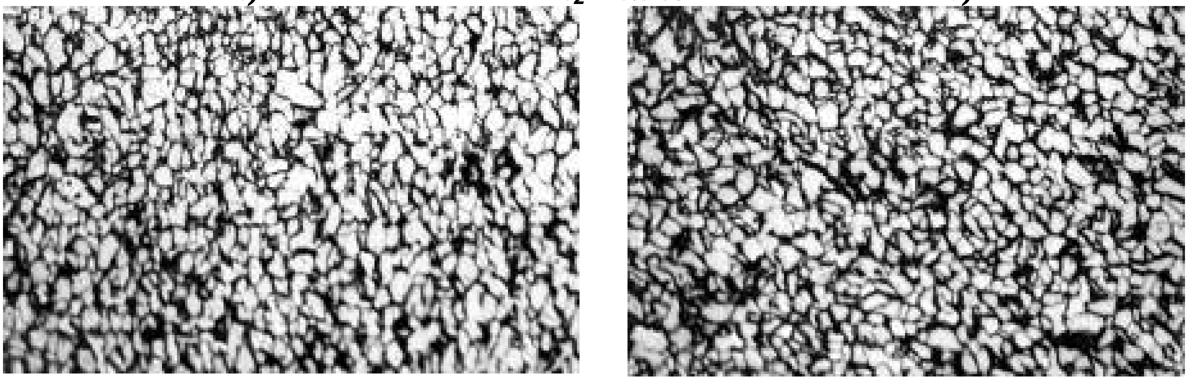

e) $\varepsilon_3 = 15.2$ ***%*** ***f)***

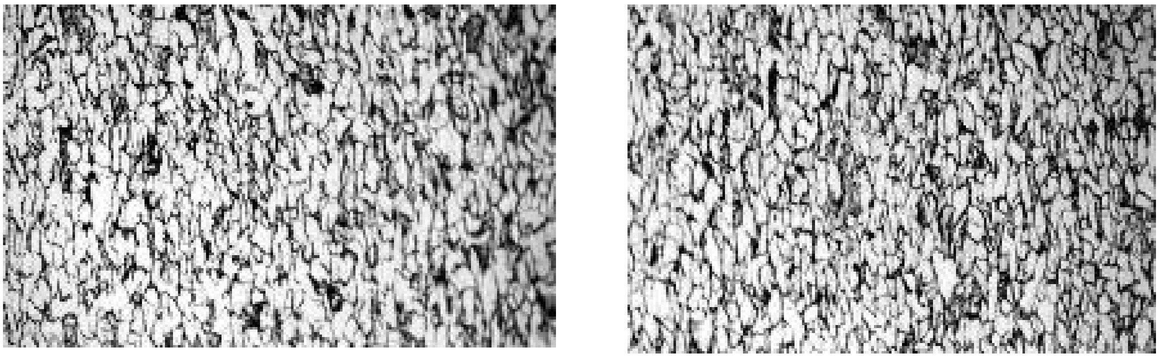

g) ***$\varepsilon_4 = 32.5$ %*** ***h)***

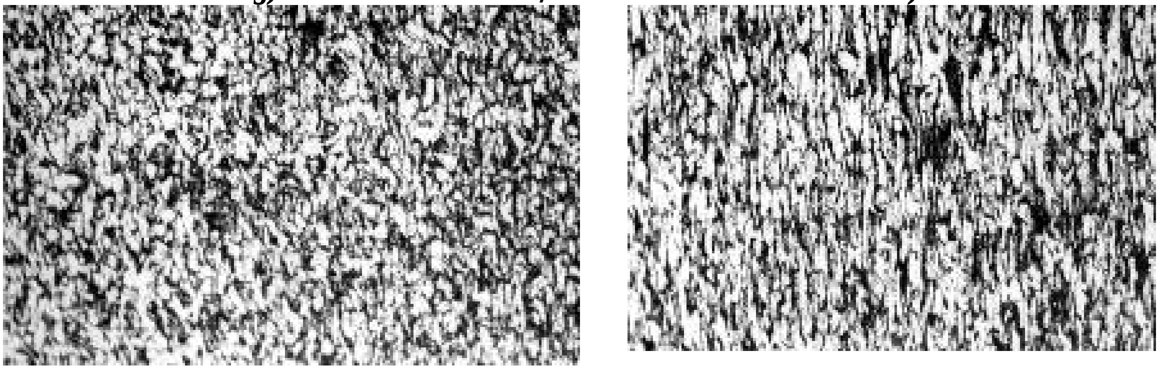

i) ***$\varepsilon_5 = 50$ %*** ***j)***

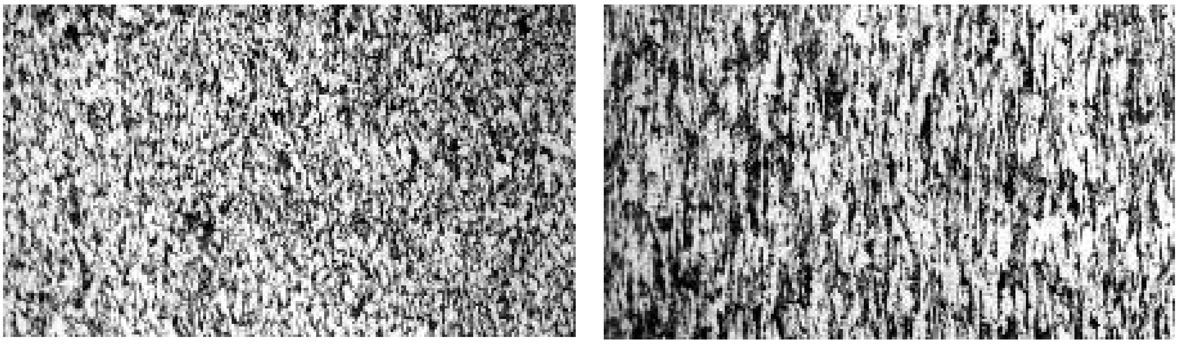

k) ***$\varepsilon_6 = 65$ %*** ***l)***

Fig. 3. The microstructures of the cold rolled assays with different deformation degree made in: a, c, e, g, i, k- longitudinal section; b, d, f, h, j, l – cross section (x250)

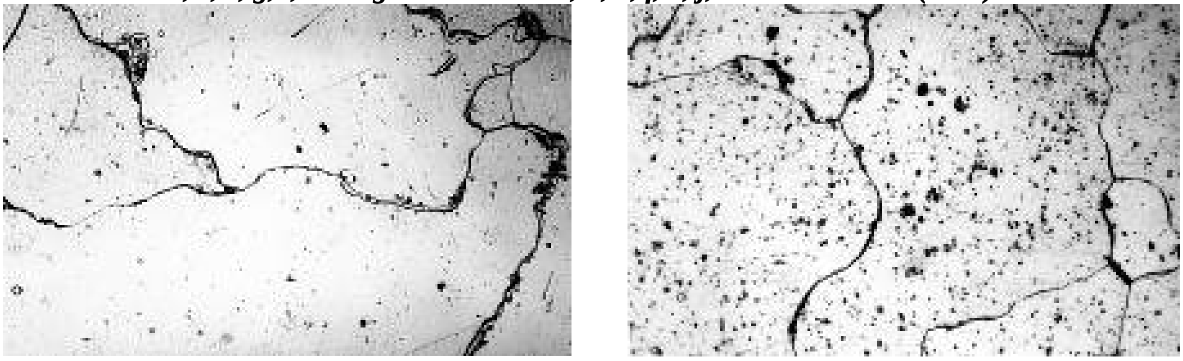

a) ***$\varepsilon_1 = 2.2$ %*** ***b)***

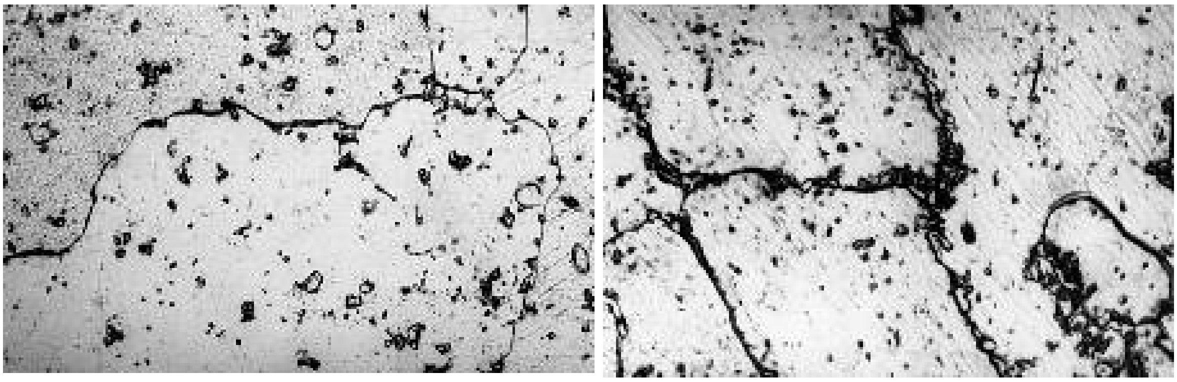

c) ***ε_2 = 6.5 %*** ***d)***

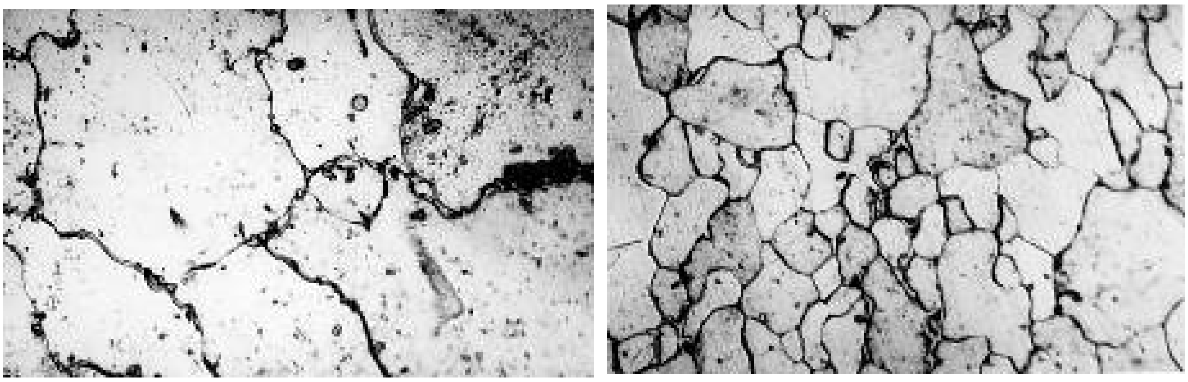

e) ***ε_3 = 15.2 %*** ***f)***

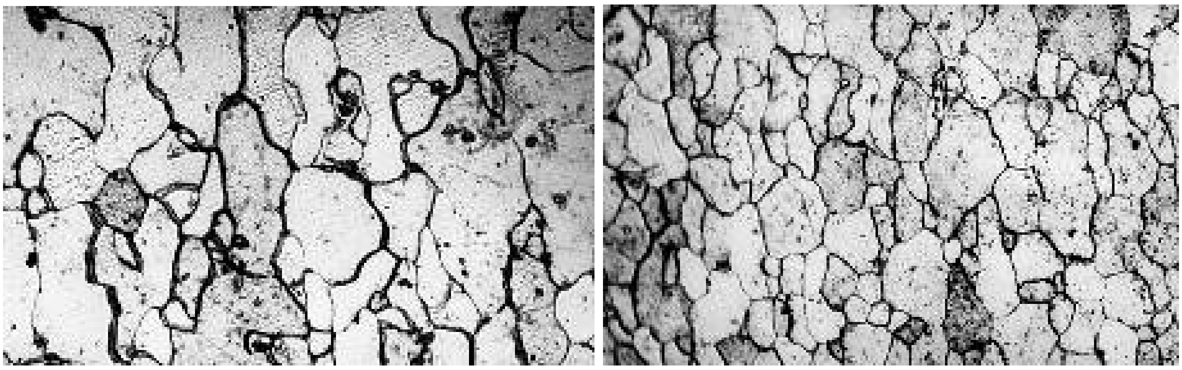

g) ***ε_4 = 32.5 %*** ***h)***

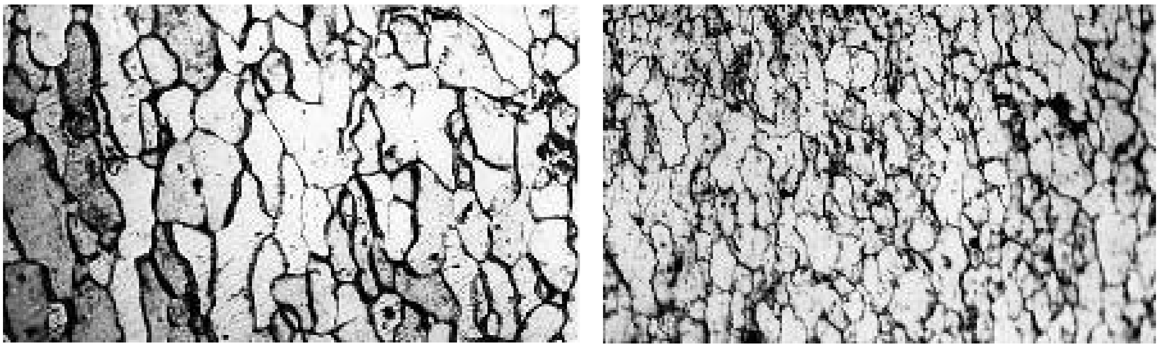

i) ***ε_5 = 50 %*** ***j)***

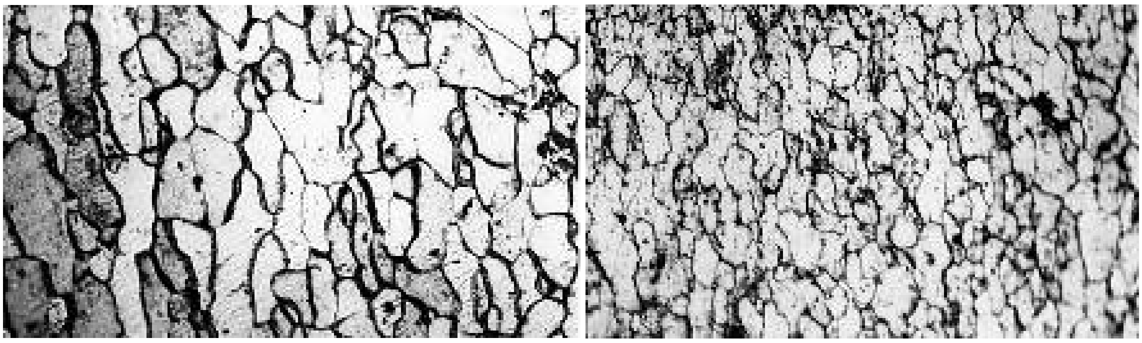

i) **ε_5 = 50 %** j)

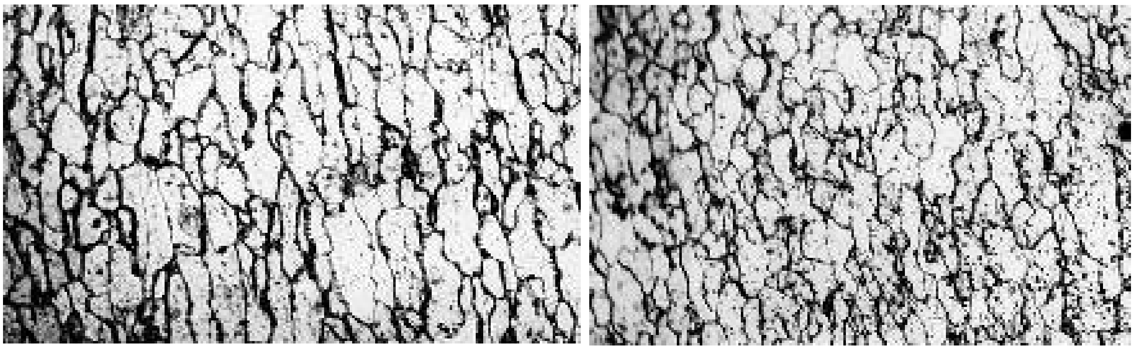

k) **ε_6 = 65 %** l)

Fig. 4. The microstructures of the cold rolled samples with different deformation degrees thermal treated in industrial bell furnace made in: a, c, e, g, i, k- longitudinal section; b, d, f, h, j, l – cross section (x250)

For the thermal treatment analyzed in this paper, one can notice that at small deformation degrees (6.5%) a coarse granulation is obtained (fig. 3), which leads to the conclusion that for the analyzed steel ***the critical degree of deformation*** is found around this value.

At high deformation degrees (over 32.5%), the granulation begins to finish itself and it gets finer as the deformation degree increases. This aspect of the microstructure appears both in longitudinal sections and in cross sections of the samples (fig. 5).

The analyzed microstructures showed that the samples analyzed under industrial conditions in bell furnace with long maintaining times, present an accentuated non-uniformity of the granulation in the strap’s section, at small deformation degrees. When increasing the deformation degree (over 32.5%), this non-uniformity is getting higher.

In fig. 5 is presented the graph with the variation of the average diameter of the grains obtained after applying the thermal treatment for a long period of time, under industrial conditions in bell furnace, for the cold deformed sample sets with different deformation degrees (**ε_1** = 2.2% ; **ε_2** = 6.5% ; **ε_3** = 15.2%; **ε_4** = 32.5% ; **ε_5** = 50.0% ; **ε_6** = 65.0%).

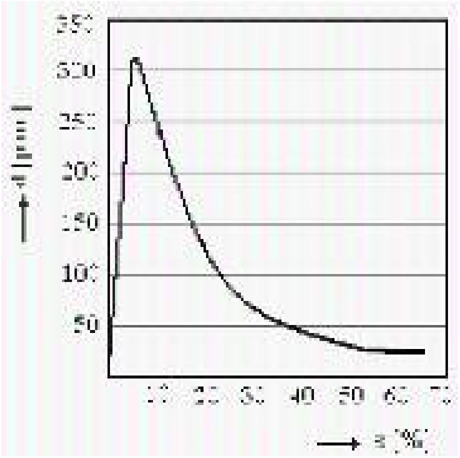

Fig. 5. The average dimension of the grains dependent on the cold deformation degree, for the heat treated assays under industrial conditions:
T= 720^{o}C and maintaining time 24 hours

3. Conclusions

The granulation of analyzed steel is strongly influenced by the cold deformation degree.

The microstructures made for different deformation degrees show, for high deformation degrees (over 50%), a fibrous structure clearly seen on longitudinal sections.

The microstructures made from samples with different deformation degrees and industrial thermal treated show that the critical deformation degree for the analyzed steel is around 6.5%, the point were the granulation starts to grow in excess. Also for deformation degrees over 32.5% the non-uniformity of the longitudinal and transversal granulation diminishes.

References

[1]. Engl, B., Potte – Schmidt, K., ***Korneigenschaften und ihr Einfluse auf dasunterbesonderer Berucksichtingung von kaltgewaltzten Feinblechstahles***: Stahl und Eisen nr.7,1994.

[2]. Wilson, AW., Spanos, G. ***Application of orientation imaging microscopy to study phase transformation in steels***. Materials characterization, 2001, volume 46, page 407.

[3]. Randle, V., Engler, O. ***Introduction to texture analysis; macrotexture, microtexture and orientation mapping.*** Taylor & Francis, London, 2003.

[4]. E.J. Drewes and B. Engl, Stahl und Eisen 108 (1988), p. 987

[5]. C.G.H. Brun and M.J.M. Munier, ***HSLA steels metallurgy and applications***, ASM International, 1986, p. 941

[6]. K. Olsson, ***Processing microstructure and properties of HSLA steels***, TMS, Warrendale (PA), 1988, p. 331

[7]. *******ASM Handbook***, Volume 1, Properties and Selection: Irons, Steels, and High Performance Alloys - Carbon and Low-Alloy Steels - Processing of Solid Steel – Annealing - Continuous Annealing

[8]. *******ASM Handbook***, Volume 4, Heat Treating - Heat Treating of Steel - Continuous Annealing of Steel

[9]. F. Potecasu, O. Potecasu, P. Alexandru - ***Influence of the deformation degree on the structure and mechanical characteristics of steel sheets intended for producing car bodies*** - The 12th International Metallurgy & Materials Congress and Fair 28-30 sept 2005 Istambul, Turcia, e-book, ISBN 9944-89-073-1, 2005 p.89-95

THE ANNALS OF “DUNAREA DE JOS” UNIVERSITY OF GALATI.
FASCICLE IX. METALLURGY AND MATERIALS SCIENCE
N^0. 2 – 2007, ISSN 1453 – 083X

BASIC MATHEMATICAL MODELING OF THE ENVIRONMENTAL PROCESSES IN THE LOWER DANUBE REGION [I]

Viorel MUNTEANU[1], Ovidiu COSTEA[2]
[1] University “Dunarea de Jos” Galaţi
[2] S.C. Industrial Parc S.R.L.,
e-mail: viorel.munteanu@ugal.ro
e-mail: ovidiu_costea@yahoo.com

ABSTRACT

In most environmental pollution problems, the pollutant is released to the environment by the, almost always, turbulent flow of a carrier fluid. The pollutant mixes with the surrounding fluid (air or water) and undergoes chemical transformations. A proper account of “where the pollutant went” and “what happened to it” necessitates a theory of turbulent reacting flows, i.e. the simultaneous treatment of mixing and chemical reactions. The important field of Air Quality Modelling is an interdisciplinary field borrowing elements from Fluid Mechanics, Atmospheric Chemistry, Meteorology and others.

KEYWORDS: Air Quality Modelling, Fluid Mechanics, Meteorology, turbulent flow

1. Introduction

1.1 Atmospheric dispersion models [1]

Atmospheric dispersion models are computer programs that use mathematical algorithms to simulate how pollutants in the ambient atmosphere disperse and, in some cases, how they react in the atmosphere. The dispersion models are used to estimate or to predict the downwind concentration of air pollutants emitted from sources such as industrial plants and vehicular traffic.

2. Air Quality Modelling and plume dispersion

2.1 Box models [2]

Consider the following Fig. 2.1: where we have enclosed a whole city in a control volume. Assume that the air in the box is ***fully uniform*** in concentration and that there is uniform wind of velocity ***U*** flowing along the x-direction. Assume that the box extends up to the mixing height ***H***. Assume that there is background pollution ***b*** (a convenient and common unit is in kg of pollutant per m^3 of air) that is being advected towards the city by the wind and that the city itself generates ***q*** kg/m^2 /s of the pollutant.

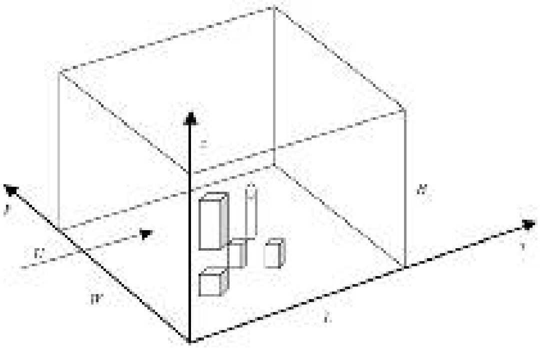

Fig. 2.1

Then, the conservation of mass for this pollutant gives for its concentration ***c*** in the box (in the same units as ***b****):*

$$WLH\frac{dc}{dt} = UWHb - UWHc + qWL - WHL\dot{w}_c \qquad 2.1$$

$$\Leftrightarrow \frac{dc}{dt} = (b-c)\frac{U}{L} + \frac{q}{H} - \dot{w}_c \qquad 2.2$$

The l.h.s. of Eq. (2.1) is the unsteady accumulation of the pollutant. The first term on the r.h.s. is the amount of pollutant advected ***into*** the box by the wind; the second term is the amount advected ***out*** of the box (note that what is being advected out has concentration c, the concentration of the wellmixed box); the third term shows how much c per unit time is released in the city (e.g. by factories or cars); the last denotes how much c is being generated by chemical reactions (e.g. by transformations from other pollutants). The reaction rate w_c has units kg of pollutant per unit volume. Very often we are interested only in the steady state, i.e. dc/dt = 0. Let us also neglect reactions, which is a good approximation if the particular pollutant reacts very slowly compared to the residence time L/U. Then, Eq. (2.2) gives that the pollutant will be in a concentration c_{bm} above the city, given by:

$$c_{bm} = b + \frac{qL}{UH} \qquad 2.3$$

This is the "standard" box model result used in Air Quality Modelling practice and hence the subscript ***bm*** in Eq. (2.3). Equation (4.3) involves many assumptions, the most important of which are that the pollutant is uniformly distributed in the box, that the wind is uniform (despite the boundary layer!), and that the emission is uniformly distributed across the area of the city. Clearly, none of these assumptions is really justified. Nevertheless, Eq. (2.3) shows the correct scaling with H and U : low mixing heights and low winds imply a higher concentration of pollutant. Note also that the local city meteorology affects the pollution concentration through the wind U and the mixing height H. Hence we expect a larger concentration of pollutant at night (small H, small U) than at day, although this may be counterbalanced by the higher emissions during daytime (e.g. from traffic).

Emphasis on chemistry

Equation (2.2) is not restricted to a single pollutant. Various researchers use it for examining also the chemistry and emphasize the reaction rate term, rather than the wind transport. In such box models, the governing equation for each species i becomes:

$$\frac{dc_i}{dt} = w_i \qquad 2.4$$

Equation (2.4) is solved by numerical methods subject to a particular set of initial conditions and the solutions can help identify how the various pollutants are transformed during the day. Comparisons with experimental data can then assist in developing chemical mechanisms, such as "tuning" the rates of the various reactions like the smog-forming reactions. Developing detailed chemical mechanisms for atmospheric pollution is a very active research area at present, not least because more and more chemicals come under regulation.

Emphasis on inhomogeneity

It is not a bad assumption to take the pollutant concentration as uniform in the z-direction, especially during unstable stratification. However, the assumption of homogeneous concentration in the wind direction is usually much worse because often q is a function of x. This can be partly dealt with by re-deriving Eq. (2.2) for a thin strip of thickness Δx and hence obtaining a differential equation for dc/dx.

Emphasis on yearly averages

Very common in Air Quality Modelling, Eq. (2.3) is used for a range of wind directions and speeds and a range of mixing heights, so that various meteorological conditions can be examined to find the corresponding pollutant concentrations. These are then weighted by the probability of occurrence of these particular conditions and hence a yearly average pollutant concentration can be calculated. Such calculations are important, e.g. for planning anti-pollution measures, for calculating the extra environmental burden of new industrial plants, etc.

2.2 Gaussian dispersion models

Model problem

The paradigm problem concerning pollution relatively close (e.g. a few km) to a source is the ***„chimney plume”***. This is shown on the following Fig. 2.2:

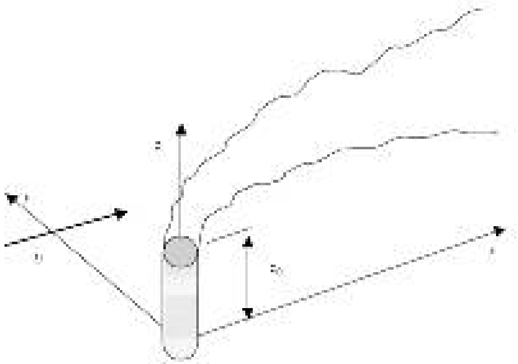

Fig. 2.2.

We are interested in: (a) the width of the plume downwind; (b) the concentration of the pollutant across the plume and particularly on the ground; (c) the difference between a steady emission (a ***„plume”***) and an unsteady emission (a ***„puff”***). To calculate these items is very important from a practical point of view and forms the topic of this chapter [4].

Governing equation for a reacting scalar

<u>Conservation of mass</u>

Consider an infinitesimal control volume ΔV. Inside the CV we have a uniform mixture of species undergoing chemical reactions.

Mass may cross the surfaces of the CV. For simplicity of presentation we assume a one-dimensional geometry.

Then, the principle of mass conservation of each species ***i*** reads:

[Rate of accumulation] = [Rate at which species comes in] – [Rate at which species leaves]+ [Rate of generation due to reaction]

In mathematical terms:

$$\frac{\partial(m_V Y_i)}{\partial t} = m_i'' \Delta y \Delta z - (m_i'' + \Delta m_i'')\Delta y \Delta z + \dot{w}_i \qquad 2.5$$

where: $\boldsymbol{m_V}$ (Kg): total mass of mixture inside the CV,

$$m_V = \boldsymbol{\rho}\Delta x \Delta y \Delta z$$

$\boldsymbol{Y_i}$: mass fraction of *I;* $\boldsymbol{\rho}$ (Kg/m^3): mixture density; $\boldsymbol{m_i''}$ (Kg/m^2/s): mass flow of species I per unit time per unit surface, the ***mass flux;*** $\boldsymbol{\dot{w}_i}$ (Kg/m^3/s): mass of species generated per unit volume per unit time due to chemical reactions

Letting Δ*x* go to zero, we obtain the ***species conservation equation***:

$$\frac{\partial(\rho Y_i)}{\partial t} = -\frac{\partial m_i''}{\partial x} + \dot{w}_i \qquad 2.6$$

The mass flux $\boldsymbol{m_i''}$ for each species that appears in the species conservation equation is composed of two parts: an ***advective*** and a ***diffusive*** part.

$$m_i'' = m_{i,ADV}'' + m_{i,DIFF}'' \qquad 2.7$$

The advective mass flux is due to the bulk fluid motion and is given by:

$$m_{i,ADV}'' = Y_i m'' = Y_i \rho u \qquad 2.8$$

The diffusive mass flux is given by ***Fick’s Law***:

$$m_{i,DIFF}'' = -\rho D \frac{\partial Y_i}{\partial x} \qquad 2.9$$

Fick’s Law states that the mass flux is proportional to the gradient of the mass fraction of the species. This is a diffusion process because it tends to make concentration gradients more uniform, i.e. it mixes the various species together. The coefficient ***D*** (m^2/s) is the ***diffusion coefficient*** and, in general, depends on the nature of the diffusing species. For gases, it is a common approximation that the diffusion of heat and mass follow the same rate, i.e. ***D*** is related to the conductivity $\boldsymbol{\lambda}$:

$$\rho D = \frac{\lambda}{c_p} \qquad 2.10$$

Final instantaneous species conservation equation

With these expressions, the species conservation equation takes the final form:

$$\frac{\partial(\rho Y_i)}{\partial t} + \frac{\partial(\rho u Y_i)}{\partial x} = \frac{\partial}{\partial x}\left(\rho D \frac{\partial Y_i}{\partial x}\right) + \dot{w}_i \qquad 2.11$$

It is important to know the physical mechanisms contributing to this equation: the first term in the l.h.s. corresponds to accumulation of species *i*, the second to advection by the bulk fluid motion, the first term in the r.h.s. corresponds to molecular diffusion and the last to the generation by the chemical reactions.

In more dimensions and for a generic scalar ***Ø*** that is proportional to the mass fraction (e.g. our usual concentration in atmospheric pollution expressed in kg/m^3), the governing transport conservation equation becomes:

$$\frac{\partial \phi}{\partial t} + u_j \frac{\partial \phi}{\partial x_j} = D \frac{\partial^2 \phi}{\partial x_j^2} + \dot{w} \qquad 2.12$$

in Cartesian tensor notation, where we have assumed an incompressible flow and a constant diffusivity, typically excellent assumptions in environmental fluid mechanics. If the scalar is inert, then simply $\boldsymbol{\dot{w}} = 0$. Equation (2.12) is the starting point for examining turbulent mixing.

Averaged species conservation equation

In a turbulent flow, we can write that the instantaneous mass fraction of a scalar is $\boldsymbol{\varphi = \bar{\varphi} + \varphi'}$ and that the velocity is $u = \bar{u} + u'$ .It is easy to see that, by performing Reynolds decomposition and performing the averaging procedure on the Eq. 2.12 we get :

$$\frac{\partial \bar{\phi}}{\partial t} + \frac{\partial(\bar{u}_j \bar{\phi})}{\partial x_j} + \frac{\partial(\overline{u_j' \phi'})}{\partial x_j} - D \frac{\partial^2 \bar{\phi}}{\partial x_j^2} + \dot{w} \qquad 2.13$$

The first term in the l.h.s. is the unsteady accumulation of $\boldsymbol{\varphi}$, the second is due to mean advection, and the third is due to turbulent transport (or turbulent diffusion). The first term in the r.h.s. is due to molecular diffusion and the second is the mean reaction rate.

Modelling the scalar flux – the eddy diffusivity

It is usual engineering practice to model the turbulent transport term using the ***eddy diffusivity*** concept, also known as the ***gradient approximation***. This model is motivated from the Kinetic Theory of Gases, where the mass flux is found to be proportional to the gradient of the mass fraction (Eq. 2.9) and the molecular diffusivity ***D*** is found to be proportional to the mean molecular speed and the mean free path between molecular collisions.

By making an analogy between the random turbulent motions of “fluid particles” and the random molecular motion in a fluid, the turbulent transport term is written as:

$$\overline{u'_j\phi'} = -D_T \frac{\partial \bar{\phi}}{\partial x_j} \qquad 2.14$$

with the eddy diffusivity D_T given by

$$D_T = C\,u'\,L_{turb} \qquad 2.15$$

By a trial-and-error procedure and comparison with experimental data, the constant C is found to be around 0.1, but this depends on how L_{turb} is defined. There is a lot of criticism behind the use of the gradient approximation for modelling turbulent transport and indeed sometimes Eqs. (2.14) and/or (2.15) fail to predict the correct magnitude of mean (u_j**’ϕ**) . Nevertheless, the eddy diffusivity concept remains a very useful approximation for providing a tractable closure to Eq. (2.13), which then becomes:

$$\frac{\partial \bar{\phi}}{\partial t} + u_j \frac{\partial \bar{\phi}}{\partial x_j} = \frac{\partial}{\partial x_j}\left[(D + D_T)\frac{\partial \bar{\phi}}{\partial x_j}\right] + \dot{w} \qquad 2.16$$

Note that D_T may be a function of space and hence should be kept inside the derivative in the r.h.s. of Eq. (2.16). The eddy diffusivity concept is usually much better for an ***inert*** scalar than for a ***reacting*** scalar, but we use it anyway.

For high Reynolds numbers, $D \ll D_T$, which suggests that the molecular diffusion may be neglected. To illustrate this, consider a wind flow of 5 m/s with a typical turbulence intensity of 10%, so that u' = 0.5 m/s. In the atmospheric boundary layer, the lengthscale is proportional to the height above the ground. Let us take that L_{turb}=500 m. Then D_T = 25 m^2/s. At standard temperature and pressure, the molecular diffusivity of air is 2.2 x10^{-5} m^2/s (see Eq. 2.10). Therefore the diffusion caused by molecular motions is negligible compared to the diffusion due to turbulence, which is a typical feature of turbulent flows at large Reynolds numbers. Molecular action is ***always*** present at the smallest scales, but these contribute very little to the overall diffusion of the scalar (the small eddies just don’t “move far enough”). In other words, “where the smoke goes” is a function of the large scales only and the turbulent diffusivity suffices.

Turbulent diffusion of an unsteady puff

In many cases, we are interested in the way a pollutant spreads under the action of turbulent diffusion, when the emission of the pollutant is not continuous, but occurs only for a short time. Our full governing equation (Eq. 2.16) is our starting point, but to demonstrate how the solution comes about, let us assume zero mean velocities and finite and spatially-uniform turbulent diffusivity.

Then, Eq. (2.16) becomes:

$$\frac{\partial \bar{\phi}}{\partial t} = K_j \frac{\partial^2 \bar{\phi}}{\partial x_j^2} + \dot{w} \qquad 2.17$$

The overbar denotes the mean concentration of the pollutant and the eddy diffusivity is now allowed to be a function of the direction. This is usually the case in atmospheric turbulence: the velocity fluctuations are not really equal in the three directions, and hence the eddy viscosity is strictly speaking a (diagonal) tensor. Hence the appearance of the subscript ***j*** in ***K*** in Eq. (2.17). We have also denoted the turbulent diffusivity by the symbol ***K*** (rather than D_T) to conform to the standard notation in atmospheric pollution.

For an inert pollutant, Eq. (2.17) is identical to the unsteady heat conduction equation for an “instantaneous source” and has a known solution. If ***Q*** kg/s of pollutant are released over a (very short) time **Δt** at point (x_0,y_0,z_0), the solution of Eq. (2.17) gives for the mean pollutant concentration $\bar{\boldsymbol{\varphi}}$ in one, two, and three dimensions (in kg/m, kg/m^2, kg/m^3 respectively):

$$\bar{\phi}(x) = \frac{Q\Delta t}{2(\pi t)^{1/2}(K_x)^{1/2}}\exp\left[-\frac{1}{4t}\frac{(x-x_0)^2}{K_x}\right] \qquad 2.18$$

$$\bar{\phi}(x,y) = \frac{Q\Delta t}{4(\pi t)(K_x K_y)^{1/2}}\exp\left[-\frac{1}{4t}\left(\frac{(x-x_0)^2}{K_x}+\frac{(y-y_0)^2}{K_y}\right)\right] \qquad 2.19$$

$$\bar{\phi}(x,y,z) = \frac{Q\Delta t}{8(\pi t)^{3/2}(K_x K_y K_z)^{1/2}}\exp\left[-\frac{1}{4t}\left(\frac{(x-x_0)^2}{K_x}+\frac{(y-y_0)^2}{K_y}+\frac{(z-z_0)^2}{K_z}\right)\right] \qquad 2.20$$

where t is the time from the release. Note the “symmetry” of the terms in the exponential, but also note that the behaviour of the maximum concentration at the centre of the cloud (i.e. at x_0,y_0,z_0) has a different scaling with time depending on the dimensionality of the problem.

In practical atmospheric dispersion of pollutant clouds, the wind has to be taken into account. The situation is visualized in the following Fig. 2.3.

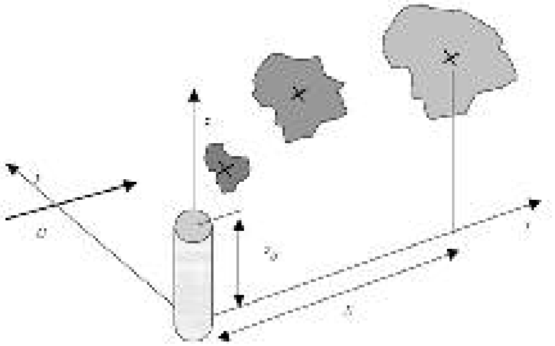

Fig. 2.3.

The governing equation becomes (for an inert pollutant):

$$\frac{\partial \bar{\phi}}{\partial t} + U\frac{\partial \bar{\phi}}{\partial x} = K_x\frac{\partial^2 \bar{\phi}}{\partial x^2} + K_y\frac{\partial^2 \bar{\phi}}{\partial y^2} + K_z\frac{\partial^2 \bar{\phi}}{\partial z^2} \qquad 2.21$$

The solution of Eq. (2.21) is again Eq. (2.20), but now we must interpret the time ***t*** as the downwind distance ***X*** of the ***centre of the pollutant cloud***, divided by the wind speed ***U***, and ***x,y,z*** as the distances from the centre of the cloud. In Eulerian coordinates (more useful!), ***x*** should be replaced by (***x-X***), with ***X=Ut***. Usually, the coordinate system we use has an origin immediately underneath the release point on the ground (i.e. $x_0=y_0=0$) (Fig. 2.3) and so the “standard” form of the solution of Eq. (2.21) reads:

$$\bar{\phi}(x,y,z)=\frac{Q\Delta t}{8(\pi t)^{3/2}(K_xK_yK_z)^{1/2}}\exp\left[-\frac{1}{4t}\left(\frac{(x-Ut)^2}{K_x}+\frac{y^2}{K_y}+\frac{(z-z_0)^2}{K_z}\right)\right]$$

Depending on the relative magnitude o 2.22 , the cloud may take a spherical or ellipsoidal or even a disk-like shape.

Final equation

Very often in atmospheric dispersion, we do not use the eddy diffusivities directly, but we work with the ***dispersion coefficients*** [5] , defined by:

$$\sigma_x^2=2\frac{X}{U}K_x,\qquad \sigma_y^2=2\frac{X}{U}K_y,\qquad \sigma_z^2=2\frac{X}{U}K_z \qquad 2.23$$

Using the dispersion coefficients (units: m), Eq. (2.22) becomes:

$$\phi(x,y,z,t)=\frac{Q\Delta t}{(2\pi)^{3/2}\sigma_x\sigma_y\sigma_z}\exp\left[-\left(\frac{(x-Ut)^2}{2\sigma_x^2}+\frac{y^2}{2\sigma_y^2}+\frac{(z-z_0)^2}{2\sigma_z^2}\right)\right]$$

2.24

which is a “**standard**” **Gaussian expression**. The dispersion coefficients are usually functions of ***X***. It is important to note that Eq. (2.24) is valid even if the eddy diffusivities ***K*** are not constant. This would be the case for short times from the release because then the constant eddy diffusivity idea breaks down: for small cloud widths, the pollutant is being dispersed by the action of only a small range of the turbulent eddies.

This makes the diffusivity a function of time, until the cloud becomes large relative to the turbulence lengthscale. In atmospheric problems, this is hardly ever achieved and the dispersion coefficients in the above equations must be provided empirically.

Equation (2.22) (or Eq. 2.24) is called the “**Gaussian puff equation**” and is very useful in providing numerical estimates on the average amount of pollutant reaching a given point at a given time after a release. Such estimates are crucial for assessing the danger after accidents, such as the Chernobyl nuclear disaster or chemical releases. They are also used to assess the origin of the pollutant, given a set of measurements of the pollutant concentration at a particular point and the meteorological conditions prevailing at that time.

Cloud width

Another use of Eq. (2.24) is to find the width of the cloud. This can be defined in various ways, since the concentration reaches zero asymptotically towards the edge of the cloud. A common way is to use the length:

$$\sqrt{2\sigma_y^2}=2\sqrt{K_yX/U} \qquad 2.25$$

as a characteristic half-width of the Gaussian cloud in the *y*-direction and similarly for the other directions. This length marks the location from the cloud centre where the concentration falls to 1/*e* of the centre value.

Turbulent diffusion of a steady plume

One way to understand the continuous emission from a chimney (Fig. 2.2) is to view it as a series of “instantaneous puffs”. Based on the linearity of Eq. (2.21), the overall concentration $\bar{\varphi}$ downwind would be the sum over all such puffs. Assume then that the chimney continuously releases ***Q*** kg/s of pollutant and we use ***t=x/U***. We are interested in the pollutant concentration at a particular point (***x,y,z***) at time ***t***. Equation (2.24) can be integrated over time, to give the mean concentration due to a continuous source:

$$\bar{\phi}(x,y,z)=\frac{Q}{(2\pi)^{3/2}}\int_0^{\infty}\exp\left[-\left(\frac{(x-Ut')^2}{2\sigma_x^2}+\frac{y^2}{2\sigma_y^2}+\frac{(z-z_0)^2}{2\sigma_z^2}\right)\right]\frac{1}{\sigma_x\sigma_y\sigma_z}dt'$$

2.26

It is important to remember that we are now dealing with diffusion at ***early times***, i.e. we are interested in the region close (e.g. of the order of 10 to 104 m) to the plume source. There, the width of the plume is clearly not much greater than the turbulence length scale, which is one of the conditions for validity of the constant eddy diffusivity. For short distances from the source, it turns out that the dispersion coefficients are proportional to time:

$$\sigma_x=u't,\qquad \sigma_y=v't,\qquad \sigma_z=w't \qquad 2.27$$

where u', v', w' are the r.m.s. turbulent velocities in the three directions, assumed constant. Equation (2.26) can then be integrated to give:

$$\phi(x,y,z)=\frac{Q}{(2\pi)^{3/2}}\frac{u'}{v'w'r^2}\exp\left(-\frac{U^2}{2u'^2}\right)\left[1+\sqrt{\frac{\pi}{2}}\frac{Ux}{u'r}\exp\left(\frac{U^2x^2}{2u'^2r^2}\right)\mathrm{erfc}\left(-\frac{1}{\sqrt{2}}\frac{Ux}{u'r}\right)\right]$$

2.28

with

$$r^2=x^2+\frac{u'^2}{v'^2}y^2+\frac{u'^2}{w'^2}(z-z_0)^2$$

Usually, the plume is *slender*, which implies that $r\approx x$, and usually $u'/U \equiv 0$ (0.1) $\ll$ 1. Both these assumptions are used to simplify Eq. (2.28) into:

$$\bar{\phi}(x,y,z)=\frac{Q}{2\pi}\frac{1}{U\sigma_y\sigma_z}\exp\left[-\left(\frac{y^2}{2\sigma_y^2}+\frac{(z-z_0)^2}{2\sigma_z^2}\right)\right]$$

2.29

This is **the final result for the plume diffusion problem**. It is often called the “***Gaussian plume equation***”. The x dependence comes indirectly through the dependence of the dispersion coefficients on x, while the dependence on y and z comes directly from the exponential.

2.3 Efects of Lower Danube region meteorology [6]

Effect of inversions

We mentioned previously that the case of one-dimensional diffusion in the horizontal direction approximately corresponds to the case where the plume is perfectly mixed in the vertical direction. If the mixing height is higher than the source height, i.e. if $H > (h_s+h_{pr})$, then there is every possibility that the plume will hit the inversion lid from below, from where it will be reflected downward etc. This situation is shown in the following figure (Fig. 2.5), which also demonstrates how the image source idea can be used to account for the mixing height. It is clear that the vertical direction will eventually become quite homogeneous.

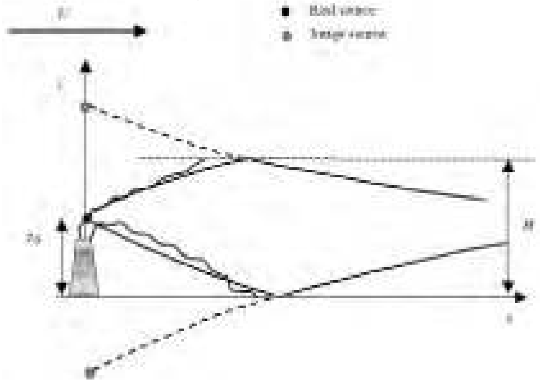

Fig 2.5. Effect of inversion lids on diffusion (source below the inversion)

Fig. 2.6. Pollution above Galati city

Low mixing heights will result in higher ground concentrations.

Inversions assist in “trapping” pollution above, for example Galati city, which can be thought as composed of a very large number of point sources. In addition to more intense photochemistry, these conditions are favorable for the creation of inversion lids and hence such city encounter high levels of pollution often, see the following Figure 2.6.

2.4 Practical Air Quality Modelling

In previous chapter, we presented the “Box Model”, which is a very useful tool for estimating the pollution above a city. Such box models are used in scales of a few km. If one is interested in finer scales (e.g. a few hundred meters), and this may be imperative for accurate calculations of dosage, e.g. from a new industrial plant or a planned motorway, then we need to consider the dispersion very close to the source. For uniform wind conditions and well-defined sources, the Gaussian plume theory is approximately correct for up to a few tens of km, but eventually our assumption of constant wind will becomes invalid. For *synoptic scales*, i.e. longer than 200 km, we need to couple our pollution dispersion models with proper meteorological (i.e. weather prediction) codes like Eulerian codes and Lagrangian codes. An atmospheric dispersion model [3] based on atmospheric boundary layer turbulence structure and scaling concepts including treatment of multiple ground-level and elevated point, area and volume sources is AERMOD. It handles flat or complex, rural or urban terrain and includes algorithms for building effects and plume penetration of inversions aloft seen in Figure 2.7 [6]

Fig. 2.7. SO2 concentrations in Galati area modeled with Aermod

3. Conclusions

The dispersion models require the input of data which includes:

- Meteorological conditions such as wind speed and direction, the amount of atmospheric turbulence (as characterized by the stability class), the ambient air temperature and the height to the bottom of any inversion aloft that may be present;

- Emissions parameters such as source location and height, source vent stack diameter and exit velocity, exit temperature and mass flow rate;
- Terrain elevations at the source location and at the receptor location;
- The location, height and width of any obstructions (such as buildings or other structures) in the path of the emitted gaseous plume.

References

[1]. Munteanu, V – Calitatea Mediului, note de curs, 2007 Universitatea „Dunarea de Jos” Galati

[2]. Mastorakos, E. – Environmental Fluid Mechanics, Hopkins Lab

[3]. Balanescu, M., Hritac, M., Melinte, I., Nicolae, A – Environmental impact assesment of an industrial accident using ISC-Aermod view, a case study

[4]. Wigley, T.M.L., Slawson, R.P., Csanady, G.T., Rennie, J.H., The behaviour of moisture laden plumes, 1972, University of Waterloo

[5]. Turner, D.B. - Workbook of atmospheric dispersion estimates: an introduction to dispersion modeling, 1994, 2nd Edition, CRC Press

[6]. Research contract RO 2004/016-941.01.01.04 – Integrated monitoring of environmental media (air, water, soil) in the Lower Danube Euroregion, Galati-Cahul area”

THE ANNALS OF “DUNAREA DE JOS” UNIVERSITY OF GALATI.
FASCICLE IX. METALLURGY AND MATERIALS SCIENCE
N^0. 2 – 2007, ISSN 1453 – 083X

PREDICTION OF BUCKLING AND POSTBUCKLING BEHAVIOUR OF COMPOSITE SHIP PANELS

Ionel CHIRICA, Elena-Felicia BEZNEA,
Raluca CHIRICA, Doina BOAZU
“Dunarea de Jos” University of Galati
email: ionel.chirica@ugal.ro

ABSTRACT

The behavior of ship plating normally depends on a variety of influential factors, namely geometric/material properties, loading characteristics, initial imperfections, boundary conditions and deterioration arising from corrosion and fatigue cracking. The analysis is presented for a uniaxially in-plane loaded, clamped, composite laminated quadratic plate. The imperfection is considered as the initial deformation due to the manufacturing operations: cosinusoidal shape in both of the longitudinal and transverse direction. Usually, the initial deformation mode appears in the form such as the fundamental mode of the buckling or vibration (figure 1) Variation of the maximum transverse displacement regarding the inplane load (displacement controlled after nonlinear buckling analysis) for three cases are presented.

Keywords: Composite panels, Buckling, Postbuckling

1. Introduction

The increasing interest in minimum weight designs for ship structures has generated important studies in the analysis of the elastic stability and postbuckling behavior of structures subjected to in-plane compressive loads. Due to their high strength and stiffness-to-weight ratios, laminated composite materials are increasingly being used in the shipbuilding industry.

The overall failure of a ship hull girder is normally governed by buckling and plastic collapse of the deck, bottom or sometimes the side shell stiffened panels. Therefore, the relatively accurate calculation of buckling and plastic collapse strength of stiffened plating of the deck, bottom and side shells is a basic requirement for the safety assessment of ship structures. In stiffened panels, local buckling and collapse of plating between stiffeners is a primary failure mode, and thus it would also be important to evaluate the buckling and collapse strength interactions of plating between stiffeners under combined loading.

The behavior of ship plating normally depends on a variety of influential factors, namely geometric/material properties, loading characteristics, initial imperfections (i.e., initial deflections and residual stresses), boundary conditions and deterioration existing local damage related manufacture imperfection or fatigue cracks.

For thin homogeneous (metallic) plates, classical plate theory predicts deformations and inplane stresses that are comparable to those of three-dimensional elasticity. In thin plates, transverse stresses are generally small compared to in-plane stresses, and thus, both classical theory and first-order shear deformation theory give satisfactory results. However, since both theories are two-dimensional, they are not accurate enough to predict transverse stresses directly.

Generally, composite plates support greater compressive load beyond the buckling load. Therefore, buckling and postbuckling behaviors of composite plates are very important factors of structural designs. There are more studies of buckling behavior than those of postbuckling behavior of composite plates. VandenBrink et al. (1987) investigated postbuckling behavior of graphite/epoxy composite plates of [qn–qn]s layup with a hole. Englestad et al. (1992) analyzed postbuckling response and failure of graphite/epoxy panels with and without holes. In this paper, a progressive failure (buckling) analysis was introduced into the nonlinear finite element analysis. Postbuckling behavior and compressive strength of composite plates was studied through analyses.

Parametric studies were performed in order to investigate the effects of initial deformations sizes on buckling load and postbuckling compressive strength.

Buckling and postbuckling analysis are essential to predict the capacity of composite plates carrying considerable additional load before the ultimate load is reached, and manufacturing-induced geometric imperfections often reduce the load-carrying capacity of composite structures. The nature of initial geometric imperfection induced during manufacturing is accounted for in the analysis. The stiffeners presence induces the cosine shape of the initial deformation. Examples of postbuckling analyses of symmetric cross-ply, angle-ply are presented, and the accuracy and performance of the method are examined. The numerical methodology presented can be used as an accurate and efficient tool for postbuckling analysis of imperfect composite plates.

2. Analytical study of global buckling of clamped orthotropic rectangular plate

For global buckling may be considered the theoretical study of the orthotropic, rectangular plate, without imperfections, clamped on the sides, and compressed along the ***x***-axis. The external loading is considered as uniform one. The main orthotropic directions are considered as parallel with the sides. The critical value of the buckling load, p_{cr}, will be determined.

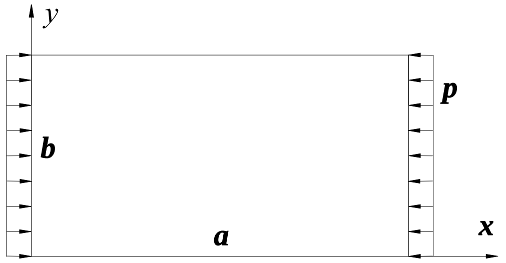

Fig. 1. The perfect plate model

The sides ratio is considered as $c=a/b$, and the loading per unit length is ***p***. According to the figure 1, the coordinate system axis are considered parallel with the sides.

Before the buckling, the plate is considered loaded as in plane stress, with $N_x=-p$, $N_y=0$, $N_{xy}=0$.

The solution may be determined by choosing the static method. The equation of the deformed plate is

$$D_1\frac{\partial^4 w}{\partial x^4}+2D_3\frac{\partial^4 w}{\partial x^2\partial y^2}+D_2\frac{\partial^4 w}{\partial y^4}+p\frac{\partial^2 w}{\partial x^2}=0$$

(1)

where

$$D_1=\frac{E_1h^3}{12(1-\mu_{21}\mu_{21})},\quad D_2=\frac{E_2h^3}{12(1-\mu_{12}\mu_{21})},$$

$$D_k=\frac{G_{12}h^3}{12},\ D_3=D_1\mu_{21}+2D_k.$$

E_1, E_2, E_3, G_{12}, μ_{12}, μ_{21} are material characteristics.

The solution of the equation (1) is to satisfy the boundary conditions

- For $x=0$ and $x=a$: $w=0,\ \frac{\partial w}{\partial x}=0$; (2)

- For $y=0$ and $y=b$: $w=0,\ \frac{\partial w}{\partial y}=0$. (3)

The boundary conditions may be satisfied by the any term of the Fourier series

$$w(x,y)=\sum_m\sum_n C_{mn}+A_{mn}\cos\frac{2m\pi(x-a/2)}{a}\cos\frac{2n\pi(y-b/2)}{b}$$

(4)

where C_{mn} and A_{mn} are constant coefficients and ***m***, ***n*** are integers. By substituting (4) in (1) it is obtained

$$p=\frac{4\pi^2\sqrt{D_1D_2}}{b^2}\ \sqrt{\frac{D_1}{D_2}}\ {\frac{m}{c}}^{2}+\frac{2D_3}{\sqrt{D_1D_2}}n^2+\sqrt{\frac{D_2}{D_1}}\ {\frac{c}{m}}^{2}n^4\ .$$

(5)

The constants A_{mn} are undetermined. Equation (5) delivers all values of ***p***, associated to the pairs of indices $m=1, 2, 3,...$, $n=1, 2, 3...$ as possible deformed forms of the plates, such as the equation (4). From the all values, the smallest one will be chosen, this being the critical value. Obviously, the smallest value of ***p*** is obtained for $n=1$, that is corresponding to the shape with one semi-wave along the side ***b***.

In the following, the value of ***m*** for the smallest value of ***p*** (named critical value) will be determined.

For n=1, the expression of ***p*** is

$$p=\frac{4\pi^2\sqrt{D_1D_2}}{b^2}\ \sqrt{\frac{D_1}{D_2}}\ {\frac{m}{c}}^{2}+\frac{2D_3}{\sqrt{D_1D_2}}+\sqrt{\frac{D_2}{D_1}}\ {\frac{c}{m}}^{2} \qquad (6)$$

3. Numerical results obtained for buckling and postbuckling behaviour of clamped orthotropic imperfect plate

Numerical studies were performed on the buckling and postbuckling behaviour of the imperfect plate. In this case, the initial deformation is in the form given by the first buckling modal shape for the same plate but considered as a perfect one.

Table 1. Plate lay-up

α	t [mm]
$+45^0$	0.195
-45^0	0.195
4×0^0	2.36
$+45^0$	0.195
-45^0	0.195
6×0^0	3.54
α	t [mm]
$+45^0$	0.195
-45^0	0.195
4×0^0	2.36
$+45^0$	0.195
-45^0	0.195

Maximum initial deformation magnitude is considered as a rate from the thickness, t, that is

$$w_o = \gamma \ t.$$

In the analysis, for the rate γ the following values were chosen: 0.002, 0.32 and 0.96.

The FEM model, composed of shell elements, for geometric representation of a plate sized 320×320, with the thickness of 10 mm, having an initial deformation, was made.

The material used for the plate has the characteristics:

- E-glass/Polyester

E_1 = 46 GPa, E_2 = 13 GPa, E_3=13 GPa
G_{12} = 5 GPa, G_{13} = 5 GPa, G_{23} = 4.6 GPa
μ_{12} =0.3, μ_{23} =0.42, μ_{13} =0.3

- UD layers: t_1 = 0.59 mm
- Biaxial layers: t_2 = 0.39 mm, modeled as two UD layers having thickness $t_2/2$, at ±45°
- Lay-up is presented in Table 1.

Numerical studies, non-linear analysis (large displacements), were performed with FEM package COSMOS/M. For FEM analysis 3-node structural layered shell element (SHELL3L) were used.

Boundary conditions introduced on the sides were:

- On x=0 edge, completely fixed;
- On x=a edge, all DOF fixed, except x-translation;
- On y=0, y=b edges, all DOF fixed, except x and y translations and z rotation.

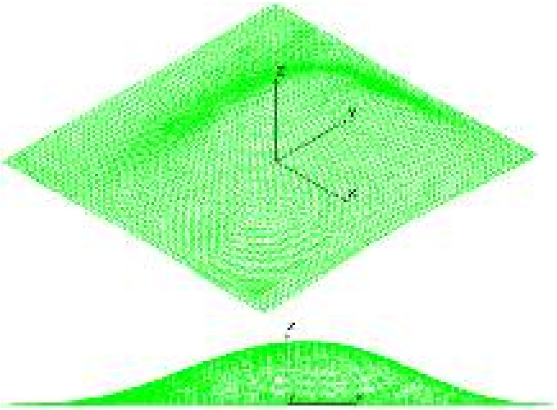

Fig. 2. The plate geometry

For the perfect plate, the critical value is
p_{cr}=172.45 MPa.

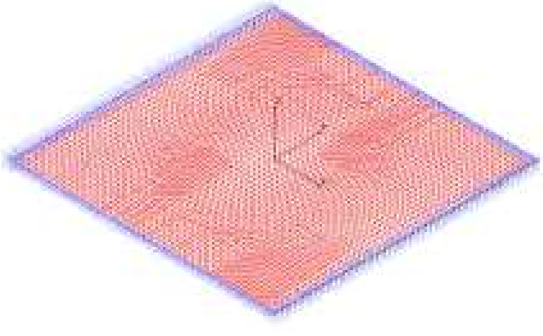

Fig. 3. Plate mesh

The theoretical buckling load obtained for a perfect plate is 207.21 MPa, determined only for future experiments calibrations.

Table 2. Buckling load

Case		Buckling load [MPa]
Theory		207.21
Perfect		172.45
Imperfect	Case 1: w_0=0.02 mm	181.66
	Case 2: w_0=3.2 mm	203.59
	Case 3: w_0=9.6 mm	288.56

Buckling load values obtained for the three cases of imperfect plates are presented in table 2.

As it is seen, the buckling load value obtained according to the equation (6) is far from that obtained for perfect plate, but is more closed to the value obtained for Case 3.

In figures 4, 5 and 6 the postbuckling behaviour of the imperfect plate for the three cases are presented. The results obtained after non-linear analysis show that the collapse does not occurs at buckling load value. The vertical dashed line corresponds to the buckling load for the perfect plate (172.45 MPa).

As it is seen, the buckling load is increasing with the increasing of the initial deformation.

4. Conclusions

This paper presents buckling and postbuckling results for composite imperfect plates, subjected to longitudinal compressive loading. The side edges of the plates are clamped. The imperfection is considered as initial deformation in the form given by the first buckling modal shape for the same plate but considered as a perfect one.

Based on the numerical results, there can be derived out the following conclusions of this study:

Values of the buckling load, p_{cr}, are increasing with the increasing of the initial deformation. That is, the stiffness of the plate is increasing with the increasing of the initial deformation.

Study made for the nonlinear buckling analysis show that the collapse does not occurs at buckling load value.

The displacement controlled nonlinear buckling analysis shows that at the same postbuckling load the maximum displacement is decreasing with the increasing of the initial maximum displacement.

The FEM models can deliver the whole range of the eigen modal buckling for the panel structure.

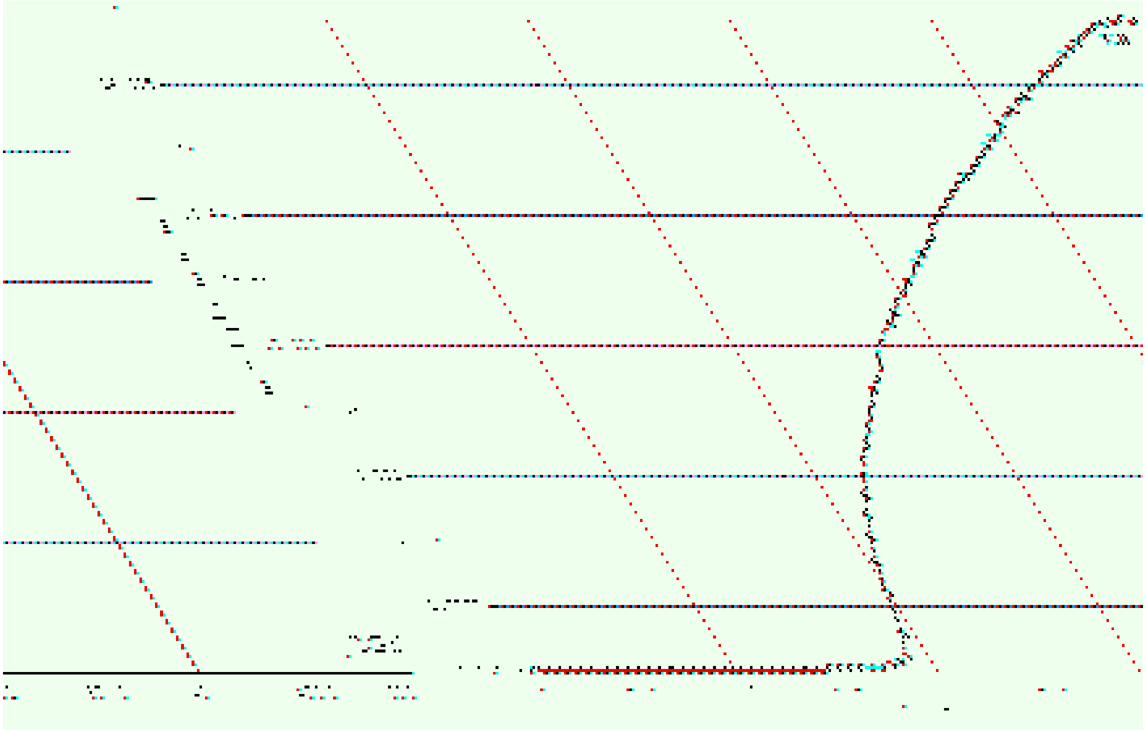

Fig. 4. Case 1: Displacement controlled nonlinear buckling analysis

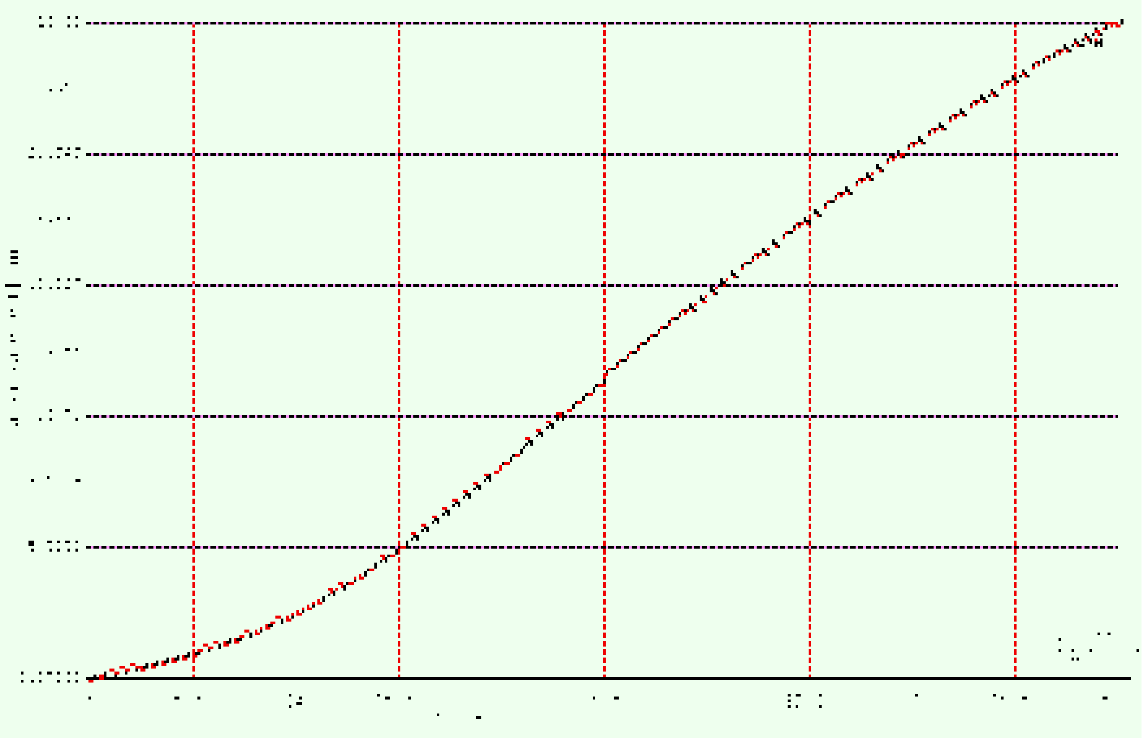

Fig. 5. Case 2: Displacement controlled nonlinear buckling analysis

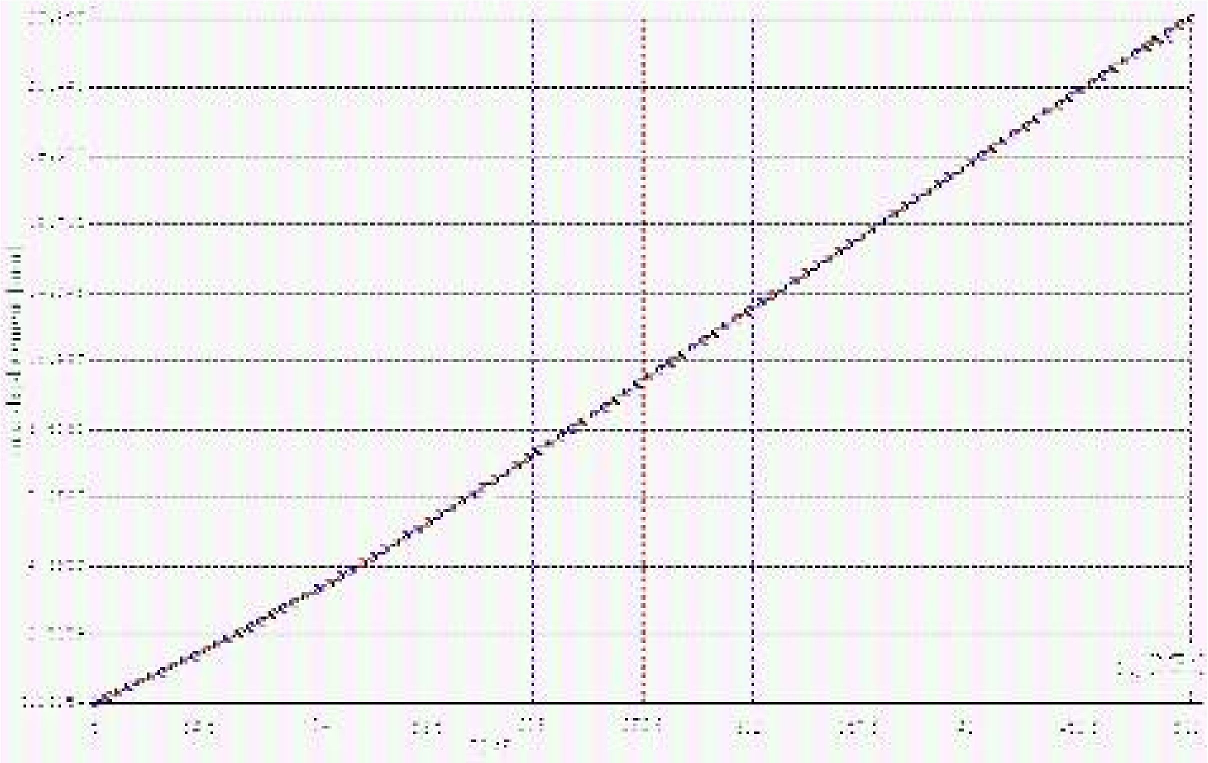

Fig. 6. Case 3: Displacement controlled nonlinear buckling analysis

Acknowledgements

The work has been performed in the scope of the project MARSTRUCT, Network of Excellence on Marine Structures, (www.mar.ist.utl.pt/marstruct/), which has been financed by the EU through the GROWTH Programme under contract TNE3-CT-2003-506141 (Task 4.3).

References

[1]. Chirica, I., Beznea, E.F., Chirica, R., ***Orthotropic Plates***. Galati: The University Dunarea de Jos Publishing House, 2006,

[2]. Engelstad, S. P. & **Reddy, J. N.,** ***Postbuckling Response and Failure Prediction of Graphite-Epoxy Plates Loaded in Compression***, AIAA J., 1992, 30:2106–2113.

[3]. VandenBrink, D. J. & **Kamat, M. P.,** ***Post-Buckling Response of Isotropic and Laminated Composite Square Plates with Circular Holes***, Finite Elem. Anal.&Design, 1987, 3:165–174.

THE ANNALS OF “DUNAREA DE JOS” UNIVERSITY OF GALATI.
FASCICLE IX. METALLURGY AND MATERIALS SCIENCE
N^{0}. 2 – 2007, ISSN 1453 – 083X

SOME RESULTS OF RESEARCHES TO DEVELOP THE PROPER RECYCLING METHODS OF TECHNOLOGICAL RESIDUES FROM SECONDARY ALUMINUM INDUSTRY

Maria ROMAN[1],Romanița TEODORESCU[1],Lucia FIRESCU[1],
Aurel CRIŞAN[2],Ioan MĂRGINEAN[3], Adrian COCOLAŞ[3]
[1]INCDMNR-IMNR,
[2]”Transilvania” University of Braşov,
[3]”Politehnica” University of Bucureşti
email: mroman@imnr.ro

ABSTRACT

The objective of the research is to identify new suitable process to use residual waste (like aluminium secondary dross, salt slag or fly ashes) in concrete products according with sustainable industry concepts. The paper presents some results and directions of researches of recycling secondary aluminum industry by-products in Romania.

KEYWORDS: secondary aluminium dross, moulding mixture, casting, aluminium sulphate

1. Introduction

Aluminium technological residues named; dross, salts slag, black dross or salt cakes, are hazardous waste because it contains contaminants like soluble salts, oxides, carbides and sulphides as well as metallic aluminium which is entrapped in the slag. In contact with water it emits flammable gases such as acetylene or it is liable to give off toxic gases, such as ammonia, in dangerous quantities. Traditionally, aluminium wastes are disposed in landfill, costing the world aluminium industry an estimated $70 million. Resolutions of European Community regulation and spiralling costs are forcing the industry to consider alternatives. [2]. Worldwide Secondary Aluminium Industry produces nearly five million tonnes of furnace waste each year. Residual waste material is produced from any process in which aluminium is melted. For all that reasons a consortium of 7 partners decided to study the possibilities to process of technological residues from secondary aluminum industry and develop the proper methods to cut the production cost and to minimize or eliminate their disposed of in landfill. In the project there are involved three universities, two researches institutes and two aluminium companies. Transilvania Universiy Braşov, the manager of the project; National R&D Institute For Nonferrous And Rare Metals - IMNR, Technical University Of Civil Building Bucharest, Politehnica University – CCEEM Bucharest, INCDPM–ICIM Bucharest, partners, SC ALMET SA Năvodari, SC SILNEF SA, co-financing partners.

Romania has developed researches to find new methods to reduce landfilling of furnace waste and recover saleable products by soluble salts removal, use secondary aluminum technological waste for moulding mixture in foundry for iron heavy casting, obtain products which can be utilized like coagulants. Directions researches for process industrial secondary aluminium by products are showed in figure 1.

2. Experimental researches and results

The first researches were on the influence of technological process on mineralogical matrix of technological wastes from three secondary aluminium processors and their difference in function of their process conditions. As much as ranges of secondary aluminium technological wastes are large, the larger, there are metallic compounds spectrums, which are in the dross and ashes. As much as mineralogical compositions is complex the more difficult there is to process them for obtain useful products.

Complex mineralogical compositions need supplementary operations to separate, to soluble or to purify the useful compounds and for that there have to spend supplementary cost to process them.

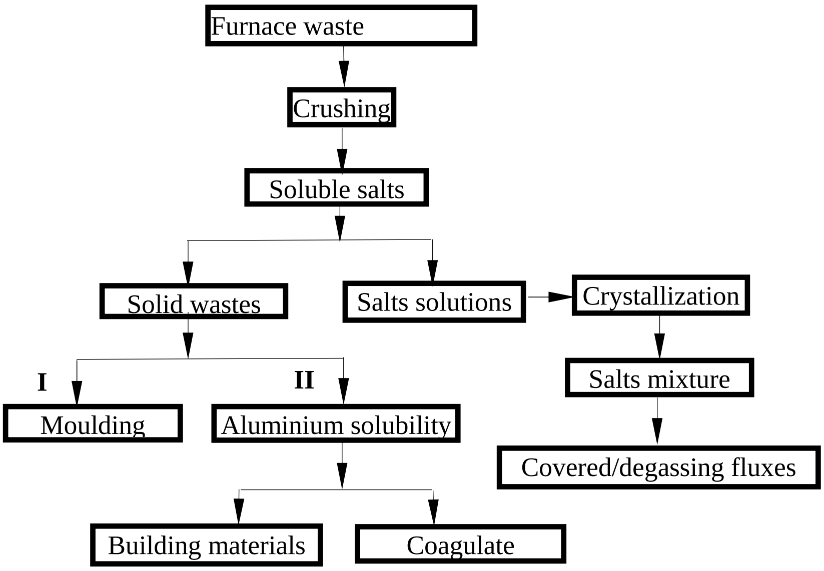

Fig. 1. Directions researches for process industrial secondary aluminium by products

To study influence of technological process on mineralogical matrix of residues of the secondary aluminum industry there were take samples, from three different secondary aluminum companies:

The first company is SC ALMET SA Năvodari, which process scrap and spills to obtain casting alloys and wrought alloys for extrusion. For scrap melting they use revolving cylindrical furnace or crucible melting furnace. They work in quality system in conformity with SR EN ISO 9001:2001, SR EN ISO 14001:2005 and OHSAS 18001:2004 standards. To increase performance rating they use scrap sorting, melting deoxidizing, refining and filtering operations. The skimming from the first melt is in part reuse in their foundry circle. Technological residues are kept on the authorize slag dump till they are delivery to aluminum dross specialize processors. The second company is SC FABRIMIXT SA Câmpina, which process scrap, spills and dross to obtain ingot casting alloys. Technological residues are kept on their the authorize slag dump. For scrap melting they use revolving cylindrical furnace or crucible melting furnace. To increase performance rating they use melting deoxidizing, refining and filtering operations. The skimming from the first melt is in part reuse in their foundry circle. The third company is SC GEORGE IMPEX SRL Potcoava which process only aluminum dross from primary and secondary aluminum companies. For dross melting they use revolving cylindrical furnace or crucible melting furnace. The dross is crushed and the metal particles are sort from nonmetals components by shaking sieve. In the coarse faze there is more aluminum metallic thereby this part is melt to recover aluminum. The fine faze is technological residues and they are kept on the authorize slag dump. Then, those three secondary aluminum processors use the same furnace for melting but thy use the different starting material and they use different technological methods. One of the first analyses of process metallurgical methods influence can be observed from preliminary solid material balance for each company, table 1.

Table 1.

MATERIAL	Company					
	FABRIMIXT		ALMET		GEORGE IMPEX	
	t/ month	%	t/ month	%	t/ month	%
Aluminum scraps	160	73	250	71		0
Raw materials	10	5	30	9	10	10
Purchase dross	30	14		0	90	90
Dross from their foundry circle	20	9	70	20		0
Total	220	100	350	100	100	100
Casting alloys and wrought alloys	160	76	280	82	40	43
Technological residues	50	24	63	18	53	57
Loss	10	5	7	2	7	8
Total	210	100	343	100	93	100

These results show that technological residues percent depends on quality of started materials, which are processed. If for SC ALMET SA company the residues percent is ~18 % and ~ 24% for SC FABRIMIXT SA Câmpina company, for company SC GEORGE IMPEX SRL this percentage is more high ~57%. The samples were characterization by chemical analysis, particle size distribution analysis and phase analysis.

Chemical analysis were performed conform specific metallurgical nonferrous Romanian standards on each particle size distribution. The results show that the elemental compositions are distinct for each company. The results of our study show that the most important quantity of metallic aluminium there are in FABRIMIXT residues, which is follow by GEORGE IMPEX. Technological residues of ALMET contain more alumina, or different mineral combination of aluminium. So, content of different compounds of aluminium ~45%, like; aluminium nitride, aluminium spinely / spinelide, corindon in ALMET residue suggest that these residues can be use for refractory or fireproof materials. Such materials can be research to recovery aluminium nitride, which is in content ~36%.

Technological residues of FABRIMIXT and GEORGE IMPEX contain more metallic aluminium. That suggests that those two companies have to examine their method to process the aluminium scrap to improve their efficiency. These materials can be turning to account to obtain aluminium sulphate, or aluminium hydroxide, which has different utilizations. The second researches were on possibilitys to decrease soluble salts content from secondary aluminium dross for their recycling.

To establish optimum work parameters and the flow sheet, which are necessary for an efficient technology for removing of the soluble salts from fine fraction of secondary aluminum salt slag, there were sampled salts slag resulted on three platforms with similar profile: ALMET from Năvodari, GEORGE IMPEX from Potcoava, SILNEF from Braşov. The samples were sifted, washed with/without simultaneous grinding, dry and disintegration.

There was studied the washing of the salt slag under many aspects to determine influence of different condition of salt solubilization like, work conditions, number of counter current washing step (one, two, three or four), with or without grinding.
Experiments were made with ordinary laboratory equipment, which was composed by washing vessel with electric agitator, gas bulb, ball mill, aspirator bottle, Buchner funnel, drying cabinet.

The experiments show there are possible to obtain solutions with high content in Na and K in the following conditions: the washing in counter current with grinding in 4th step at 400^{0}C and ratio S:L = 1:1. The washing with grinding in 4th step offer in the mean time a high fineness of the slag and high concentration of the solutions in NaCl and KCl. The washing efficiency of NaCl and KCl on every step at 20^{0}C are between 8÷16%, the final washing efficiency after 4 re-pulping being aprox.70% for KCl and 75% for NaCl. The removal of NaCl and KCl from solutions resulted in aluminum slag washing with water, was realized by their concentration by evaporation at the temperature and then the separation of the crystals in two cooling steps at 350C for NaCl and 200^{0}C for KCl. Finally there was proposed a proper flow sheet, for the counter current washing of the slag salts and conditions to obtain NaCl and KCl salts from the washing solution. The third experiment was to test possibilities to use secondary aluminum technological waste at moulding mixture in foundry for iron heavy casting and to see their influences on solidification processes and on casting parts quality.

There is known that in foundry is used aluminothermy process to maintain high temperature in the mould. The process is based on reaction of aluminium oxidize. In pouring time the iron has 1200-1450^{0}C, which permits to initiating oxidize reaction of aluminium from mould material. In this way it brings more energy, which maintains the high temperature and permit to pour all the metal with optimal pouring rate. In aluminium dross there are fine aluminium particles, which can be exothermic material and there are metal oxides which have good refractory characteristics because they have high melting point, low coefficient of heat transmission, good temperature stability, etc. These characteristics permit to prevent heat transmission from mould and solidification process is slowly. This process is necessary in pouring iron heavy parts. Aluminium dross granulation is bigger and irregular, while aluminium ashes granulation is smaller and uniform then siliceous sand. These differences can affect row casting surface quality.

The experiments were made in two stages;

- manufacture of the sand mould and watch their behaviour or their changes in time;
- samples pouring and examine surface quality and their porosity.

There were made sand moulds for pouring samples which have form named "Shrinkage cone". These samples have cylindrical pyramid form with, 70 mm diameter of top and 40 mm diameter of bottom like in figure 2.

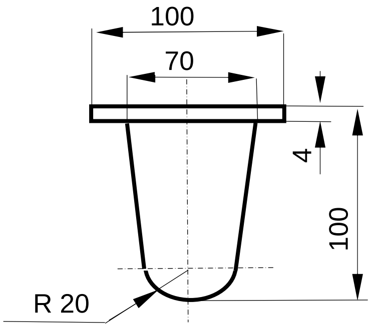

Fig. 2. “Shrinkage cone” form

The aluminium dross were mixed with four kind of moulding materials siliceous sand, furan resin, soda water glass and Fortera with proper bonding agent and then the mixture was introduce in sand mould at the contact surface with wood casting pattern. The thickness of layer was from 6 to 10 mm.

The experiments of metal pouring were made in two methods: open kind named “direct pouring” and closing kind named “rain pouring”. The samples were watched 48 hours from their manufactured. There were notice the process of chemical interaction between furan resin and components of testing material. For samples with resin furan it was remarked strong reaction between dross oxides and resin components. The experiments showed that the sample of furan resin increase their volume, because of air from chemical reactions. Sand mould with dross present weak tendencies to increase their volume, but sand mould with ashes after 3 hours present important deformations and they cant be use. Fragility of sand moulds permits easy rapping the pattern and easy cleans the cast parts. Thus, the sand moulds with dross or ashes mixed with furan resin can be use in shot time for metal pouring. The samples of sand moulds with dross or ashes mixed with soda water glass and Fortera maintain their form in time, without modification of their forms or dimensions. Some aspects of moulds samples are sowed in figure 3. The experiments show that it is possible to use these furnace wastes in iron foundry, but it is necessary to continue these researches to find the proper ration between components of moulding mixture.


a b c d e

Fig. 3. a, b - Sample with dross and furan resin; c, d -. Sample with dross and soda water glass and Fortera; e- Samples after 48 hours

The fourth experiment was to test possibilities to obtain products which can be utilized like coagulants.

The row material, with particle size under 1 mm, was a mixture in equal parts of residual aluminum waste from three platforms. The row material was introduced, for 30 minutes in a perfect mechanic homogenization phase. The experiments were made in two steps: in the first step it was bring in solution of the soluble impurities by washing of the dross with water at the various S:L ratio and temperatures and, in the second step the extraction of the aluminum in sulphuric acid solution like aluminum sulphate. In all experiments was utilized a washing, grinding and dried material resulted by equal homogenization of the dross from those three companies, previous mentioned, with medium chemical composition, show in table 1, and sulphuric concentrate acid, which was diluted with water at desired concentration, function of work parameter which ware established. The experiments were carry out in a laboratory installation composed by: leaching vessel (usually Berzelius glass), with electric agitator, gas bulb, ball mill, aspirator bottle, Buchner funnel, drying cabinet. Firstly, it was calculated the quantity of acid and water of dilution according to chemical composition of the dross. The recipe was: 100 g dross + H_2SO_4

conc. (resulted from calculate) + H_2O (for dilution of the acid). The influence of different parameters on the aluminium release from dross was widely studied in many research aspects, like: the phases contact time was varied between 60÷300 minute; reaction temperature was varied between 80÷1200C; sulphuric acid concentration was varied between 5÷55%; acid excess over stoichiometric necessity; 10, 20% under - stoichiometric; stoichiometric; excess 10, 20, 30, 40 %; S:L ratio was varied between 1:6 ÷1:10; leaching in two steps and leaching in two steps in countercurrent, to decrease the free acidity of the aluminum sulphate solutions; it was varied pH of the solutions.

Table 2. The composition of the washed, grinding and dried dross, %

Al	**Cu**	**Mg**	**Mn**	**Ni**	**Pb/ NH_4^+**	**Zn**	**Cr**	**Ca**	**Ti**
39 – 42	0,9 – 1,15	1,5 – 1,8	0,18-0,21	0,02–0,04	0,076 / **0,92**	0,9-1,24	0,02 – 0,04	0,96-1,4	0,2-0,35
Fe	**B**	**Si**	**Na**	**K**	**Cl**	**SO_4**	**NO_3**	**CO_3**	**F / P**
1,6-2,4	0,03-0,04	5,5-6,7	0,6 - 1,2	0,1-0,35	0,02-**0,03**	0,1 - 0,5	6,0 - 13	1,6-2,8	1,3 / 0,033

For all experiments the suspensions were decanting 20 minutes in the mean time with cooling at 900C, filtering at high temperature, washing of the residue with boiled water and drying. The aluminum sulphate solution together washing waters of the residue was analyzed for determination the content of aluminum and the main impurities. The content of anions and cations were determined by: a) - atomic absorption spectrophotometry (AAS or FAAS) and b) - induced coupled plasma spectroscopy (DCP-AES or ICP-AES). To study the influence of the ***phases contact time*** on leaching efficiency of aluminum, the time was varied between 60÷300 minute. There were analyzed content of aluminum and iron in finale solutions. The results’ analyze shows that: the leaching aluminum degree grows in time, especially in the first three hours of the reaction; next to the aluminum are presented, in solutions, many impurities like: Fe, Zn, Ni, Cu, function of the work conditions; sometimes the leaching degree of iron is higher then aluminum; the leaching degree of the iron grows in the first three hours of the reaction then it take place, a re-precipitation of this element from the solution, in time, figure 4.

To study the influence of temperature on leaching efficiency, the temperature was varied between 80÷1200C. The results show that: the leaching efficiency of aluminum grows with temperature at 1100C being 69.84%; the leaching efficiency of iron grows with temperature till 1000C when the values are 90%, then the values decrease, at 1100C beginning the re-precipitation of iron from the solution, figure 5.

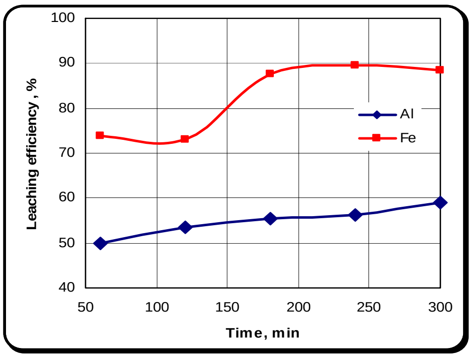

Fig.4. Variation of leaching efficiency of Al / Fe function of time

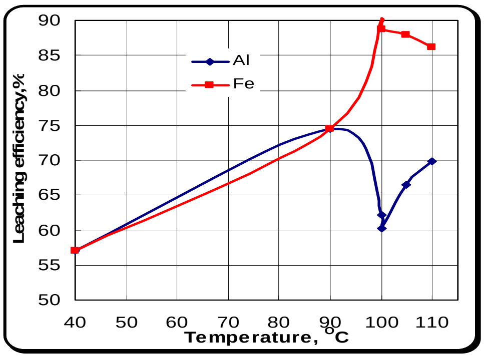

Fig. 5. Variation of leaching efficiency of Al / Fe function of the temperature

To study the influence of sulphuric acid concentration on leaching efficiency, for each experiment was utilized: 100 g washed, dried material, like leaching agent sulphuric acid with various concentrations. Work conditions: continuous mixing of the suspension, reaction time 2.5 hours at 85÷900C. The results show that efficiency of leaching aluminum increases from 18.6% to 60.78 % when sulphuric acid concentration increase from 5% to 55 %. Efficiency of leaching iron decreases from 83.3 % to 73.75 % when sulphuric acid concentration increases from 20% to 55 %, figure 6.

To study the influence of sulphuric acid quantities on leaching efficiency for each experiments ware utilized: 100 g washed, dried material, like leaching agent concentrated sulphuric acid with 1.84 g/l density, in the following quantities: 10.20% under-stoichiometric; stoichiometric; excess 10, 20, 30, 40 %. The results show that: the leaching efficiency of aluminum and iron increase till 20 % excess of the acid. In that case efficiency of aluminum leaching achieve 55.6 % and for iron >95%. For 40% excess of acid the leaching efficiency decrease at 52.5 % for aluminum and 81.68% for iron, figure 7.

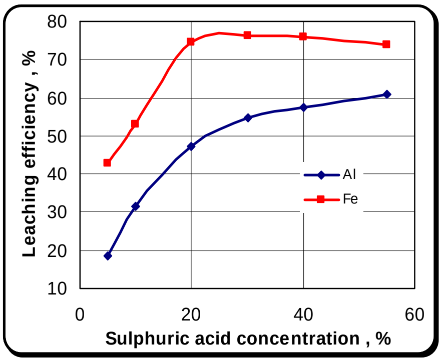

Fig. 6. Variation of leaching efficiency of Al/Fe function by the sulphuric acid concentration

The experiments of aluminum leaching from the dross have like goal to find the conditions to increase the leaching efficiency of aluminum in sulphuric acid and to decrease the free acidity of the finale crystals of aluminum sulphate. For that, the experiments were realized in one or two steps.

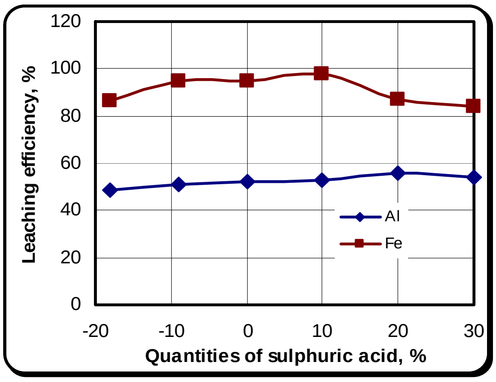

Fig. 7. Variation of leaching efficiency of Al/Fe function by the sulphuric acid quantities

The one step, whole quantity of the dross was used with 55% sulphuric acid (under-stoichiometric quantity) at S:L ratio = 1:8. In the second step the difference 45% acid was added over wet solid faze resulted in the first leaching step. It was establish that leaching efficiency on the step is 37.7 / 28.2 % for aluminum and higher for iron 59.11/31.65%. In comparison with the results obtained in the leaching in one step when the leaching efficiency was 56.15 % for aluminum and 89.6 % for iron, in variant in 2 steps it was establish similarly results 55% for aluminum total but 72.7% for iron. To study the influence of S:L ratio on leaching efficiency experiments were realize at various S:L ratio between 1:6÷1:10. The experiments show that at S:L ratio under 1:8, in time, begin crystallization processes of aluminum sulphate from the solutions and the filtration of the suspension is very difficult. To study the influence of pH on leaching efficiency were made experiments with perfect contact fazes, time 2 hours at 950C, at S:L ratio = 1:8, leaching agent sulphuric acid. The results shows that: increasing of sulphuric acid quantities lids to increase of acidity of the solution and at decrease of pH value from 2.13 at 0.36; with increasing of contact time of fazes increase leaching efficiency of aluminum and iron, the consumption of sulphuric acid introduced in reaction, and increase of pH from 1.4 at 2.66.

4. Conclusions

The experiments show that it is possible to use secondary aluminium dross in iron foundry, but it is necessary to continue these researches to find the proper ration between components of moulding mixture. The experiments show that it is possible to obtain products which can be utilized like coagulants from the secondary aluminium dross. The aluminum recovery from dross with high aluminum content is possible to realize with efficiency over 80% in report with soluble aluminum.

The present results establish the bases of a complex, ecologic technology for aluminium recovery from slag with high content of aluminum at coagulants preparation, which have to continue.

References

[1]. ***Hazardous Waste Section Department of the Environment and Heritage***, www.deh.gov.au/industry/chemicals/hazardous-waste;

[2]. ***Waste management***, www.sims-group.com/au/divisions/aluminium;

[3]. Maria Roman, Viorel Badilita, Lucia Firescu, Florin Stoiciu, L.O. Mărginean, *Some aspects of recycling Romanian Aluminum Industry by-products”*, International Conference on Materials Science and Engineering-Braşov 2005;

[4]. Anisoara Ciocan, *Waste recycling– Process Techniques and Aluminium Waste Recycling*. Editor Matrix Rom, Bucharest, 111-118, 2003;

[5]. Ioan Marginean, Maria Roman, *„Sistem ecologic de procesare a deşeurilor de aluminiu cu utilizarea completă a reziduurilor de proces”*, Proiect RELANSIN 2004.

[6]. Maria Roman, V. Bădiliţă, Romaniţa Teodorescu, I. Mărginean, Monica Făgărăşanu, L. Mărginean, *Researches of recycling Rumanian secondary aluminum industry by- products*, Scientific Bulletin of the „Politehnica" University of Timisoara Transactions on Mechanics, Tom 51 (65), Fascicola 2, 165-170, 2006.

THE ANNALS OF “DUNAREA DE JOS” UNIVERSITY OF GALATI.
FASCICLE IX. METALLURGY AND MATERIALS SCIENCE
N^0. 2 – 2007, ISSN 1453 – 083X

STUDY AND RESEARCHE REGARDING BINARING SISTEM WITH TIOBIS - β – NAFTOL

Olga MITOSERIU, Stela CONSTANTINESCU,
Lucica ORAC
“ Dunarea de Jos” University of Galati
email: stelaconstantinescu@email.ro

ABSTRACT

This paper presents the results for contribution of determining the manganese from waters and steel. Manganese, due to its properties, cannot be found but in acid waters and usually associated with iron. In small amounts, the manganese is a necessary nutrient above all as activator of certain enzymes. In large amounts, though, coming from contaminated waters , the manganese is noxious and may cause brain damage l. It is considered that drinking water should not contain more than 0,1 ppm manganese. From the studies carried out , the tiobis-β-naftolul dissolved in etilic alcohol or isobutilic alcohol may be used to determine the Mn (II) ion , under certain conditions as described in the paper. To determine manganese (II) in water, a photometric extraction method has been developed. The method is new, useful and accurate and enables determining Mn in surface , underground and fishery waters.

KEYWORDS: manganese, tiobis-**β**-naftolul, waters, photometric extraction method

1.Introduction

Finding efficient extraction agents is one the major research directions in the field of extraction process chemistry. From an anlytical point of view, the metal ion extraction systems using organic reactants are higly important. The chelate polyketides agents containing acid and coordination groups in their molecule are the most widely used for this purpose. Metal separation by means of etheric sulphide organic compounds is, however, less studied than other classes of compounds.[1] Researches have revealed that certain substances from tiobisphenol class can be used as remarkable reactants for the separation of metals by extraction. Thus, di-β-naftolmonosulphide has groups of–OH in its molecule, with mobile hydrogen and etheric sulphide which, under favorable conditions, produces donor-acceptor bounds therefore it can form complex combinations.

The literature only points out to combinations reached by ions Ca(II) and Ba(II) [2], Pb(II) [3], Cu(II) [4] and alkaline metals. [5,6,7,8]

Di-β-naftolmonosulphide, dissolved in a suitable organic solvent, non-miscible with water, extracts the metal ions from the water environment, thus proving to be a very good extracting agent.

2.The extraction mechanism

Di-β-naftolmonosulphide is a poor-acid organic ligand . Dissolved into organic solvents such as higher alcohols, it is able to form with ion Mn(II) extractable soluble green species. To study the extraction mechanism a calculation model was used and applied to the chelate extraction system.[9,10,11]

In a first approximation, the extraction balance may be written as:

$$M_{aq}^{n+} + m(HR)_0 \leftrightarrow \left[MRn\,(m-n)HR\right]_0 + n\left[H^+\right]_{aq} \qquad (1)$$

Symbols ***0*** and ***ap*** represent the compounds in organic-phase and water –phase respectively .

As to the balance this can be written as :

$$K_{ex} = \frac{\left[MRn\ (m-n)HR\right]_0 \left[H^+\right]_{aq}^{n}}{\left[M^{n+}\right]_{aq}\left[HR\right]_0^{m}} \qquad (2)$$

For the case under study the authors suggest:

- Under the conditions provided the metal ion does not form significant amounts of acid-compounds;
- Concentration of species M(OH), formed by auxiliary balances, becomes neglijible due to the more stable chelate MRn, and its extraction in organic phase;
- Concentration of species MRn in water phase and those of the intermediate water species are also small and therefore neglijible.

By denoting ***D*** the repartition coefficient , and by applying logarithms and differential calculation to equation (2) with respect to pH, we have:

$$\left.\frac{\partial \lg \boldsymbol{D}}{\partial \boldsymbol{pH}}\right|_{(\boldsymbol{HR})_0} = \boldsymbol{n} \qquad (3)$$

Relation (3) enables determination of n, i e the cathion charge and implicitly the form of thre species where the metal ion in water phase is to be found.

The graphic illustration is performed in the coordinates lgD- pH, while keeping constant the concentration of the reactant HR.

At the pH where an extraction of 50% lgD=0 is obtained we shall have:

$$\boldsymbol{pH}_{50\%} = \frac{1}{\boldsymbol{n}}\lg \boldsymbol{K}_{\boldsymbol{ex}} - \frac{\boldsymbol{m}}{\boldsymbol{n}}\lg[\boldsymbol{HR}]_0 \qquad (4)$$

From the graphic $pH_{50\%}$ - $\lg[HR]_0$ the value of m can be determined.

When the variation of the metal ion concentration influences the repartition coefficient, some polymer species are assumed to be in organic phase.

This balance is expressed by the equation:

$$\boldsymbol{M}^{n+}_{aq} + \boldsymbol{m}(\boldsymbol{HA})_0 \leftrightarrow \frac{1}{x}\left[\boldsymbol{MRn}\ (\boldsymbol{m}-\boldsymbol{n})\boldsymbol{HR}\right]_0 + \boldsymbol{n}\left[\boldsymbol{H}^+\right]_{aq} \qquad (5)$$

Where x is the number of monomer units in the polymer phase.

For the repartition coefficient, we have:

$$\boldsymbol{D} = \frac{[\boldsymbol{M}]_0}{[\boldsymbol{M}^{n+}]_{aq}} \quad ; \quad \boldsymbol{D} = \frac{\left(\frac{[\boldsymbol{M}]_0}{\boldsymbol{x}}\right)^{\frac{1}{x}} [\boldsymbol{M}]_0^{\frac{x-1}{x}}}{\boldsymbol{M}^{n+}_{aq}\left(\frac{1}{\boldsymbol{x}}\right)^{\frac{1}{x}}} \qquad (6)$$

By applying a logarithm and re-arranging the terms in the extraction constant relation, we have:

$$\lg \boldsymbol{D} = \lg \boldsymbol{K}_{\boldsymbol{ex}} + \boldsymbol{n}\boldsymbol{pH} + \boldsymbol{m}\lg \boldsymbol{HA} + \frac{1}{\boldsymbol{x}}\lg \boldsymbol{x} + \frac{\boldsymbol{x}-1}{\boldsymbol{x}}\lg \boldsymbol{M}_0 \qquad (7)$$

At the pH where extraction is 50% M_0 =M total/1 therefore:

$$\left.\frac{\partial \boldsymbol{pH}_{50\%}}{\partial \lg[\boldsymbol{M}]_{total}}\right|_{\boldsymbol{HR}_{0},\boldsymbol{x}} = -\frac{\boldsymbol{x}-1}{\boldsymbol{n}\boldsymbol{x}} \qquad (8)$$

The graphic representation under coordinates lgD V_s–$pH_{50\%}$ at different metal concentrations shall have, in some areas, strainght lines. From the slope of this line it can be calculated the x value .[12]

2.Experimental

The experiments were carried out using an organic phase -water phase ratio =1:2. The pH was varied by different buffer solutions (NH_4OH + NH_4Cl). Funnels were stirred for 20 minutes; after the balance had become stable, the water solution was analyzed to determine the pHl (with a pH-meter MV-S4) and the concentration M(II) (complexonometric titration in the presence of ascorbic acid, using violet pirocatehine as indicator). The ion strength was still present with solution of KNO_3 1m.

3.Rezults and discussions

The experimental results concerning the variation of the repartition coefficient depending on the pH value are presented in fig.1. Applying the mathematical quantitative approach to the described extraction procedure the slope of the straight lines of ***n***=1,92≈ 2 is obtained. The ***n*** value , even at this pH, is consistent with the second oxidation state of the manganese; this takes part in the complexion reaction with di-β- naftolmonosulphide as a Mn^{2+} species and complexes two ligand molecules. The occurence of a family of straight parallel lines in the lgD-pH graphic, for different ligand concentrations, indicates the possibilitity of solvating the complex compound consisting of two reactive molecules. From the graphic illustration under coordinates $pH_{50\%}$ - $\lg C_{HR}$ (fig.2), we get a straight line from which slope we can calculate m ≈ 3.

The species extracted will add a ligand molecule which can be written as:

$$[MnR_2 \bullet HR]$$

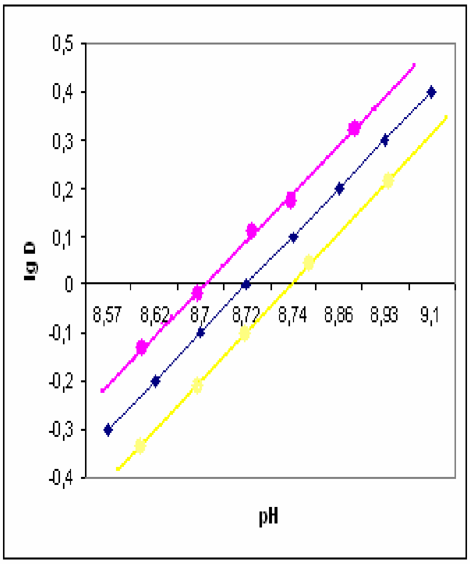

Fig.1. Extraction Mn(II) with di - β- naftol lgC_{HR} upon Mn(II) extraction

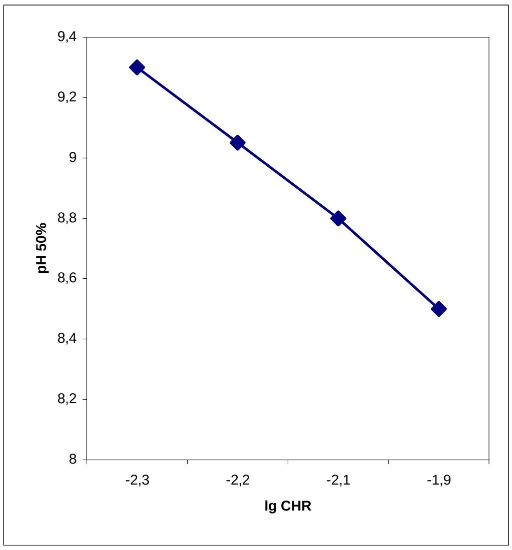

Fig.2. Variation of $pH_{50\%}$ with monosulphide C_{Mn}=const., C_{HR}=variable

Experimental researches performed, while keeping the reactive concentration constant, at different metal ion concentrations, were focused on the variation of the repartition coefficient depending on the pH of the water phase. Within the concentration range concerned , $4 \bullet 10^{-4}$ - $6 \bullet 10^{-4}$ mol Mn^{2+}/ 1, the repartition coefficients do not depend on the initial concentration of the Mn^{2+} ion which indicates the absence of the polymerization of the species extracted in organic phase (fig.3.)

Therefore, the di-β-naftolmonosulphide, dissolved in isobutilic alcohol forms with Mn^{2+} ion a green combination, extractable in non water medium.

The extraction balance is described by the following chemical equation:

$$M\,n^{2+}_{aq} + 3C_{20}H_{14}O_2S_0 \leftrightarrow Mn\left(C_{20}H_{13}O_2S\right)_2\ \left(C_{20}H_{14}O_2S\right)_0 + 2H^{+}_{aq} \qquad (9)$$

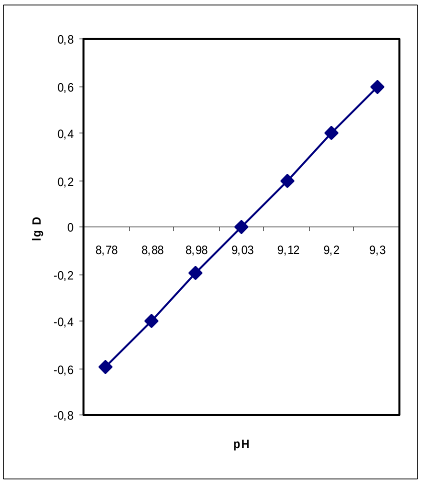

Fig.3. Extraction Mn(II) with di- β- naftolmonosulphide: C_{Mn}= variable; C_{HR}=const.

Based on the studies carried out the optimum extraction conditions have been established (wave length , pH, reactive concentration, extraction time , influence of foreign ions) and an efficient method of determining the manganeese from waters was finally reached.

The following way of working is recommended: in a separating funnel of 50 ml, 10ml reactive solution is poured into $1 \bullet 10^{-2}$ mol/l isobutilic alcohol, 10 ml buffer solution of pH 10 (clorura de amoniu- ammoniac) and V ml solution to be analyzed are poured. After 5 min stirring , phases are separated and the water layer is removed.

The extract in isobutilic alcohol is brought to level in a measuring flask of 25 ml. With higher Mn^{2+} concentrations, it is recommended to repeat extraction.

To remove water traces, the extract is filtered through cutton or a layer of anhydrous Na_2SO_4.

The absorbance of solutions flasks supplemented with isobutilic alcohol was measured after 30 minutes.

The variation of absorbance versus the Mn^{2+} ion concentration results in a linear dependence, in a very large range of $[Mn^{2+}]$(Table1).

Table 1. Processing the experimental results to verify Lambert- Beer law

C_{Mn}•10^{-2} mol/litru x_i	**A_{560} y_i**	**x_i^2 • 10^8**	**X_iy_i • 10^4**	**A calculate Y_i**	**$(y_i - Y_i)$• 10^3**	**$(y_i - Y_i)^2$ • 10^6**
1	0,072	1	0,072	0,073	-1	1
2	0,145	4	0,290	0,145	0	0
3	0,220	9	0,660	0,218	2	4
4	0,290	16	1,160	0,290	0	0
5	0,362	25	1,810	0,363	-1	1
6	0,435	36	2,610	0,436	-1	1
7	0,508	49	3,556	0,508	0	0
8	0,582	64	4,656	0,581	1	1

$y = 0,5 \cdot 10^{-4} + 0,0726 \cdot 10^4\ x$
$y_{sup} = 2,88 \cdot 10^{-3} + 0,0726 \cdot 10^4\ x$
$y_{inf} = -\ 2,88 \cdot 10^{-3} + 0,0726 \cdot 10^4\ x$

where:
y- absorbance
x – concentration C_{Mn}

5. Conclusion

- Di–β-naftolmonosulphide, organic polydentat ligand , can be used as an efficient extract agent in the extract process chemistry;

- The Mn^{2+} ion reacts with di–β-naftolmonosulphide resulting in a green compound, extractible in organic water non-miscible solvents, such as high alcohol;

- When isobutilic alcohol is used as solvent in the concentration range concernd , at pH 8-10, the extraction balance of Mn^{2+}, is written as:

$$Mn^{2+}_{aq} + 3C_{20}H_{14}O_2S_0 \leftrightarrow Mn\left(C_{20}H_{13}O_2S\right)_2\ \left(C_{20}H_{14}O_2S\right)_0 + 2H^{+}_{aq} \tag{10}$$

- The extraction procedure depends on the pH of the water phase, the ligant concentration in organic phase and the stirring time. Under certain conditions, the extraction can be carried out quantitatively.

References

[1]. Mitoşeriu O., *Doctor's degree thesis*, Jassy Polytechnic Institute, 1980

[2]. Mitoseriu O., Constantinescu S., sa., ***Metode moderne de investigare a proprietatilor materialelor metalice,*** Editura Universitatii „Dunarea de Jos” Galati, 1998, p. 56-83.

[3]. Constantinescu S., Mitoseriu O., Orac L., *Influence of manufacturing technology on chemical and structural homogeneity of X60 steel*, TEHNOMUS XIV a XIV-a Conferinta Stiintifica Internationala, 4-5 Mai 2007, Suceava, p. 267-272.

[4]. Mitoseriu L., Nastase G., Orac L., *“Identificarea ionilor Fe(II) si Cu(II) din materiale metalice”,* Lucrarile Conferinţei Ştiinţifice cu participare Inetrnaţională ,***ARTCAST 2006,*** 4-5 mai,Galati, Faculty of Metallurgie and Science Materials, Editura ***ACADEMICA***“ ,2006 ,p.237-241, ISBN973-8937-00-0

[5]. Popa G., Moldovanu S., *Reactivi organici în chimia analitică,* Editura Academiei, Bucureşti, 1976.

[6]. Liteanu C., *Volumetric quantitative analytical chemistry*, Didactic and Pedagogic Publishing House, Bucharest,1964

[7].Odochian L., Mihai E., Fişel S., Mitoşeriu O., ***Rev. Roumain Chim. R.S.R, 26, 3***, 1981 p. 383.

[8]. Mitoşeriu O., Hartopeanu A., Cioroi M., *Analytical chemistry. Separation and identification of cations*, Ed. “Ars Docendi” University from Bucharest , 2001, ISBN 973-8118-51-4.

[9].Holzbecher Y., Divis L., Kral M., Lucha L., Vlacil F., *Organiceschie reagenti v neorganicescom analize*, Izd., Mir, Moscova,1979, p 427.

[10]. Mitoseriu O. , Musat V. , Popescu M., Benea L., Bodiu V., *Analize tehnice* , Universitatea Dunarea de Jos Galati, 1995.

[11]. Liteanu C., *Studii şi cercetări*, Chimie, Cluj, 1, 1963, p.181

[12]. Ceauşescu D., ***Use of mathematical statistics in analytical chemistry***, Technical Publishing House, Bucharest ,1982.

[13] Mitoseriu O., Levcovici D., Filip G., ***Reactiv organic selective pentru determinarea mai multor metale grele din diferite materiale*** , The Anals of “ Dunărea de Jos “University of Galaţi Fascicula IX, Faculty of Metallurgy and Materials Scientice, year XXIV (XXIX), May 2006, no.1, ISSN 1453-083X, p.95-101

[14] Mitoseriu O., Levcovici D., Filip G., *Determinarea mercurului din apele poluate accidental prin metoda colectării gravimetriceIn stadiul organic,* The Anals of “ Dunărea de Jos “University of Galaţi. Fascicula IX, Faculty of Metallurgy and Materials Scientice, year XXIV (XXIX), May 2006, no.1, ISSN 1453-083X, p.31-35

THE ANNALS OF “DUNAREA DE JOS” UNIVERSITY OF GALATI.
FASCICLE IX. METALLURGY AND MATERIALS SCIENCE
N^0. 2 – 2007, ISSN 1453 – 083X

IMPROVEMENT OF STEEL SHEET CORROSION RESISTANCE BY THERMIC COVERAGE METHOD WITH ZINC- ALUMINIUM ALLOYS

Maria VLAD, Olga MITOSERIU,
Stela CONSTATINESCU, Emil STRATULAT
“Dunarea de Jos” University of Galati
email: mvlad@ugal.ro

ABSTRACT

The paper presents the main physico-chemical characteristics (viscosity and superficial tension of zinc-aluminium liquid alloy in view of carry out protected layers on steel sheet with very good properties by thermal method. Tacking into account of experimental researches have been analysed alloy melted conditions and metallic covering according established technology

KEYWORDS: alloy, viscosity, superficial tension, corrosion

1. Introduction

Out of all protection coatings Zinc- coated plates are the most widely used.

Zinc coatings can be achieved by immersion into melt bath for film thickness of 20-50 µm or electrolitically for film thickness down to 10 µm .

The increased aggressiveness of the environment, the emergence of new fields of applications (automotive industry, chemistry, construction materials, etc) along with the world market price evolution and scarcity of some raw materials sources have all called for the development of Zn and alloys protection coats that basically form the Zn -Al binary system.

2. Experiments and results

The experimental researches are focused on determining physical-chemical properties of Zn-Al melts so as to establish a technological flow for the thermal plating/coating.

2.1.Zn - Al melt viscosity for different percentages of Al in Zn

The dynamic viscosity of Zn- Al alloys having 1 to 10 % Al, has been determined by Mayer Svidkovski method.

Viscosity variation vs. Al- content and temperature is illustrated in figure no.1

The experimentally determined values are consistent with those obtained by relation:

$$\eta = \eta_{Zn}\frac{\%Zn}{100} + \eta_{Al}\frac{\%Al}{100}$$

where: $\eta_{Al,Zn} = \eta_0$ exp (Ev/RT); η_0 - is pure metals viscosity, Ns/m^2; Ev – viscous flowing activating energy, J

Ev = 3,8 RTf
R = 8,3144 J/mol.K;
Tf – metal boiling temperature, K;
T – temperature at which measuring is performed, K.

The melt viscosity decreases with increased Al content and temperature (figure no.1); the decrease is severer within the concentration range 0-5% Al.

Decreased viscosity results in higher fluidity and further to the discharge of exceeding alloy thus improving coating quality

The viscosity of the Zn –Al alloy is also influenced by the presence of some small amount of alloying elements. This is better highlighted when such alloying elements are poured into the melt as pre-alloy, not in metal state.

The non- homogeneity of the alloy, due to the presence of metal inclusions in the metal bath, can be assessed through chemical or metallographic analyses.

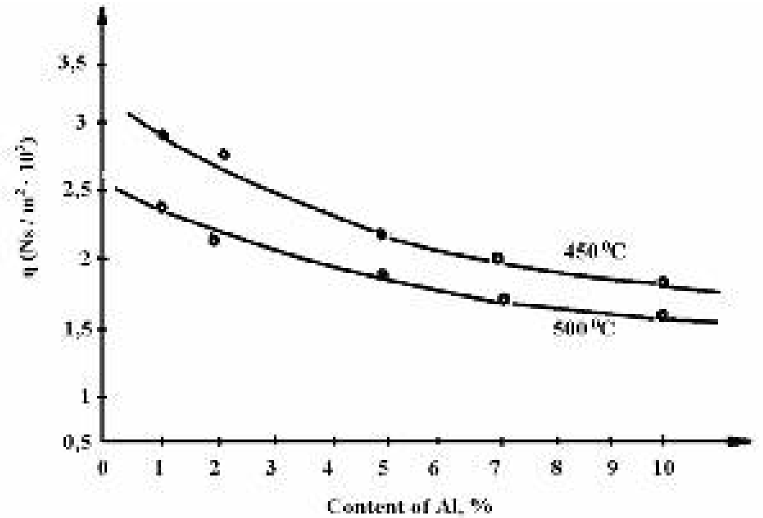

Fig 1. Viscosity variation function of aluminum and temperature

Fig.2 illustrates the microstructure of a sample from a homogenous bath while Fig. 3 shows the microstructure of a sample from a non homogenous bath.

The admissible Fe content in the melt alloy is max.0,2% because higher amounts form inter-metallic compounds of Fe with Zn (Fe Zn_3 , $FeZn_7$ etc).

The Fe and Zn compounds float away with the melt alloy and therefore the alloy viscosity increases.

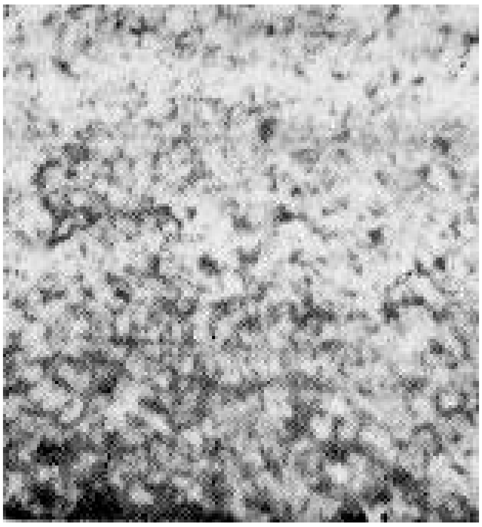

Fig 2. Microstructure of the sample from the homogenous baths of ZnAl 7 with 0,08% Sb and 0,15% Si. Magnification 200X

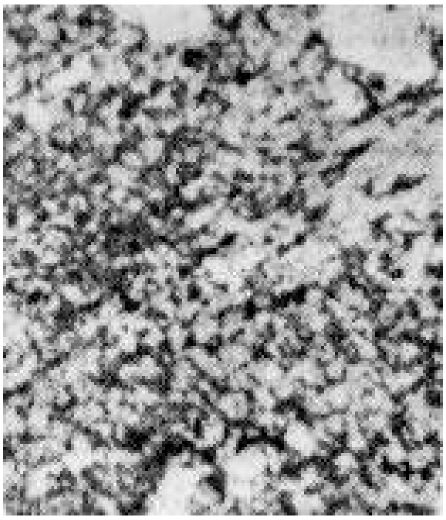

Fig 3. Microstructure of the sample from the non homogenous baths of ZnAl 7 with 0,08% Sb and 0,15% Si. Magnification 200X.

2.2. Superficial tension

With Zn-Al alloys the surface stress has been determined by the method of max air-bubble pressure. From a comparative study of the equilibrium diagram for the system Zn – Al, fig. 4, and the curve standing for the superficial tension vs. composition variation at a temperature higher by 50 °C than the melting temperature of composition alloy, fig. 5, it can be seen that between the remarkable points of the equilibrium diagram there is a certain correspondence (max is for eutectic, min for eutectoid).

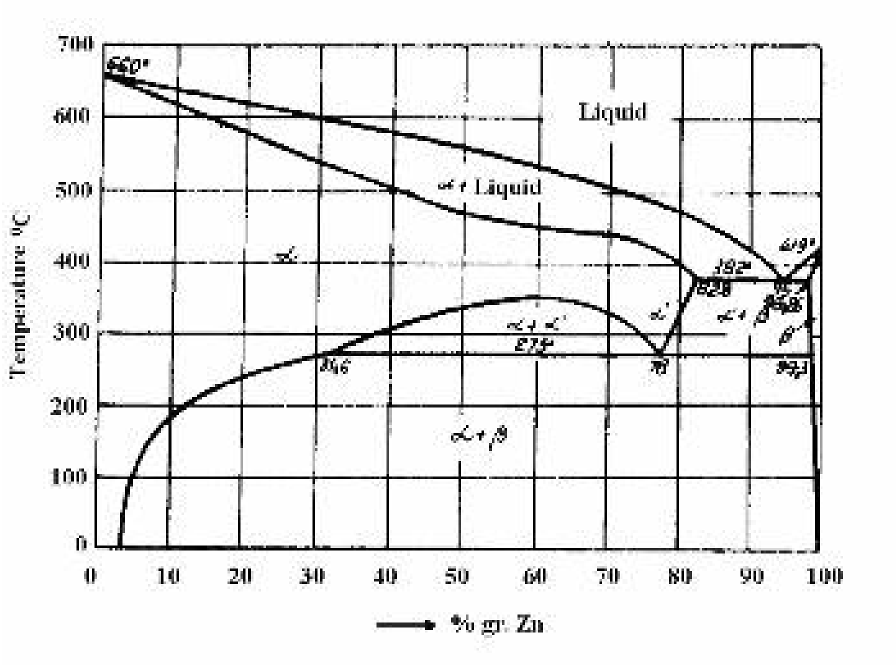

Fig 4. Equilibrium diagram Al-Zn

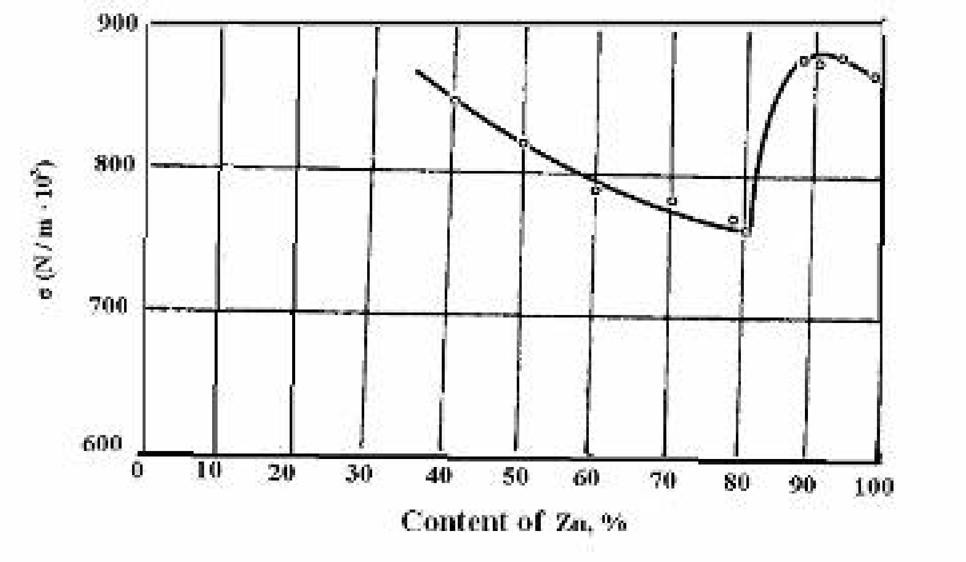

Fig 5. Superficial tension function of composition variation and temperature

In general, the alloying elements having a generalized moment higher than the generalized moment of the base metal (solvent) increase the alloy superficial tension.

For the generalized moment $m = \frac{e\ z}{r}$ of both Zn and Al the following values have been determined:

for Al; $m=9{,}61.10^9$;
Zn; $m=4{,}33.10^9$.

According to the diagrams in figs. 5,6, the alloy superficial tension decreases with increased temperature at certain concentrations of Al in Zn (up the eutectic composition of 5% Al in Zn) and at higher Al concentrations, the alloy superficial tension increases.

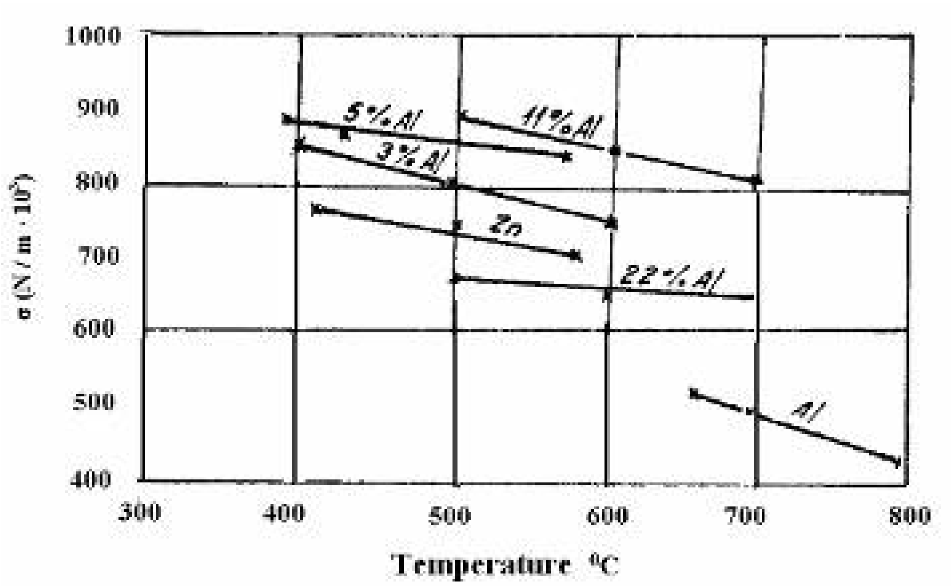

Fig 6. Superficial tension vs. temperature variation at varied contents of aluminum

With higher concentrations of the second alloy component, the basic molecular field is significantly modified which implies a modification of the number of free electrons assigned to one atom and the generalized moment of the metal dissolved is a function of the solvent metal concentration.

At high values of the superficial tension, the coating surface seems smooth.

Since for metallic coatings a certain temperature is imposed, the superficial tension can be increased by adding small amounts of Sb or max 0,2% Pb.

2.3 Influence of alloying elements in the metal bath on the coating quality

The Zn- Al alloys used for the coating achieved under the above mentioned conditions were prepared by re-melting the pre-alloys previously made in a (flame or electrical crucible) furnace. When pre-alloys are made, part of the Zn is melted (rectified Zn) and the melt thus obtained is overheated up to 500 °C Al is poured into it and everything is stirred and finally the remaining Zn is added acc. to the desired chemical composition.

The melt is kept at 475 ^{0}C for 10 min., the slag is removed, dezoxidation can be made, if applicable, with 0,03%-0, 8% Mg while keeping on stirring, slag is further removed, and finally the melt alloy is poured into ingots for further re-melting.

Taking into account the strong tendency of any Zn based alloy to inter-crystalline corrosion and grooves formation due to the presence of Cd, Sn, Pb and Fe, it is suggested to employ as pure as possible and rigorously controlled Zn and Al as raw materials. It is forbidden to overheat pre-alloys containing max 10% Al over 480 °C because otherwise a decreased oxidation of the alloy is found out along with lower physical – chemical properties of the coating.. In order to improve the coating technology and the qualities of the protection alloy film , the influence of different metals added in small amounts to the Zn-Al bath was studied. The presence of Pb amounts higher than 0 1% and Sn over 0.02% increase the coating tendency to exfoliations. Small amounts of sodium and berilium increase the melt surface stress and 01% Mg increase the coat corrosion resistance. The most efficient micro-alloying elements proved to be Si , Sb and Mg.

The max. 1% Si in Al added to the bath modifies the microstructure, improves the appearance, provides a smooth shiny texture, decreases the thickness of the inter-metallic layer.

Aluminum, an alloying element to be found in larger amounts than the others, favorably influence the coat quality as regards adherence, corrosion resistance, coating thickness, coating weight, while decreasing the inter-metallic film thickness.

2.4 Determining the technological flow to make Zn-Al alloy coatings

The laboratory and industry experimental researches on the different possible variants made it possible to establish the technological flow for the thermal achieving of Zn -Al alloy coated steel plates by immersion into melt while the main stages of the flow and the associated working parameters are given in table 1.

Table 1. Determining the technological flow to make Zn- Al alloy coatings

Substances used in composition	**Temperature °C**	**Time, s**
NaOH-80-100 g/l		
Na_2CO_3-40 g/l	80-90	1800
Na_2SiO_3-5 g/l		
NaOH-30-40 g/l		
Na_2CO_3-40-50 g/l	80-90	1800
Na_3PO_4-5 g/l		
	80-90	
H_2SO_4 15-20% sau HCl 15%	40-50 20	1800
$ZnCl_2$;NH_4Cl 6,6:1		40-60
$ZnCl_2$:NH_4Cl 12:1		40-60

Due to the high aluminum affinity to oxygen, slag is formed on top of the alloy; the slag grows and affects the coating quality with increased amount of Al.

Table 2. Composition of fondants

Composition, %									**Temp. °C**
Na_2SO_4	**$MgCl_2$. $6H_2O$**	**NaCl**	**$ZnCl_2$**	**KCl**	**$KHSO_4$**	**Na_3AlF_6**	**NaF**	**CaF_2**	
-	55	-	-	34	-	-	-	11	500
-	17	25	-	-	50	-	8	-	550
35	20	20	-	10	-	15	-	-	480
62	-	12,5	-	12,5	-	13	-	-	450
-	-	-	-	40	-	-	-	60	S
-	-	10	-	10	-	-	-	80	S
-	-	-	-	-	-	80	-	20	S
-	-	-	-	-	-	100	-	-	S
-	-	-	100	-	-	-	-	-	313

Table 3. Experimental results regarding deposition quality.

Technological flow	**Temperature, °C**	**Al,%**	**Si,%**	**Sb,%**	**Deposition quality**		
					Aspect	**Weight**	**Adherence**
$ZnCl_2$:NH_4Cl 87:13	450	1	-	-		Weight 260-430 g/m^2	**C***
	450	3	-	-	shiry		C
$ZnCl_2$:NH_4Cl 10:1	430	6	-	-			C
	460	10	-	-			C
$ZnCl_2$:NH_4Cl 87:13	450	1	-	0,02			C
	450	3	-	0,02			C
$ZnCl_2$:NH_4Cl 10:1	430	6	-	0,02			C
	460	10	-	0,02			C
$ZnCl_2$:NH_4Cl 87:13	450	1	-	-			C
	450	3	-	-			C
$ZnCl_2$:NH_4Cl 10:1	420	6	0,2	-			C
	460	10	0,2	-			C
$ZnCl_2$:NH_4Cl 87:13	450	1	-	0,02			C
	450	3	-	0,02			C
$ZnCl_2$:NH_4Cl 10:1	430	6	0,2	0,02			C
	460	10	0,2	0,2			C

* C=good

3. Conclusions

1. Viscosity and superficial tension have been determined for different temperatures and aluminum contents in the alloys used to thermally prepare metallic coatings;
2. Experimental results regarding steel plate coatings from Zn-Al alloys have allowed for a suitable technological flow to be established;
3. Elements of Si and Sb micro-alloying at low concentrations decreases the alloy viscosity so that metallic melt fluidity is improved and thinner films can be obtained;
4. The quality of the protecting layers has been assessed in terms of aspect, weight and adherence to the base metal

References

[1]. Muizeh, K. s.a. In: Hutnik, Polonia, nr.2, pp. 34., 1981
[2]. Schulz, D.W. In: Neue Hűtte, R.D.G., nr.6, pp. 202., 1982
[3]. Junker, H.L. si Korner, W. In: Metallurgical Plant and Techn., S.U.A., nr.3, pp.59, 1983
[4]. Redsel, U. In: Metallurgical Plant and Techn., S.U.A., nr.4, pp. 72, 1984
[5]. Oprea F. s.a. Teoria proceselor metalurgice, Bucuresti, Ed., did. Si ped., 1978.
[6]. x x x Brevet de inventie nr. 77078811, S.U.A.< 4056366, India.
[**7]. Sivan, V.** In: Metal Finishing, Japonia, noe. pp. 21, 1980
[8]. Koyuhiro, T. s.a. In: Jap. Metal Finishing., Japonia, 33, nr.10, pp.516, 1982
[9]. Peisker P. In: Neue Hűtte, R.D.G., 6, pp. 205, 1982
[10]. Constantinescu,S., ***Influence of manufacturing process on chemical and structural homogeneity of welded pipe sheets for tanks and vessels working under pressure.*** “ Proceeding of the International Conference on Advances in Materials and Processing Technologies, 2001, Leganes, Madrid, Spain, p.57.

THE ANNALS OF “DUNAREA DE JOS” UNIVERSITY OF GALATI.
FASCICLE IX. METALLURGY AND MATERIALS SCIENCE
N^{0}. 2 – 2007, ISSN 1453 – 083X

HYDROGEN PRODUCTION BY STEAM REFORMING OF RENEWABLE RAW MATERIALS

Vasile MATEI, Oana MIHAI, Traian JUGANARU,
Daniela MOVILEANU, Anca BORCEA, Dorina MATEI
Petroleum-Gas University of Ploiesti
email: vmatei@upg-ploiesti.ro, mihaioana2006@yahoo.com

ABSTRACT

The paper is based on study of steam reforming of renewable raw materials (bioethanol, biomethane) in stainless steel fixed bed reactor. The β-alumina catalysts with nickel has been synthesized and tested supported. The influence of operating conditions about steam reforming reaction and methanation reaction was studied.

KEYWORDS: reforming, methanation, catalyst, fixed bed reactor, bioethanol, biomethane

1. Introduction

Knowing that hydrogen is the less pollutant fuel, having a lot of utilizations – internal combustion engines, combustion cells, heating fuels - many technologies for hydrogen production were developed. The one of most important technologies is steam reforming of hydrocarbons and alcohols, from which steam reforming of bioethanol and biomethane are realized on industrial range [1]. In steam reforming process for obtains syngas and hydrogen production can be analyzed a lot of raw materials such: methane, GPL, gasoline fractions, methanol and ethanol. For steam reforming process a wide variety of supported nickel catalysts, supported alumina and silica catalysts are used. The more frequent raw materials are hydrocarbons, methanol being used at smaller range and in special situations. Increases of bioethanol production and other compounds from biotechnologies (e.g. biomethane) increased interest for study of these processes as hydrogen source [2, 3].

The presence of an efficient steam reforming catalyst represents the key of this process for hydrogen production.

In literature are presented alternatives of hydrogen production from ethanol. Thus, recent studies [4] show that ethanol can be used with water in partial oxidation or total oxidation and steam reforming, processes that convert ethanol in hydrogen such in reaction:

$$C_2H_5OH + H_2O + \frac{1}{2} O_2 \rightarrow 2CO_2 + H_2$$

This reaction occurs at high temperatures (800°C), to obtain as mainly product hydrogen through partial oxidation and steam reforming of ethanol by exothermal process. The water obtained in excess by partial oxidation is used in steam reforming process.

This study aim is to promote vegetable sources as raw materials, by revaluation of renewable resources as biomass through pure technologies which can generate hydrogen production. Bioethanol is product of biocatalyst and enzymatic convert of some compounds by photosynthesis. Enzymatic conversion of polysaccharides in bioethanol is a process that demands less energy consumption related to petrochemical processes of ethanol conversion. Technology for bioethanol obtaining needs to extend farming cultures with high polysaccharides potential, preserving the equilibrium between photosynthesis and biological degradation and the natural cycle of oxygen and carbon dioxide.

The motivation of bioethanol use in hydrogen production presents a lot of advantages, such that bioethanol is available from renewable sources, bioethanol has low impact on greenhouse gases, that bioethanol is economic and has a high content of hydrogen and the fact that bioethanol is miscible with water.

Bioethanol can be considered, in present, a good raw material, because of its availability, non-toxicity and safe storage and control conditions and because UE promotes policies concerning acquirement of fuels from renewable sources, as an alternative of irreversible combustion of fossil-based materials. In the same time with cell combustion systems implementation and increases of fuels with low sulfur content demand, hydrogen production will be remarkably developed [5].

Hydrogen production from renewable raw materials can be realized converting the conventional technology of methane steam reforming to reforming of biomethane derived from fermentation of some animal wastes [6], which is studied in present in current research project [7]. In these actual studies for this alternative, the catalysts are supported ruthenium catalysts [8] and nickel and lanthanum catalysts [7].

Biogas composition can be variable due to carbon dioxide content.

2. Experimental study

Research aim is to obtain hydrogen from renewable raw materials in advantageous conditions.

Objectives:

-bioethanol steam reforming to obtain syngas;

-study of selected catalyst efficiency for bioethanol steam reforming;

-influence of operation conditions (temperature and space velocity) on the steam reforming of bioethanol and biomethane. Raw material representing bioethanol was prepared as a solution by diluting 10% ethanol with 90% deionized water, which similar concentration obtained by renewable raw materials. For biomethane steam reforming was used raw material like that result from fermentation processes, having composition 60% vol. methane and 40% vol. CO_2. Experimental studies concerning steam reforming of bioethanol was carried out in a stainless steel fixed bed reactor having the thermocouple for measure of temperature in zone reaction. Biomethane flow was realized for mixture between methane and CO_2, which was controlled as a flow on each flux. In case of biomethane experiment, catalyst volume was 20 cm^3, respectively for biomethane steam reforming, catalyst volume was 15 cm^3. In this study, was used supported nickel ZSM5/ Zn catalyst for reforming of bioethanol, respectively supported β-alumina catalysts with Nickel and Lanthanum for biomethane reforming. The study was carried out by varying the operating conditions, such as reaction temperature, water to ethanol ratio, respectively methane to CO_2 ratio, space velocity and constant compositions of raw material. Values between 1.5 - 4 h^{-1} has been chosen for space velocity for bioethanol steam reforming, respectively constant gaseous space velocity for biomethane reforming. The used catalysts were prepared by impregnation with nickel. Nickel, as a precursor (from aqueous solution of nickel nitrate) was impregnated on zeolitic support modified by zinc, in many steps and than dried at 120°C. The impregnated catalyst is calcinated for six hours at 550°C with nitrogen oxide elimination.

For reforming of biomethane catalyst was obtained by impregnation with nickel (from aqueous solution of nitrate nickel) and lanthanum as lanthanum nitrate. The support was β alumina. After drying, it was calcinated at 600°C for six hours.

The reactor can be both liquid and gaseous charged by the charging system in the reactor superior zone. The experimental system also includes cooling, condensation and separation systems, as well as electrical heating system.

The reaction products and raw material were analyzed by Gas Chromatography with a Carlo Erba HRGC 5300 Mega Series. Chromatographic column is stainless steel, with 12 m length, 4 mm interior diameter and 6 mm exterior diameter. The stationary phase is PORAPAQ O+R adsorbent. The detector is catarometer. Carrier gas is helium. Sampling and processing soft of analytical results was Crom Card for Windows. The experiments for bioethanol steam reforming carried out at three temperatures: 520°C, 560°C, 600°C and two liquid space velocities: LHSV =2,5 h^{-1}, respectively 4 h^{-1}. For biomethane reforming the experimental program includes four experiments at reaction temperatures: 660°C, 705°C, 760°C, 800°C and constant gaseous space velocity: GHSV = 960 h^{-1}.

3. Results and discussions

Experimental data using the above mentioned experimental program, confirm the hypothesis that hydrogen could be obtained from renewable sources, such are bioethanol and biomethane.

Experimental conditions in laboratory micro pilot are presented in table 1 (reaction temperature, space velocity, feed-stock flow in cm^3/min– ethanol and water – for 20 cm^3 catalyst reaction zone).

Table 1. Work conditions for bioethanol steam reformings

Experiment	**Temperature, °C**	**LHSV*, h^{-1}**	**Flow,** cm^3/min
BE 1**	520	2,5	0,833
		4	1,333
BE 2**	560	2,5	0,833
		4	1,333
BE 3**	600	2,5	0,833
		4	1,333

*LHSV – hourly space velocity for liquid raw material (flow of liquid raw material divide to catalyst volume).

**BE1, BE2, BE3-indicator for bioethanol experiments.

Because water in the effluent is condensed and separated in reaction medium, in gaseous reaction product are only H_2, CO, CO_2, CH_4.

Experimental results to bioethanol reforming are presented in table 2 and they prove the possibility to obtain hydrogen and carbon oxides from bioethanol as well as the limits of methanation following reforming.

We can see the significant conversion of ethanol in hydrogen and carbon oxides. It is important to emphasize that the main reaction (reforming) is always accompanied by methanation reaction. During this reaction the mixture of CO, CO_2 and H_2 are transformed in methane. This reaction increases with reaction temperature increasing. The key of this reaction is the catalyst.

Table 2. Composition of final products (H_2, CO, CH_4, CO_2,) for bioethanol steam reformings, % vol.

Experiment	**Temperature, °C**	**LHSV, h^{-1}**	**H_2**	**CO**	**CH_4**	**CO_2**
BE 1	520	2,5	1,7065	50,5119	16,3823	31,3993
		4	4,9689	36,0249	37,8882	21,1180
BE 2	560	2,5	4,0816	42,8571	32,1429	20,9184
		4	6,8627	40,1961	38,2353	14,7059
BE 3	600	2,5	4,9080	13,4969	40,4908	41,1043
		4	5,8824	21,5686	43,1373	29,4118

Concerning the effect of operation conditions over bioethanol reforming reaction, especially concerning hydrogen formation, from table 2 data and figure 1 we can easily observe that higher temperatures favor bioethanol reforming, hydrogen content increasing continuously. (from 1,5 % vol. to 5 % vol.).

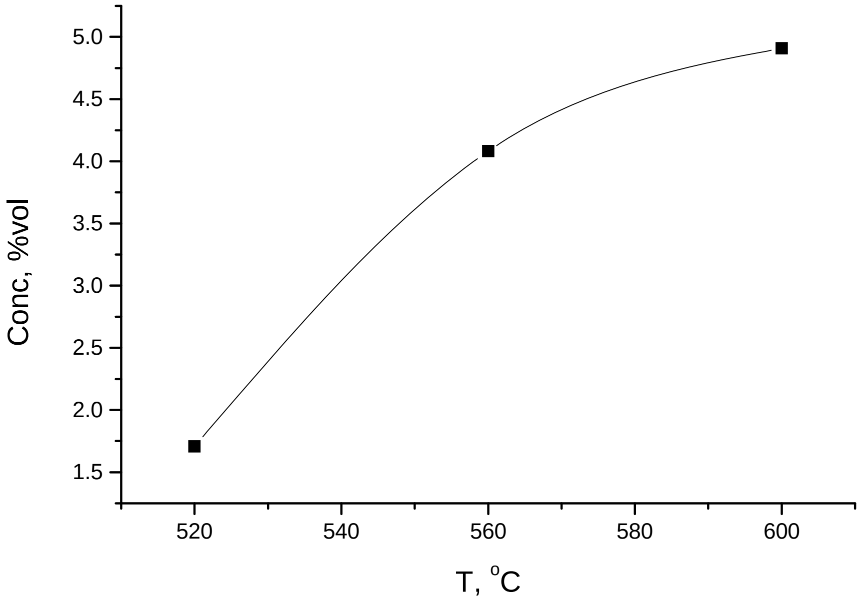

Figure 1. Variation of hydrogen concentration from gaseous reaction product from bioethanol reforming at liquid space velocity LHSV = 2,5 h^{-1}.

For experiments carry out to LHSV=4 h^{-1} (figure 2), hydrogen concentration in gaseous products as a function of temperature vary to a maximum, followed by a slightly decrease due, the most probably, to methanation reaction ($CO + H_2 \leftrightarrow CH_4 + H_2O$), related to the important concentration of methane - 43 % vol.

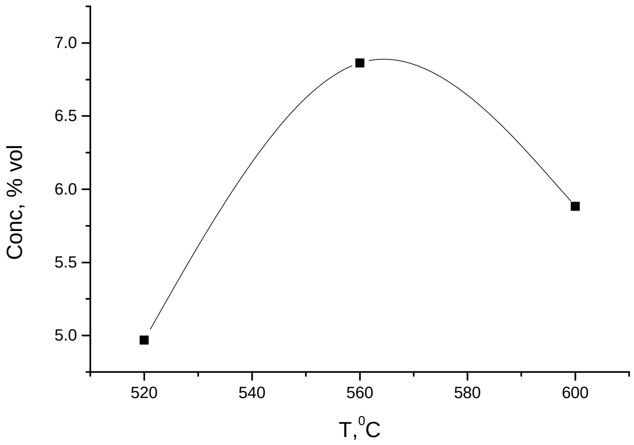

Figure 2. Variation of hydrogen concentration from gaseous reaction product from bioethanol reforming at liquid space velocity LHSV = 4 h^{-1}.

Table 3. Composition (% vol.) of final products for biomethane reforming

Experiment	Temperature,^{o}C	LHSV, h^{-1}	H_2	CO	CH_4	CO_2
BM 1***	660	960	1,04	18,09	75,66	5,19
BM 2***	705	960	1,05	19,31	72,58	7,06
BM 3***	760	960	1,19	16,39	78,25	4,16
BM 4***	800	960	0,44	9,05	89,56	0,94

***BM1, BM2, BM3, BM4 - indicator for biomethane experiments.

Concerning biomethane steam reforming, the mixture used in these experiments as feed stock have an initial composition of 40% vol CO_2 and 60% vol methane. Experimental conditions and gaseous effluent at the exit from reaction system, (after water condensation and separation) are presented in table 3.

From experimental data in table 3 it can be observed that CO_2 from feedstock was converted in methane due to methanation reaction, following reforming reaction. This explains the higher methane content in reaction products and the small hydrogen amount used for methanation.

To reduce undesirable effect of CO_2 methanation at biomethane steam reforming, the catalyst composition and preparation could be modified. Another way to block methanation process is a lower CO_2 content in the feed-stock.

4. Conclusions

ü ZSM5 catalyst modified with Zn impregnated with 10% Ni is suitable for bioethanol steam reforming

ü Higher hydrogen concentrations were obtained at 560 and 600ÛC for LHSV= 2,5 h^{-1}.

ü Space velocities low values influence the bioethanol steam reforming process in the sense of a higher hydrogen concentration and lower valuables for CO_2 and CO.

ü The presence of CO_2 in biogas influences methane conversion.

ü The catalyst significantly influences the methanation reaction of CO_2.

References

[1]. Ghejan, I., Feyer Ionescu, S., Opris, I., ***Ingineria prelucrarii hidrocarburilor***, vol.5, cap.7, p.309-315, Editura Tehnica, Bucuresti, 1999.

[2]. Therdthianwong, A., Sakulkoakiet, T., Therdthianwong, S., ***Hydrogen Production by Catalytic Ethanol Steam Reforming***, ScienceAsia, nr.27, p.193-198, 2001.

[3]. Haryanto, A., Fernando,S., Murali, N., Adhikali, S., ***Current Status of Hydrogen Production Techniques by Steam Reforming of Ethanol***, Energy Fuels, vol.19, nr.5, p.2098-2106, 2005.

[4]. Deluga, G.A., Salge, J.R., Schmidt, L.D., Verykios, X.E., ***Renewable Hydrogen from Ethanol by Autothermal Reforming,*** Science, vol.303, nr.5660, p.993-997, 2004.

[5]. Benito, M., Sanz, J.L., and all, ***Bio-ethanol Steam reforming: Insights on the mechanism for hydrogen production***, Journal of Power Sources, vol.151, p.11-17, 2005.

[6]. Czernichowski, A., Wesolowska, K., ***Pox-Reforming of bio-methane into synthesis gas***, Am. Chem. Soc. Div. Fuel. Chem., vol.51, nr.2, 2006.

[7]. Proiect de cercetare, ***HyRes***–Dobrogea, "Proiect de cercetare asupra tehnologiilor energetice pe baza de hidrogen utilizabile in vederea valorificarii surselor energetice regenerabile din zona Dobrogei", director coordinator Mamut Eden, Universitatea Ovidius, Constanta, 2006-2008.

[8]. Bobrova, I.I., Bobrov, N.N., and all, ***Catalytic Steam Reforming of Methane: New data on the contribution of homogeneous radical reactions in the gas phase: ruthenium catalyst***, Kinetics and Catalysis, vol.42, nr.6, p.805-812, 2001.

THE ANNALS OF “DUNAREA DE JOS” UNIVERSITY OF GALATI.
FASCICLE IX. METALLURGY AND MATERIALS SCIENCE
N^0. 2 – 2007, ISSN 1453 – 083X

STUDY OF HEAT TREATMENT INFLUENCE ON ALUMINUM -BASED ALLOY ATN-Si10Cu4

Elisabeta VASILESCU, Simona BOICIUC
“Dunărea de Jos” University of Galaţi
email: elisabeta.vasilescu@yahoo.com

ABSTRACT

This work presents the experimental results concerning the behavior on heat treatment of on aluminum based alloy. The laboratory level experiments achieved on samples of ATN-Si10Cu4 (4145 series) alloy illustrate the variation of properties depending on the variation of heat treatment technological parameters specific to different heat treatment. We have experimented more variants of heat treatment in order to establish the optimal variant treatment. The samples were characterized by HB hardness and microstructure analysis.

KEYWORDS: heat treatment, quenching in solution and heat ageing, aluminum based alloy.

1. Introduction

ALUMINUM, the second most plentiful metallic element on earth, became an economic competitor in engineering applications as recently as the end of the 19th century. It was to become a metal for its time. The emergence of three important industrial developments would, by demanding material characteristics consistent with the unique qualities of aluminum and its alloys, greatly benefit growth in the production and use of the new metal.

The properties of aluminum that make this metal and its alloys the most economical and attractive for a wide variety of uses are appearance, light weight, fabricability, physical properties, mechanical properties, and corrosion resistance.

Aluminum has a density of only 2.7g/cm^3. It can display excellent corrosion resistance in most environments, including atmosphere, water, petrochemicals, and many chemical systems. Aluminum surfaces can be highly reflective. Aluminum typically displays excellent electrical and thermal conductivity, but specific alloys have been developed with high degrees of electrical resistivity. It is nonferromagnetic, a property of importance in the electrical and electronics industries [1, 2, 3, 4, 5, 6].

It is convenient to divide aluminum alloys into two major categories: casting compositions and wrought compositions. A further differentiation for each category is based on the primary mechanism of property development. Many alloys respond to thermal treatment based on phase solubilities.

These treatments include solution heat treatment, quenching, and precipitation, or age, hardening. For either casting or wrought alloys, such alloys are described as heat treatable. A large number of other wrought compositions rely instead on work hardening through mechanical reduction, usually in combination with various annealing procedures for property development (Fig.1). These alloys are referred to as work hardening. Some casting alloys are essentially not heat treatable and are used only in as-cast or in thermally modified conditions unrelated to solution or precipitation effects [1, 2].

1*xxx* Series. Aluminum of 99.00% or higher purity has many applications, especially in the electrical and chemical fields. These grades of aluminum are characterized by excellent corrosion resistance, high thermal and electrical conductivities, low mechanical properties, and excellent workability. Moderate increases in strength may be obtained by strain hardening. Iron and silicon are the major impurities. Typical uses include chemical equipment, reflectors, heat exchangers, electrical conductors and capacitors, packaging foil, architectural applications, and decorative trim.

2*xxx* Series. Copper is the principal alloying element in 2***xxx*** series alloys, often with magnesium as a secondary addition. These alloys require solution heat treatment to obtain optimum properties; in the solution heat-treated condition, mechanical properties are similar to, and sometimes exceed, those of low-carbon steel. In some instances, precipitation heat treatment (aging) is employed to further increase mechanical properties.

This treatment increases yield strength, with attendant loss in elongation; its effect on tensile strength is not as great.

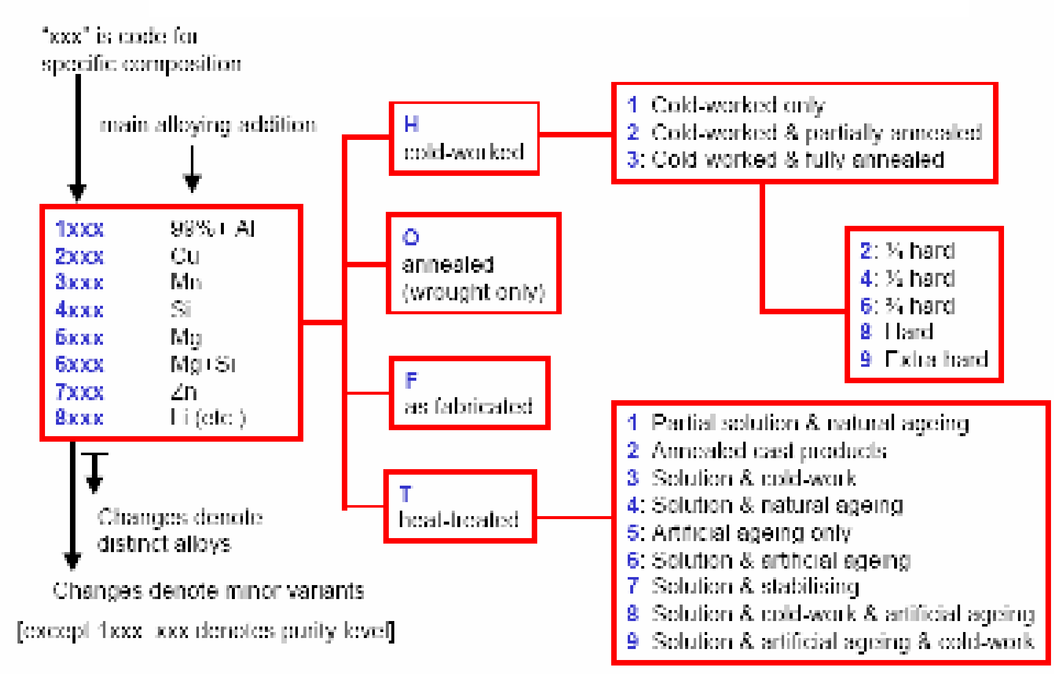

Fig.1. Al alloys and treatment classification system

Table 1. Characterization of aluminum based alloys

Alloy series	**Composition**	**σ_c** [MPa]	**σ_r** [MPa]	**ε** [%]	**Notes**
1000	Pure Al	30 - 100	100 - 135	Up to 50	Foil, decoration, electrical conductors
2000	4.5%Cu (+Mn, Si, Mg) age - hardened	Up to 480	Up to 520	5 - 20	General purpose forgings and extrusions, esp.airframes
3000	1%Mn, Mg cold - worked	Up to 215	Up to 290	5	Ductile sheet for cladding trucks, trailers; food containers, drink cans.
4000	12%Si (+Mg, Ni, Cu) forgeable, age - hardened	295	325	0.5	IC engine pistons
5000	5%Mg (+Cr, Mn)cold - worked	Up to 350	Up to 415	15	Good formability and weldability; excellent corrosion resistance; structural applications, esp. marine.
6000	Up to 1% Mg – Si, age - hardened	275	310	12	Hot extrusions; window frames.
7000	Up to 8% Zn (+Mg, Cu, Cr) age - hardened	500	575	11	Highest strength alloys; aircraft structures.
8000	Other, e.g. up to 2.5% Li				Novel and specialist alloys
Cast	Near Al – 13%Si eutectic + 0.01% Na	Up to 200	Up to 300	2 - 5	Automotive castings; can age – harden if Cu and Mg added.

The alloys in the 2***xxx*** series do not have as good corrosion resistance as most other aluminum alloys, and under certain conditions they may be subject to intergranular corrosion. Therefore, these alloys in the form of sheet usually are clad with a high-purity aluminum or with a magnesium-silicon alloy of the 6***xxx*** series, which provides galvanic protection of the core material and thus greatly increases resistance to corrosion. Alloys in the 2***xxx*** series are particularly well suited for parts and structures requiring high strength-to-weight ratios and are commonly used to make truck and aircraft wheels, truck suspension parts, aircraft fuselage and wing skins, and structural parts and those parts requiring good strength at temperatures up to 150 °C (300 °F). Except for alloy 2219, these alloys have limited weldability, but some alloys in this series have superior machinability.

3*xxx* Series. Manganese is the major alloying element of 3***xxx*** series alloys. These alloys generally are non-heat treatable but have about 20% more strength than 1***xxx*** series alloys. Because only a limited percentage of manganese (up to about 1.5%) can be effectively added to aluminum, manganese is used as major element in only a few alloys. However, three of them--3003, 3X04, and 3105--are widely used as general-purpose alloys for moderate-strength applications requiring good workability. These applications include beverage cans, cooking utensils, heat exchangers, storage tanks, awnings, furniture, highway signs, roofing, siding, and other architectural applications.

4*xxx* Series. The major alloying element in 4***xxx*** series alloys is silicon, which can be added in sufficient quantities (up to 12%) to cause substantial lowering of the melting range without producing brittleness. For this reason, aluminumsilicon alloys are used in welding wire and as brazing alloys for joining aluminum, where a lower melting range than that of the base metal is required. Most alloys in this series are non-heat treatable, but when used in welding heat-treatable alloys, they will pick up some of the alloying constituents of the latter and so respond to heat treatment to a limited extent. The alloys containing appreciable amounts of silicon become dark gray to charcoal when anodic oxide finishes are applied and hence are in demand for architectural applications. Alloy 4032 has a low coefficient of thermal expansion and high wear resistance, and thus is well suited to production of forged engine pistons.

5*xxx* Series. The major alloying element in 5***xxx*** series alloys is magnesium. When it is used as a major alloying element or with manganese, the result is a moderate-to-high-strength work-hardenable alloy. Magnesium is considerably more effective than manganese as a hardener, about 0.8% Mg being equal to 1.25% Mn, and it can be added in considerably higher quantities. Alloys in this series possess good welding characteristics and good resistance to corrosion in marine atmospheres. However, certain limitations should be placed on the amount of cold work and the safe operating temperatures permissible for the higher-magnesium alloys (over about 3.5% for operating temperatures above about 65 °C, or 150 °F) to avoid susceptibility to stress-corrosion cracking.

Uses include architectural, ornamental, and decorative trim; cans and can ends; household appliances; streetlight standards; boats and ships, cryogenic tanks; crane parts; and automotive structures.

6*xxx* Series. Alloys in the 6***xxx*** series contain silicon and magnesium approximately in the proportions required for formation of magnesium silicide (Mg2Si), thus making them heat treatable. Although not as strong as most 2***xxx*** and 7***xxx*** alloys, 6***xxx*** series alloys have good formability, weldability, machinability, and corrosion resistance, with medium strength. Alloys in this heat-treatable group may be formed in the T4 temper (solution heat treated but not precipitation heat treated) and strengthened after forming to full T6 properties by precipitation heat treatment. Uses include architectural applications, bicycle frames, transportation equipment, bridge railings, and welded structures.

7*xxx* Series. Zinc, in amounts of 1 to 8% is the major alloying element in 7***xxx*** series alloys, and when coupled with a smaller percentage of magnesium results in heat-treatable alloys of moderate to very high strength. Usually other elements, such as cooper and chromium, are also added in small quantities. 7xxx series alloys are used in airframe structures, mobile equipment, and other highly stressed parts. Higher strength 7xxx alloys exhibit reduced resistance to stress corrosion cracking and are often utilized in a slightly overaged temper to provide better combinations of strength, corrosion resistance, and fracture toughness.

2. Experimental conditions

The experiments have been made on ATN-Si10Cu4 aluminum alloy (4145 series) having chemical composition shown in table 2.

Table 2. Chemical composition of Al-Si-Cu- Mg

Cu	Fe	Mn	Ni	Zn	Si	Mg	Pb	Al
4.5	0.93	0.61	0.67	3.0	11.05	0.84	0.102	rest

The laboratory experiments have been made of the specific heat treatments: quenching in solution and heat ageing with different experimental conditions.

The researches shown the optimal technological parameters into experimental conditions, fig. 2:

ü The optimal temperature for quenching in solution;

ü Time maintaining at optimal temperature for quenching in solution;

ü Optimal time and temperature for ageing.

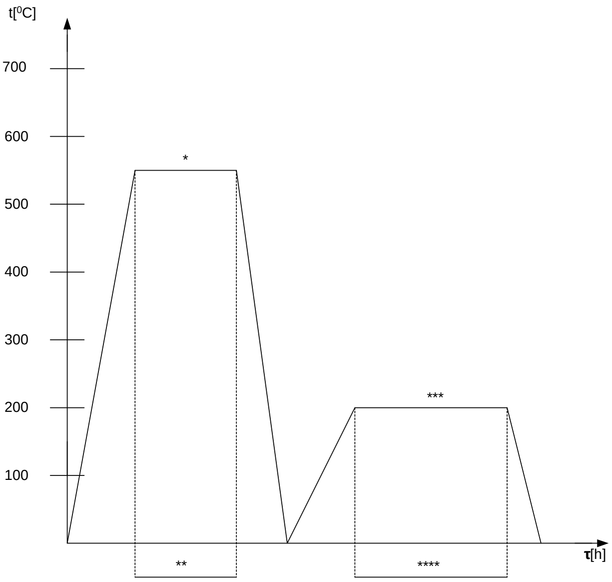

Fig.2. Experimental conditions for heat treatment: * - temperature for quenching in solution 300 °C, 350 °C, 400 °C, 450 °C, 500 °C, 550 °C; ** - Time maintaining for quenching in solution, 5 – 8 min/mm in thickness; *** - ageing temperature 120 °, 150 °, 200 °C; * - Time maintaining 1, 3, 6 ore.***

The effect of heat treatment on alloy structure and physical-mechanical properties was valued by hardness measurements (Brinell method, F=62.5 daN, bowl diameter D=2.5mm, maintaining time **τ**=15s).

Analyzing this experimental results (Fig.3 and Fig.4) we considered that the optimal temperature is 480 °C and the maintaining time is 2 h.

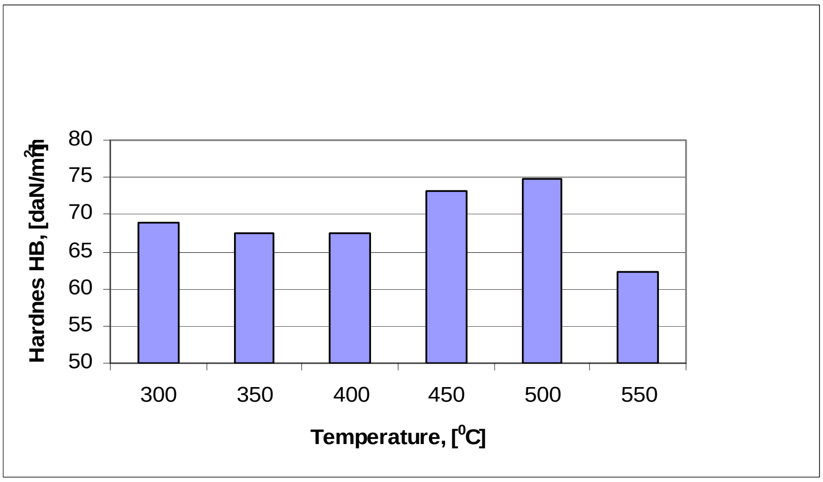

Fig.3. The influence of quenching in solution temperature on hardness

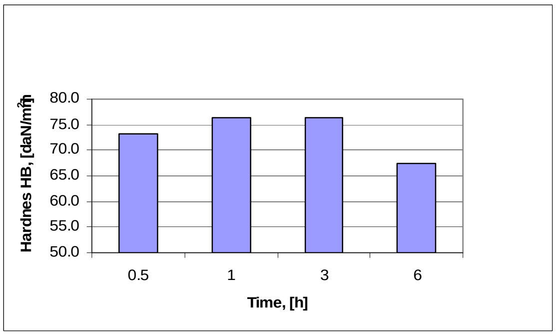

Fig.4. The influence of time maintaining at 480 °C (optimal one) on hardness.

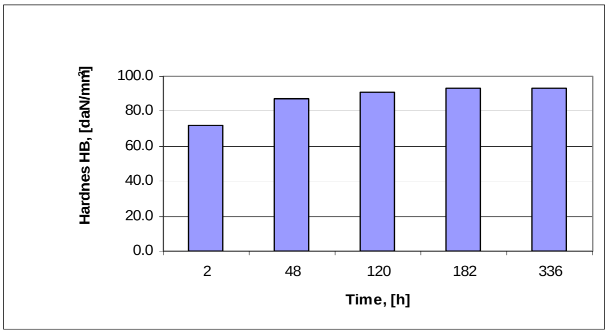

Fig.5. The influence of time maintaining on alloy natural ageing in state of quenching in solution at 480 °C and 2 h.

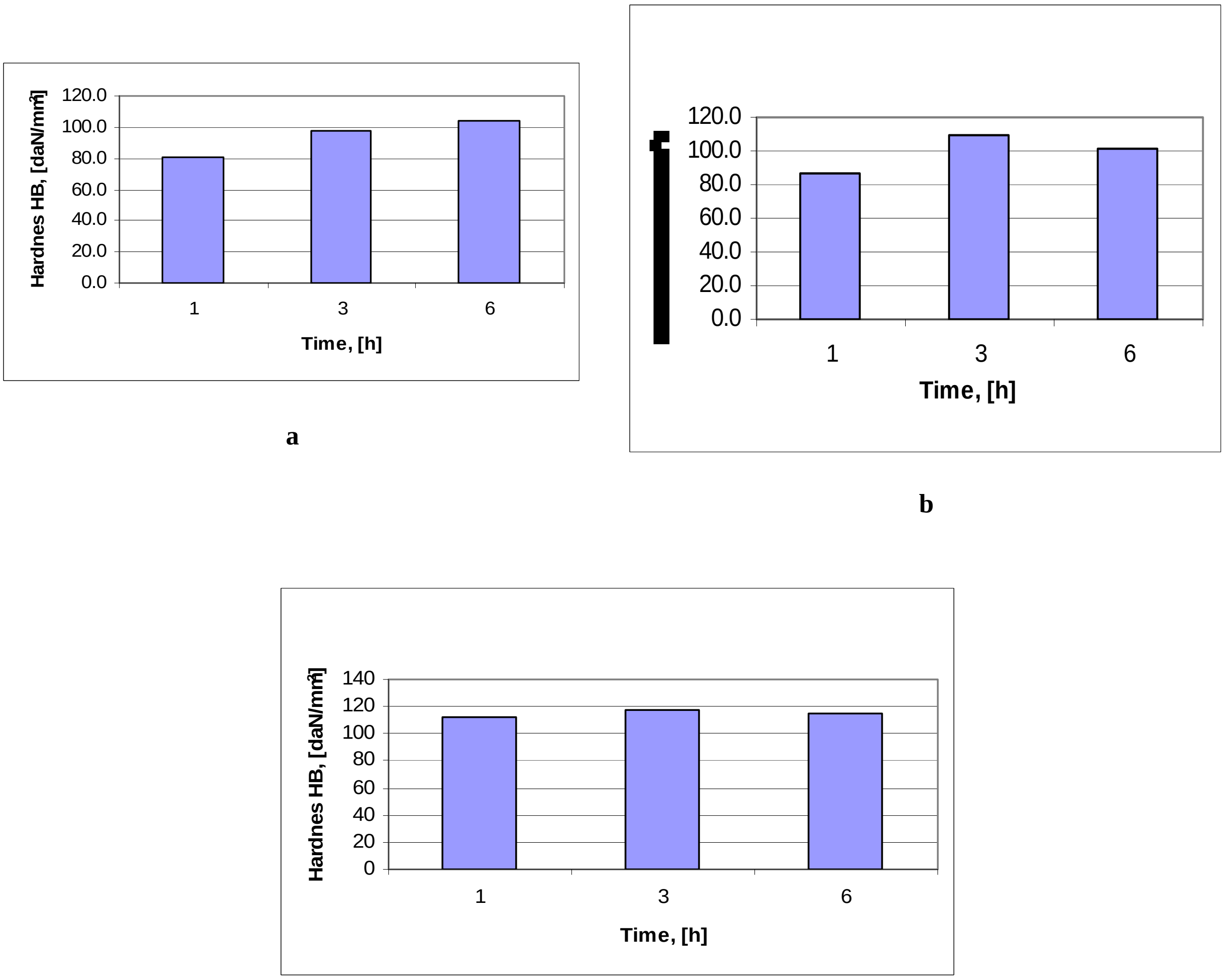

a

b

c

Fig.6. The influence of time maintaining on alloy artificial ageing at different temperatures:a - 120 °C; b - 150 °C; c - 200 °C.

3. Microstructural aspects

Figure gives the microstructural aspect of the Al alloy to enlargement power 250x, attack with 5% HF.

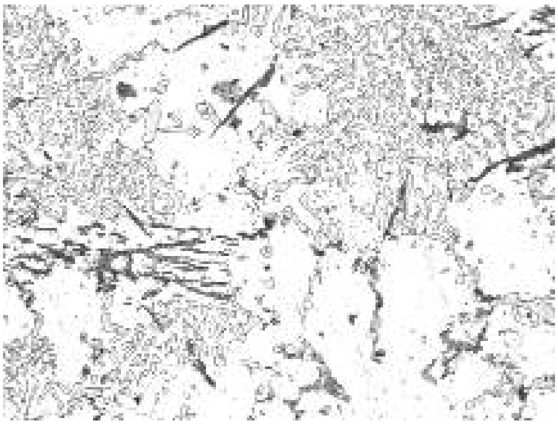

The microstructure of the Al alloy after quenching in solution

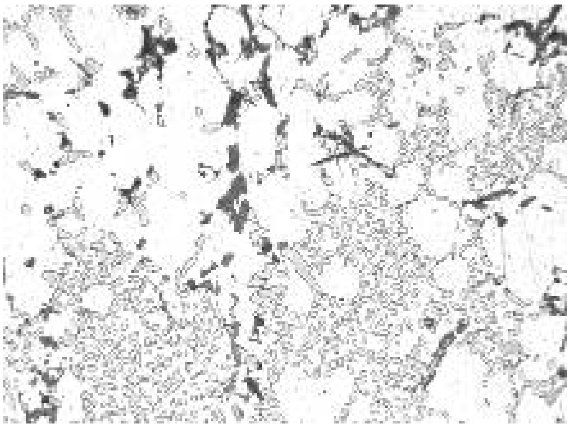

The microstructure of the Al alloy after quenching in solution and artificial ageing at 120°C for 6hours

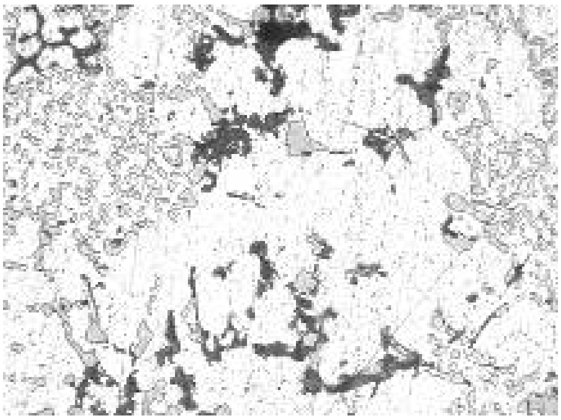

The microstructure of the Al alloy after quenching in solution and artificial ageing at 150°C for 3 hours

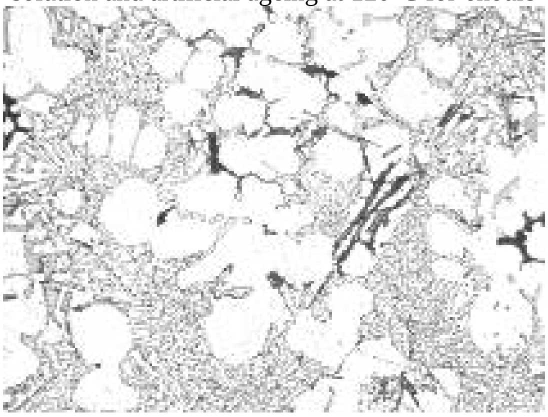

The microstructure of the Al alloy after quenching in solution and artificial ageing at 200°C for 3hours

4. Conclusions

The experimental conditions applied shown that this alloy is sensible at structural and properties modifications (considering hardness as a measure for the variation of the mechanical properties).

It was established for the alloy with given chemical composition (table 1) the optimal temperature of quenching in solution - 480 °C for maintaining time 2 hours. The increase of the temperature over this value or the increase of the maintaining time lead to the decrease of hardness. Concerning the heat treatment of ageing it comes out that at natural ageing the increase of maintaining time over 5 – 6 days, didn’t influence the hardness, which become constant.

The artificial ageing achieved at different temperatures and different maintaining times show:

ü The maximum hardness (120 HB) was achieved at 200 °C, this value couldn’t be achieved over a maintaining time of 6 hours for 120 °C and 150 °C.

ü The maintaining time for artificial ageing at optimal temperature 200°C, mustn’t prolonge over 3 hours, because the hardness decreases.

References

[1]. ASM HANDBOOK – Volume 2 – ***Properties and selection: Nonferrous alloys and special – purpose materials***, 1990.

[2]. S. G. Roberts – ***Engineering “C” – High performance alloys***, Department of Materials, University of Oxford.

[3]. Dulamita T, Florian E – ***Tratamente termice şi termochimice***, E.D.P. Bucureşti, 1982.

[4]. Popescu N, şa – ***Ştiinţa materialelor vol*** 2, Editura Fair Partners, Bucureşti 1999.

THE ANNALS OF “DUNAREA DE JOS” UNIVERSITY OF GALATI.
FASCICLE IX. METALLURGY AND MATERIALS SCIENCE
N^0. 2 – 2007, ISSN 1453 – 083X

SEMI-PLANETARY ROLLING AND CHANGES OF FINE STRUCTURE AND MICROSTRUCTURE

C. GHEORGHIES, N. CANANAU, P. ALEXANDRU, I. PETREA
“Dunarea de Jos” University of Galati
email: cgheorg@ugal.ro

ABSTRACT

The strain intensity in the proximity of planetary cylinder, in the case of semi-planetary rolling is greater than in the proximity of the massive cylinder. This fact leads at the variation of the microstructure and fine structure characteristics: the mosaic block dimension, second order stresses, dislocations density, micro-hardness into the thickness of rolled body. In the paper it presents the research results for identify and evaluate the structure modifications at the semi-planetary rolling.

KEYWORDS: semi-planetary rolling, fine structure, X ray diffraction.

1.Introduction

Plastic deformation strongly affects the microstructure and mechanical properties of the material. Thus plastic deformation leads to the variation of the dimension of mosaic blocks, dislocation density, value of second order stress, at the fine structure level and, consequently, change of the mechanical properties (for example micro-hardness).

The microstructure evolution and the changes of the mechanical properties induced by plastic deformation depend not only on the deformation process but also on the properties of the material, in particular on its crystalline structure, stacking fault energy and the value of the self-diffusion coefficient [1].

The semi-planetary rolling model is presented in figure 1 and it leads to an asymmetrical stress and strain state on the thickness of the semi-product [2].

The strain developed in the proximity of the superior planetary cylinder has greater intensity then the strains developed in the proximity of massive cylinder.

As effect, after semi-planetary rolling the body, with initial rectilinear form, becomes curve body. Also, as a reversible process, the curved body may take a final rectilinear form.

An important application of semi-planetary rolling, which may become a solution for quality assurance of the metallurgical products, may be the unbending of the continuous cast slabs of different metallic materials that have in certain temperature range a fragility domain.

Thus is the case of the construction steels with great mechanical resistance, micro and low alloyed steels with fine microstructure.

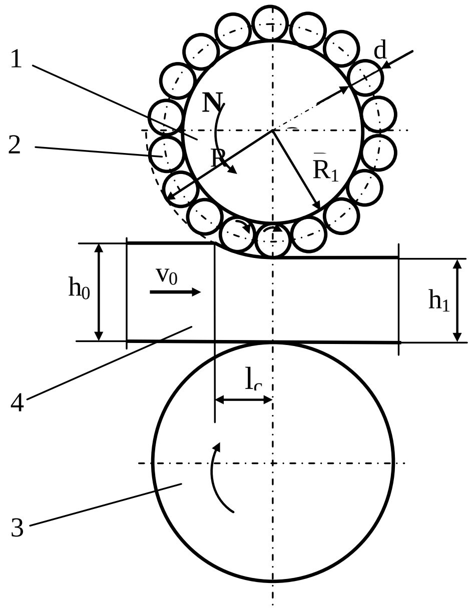

Fig.1. Scheme of semi-planetary rolling process: 1-planetary cylinder, 2-sattelite cylinder, 3-massive inferior cylinder, 4-rolled body

At the same time in the unbending zone, into the proximity of interior surface of slab section, a plane tensile stress state is developed. Coupled, these two causes, respectively, the reduced plasticity of steel and the bi-axial tensile stress state may lead at the appearance of the superficial fissures and the discontinuity defect.

The semi-planetary rolling applied at unbending zone, to the exit of slab from curve thread of the continuous casting machine, for example placing a semiplanetary rolling mill into the drawing mill, induces an unbending moment in the condition of the compression stress state [3, 4].

The semiplanetary rolling is characterized by the variation of strain intensity in the thickness of the body, grater in the proximity of the planetary cylinder, smaller in the proximity of the massive cylinder and minimum values at the half of thickness.

This fact will lead at the changes of the crystalline lattice and variation of microstructure and of the properties of deformed material.

2.Research conditions

In the aim of the observing of the influence of the deformation on the structure and properties of deformed material we made a metallographic study, analyze by diffraction of the X-radiation and the measurement of the micro–hardness [5 - 7].

The samples were prepared form aluminum and their shape was rectangular prism having dimension of 10×12×100 mm.

The deformation has been performed on a original semiplanetary rolling mill which is composed of a planetary cylinder with appearance surface of 80mm, composed by a support cylinder and 18 satellite cylinders with active surface dimensions of Ø12×50mm, and the massive cylinder surface of Ø80×50mm. The revolution of the planetary cylinder is 200 rpm and of massive cylinder is 2 rpm.

Analysis of fine structure modifications induced of the semiplanetary rolling has been performed on a diffractometer type DRON 3. This apparatus has following work parameter: copper anti-cathode (λ=1.541 Å), U= 34 kV, I=30 mA, and monocromathor in the diffracted beam.

The micro-hardness was measured with an adequate apparatus type PMT-3 and for micro-structural analysis an optical microscope equipped with a digital system for quantitative analysis.

3.Experimental results

In the figure 2 the microstructures of the initial (non-deformed) and deformed aluminum samples are presented, respectively. Because the deformation degree is relatively small, the semiplanetary rolling does not produce a visible modification of the crystalline grains. The dimension of crystalline grains increases in the proximity of the planetary cylinder and near the massive cylinder this structural parameter is not modified.

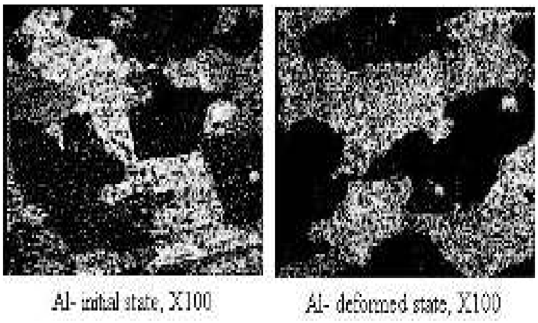

(a) (b)

Fig. 2. Microstructure of aluminum samples before (a) and after (b) deformation

According to the X-ray diffraction analysis the aluminum sample was cross scanned with the advance step of 2 mm, resulting 6 measuring points. In figure 3 is shown the irradiation scheme of the samples.

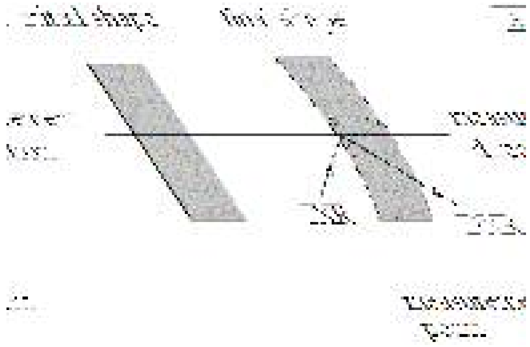

Fig. 3. Irradiation and X-ray scanning scheme of deformed sample

In order to analysis of fine structure of aluminum samples the diffraction lines (111) and (311) are considered. First diffraction line is used at the evaluation of the dimension of mosaic blocks in the $\langle 111 \rangle$ crystallographic direction. The evaluation of the second order internal stress and the dislocation density levels is done from the analysis of the second diffraction line.

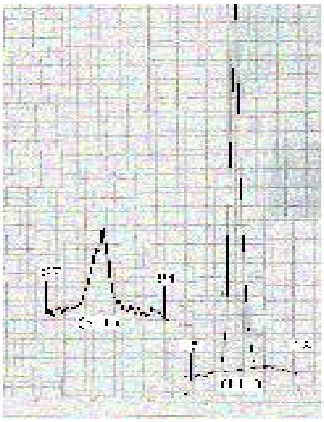

Fig. 4. Aspects of the diffraction lines (111) and (311) for deformed aluminum sample

The (111) diffraction line appears into angular range, $2\theta \ \left(42^0, 45^0\right)$ and the (311) diffraction line is in angular domain, $2\theta \ \left(94^0, 97^0\right)$. In figure 4 the shape of above mentioned diffraction lines is displayed.

In figure 5 the variation of the (111) diffraction line width, $B_{(111)}$, that is inverse proportional with the mosaic blocks dimensions, $D_{(111)}$, is carried out. Between the two sizes there is the relation:

$$D_{(111)} \approx \frac{1}{B_{(111)}} \qquad (1)$$

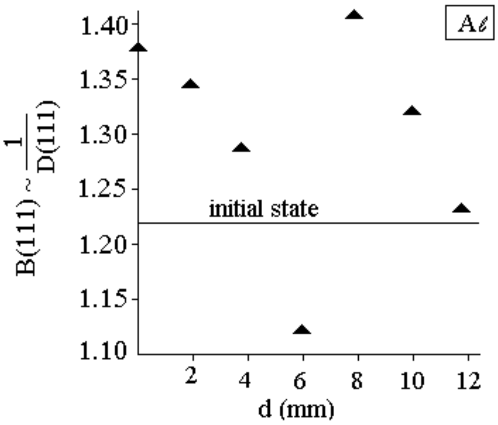

Fig. 5. Cross distribution of the width of diffraction line on cross section

The analysis shows that the deformation determines the increasing of the mosaic block dimensions.

The mosaic block dimensions have an important variation. In the marginal layer, at the proximity of the contact surface with the planetary cylinder the dimension of the mosaic block decreases. The value of the mosaic block dimension follows the variation of deformation intensity. At the middle of the thickness an abrupt jump of the mosaic block dimensions is observed. This fact may be determined by the extension of the mosaic blocks at the very small plastic deformation. In the part of the massive cylinder the value of mosaic blocks dimension it maintains at the contact surface and decreases to the interior layers. This aspect is explained by the action of the dead zone into the marginal layer at the contact surface with the massive cylinder.

It denotes because of the small value of the b/h ratio the deformation in the width direction of sample is great enough for determine smaller deformation intensity in direction of the thickness.

In figure 6 it presents the distributions of the widths of diffraction lines (311).

The width of diffraction line is direct proportional to the level of the second order internal stress, according to the relation:

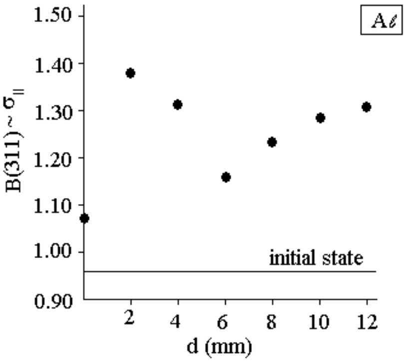

Fig. 6. Cross distribution of the second order internal stress

The second order stress registers a minim value at the middle of the deformed body. At the contact surface with the planetary cylinder the second order stress has a lower value.

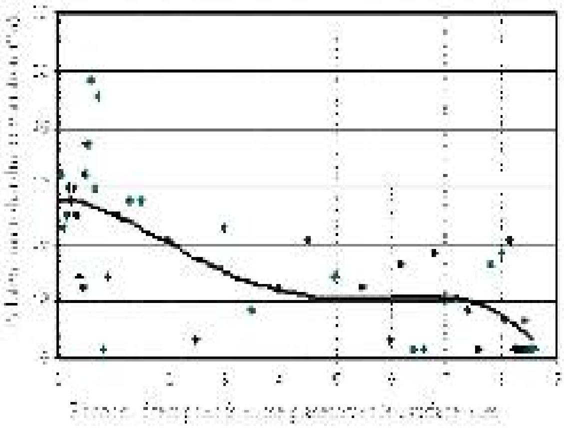

Fig. 7. Cross distribution of micro hardness

This fact can be explained by the effect of mechanical relaxation induced by the deformation in width direction, because the ratio b/h is small, relatively. Consequently, the second order stresses really correspond to the repartition of the strain intensity in the thickness of sample. Therefore the repartition of the second order stresses is the most factors for study of influence of asymmetrical deformation of the fine structure of metallic material.

The variation of micro-hardness is showed in figure 7 and its can be connected with distribution of second order stresses.

4. Conclusions

Semiplanetary rolling is an interesting deformation process for the obtaining of the curve pieces or for unbending of the curved parts. Because the diameter of the satellite cylinder is much smaller of the diameter of massive cylinder the strain intensity is variable in the section of the body.

This is greater at the proximity of planetary cylinder, smaller at the proximity of massive cylinder.

Between the strain intensity and the modification of micro and fine structure is a correlation. The experimental researches proved this correlation. The dimension of the crystalline grain is very small influenced.

The dimension of the mosaic blocks follows the variation of the strain intensity for the value of the ratio b/h great, relatively. Thus, in the proximity of the planetary cylinder this factor has great value, registers a minimum at the middle of the thickness

The best parameter of the fine structure what very good corresponds at the variation of the principal deformation factor of the semiplanetary rolling process, respectively, local strain intensity is the second order internal stress. Thus, in case of the deformed body with the geometrical ratio b/h small, because the deformation to the width direction is enough great, in the proximity of the planetary cylinder appears a relaxation of the second order stresses.

The second order stress has a minimum value at the middle of the thickness and increases slowly to the massive cylinder proximity. In case of the geometrical ratio greater of 2 the deformation in the width direction is negligible and the second order stress has the maximum value at the proximity of the planetary cylinder where the strain intensity has maximum value.

The micro-hardness increases with 25% almost in the proximity of the planetary cylinder and littler, 5% approximately, at the proximity of the massive cylinder.

References

[1]. Kurzydowski K. J. et al. ***Effect of severe plastic deformation on the microstructure and mechanical properties of Al and Cu***, REV. ADV. SCI. 8 (2004)

[2]. Cănănău N., Ivănescu A., Cănănău D., ***Study on the Deformation Process at the Semi-planetary Rolling,*** ACTA MECHANICA SLOVACA, Kosice, nr.3 (2001).

[**3]. Cănănău N., Potecasu O., Gurău G., Preda A.,** ***Experiemntal researches on the thickness reduction influence to the bending slab billet in the semiplanetary rolling process, The Conference,*** UGALMAT-2005, 91-95, oct. (2005).

[4]. Cănănău N., Gurău G., ***Researches concerning the semiplanetary rolling process,*** The 12th International Congres „METALURGY AND MATERIALS", Istanbul Turkey, sept. (2005).

[5]. Heidelbach F., et al. ***Orientation and misorientation characteristics of annealed, rolled and recrystallized copper.*** MAT. SCI. ENG. A215, 39-49, (1996).

[**6]. Kocks U. F., Tomé C., Wenk H.-R.,** ***Texture and Anisotropy. Preferred Orientations in Polycrystals and Their Effect on Materials Properties.*** Cambridge University Press, 1998.

[7]. Gheorghieş, C. ***Controlul structurii fine a materialelor cu radiaţii X,*** Editura tehnică, Bucureşti , 1990.

THE ANNALS OF “DUNAREA DE JOS” UNIVERSITY OF GALATI.
FASCICLE IX. METALLURGY AND MATERIALS SCIENCE
N^0. 2 – 2007, ISSN 1453 – 083X

THE MONITORING OF CHATTERING IN COLD ROLLING MILL SYSTEM WITH FIVE STANDS FOR THIN STRIP

**Stefan DRAGOMIR, Georgeta DRAGOMIR,
Constantin SPÂNU**
“Dunărea de Jos” University of Galati
email: doromir_dragomir@yahoo.com

ABSTRACT

Each system (stand – driving) and the continuous rolling line to which it belongs have its own functional and energetically parameters. To reduce any faults of the strip surface it is also necessary to check (eventually having a control line) the roll surface quality, the work roll eccentricity, and depending on the disposal by compensation, of eccentric lobes. The appearance of the specific faults on the rolled strip-during the experiments carried out is duet o the vibrations covered by the range of 100-300 Hz. This many-sided theme needs mathematical patterns to correlate the factors and the dimensions (strip types, technological flow, driving) which should be able to basically support the monitoring system. Taking into account the aspects regarding the quality of the surfaces, the geometry of strips and the costs, it necessary to do a monitoring

KEYWORDS: chatter, monitoring, stand, work parameters, accelerometer

1. Introduction

In this paper is show the most important dynamics’ loads and there influence on the cold rolling mill process.

The most rolling mills equipments work in very hard dynamics conditions and loads [4].

A lot of equipments (machines, components etc.) are singulars and have greatest influence on the price and productivity.

In work, is very important to reduce the dynamics load [5], to choose the optimal parameters, to foresee the adequate dumping device and moderns systems to deaden the stresses and tensions in equipments of rolling mill.

Greatest dimensions for strip have an important influence on the mills equipments.

In the fig. 1 is show the schedule of rolling mill machine with five stands and the position of the accelerometers (on the chocks of the work and backup rolls).

It is important to diminish the dynamics loads from the beginning of work program for obtain an optimal cinematic scheme for all components of mill.

The High-Tech Rolling Mill is distinguished by the use the integrated adjusting mechanism and control systems foe quality assurance in the final product.

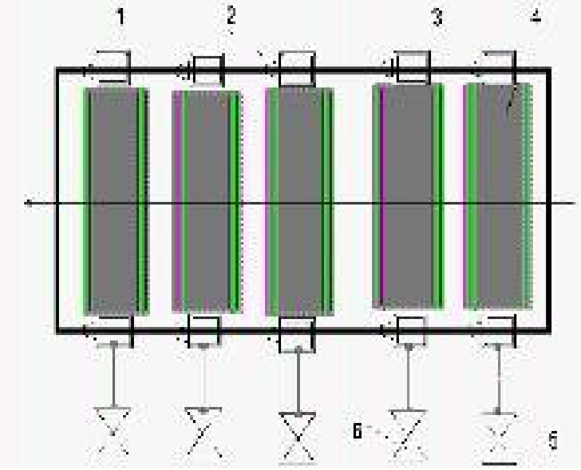

Fig. 1. Measurement vibration system on the mill stand: 1. Rolling mill frame; 2.Accelerometer; 3.Backup roll; 4. Mill roll; 5.Coupling bar; 6.Engine.

Using the rapidly reacting work roll bending facility for roll gap correction is made an outstandingly dynamic adjusting system [2].

The work bending system installed at the five stand of the mill machine carry out the adjustment commands transmitted from the flatness control system.

Hydraulic screw down is an operationally reliable and dynamic adjustment mechanism for controlling the strip thickness. Expansion of strip products and different size and strip thickness determine the construction of universally coilers for complete the all range of cold strip thickness and width. The sturdy wrapper roll system guides the strip head to the start of the coiling operation around the mandrel. As the wound material passes over the strip head position the wrapper rolls must be able to very quickly deflect otherwise the large moment of inertia of the system would cause damage to the strip. It is not possible to achieve this objective deflection of the roll with conventional method operated coilers.

2. Studies of vibrations on the cold rolling mill

In previous study of hot cold strip mill vibration we established a relations ship between mill chatter, mill speed and the phasing and number of teeth in the mill spindles.

The specific problem studied was chatter occurring at finishing stand of strip mill, when is produced an accelerated roll wear on the bottom work roll and is observe a strip marching.

The strip and roll marking (like a pattern) is visible occurred, when the chatter was present. The vibration has been exists on the cold rolling mil machine for a considerable time and, for unknown reasons, the frequency and intensity of occurrence varied in time [1].

The case study consisted of the following phases:

-Finite element modeling to determine natural (frequencies and vibration mode shapes of mill stand [3];

-Analysis of load cell signals with strip recorder and spectrum analysis;

-Drive train analysis to establish forcing function;

-Tests in which spindle teeth phase angles were adjusted to minimize chatter.

A correlation between chatter and spindles has been established. A better understanding of this problem will permit a further reduction in chatter and increased roll life. In our analysis, the inclusion of spindles in the model has provided additional information on the important subject of low frequency mill stand vibration [6]. The transition from the operator side elevation shows us the deflection of mill stand at a particular frequency. The chatter are measured (between 110-320 Hz.) and identified with accelerometer fixed on the backup roll chock. The measured system has a filter, signal amplifier, a process interface, a computer and a printer (fig. 2).

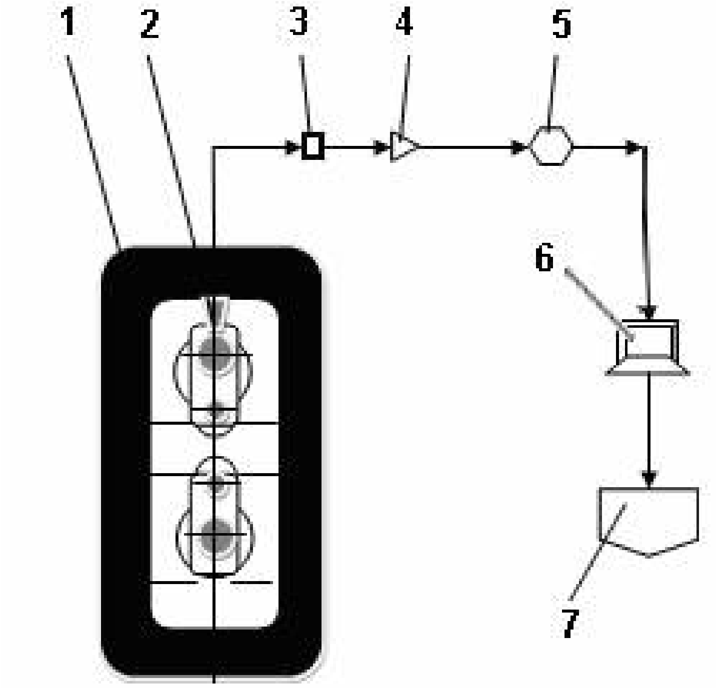

Fig. 2. Measurement vibration system on the mill stand: 1. Rolling mill frame; 2.Accelerometer; 3.Filter 4. Signal amplifier; 5. System interface; 6.Process computer; 7. Printer.

Finite element analysis models, confirmed by mill tests, indicate that spindles and their subsequent effect on work roll neck deflection are a potential source of mill chatter.

During a production run (identical coils), vibrations were measured with an accelerometer.

Finite element analysis models, confirmed by mill tests, indicate that spindles and their subsequent effect on work roll neck deflection are a potential source of mill chatter [3].

During a production run (identical coils), vibrations were measured with an accelerometer.

At the last the finite model was in agreement with the vibration measured on the work roll necks.

If vibration propagation started at the drive, the chatter marks on the bottom roll land strip should be intense on the drive and of the work roll land strip.

The stress is still less than the yield strength, which implies that there might be a fatigue failure problem but the housing of mill will not fail duet o yield under the normal operating force. If the housing has the possibility of fatigue failure what is the life expectancy based on current and projected future production. For the growth of the housing mill life we must to found a new type of design for that. The variations of the strip thickness during acceleration and deceleration are caused by fluctuation of the friction coefficient between the rolls and strip the inter stand tension and roll force at each stand [6].

When the roll gap is constant, the relationship between the change of roll force (ΔF_1)and the change of strip thickness (Δh) is:

$$\Delta h = \frac{\Delta F_1}{M}$$

where: M is the equivalent mill rigidity modules.

Equation is applied at each stand in tandem cold rolling mill and the inter stand tension connects all stands simultaneously.

During acceleration and deceleration, rolling condition change and simulation is affective to study total characteristics during non steady state rolling.

Top backup roll and bottom backup roll, generated occurrence and oscillatory vibration. That is not influenced by the structural resonance’s of the mill, is caused by roll eccentricities. Most modern cold mills are equipped with x – ray or beta – ray gage measurement equipment that can detect fluctuation in the gage of the rolled product at frequencies up to 25 Hz.

The frequency spectrum of the gage deviation can be seeing in fig. 3.

In the case of unstable vibration due to feedback mechanism, the vibration amplitude (fig. 4) will continue to grow in amplitude at an exponential rate until the forcing function is reduced enough to counteract the effect of instability.

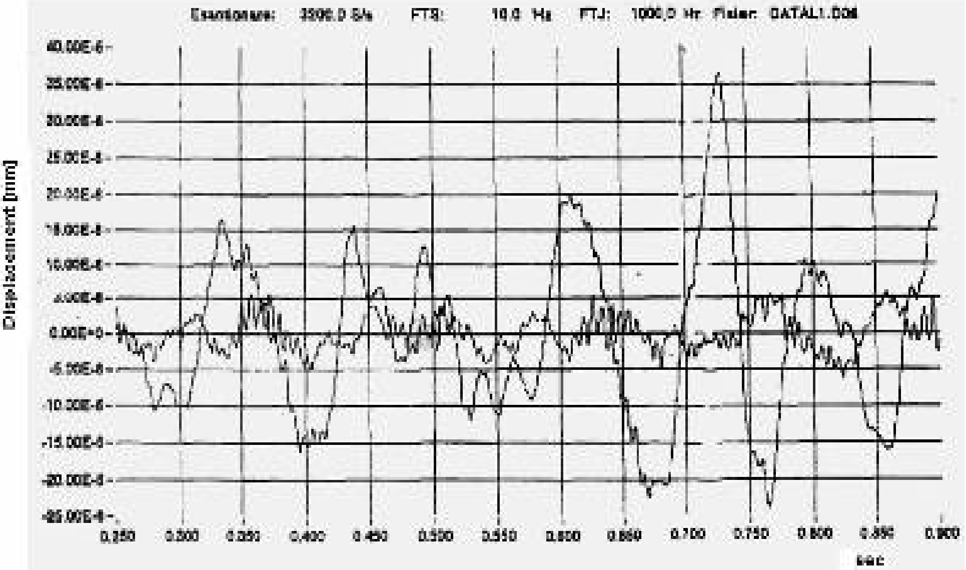

Fig. 3 Displacement frequency spectrum.

Some problems types that occur frequently in cold rolling mills are:

Sources of excitation are: excessive reduction; fluctuation of tension between entry and exit side; backup rolls wear pattern; the work roll bearing is defect; entry tension is excessive; oil temperature bearing is increase; uncontrolled quantity of lubricant on the strip.

In the normal operation speed of the mill, the cause of the third octave chatter is the strip surface.

For the fifth octave chatter (520-710 Hz.) the most important sources of excitation are: defective work roll bearing; strip with chatter marks; a wear pattern on the backup roll, the work roll bearing is defect; the surface of work roll has some undulation.

In most cases the vibration signal received by the housing is much smaller than that of the roll chocks.

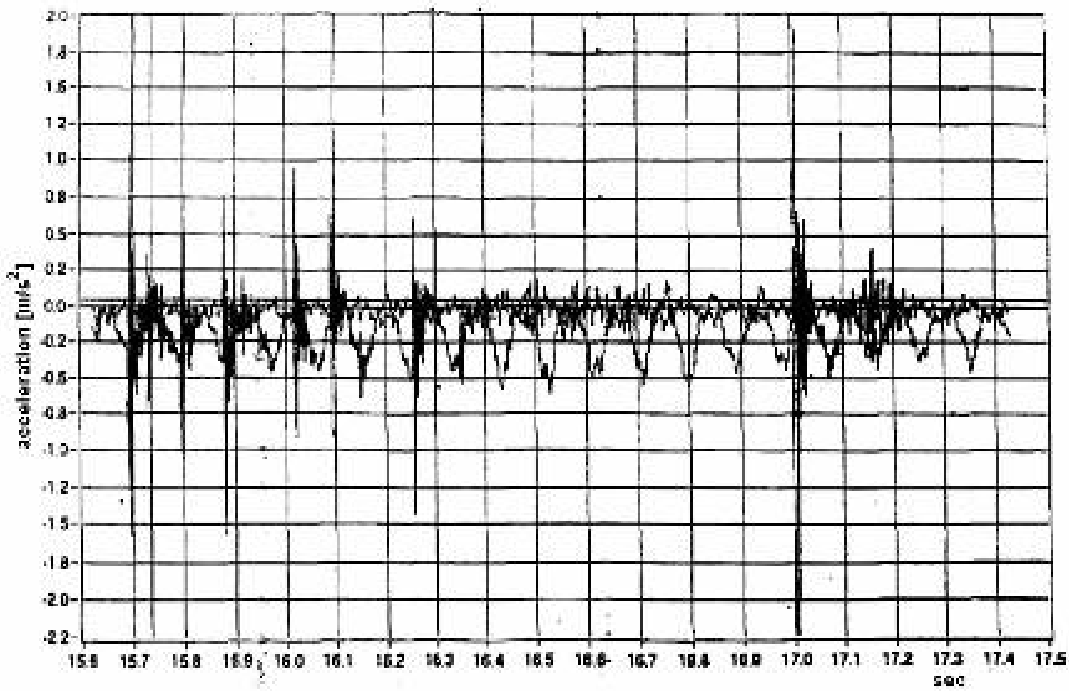

Fig. 4. Acceleration spectrum for mill plate.

The vibration of mill is influenced by one on more resonant frequencies of the system. Vibration becomes unstable duet o the influence of some force feedback mechanism which is direct result of the initial vibration caused by variation of technologically parameters, like: strip speed (acceleration, deceleration, displacement, fig. 3, 4), tension and roll force at each stand, strip thickness etc.

3. Conclusions

The study revealed that the maximum vibration occurs at the work roll. For vibration monitoring the best location for an accelerometer would be the roll chocks. A force spectrum, including instantaneous force changes can be established by combining the average in coil force variation and coil to coil force variation. The former is usually obtained directly from force and strain gage measurement. The amplitude stress can be computed for the amplitude to mean ratio. Further mathematical derivation and assumptions lead to the upper and lower bound estimate can eliminate the measurement of in coil force variation which is costly. The average amplitude force can be roughly estimated by observing the rolling force in work of mill. A detailed finite element analysis on the mill housing is necessary to convert the force into stress using the proportion rule. At the end we see the correlation between the measurement signals, load and vibration and characteristics defects of installation. A complete system of chatters monitoring, could advertising at time the moment when something is wrong – a malfunction – with the rolling mill. By using a combination test and analytical methods to initially diagnose problems, combined with continuous and automated monitoring for rolling mill to detect further occurrences defects in function.

References

[1]. Keller, N. et al., 2005, ***Vibration analysis of Stand F2 in Cold Strip Mill***. AISE Year Book, pp. 205-210.

[2]. Lin, Y. J., Suh, C. S., Langari, R., Noah, S. T., 2003, ***On the Characteristics and Mechanism of Rolling Instability and Chatter***, Journal of Manufacturing Science and Engineering, Vol. 125(4), pp. 778-786.

[3]. Poplawski, J.V., and Seccombe, D.A., 1980, ***Mathematical Modeling of Cold Rolling in Tandem Mills***, Iron and Steel Engineer, Vol. 58, pp 47- 59.

[4]. Rusinski, E., Moczko, P., Przybyłek, G., 2005, ***Degradation of roller mills load carrying structure -experimental and numerical identification and investigation of reasons***, http://cdm.unipr.it/das2005/papers/88.pdf, accesat 05.2007.

[5]. Voinea, R., Voiculescu D., 1989, ***Introducere în mecanica solidului cu aplicaţii în inginerie***, Editura Academiei.

[6]. Yarita I., Furukawa K. et al., 2004, ***An Analysis of Chattering in Cold Rolling for vibration gage strip steel***. Transaction of the Iron Steel Institute of Japan, 19, nr. 1, pp. 1-10.

THE ANNALS OF “DUNAREA DE JOS” UNIVERSITY OF GALATI.
FASCICLE IX. METALLURGY AND MATERIALS SCIENCE
N^0. 2 – 2007, ISSN 1453 – 083X

THE ACTION OF THE ULTRASONIC VIBRATIONS OVER THE DIFFUSION PROCESS IN GASES AND LIQUIDS

Aurel CIUREA, Marian BORDEI
Universitatea “Dunarea de Jos” din Galati
email: ciurea.aurel@ugal.ro

ABSTRACT

Among the new method of studying the properties of the substance and the influence over the most various physical and chemical processes, used in different industrial domains, the main place is occupied by the usage of sound and ultrasound oscillations. Of course, nowadays we consider the acceleration of the diffusion processes, the degassing of the liquids under the action of the sound field, in melt, over the crystallisation process as being very important.

KEYWORDS: ultrasonic vibrations, diffusion, liquides, gases

1. The kinetics diffusion in gases and liquids

Numerous experiments demonstrated that the rate of the heterogeneous reaction taking place according to the kinetics diffusion are defined through the diffusion which appears as a result of the presence of different concentrations of the substance among the adhered substance layers directly at the surface and the liquid thickness.

Mathematically, this confirmation is expressed by Fick’s law:

$$I = D\int_S \frac{\delta c}{\delta n}\Big|_{S=0}\, dS \qquad (1)$$

where: is the flux of the substance towards the surface; D - the molecular coefficient of diffusion; $\frac{\delta c}{\delta n}\Big|_{S=0}$ - the concentration gradient at the surface;

S - surface.

For the practical calculus Nusselt coefficient is used:

$$N_u = \frac{J_e}{\Delta CSD} = \frac{\delta c}{\delta n}_{S=0}\frac{e}{\Delta C} \qquad (2)$$

where: e is a characteristic value of the surface; ΔC - the concentration difference between the surface layers and the liquid thickness.

According to a series of experiments [1] and [2] it follows that the flux of the substance, y, increases in the presence of the sound field, in other words, the heterogeneous reaction accelerates, the reaction taking place according to the diffusion kinetics.

In conformity with the relation (1), this is possible when the ultrasonic field leads to the Δ of the diffusion coefficient, or of the concentration gradient at the surface ∂c/∂n.

2. The diffusion coefficient in the sonic field

According to Einstein the diffusion coefficient has the following relation:

$$\Delta = K_0 T D \qquad (3)$$

where: K_0 is the Boltzman coefficient; T - absolute temperature; D – mobility.

For the spherical parts:

$$b = \frac{1}{6}\pi\eta r \qquad (4)$$

where: η is viscosity; r - particle radius.

From relation (3) it result that D = f(T), and the environment temperature (T) can be changed into ultrasounds field from three reasons. An important fact is that the sound wave is absorbed and the loss of its energy will lead to the change of the surrounding temperature, T_1. The temperature increase can be determined from the relation of the thermal balance.

$$Q = C_v \rho_0 \Delta T_1 \chi \qquad (5)$$

where:

$$Q = I_0\left(1 - e^{-\alpha|\chi}\right)$$

$$A^{|} = \frac{\frac{4}{3}\eta + \xi \quad * \omega^2}{2\rho_0 C_0{}^3}$$

in which: ρ_0 is the density; C_v – specific heat of the medium; x – distance covered by the sonic wave;
I_0 – sonic intensity; ξ – viscosity coefficient of the second medium; C_0 – the sonic rate in the middle;
ω – frequency of the sonic waves.

If we take as example 1 cm^3 of water, $I_0=1W/cm^2$, ω=2π MHz (In such a way that the cavitations cannot in water) from (5) rezults

$\Delta T=10^{-5}\,{}^0C$. For 1 cm^3 of air, $I_0=4W/cm^2$, ω=2 π *18KHz, results $\Delta T=10^{-2}\ {}^0C$.

In conclusion the heating of the two medium as a result of the sound absorption is proved to be insignificant. An other reason which might generated the heating would be a adiabatic compression of the middle in sonic field (ΔT):

$$\Delta T_2 = \frac{C_0 \beta^* T}{C_p} V_0 \tag{6}$$

where: C_p - specific heat at the constant pressure;
V_0 - amplitude; β^* - coefficient of the middle thermal expansion.

Using the same data of calculus it results that the change of the temperature in water $\Delta T_2=10\text{-}^3\ {}^0C$ and in air $\Delta T_2=0{,}3\ {}^0C$.

Neither this variation of temperature will not significantly influence the diffusion coefficient in sonic field. An important consequence of sonic wave absorption is the heating of the middle in capillaries and at surfaces of the phases separation.

The energy of the sounds absorbed in the capillaries can be expressed by the relation:

$$Q = E_0 \frac{\sqrt{\omega}}{\sqrt{2rc_0}} \quad \sqrt{\upsilon} + \quad \frac{c_p}{c_v} - 1 \quad * \sqrt{\chi} \tag{7}$$

where: r is capillary radius; υ-cinematic viscosity; χ-thermal conductibility; E_0-energy of the sonic wave in the capillary.

For a tube having radius of 1 cm an the length of 1 cm using the some parameters of the sonic wave the change of the temperature in capillary owing to the sound absorption in water will be $\Delta T_3=10^{-3}\ {}^0C$ and for the air $\Delta T_3=10^{-2}\ {}^0C$.

With diminish of the radius the energy inside the capillary has a sudden decreases in such a way in a thin capillary will be also small. For the real ferrous pieces, where the influence of the area unoccupied by pores in comparison with total area of the pores is equal of g the energy inside the coefficient is determined with Reily relation:

$$E_0 = \frac{4M}{2M^2 + 2M + 1} \tag{8}$$

Supposing that g = 1, meaning that the pores area is equal to the area occupied by the pores, r = 10^{-4}cm; ω=2π*10^6Hz’. It results that in the case of liquid that fills the capillaries, almost the whole energy will penetrate in them and according to the relations (5) and (7), $\Delta T_3^{|}=1^0C$. For the air, ω=2π*18KHz, r=10^{-4}cm, the part of energy that passes (penetrates) reach 3.5%, and the heating of the air in the capillaries will not surpass 4^0C. Another case of heating the middle part is possible an the condition of a normal fall of the sonic wave on a plane surface. The cause of this phenomenon is the fact that close to the rigid wall, there are transfers. However, at the surface, the temperatures that have contact with the core must be equal. In conclusion, in the thin layer close to the wall, it appears a temperature gradient which leads to an important energy dissipation.

The absorption of a sonic energy in the wall is equal to:

$$Q = \frac{2I_0\sqrt{2\omega}}{C_0} \quad \sqrt{\chi} \quad \frac{C_P}{C_V} - 1 \tag{9}$$

Using this relation and that of the thermal balance (5) it results that the variation of middle temperature as following the absorption in the wall, $\Delta T_4=0{,}1^0C$ for water and $\Delta T_4 \approx 1^0C$ for air. From the analysed data it results that the changes of temperature in ultrasonic field do not surpass several degrees Celsius. According to the relation (3) the ratio between the diffusion coefficient in sonic field D_{zv} and the diffusion coefficient in its absence is equal to:

$$\frac{D_{ZV}}{D} = \frac{T + \Delta T}{T} \approx 0{,}1\% \tag{10}$$

Consequently, the diffusion coefficient in the free middle and in the presence of the limited surfaces, practically does not change in the sonic field. Taking into account the fundamental relation (1) and the practical observations, it results that in the sonic field the gradient of the reactive substances concentrations must increase at the surface the phases separation.

3. The influence of the sonic vibrations aver the diffusion current

In order to find the concentration gradient in the most general form it is necessary to solve the consecutive diffusion equation:

$$\frac{\delta C}{\delta T} + \left(V\text{grad}\right)C = D\Delta C \tag{11}$$

where: V-the moving rate of the particles of the middle.

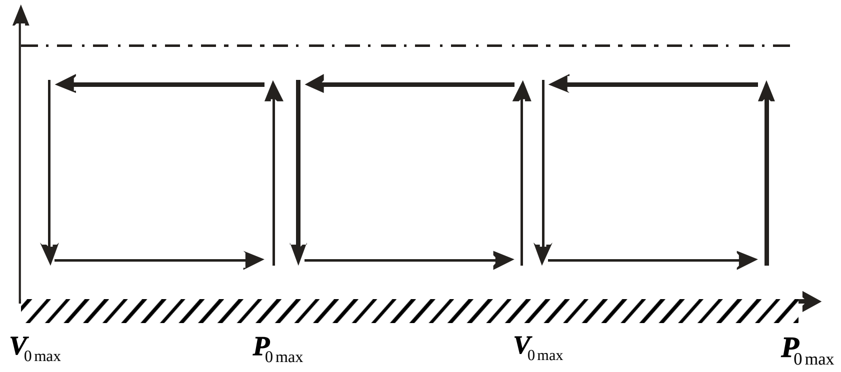

Fig.1. The acoustic currents in the tube (current configuration), V_{0max} - oscillatory rate; P_{max} - pressure.

We shall limit to the simplest condition:
$C = C_r$ (surface) (12)
$C = C_\infty$ (middle)

In the sonic field, the movement rate of the middle particles consists in the rate of consecutive movement, V_k^*, which always exists in the absence of the sound, the movement rate of the oscillations, V_{zv}, and the rate of the acoustic flows.

Because the influence of the sonic sound V_k^*, does not interest, it can be reflected, and the influence V_{zv} over the diffusion process in insignificant.

Therefore, the progress of the calculus of the diffusion processes acceleration in the sonic field consists in the necessity of solving (11) under the condition (12), understanding (concluding) that the movement rate of the middle particles is the rate of the acoustic flows. In the static sonic wave, in the rigid wall on a plane surface which is situated on the propagation direction of the wave, the turbionar acoustic currents are produced, currents that are periodically repeated. The tangent at U_x and the U_y that form (compose) the currents rate are given through the following equations:

$$U_x = -\frac{V_0^2 \sin 2kx}{8C_0}\left[e^{-\beta y}\left(4\sin\beta y + 2\sin\beta y + 1\right) - 3\right]$$

$$U_y = -\frac{2kV_0^2 \cos 2kx}{8C_0}\; e^{-\beta y} \quad \sin\beta y + 3\cos\beta y + \frac{1}{2}e^{-\beta y} \quad + 3\beta y \tag{13}$$

where: K – wave number, equal with ω/Co; β=√ω/2ν; x,y – the tangential and normal coordinates of the phases separation surface.

The rate of the acoustic currents, according to Reily corresponds to the experimental data for the small comparative levels of the sonic pressure.

If they are big, meaning:

$$V_0 > \sqrt{\nu\omega} \tag{14}$$

then the rate of the acoustic flows will be one level bigger and can be expressed:

$$U_x=2,7*10^{-4}V_0^2 \sin 2Kx\,(1-e^{-\beta y}) \tag{15}$$

The acoustic flows, appeared in the cylinder and sphere with radius a, namely, over them the sonic wave falls, are given by the following relations:

$$U_0 = \frac{3}{2}\frac{V_0^2}{\omega a}\sin 2\theta \quad e^{-\beta y} \quad \frac{2\beta y}{11}\sin\beta y - e^{-\beta y} \quad + 1 \tag{16}$$

$$\text{for } y \to \infty \qquad U_0=3/2*V_0^2/\omega_a*\sin 2\theta \tag{17}$$

where the signification of the θ and y are presented in fig.2.

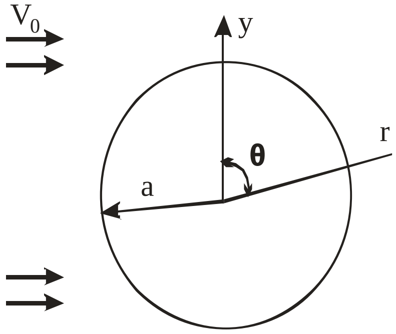

Fig.2. The signification of the θ and y.

4. Conclusions

Using the above data we can solve the mass transfer of the substance with the sphere radius, a, in sonic field.

In order to solve this problem, the diffusion equation is to be resolving (9) with condition (10), where we can consider as a movement rate of the middle the rate of the acoustic flows. Which appear around the middle.

The results can be written as follows:

$$N_{U_a} = \frac{BV_0}{\sqrt{\omega D}} \qquad (18)$$

where: B-is a constant, B = 1.7 or 2.4;

The value 2.4 gives a better concordance with the experimental results.

At the same time, the influence of the ultrasounds over the diffusion process of the gas from liquid is used at the acoustic release. The release mechanism means that under the influence of the ultrasounds over the liquid, the dissolved gas dissipates in gas and this rise at the surface and in this way the liquid is relieved.

References

[**1**]. **W.L.Nyborg**, ***Acoustic Streaming Physical Acoustics***, 2 part B, 1965

[2]. T.Tarnoczy, G.Thomas, *Uber die diffusionss teipernde Wirkung des Ultraschalts*. Elektromedizian 5,4,222,1960

[**3**]. **D.Dragan, *Ultrasunete de mari energii***, Editura Academiei, Bucuresti, 1983.

[4]. Alexandru and anothers – “***Intensifiacarea transformarilor la calirea otelurilor in amp ultrasonor***” – Metalurgia nr.10 – 1987

[5]. Dieter G.jr. – “***Metalurgie mecanica***” – Ed. Tehnica, Bucuresti 1970

[6]. Otto Aezel, Corneliu Bozan – “***Dislocatiile si frecarea intena la metale***” – Ed. Facultatii Timisoara, 1974

THE ANNALS OF “DUNAREA DE JOS” UNIVERSITY OF GALATI.
FASCICLE IX. METALLURGY AND MATERIALS SCIENCE
N^{0}. 2 – 2007, ISSN 1453 – 083X

STUDIES CONCERNING ENERGETIC CONSUMPTION OF SOME HEATING EQUIPMENTS WITH RESISTORS

Alina MINEA, Roxana CARABET
Tehnical University „Gheorghe Asachi” Iasi
email: aminea@tuiasi.ro

ABSTRACT

In order to increase the resistance of aluminium alloys a complex heat treatment is usually performed. Therefore, we must consider the reaction time between aluminium alloys and furnace atmosphera. These atmospheres contain oxygene and nytrogene. Aluminium is an active element, therefore the oxidation is a very fast one.From the experiments made, the oxidation kinetics of aluminum alloys proves to depend on many factors, such as: temperature, alloy activity, chemical saturation and partial pressure of oxygen in gaseous phase. For a heat treatment process, the oxidation time became heating time. The furnace design provides to minimize the losses by untights and to realise a uniform air stream in the furnace chamber. These facts are going to minimise the oxide layer of the treated parts. For the studied furnaces, used at aluminum alloys heat treating, the functioning curves were first made. It must be mentioned that all experiments were made in different days, in order to assure the same pre-heating conditions for the equipment. As a conclusion, studying the heat chamber geometry is a step forward to a new concept of heat treatment furnaces. This idea leads to important economical effects, on a long term, for a constant development of the industry.

KEYWORDS: Aluminum, Energy, Temperature, Consumptions

1. Introduction

The evolution of heating methods has an important role on the quantitative and qualitative development of heat treatment technologies. This evolution is decisive for the charge heating speed, for the value of energetic consumption of the process and for the technological effects subsequently obtained. These things can be achieved by the functional-constructive improvement of the furnaces used in aluminum alloys heat treatment taking into account the following aspects:

-Reduction of energetic consumption and basic materials per product unit through the optimization of work chamber construction,

-Increase of labor productivity and furnace reliability by using some new leading systems with high automation degree of the heat treatment furnace,

-Reduction of service personnel that is to be implied in heat treatment technology process and in furnace exploitation,

-Cost reduction of the furnace and of its dimensions in comparison with the existent equipments in country by using adequate refractory and thermo-insulated materials.

1.1. Methodology

Work methodology includes the next stages:

- the adoption of heat treatment technology for the used aluminum alloys;
- the election of the used installations and devices for the structural analysis of the chosen aluminum alloys;
- the election of necessary equipments and installations for making the heat treatment cycles of the chosen aluminum alloys;
- the management of the experiment and analytical interpretation of the results.

1.2.Adoption of heating technology of the used alloys

The two chosen alloys - AlCu2,5Mg and AlCu4Mg1 are Al-Cu-Mg ternary alloys used widely in machines manufacturing. The chemical composition of the alloys according to SR EN 573-3 is presented in table 1.

Table 1**.**Chemical composition of the used aluminum alloys

Alloy	**Chemical composition, %**							
	Cu	**Mg**	**Mn**	**Si**	**Fe**	**Zn**	**Ni**	**Ti**
AlCu4Mg1	3,8-4,9	1,2-1,8	0,3-0,9	0,2	0,3	0,25	-	0,15
AlCu2,5Mg	2,2-3,0	0,2-0,5	0,2	0,8	0,7	0,25	-	-

The pieces that make the charge have cylindrical geometry and the dimensions of the pieces depending on the type of the alloy are included in table 2.

Table 2.

	d_0, mm	L_0, mm
AlCu4Mg1	15	150
AlCu2,5Mg	20	104

1.3. Election of the equipments necessary to heat cycles

The heating of the pieces and blanks of aluminum alloys for quenching it will be made in electric furnaces with air-forced circulation. The adjustment and control of heating mechanisms temperature must be made with automate auto registration apparatus, with a better precision class, so that measurement precision stands in limits of ±3°C. The control and adjustment of control apparatus must be made in the moment where in workspace exist the maximum temperatures.

The researches will be directed towards the research of energetic consumption of electric furnaces that function in mean temperatures (500 - 600°C). Thus, to study the energetic consumption we chose a classical heat treatment furnace;

The classical heat treatment furnace is presented in figure 1 and has the characteristics: rapidly cooling and heating possibility, small weight and compact design; the door opens vertically; programming and control system in 8 segments for the exact adjustment of temperature; digital setting of heating curve (temperature-time) and digital indicating temperature of workspace.

Each program can have three stages that need each three parameters: heating speed, heating time or holding time.

Technical and functional characteristics of this heating device are:

- intenseness 1800 W, tension 220V c.a, 50 Hz
- programming possibility or some complex treatment programs, each program includes until 8 grades and 8 holding levels.
- Possibility of election and adjustment of the main parameters of the treatment in large limits:
  - heating speed: 0.1…400 C/s
  - holding periods on level: 0,0….999,9 h
- Possibility of using neutral treatment mediums (Ar , N_2)

Fig. 1. Unit picture of the classical furnace

Through the controller can be connected more programs or repeated the same cycle under identical conditions more than once.

2. Experimental and analytic interpretation of the results

To achieve mathematical simulation is necessary to program the experiment.

This supposes to:

- Establish the necessary and adequate number of experiences and realization conditions;
- Determination of regression equation which represents the process model;
- Determination of the optimum value for the achieved process.

Hereby, for each variable it determines the basic levels and variation intervals.

By adding the variation level to basic level the superior level is obtained and by its subtraction is obtained the inferior level of the variable.

The election of variation interval must be done so that it has as accurate values as possible from functional point of view.

A first step is the establishment of basic levels and variation intervals.

The interpretation of experimental results consist in determining some experimental variation curves of charge weight according to the energetic consumption of the equipment; the interpretation of experimental results will be finalized through the determination of some analytical equations that describe the curves experimentally obtained.

2.1. Management of the experiment

For simulating the final heat treatment process of AlCu2,5Mg aluminum alloy it is necessary a minimum number of three experiments according to 3^k factorial experiment theory previously presented. In this case k = 1 particularly it is a variation factor: heating time.

There are presented in table 3. the variation interval and basic level for programming the experiment, and to determine the energetic consumption for the two alloys.

Table 3. Programmed experiment

Factor	weight, g
Basic level	500
Variation interval	200
Superior level (+1)	700
Inferior level (-1)	300

With the help of the obtained experimental results it determines the energetic consumption for each charge. I mention that heating temperatures, holding times and cooling conditions are similar for each experiment and variable is the weight of the charge.

2.2. Experimental results for AlCu2,5Mg aluminum alloy

The experiment made in different days holding the initial heating conditions for equipments and for charges.

The experimental results for AlCu2,5Mg alloy are presented in tables 4 and 5.

Table 4. Temperature variation for classical furnace for AlCu2,5Mg alloy

Time, sec.	Temperature variation, °C					
	0	100 g	300 g	500 g	700 g	900 g
0	19	21	23	27	25	22
60	33	40	35	40	45	32
120	63	61	63	69	76	60
180	97	94	96	104	109	93
240	133	130	133	138	144	127
300	168	165	163	171	178	160
360	201	198	196	203	209	192
420	240	229	227	234	241	223
480	267	259	255	263	271	253
540	297	288	283	291	299	281
600	325	315	308	317	322	307
660	352	341	333	341	346	331
720	378	365	357	364	369	354
780	402	387	379	387	390	375
840	425	409	399	406	410	395
900	448	430	419	425	429	414
960	468	450	438	444	446	432
1020	487	469	457	461	464	449
1080	507	487	473	477	480	465
1140	525	505	492	493	495	481
1200		525	506	508	511	495
1260			525	525	525	509

Table 5. Variation of heating time and total consummated energy at heating depending on the weight of the charge for AlCu2,5Mg alloy

Weight, g	**Classic**	
	Total heating time , s	**Total energy, Wh**
0 g	1134	567
100 g	1200	600
300 g	1256	628
500 g	1256	628
700 g	1260	630
900 g	1319	659,5

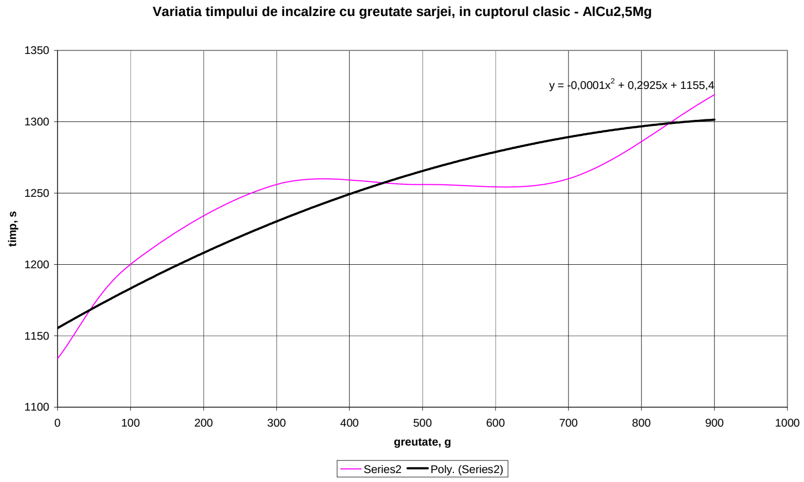

Fig. 2. The diagram of heating time variation with charge weight from AlCu2,5Mg, in classic furnace.

Total energy consummated in heating was calculate taking into account the function time at maximum power with the relation:

E = P t.

2.3. The experimental results for Cu4Mg1 aluminum alloy

The experimental results for AlCu4Mg1 alloy are presented in table 6.

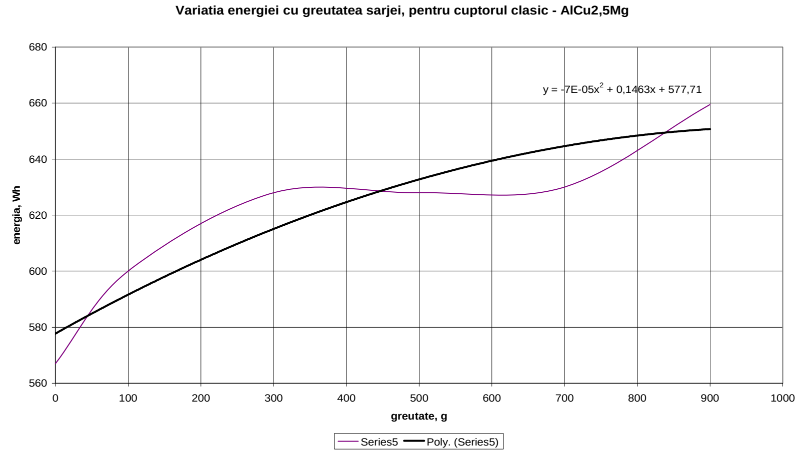

Fig. 3. The diagram of consummated energy variation with charge weight of AlCu2,5Mg, in classic furnace.

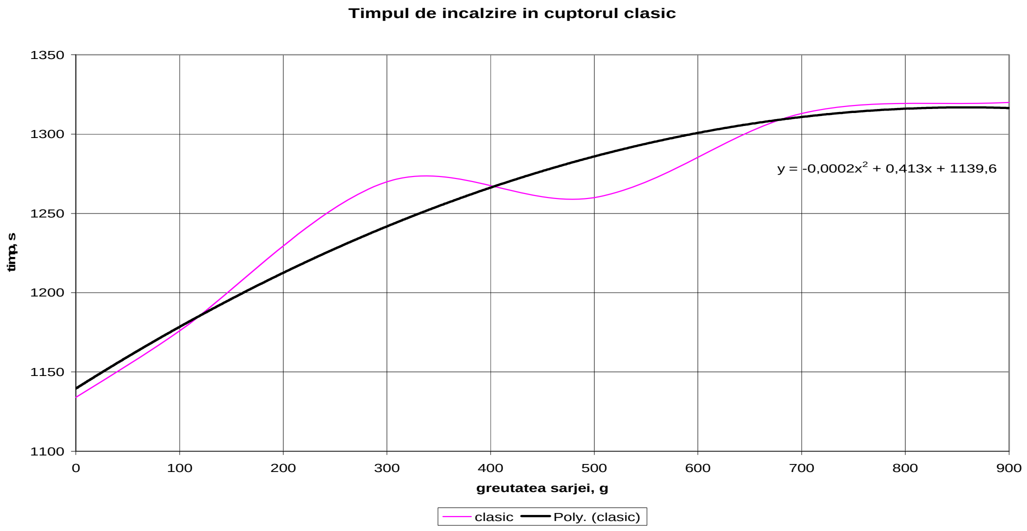

Fig. 4. The variation diagram of heating time with weight charge of AlCu4Mg1, in classic furnace

Table 6. The variation of total heating time and consummated energy according to charge weight for AlCu4Mg1 alloy.

Weight, g	Classic	
	Total time, s	Total energy, Wh
0 g	1134	567
100 g	1176	588
300 g	1270	635
500 g	1260	630
700 g	1313	656.5
900 g	1320	660

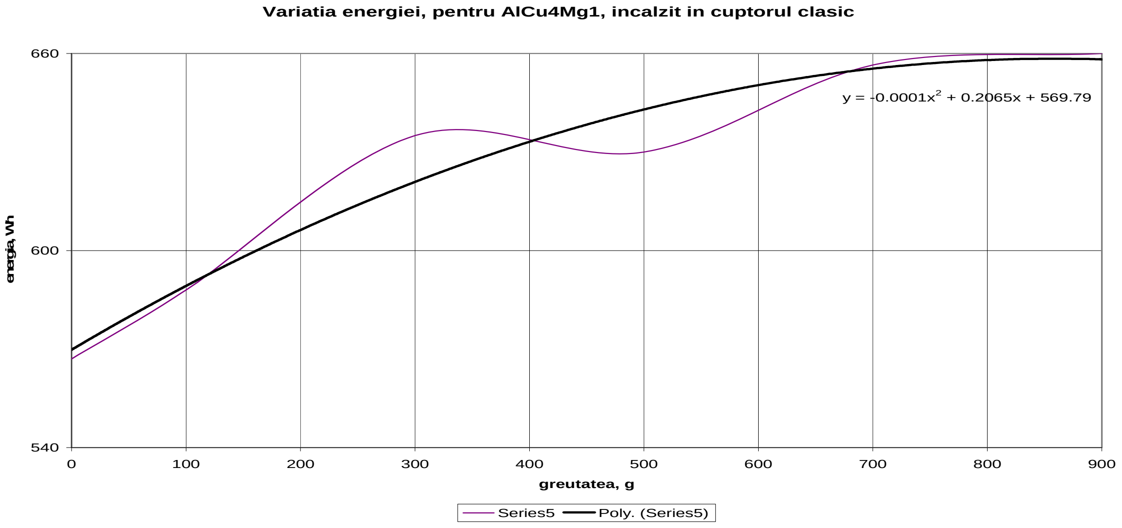

Fig. 5. The variation diagram of consummated energy with charge weight of AlCu4Mg1, in classic furnace

3. Conclusions

The chosen research methodology permits effectuation of the experiments for studying the energetic consumption of chosen heating equipments through:

- The correct adoption of a heat treatment technology for the study of the two different aluminum alloys;
- The election of some performing furnaces to control heating process for the made heating operations;
- The election of some modern installations to determine the exact chemical composition of the studied materials;
- The management of the experiment and possibility of analytical interpretations of the results.

After the experiment were made it was remarked the increase of energetic consumption respectively heating time once with the increase of charge weight. The charge weight was varied with 100g.

At the same time, there were experimentally found out the variation equations of heating time until a certain temperature with charge weight; the variation equations of the consumed energy with charge weight.

Thus, from the analysis of experimental data, there are noticed bigger heating times for AlCu2,5Mg alloy.

References

[1] P. A. Pavlov, ***Heat and Mass Transfer under the Conditions of Rapid Heating***, HeatTransRes.no.1-2/2005, pp.5

[2] Minea Alina Adriana, ***Contributii privind imbunatatirea constructiv functionala a cuptoarelor utilizate la tratamentul termic al aliajelor de aluminiu***,teza de doctorat, 2000

[3] Minea,A.A.,*Transfer de caldura si instalatii termice*, Editura Tehnica, Stiintifica si Didactica Cermi Iasi, 2003

[4] Minea, A.A., Dima A.,*Transfer de masa si energie*, Editura Tehnica,Stiintifica si Didactica Cermi Iasi, 2005

[5] Janna, W.S., *Engineering Heat Transfer*, Second Edition, CRC Press LLC, 2000

[6] Avram, N., Predescu, C. – ***Bazele teoretice ale agregatelor termotehnologice din industria materialelor metalice***, E. Printech, 2001

[7] Minea, A.A. - ***Studii privind gazodinamica cuptoarelor industriale***, Buletinul I P Iaşi, 1999, tomul XLV(IL), fasc. 1-2, p. 29-33

[8] Minea, A.A., Minea, O. - ***Studii privind determinarea geometriei camerei de lucru a unui cuptor de tratament termic pentru temperaturi joase***, Buletinul I P Iaşi, 1999, tomul XLV(IL), fasc. 1-2, p. 22-29

[9] Dima, A., Popescu, R., Vizureanu, P., Minea, A.A. - ***Cuptoare şi instalaţii de încălzire, vol. 2 – Elemente de proiectare asistată de calculator a cuptoarelor cu combustie*** , Ed. Sedcom Libris, Iaşi, 1997.

THE ANNALS OF “DUNAREA DE JOS” UNIVERSITY OF GALATI.
FASCICLE IX. METALLURGY AND MATERIALS SCIENCE
N^0. 2 – 2007, ISSN 1453 – 083X

BEHAVIOUR AT NITRIDING IN FLUIDIZED LAYER OF AUSTENITIC STAINLESS STEELS AT THE TEMPERATURE OF 1050°C

Ovidiu DIMA
“Dunarea de Jos” University of Galati
email: ovidiu.dima@ugal.ro

ABSTRACT

Nitriding at low temperatures, 450-500^{o}C of austenic stainless steels lead to the obtaining of the tough layers over 1000 HV$_{005}$ but having thicknesses of tenths of microns. Moreover, nitriding at 500ºC has determined the obtaining of layers of combinations with carbonitrades that caused a severe decrease of corrosion resistance. Nitriding at 1050ºC with an enriched nitrogen austenitic diffusion structure. The nitrogen concentration ensures, by the increase of the diffusion speed, a high layer depth of millimeter tenths,under the saturation limit lead to a reduced strength down to 500 HV$_{005}$. The nitrated layer has displayed good properties of corrosion resistance and a twofold increase of the abrasive wear strength, which recommend the treatment for numerous practical applications.

KEYWORDS: Austenite, nitriding, corrosion, abrasion

1.Introduction

By nitriding we want to improve the strength properties, mainly the superficial strength in order to ensure an abrasion resistance of the austenitic stainless steels. Such steels are characterized by a good corrosion resistance but the strength during solution tempering, the usual delivery and usage condition is low, below 200 HV$_5$.

Nitriding must ensure the formation of an improved strength superficial layer but also of a structure that should ensure the conservation of the corrosion resistance properties.

Nitriding at low temperatures of 450-500ºC in fluidized layer has lead to the obtaining of superficial layers with strength over 1000 HV$_{005}$. Strength is higher in the case of nitriding at 500ºC and over this temperature due to the formation of the layer of combinations made of iron, chromium and other elements nitrates, with high strengths. In this case, yet, the corrosion resistance of the steels has been strongly affected. In the case of nitriding at 450ºC in fluidized layer and below this temperature there have been obtained strengths of somehow lower strengths, with a little over 1000 HV$_{005}$, the superficial layer being composed of solid austenite solution enriched with nitrogen and fine separations of chromium nitrates. In this case, the mono phase austenitic layer displays good corrosion resistance properties comparable with those of the original materials or even better. Yet, in the conditions of low temperature nitriding, the nitrated layer depth is very low, of only a couple of tenths of microns, the higher the treatment temperature is higher.

In order to obtain high depths nitrated layers in the conditions of treatment times of 3-4 hours as well as in the case of low temperature nitrading, we considered necessary the testing of the austenitic stainless steels at high temperature nitrading.

For the high temperature nitrading nitrogen was used as active atmosphere. Until 900ºC, the nitrogen atmosphere represents a neutral protection atmosphere. Over 900ºC, nitrogen becomes active due to the thermal dissociation. Envisaging fact that in the case of the austenitic stainless steels, the temperatures used for austenizing for the purpose of solution dipping tempering range between 1050-1150ºC, we opted for the temperature of 1050ºC. The temperature is on the lower side of the range and satisfies the condition of nitrogen dissociation and in the same time limits the tendency of excessive granulation increase, with effects on the mechanical properties but also corrosion resistance.

For a coherent and homogenous research, the treatment has been accomplished also in fluidized layer. The nitrogen fluidizing trial at high temperatures proved to be improper, experiencing swabbing and channel formation caused by the unfavourable thermal conditions of nitrogen and mainly due to the low fluidity of the same. The improvement of the fluidizing characteristics has been obtained by adding 30% of NH3, which, by dissociation, offers hydrogen to the atmosphere, a gas with proper thermophysical properties and good fluidification.

For the research we used samples of 6 austenitic stainless steel CrNi and CrNiMo whose chemistry is presented in Table 1.

Table 1

Steel code	Related mark SR:EN 10283-98	% C	% Mn	% Si	% Cu	% Cr	% Ni	% Mo	% Ti	% V
1	X2CrNi18.8	0,12	1,24	1,64	0,06	23,2	9,8	0,11	0,01	0,02
2	X6CrNi18.10	0,06	1,55	0,65	0,08	17,1	9,3	0,05	0,60	
3	X2CrNi18.9	0,03	1,27	0,42	0,19	18,9	8,95	0,15	0,01	0,02
4	X2CrNiMo17.11.2	0,02	2,06	0,78	0,27	20,0	8,8	2,7	0,03	0,03
5	X6CrNiMoTi17.12.2	0,045	0,96	0,54	0,16	18,1	11,6	2,04	0,32	
6	X1CrNiMoCu20.18.7	0,02	1,12	0,41	0,70	20,1	18,1	6,1		0,2

The samples were prepared from sheets having the dimensions of 60x20x3mm, adjusted by grinding for the rounding of the edges and then with abrasive paper with 400 granulation pointage on all surfaces. Before treatment, the samples have been washed, degreased and dried, then nitraded in fluidized layer at the temperature of 1050ºC, being maintained for 1, 2, 3 hours.

From the nitrated samples have been cut for the strength trials and structure analysis. These have been embedded in resin, adjusted, grinded on metallographic paper and polished with diamond paste.

2. Analysis of the samples nitrated at 1050ºC

For the highlighting of the nitrated layer, layer depth and nitriding process intensity Vickers HV_{005} strength trials have been done, with a pressure load of 0.50N. The results of the trials, strength variation on the nitrated layer depth are presented in figures 1.

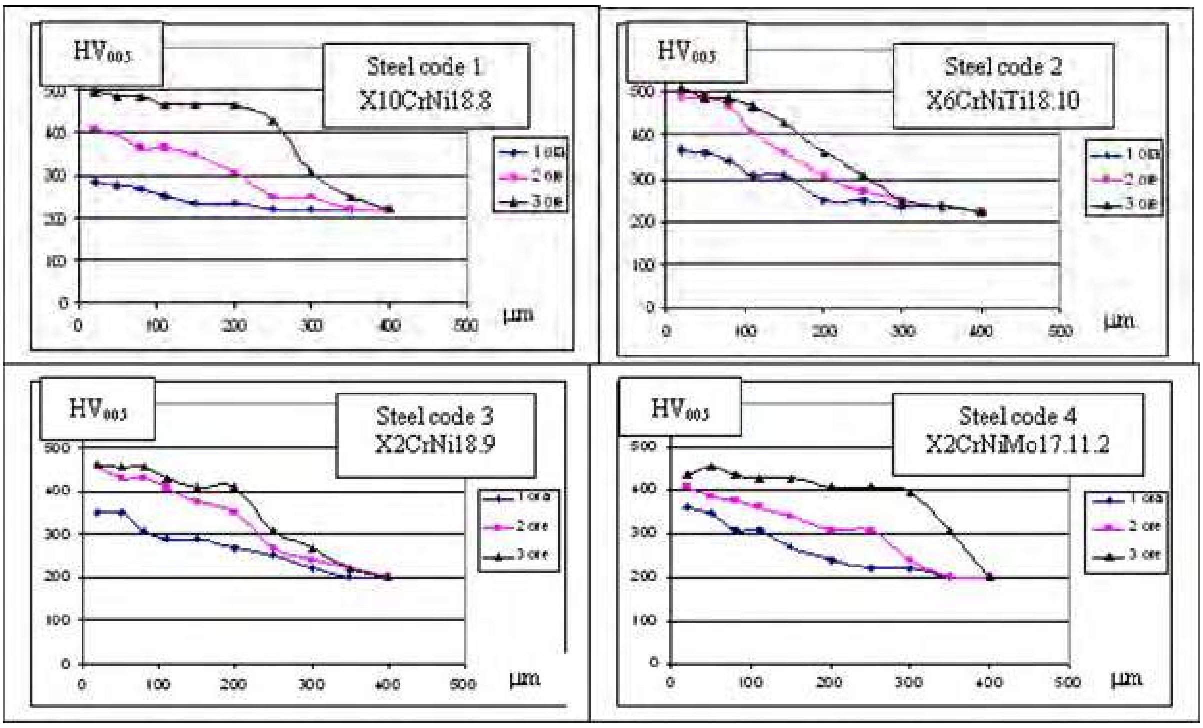

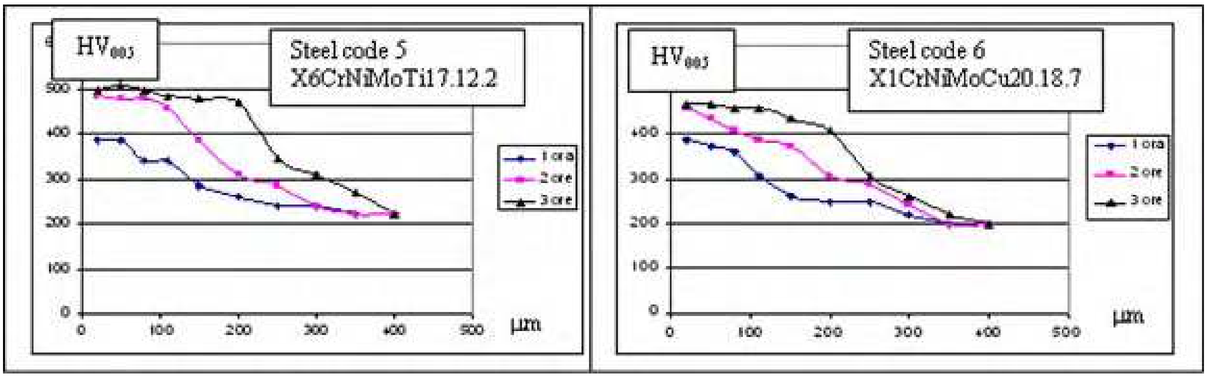

Fig. 1. Strength variation over the nitrogen enriched layer

The analysis of the strength trials show that the maximum strengths registered after the nitriding treatment at high temperature for 3 hours, range between 450HV_{005} and 500HV_{005}

Higher values, even over 500 HV_{005} occur in the case of high carbon steels, with or without stabilizing elements, titan and niobium, namely the steels coded 1, 2 and 5 and a little bit lower in the case of steels coded 2, 3 and 6. Also, the depth of the nitrated layer estimated on the basis of the strength variation curves is presented in table 2 for each material. The analysis of the values show that the highest depth is recorded at the steel code 4, where the ratio E_{Cr}/E_{Ni} has the highest value. One cannot say that this rule is valid for all materials as the process is influenced by many factors. The values of the nitrated layer depths are up to 10 times higher than in the case of low temperature nitrated steels.

Table 2

Steel code	**E_{Cr}/E_{Ni}**	**Layer thickness**	**Hardness HV_{005}**
		[µm]	**[x10 MPa]**
1-X2CrNi18.8	1,78	275	498
2-X6CrNi18.10	1,26	190	508
3-X2CrNi18.9	1,95	250	458
4-X2CrNiMo17.11.2	2,23	340	435
5-X6CrNiMoTi17.12.2	1,48	250	498
6-X1CrNiMoCu20.18.7	1,40	240	468

3. Analysis of the samples nitrated at 1050°C

The analysis of the samples nitrated at 1050°C does not show the presence of any distinct presence superficial layer, figure 2. The lower strength recorded indicates a lower nitrogen concentration, far from the saturation limit.

X-ray analysis indicates in the diffractogram from figure 3 the presence of the droplets for the diffraction angles of the γ_N phase – austenite enriched in nitrogen and γ_{Fe}– the original austenitic solid solution.

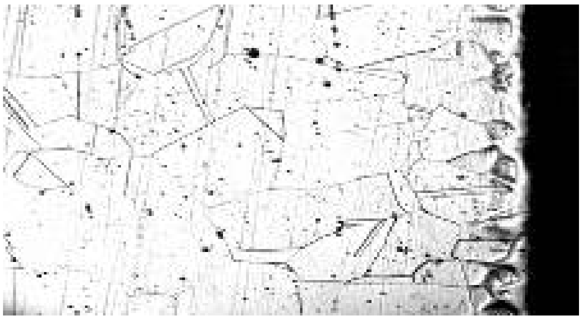

Fig. 2. Microstructure of steel code 4 X2CrNiMo17.11.2. nitrated at 1050°C.x400

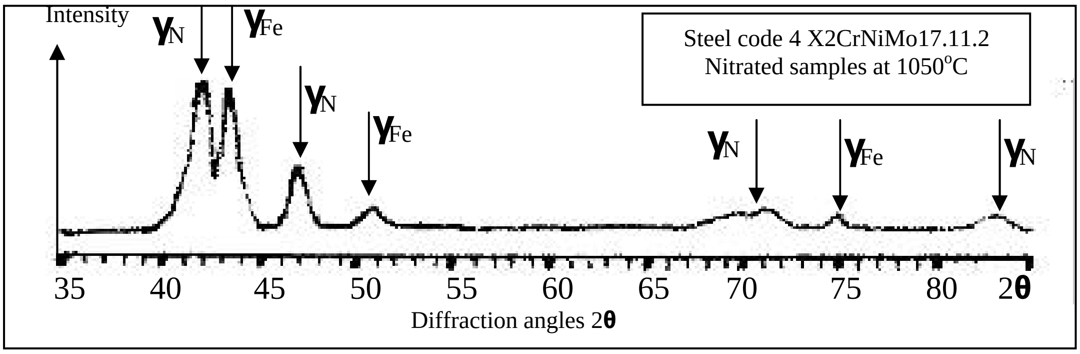

Fig. 3. Diffractogram of the nitrated samples at 1050 ºC, code 4 X2CrNiMo17.11.2.

4. The analysis of corrosion behaviour in saline mist of the nitrated steel at 1050ºC

In figure 4 there are presented comparatively the results of the corrosion resistance in saline mist STAS 9229-95 for the samples nitrated at 1050ºC and the initial samples over 300 hours of weighing every 100 hours.

The analysis of the results shows a similar behaviour of the materials at the corrosion in saline mist, mass losses and average corrosion speeds calculated being very close. In figure 5 there are presented comparatively the average corrosion speeds in saline mist for all six materials tested.

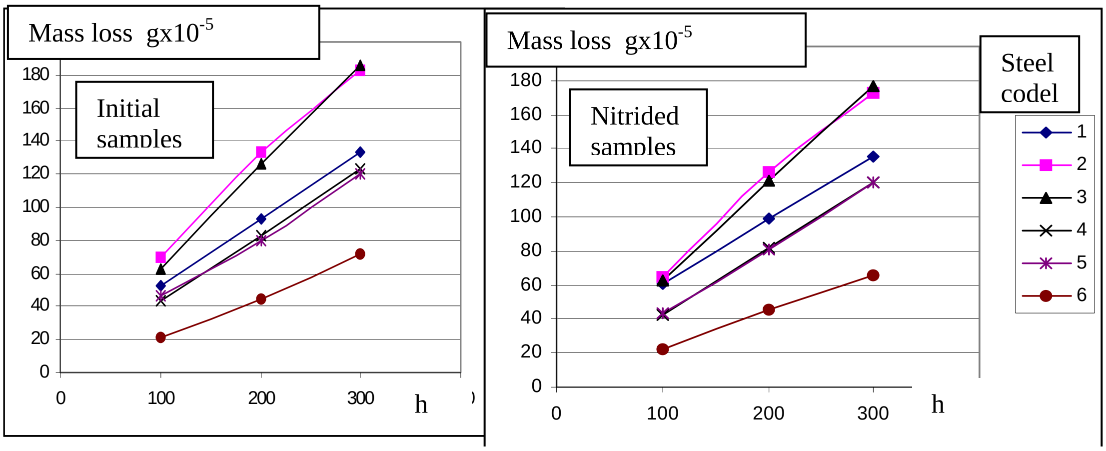

Fig. 4. Variation of mass losses in time at the corrosion in saline mist for the original samples and those nitrated at 1050ºC.

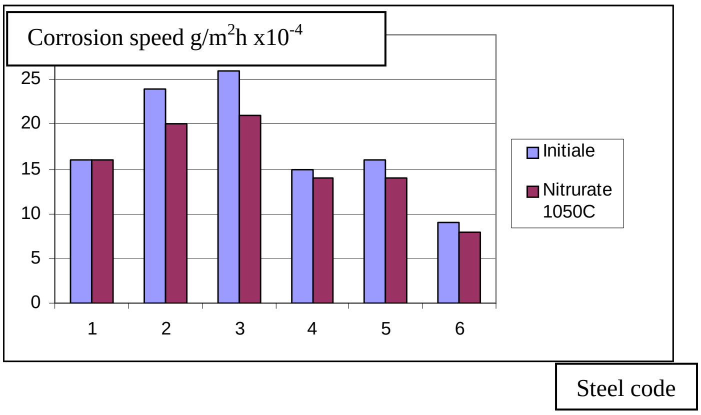

Fig. 5. Average corrosion speeds in saline mist for the original materials and those nitrated at 1050ºC

As expected, having in view the fact that the structure of the material after treatment remained mono phase, austenitic, the corrosion strength has maintained, the materials matching the ***Perfectly resistant*** material group, namely: steels code 1, 2, 3, 4, 5 class two with merit note 1.2 and steel code 6 class one with merit note 1.1. Even a slight decrease of the average corrosion speed is manifest.The high potential dynamic curves for these materials nitrated at 1050^{o}C, in comparison with the original materials confirms the maintaining and even the improvement of the corrosion behaviour by this nitrating. In figure 6 we present comparatively the polarization curves for the steel code 4 - X2CrNiMo17.11.2 in the initial stage and after nitrading at 1050^{o}C.

The analysis of these polarization curves sow a slight extension of the passive domain and its shifting towards more electropositive values, and also a slight reduction of the corrosion current in the passive domain.

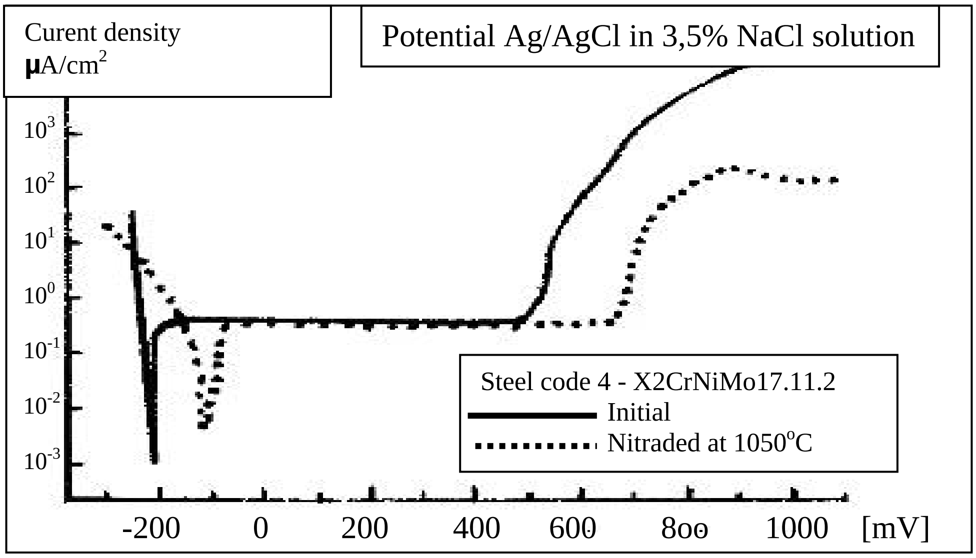

Fig. 6. The potential dynamic curves traced for the original materials and those nitrated at 1050^{o}C of steel code 4 - X2CrNiMo17.11.2

5. Analysis of the abrasive wearing strength of the steels nitrated at 1050^{o}C

The results of the abrasive wearing tests STAS 9639-81, using a friction coupling abrasive disk-pin, are presented in tab. 3. We mention that the working parameters of the trial remained the same as in the case of the trials performed before.

Tabelul 3

Steel code	**Initial samples**		**Nitraded samples at 1050^{o}C**		
	Hardness HV_{005}	**Abrasive wear**	**Layer depth**	**Hardness HV_{005}**	**Abrasive wear**
	x10 MPa	g	μm	x10 MPa	g
1-X2CrNi18.8	198	0,0062	275	498	0,0031
2-X6CrNi18.10	202	0,0065	190	508	0,0030
3-X2CrNi18.9	188	0,0065	250	458	0,0036
4-X2CrNiMo17.11.2	180	0,0069	340	435	0,0039
5-X6CrNiMoTi17.12.2	204	0,0064	250	498	0,0032
6-X1CrNiMoCu20.18.7	182	0,0071	240	468	0,0035

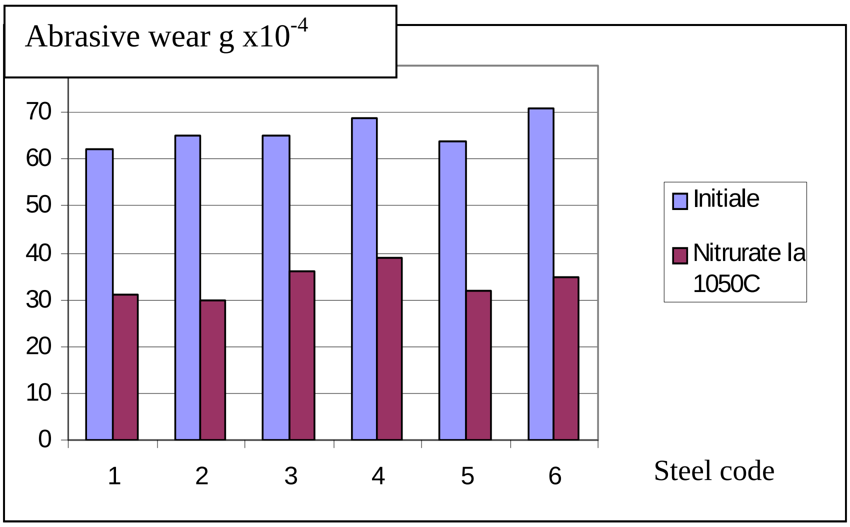

Fig. 7. ***Behaviour at wearing of the samples nitrated at 1050ºC comparatively with the initial ones.***

In figure 7 there are presented comparatively the mass losses due to abrasion for all six materials both in initial state as well as nitrated at 1050ºC in fluidized layer. From the analysis of the results an increase of the wearing strength of almost 2 times for all analyzed materials.

6. Conclusions

Nitrading in fluidized layer at high temperature of 1050ºC leads to the obtaining of layers with strength of around $500HV_{005}$ with a fairly big thickness of tenths of millimeters in 3 hours of treatment. The layer has a good corrosion resistance comparable to that of the initial materials and twofold abrasion strength.

References

[1] Berns H. ***"Case hardening of stainless steel using nitrogen"***. Ruhr University, Bochum, Germany 2002.

[2] Bard A.J., Faulkner L.R. "***Electrochemical methods, Fundamentals and aplications"*** Wiley Science Publication 2000.

[3] Dima O. Cazacu N. "***Surface hardening by nitration for some stainless austenite steel types***." Lucrarile simpozionului international "Turnatoria de la rigoarea tehnica la arta" Ed. ACADEMICA Galati 2006

[4] Dima O. Levcovici S. Georghies C. *"Aspects of nitrated layer structure for some types of austenite stainless steel" Lucrarile simpozionului international* "Turnatoria de la rigoarea tehnica la arta" Ed. ACADEMICA Galati 2006

[5] Dima O. Mitoseriu O. "***Behavior of some stainless nitrated austenite steel types to corrosion and abrasion***". Lucrarile simpozionului international "Turnatoria de la rigoarea tehnica la arta" Ed. ACADEMICA Galati 2006

[6] Fossati A., Borgioli F, Galvanetto E, Bacci T. "***Corrosion resistance properties of glow-discharge nitrided AISI316L austenitic stainless steel in NaCl solution***" Corrosion Science, Vol.48, Issues 6, June 2006, pag. 1513-1527.

[7] Gheorghies C. s.a. "***Incercarea materialelor Vol.III***" Ed. Tehnica Buc. 1994.

[8] Levcovici S.M. s.a. *"Ingineria suprafeţelor* " EDP, RA Buccureşti 2003

[9] Mirkin L.I. "***Controlul cu raze X a structurii materialelor***" Moscova 1979

[10] *STAS 9229 -1995 "Incercarea rezistenţei la coroziune in ceata salina"*

[11] *STAS 9639-1981 "Incercarea la uzura prin abraziune*"

THE ANNALS OF “DUNAREA DE JOS” UNIVERSITY OF GALATI.
FASCICLE IX. METALLURGY AND MATERIALS SCIENCE
N^0. 2 – 2007, ISSN 1453 – 083X

ANALYSIS OF STRUCTURAL COMPONENTS EXISTING IN STEEL MAKING SLAG SAMPLED FROM STEEL MAKING-CONTINUOUS CASTING FLOW SHEET

Adriana PREDA[1], Ion IVAN[2], Florin ZĂMAN[3]
[1] S.C.UZINSIDER ENGINEERING S.A. GALATI,
[2] S.C. MITTAL STEEL S.A. GALATI
[3] ICEM S.A. BUCHAREST
email: research@uzineng.ro

ABSTRACT

Hereby paper work aims to identify and analyze the structural constituents from the steel making shop slag. Therefore, slag specimens sampled from different stages of steel making-continuous casting flow sheet in Mittal Steel Galaţi: after desulphuration, after converter tapping, from LF area, after continuous casting. By X ray difractometer analysis the existing phases in investigated stages based on diffracted crystallographic planes enhanced the variation graphs of lines intensity depending on diffraction angles drawn. The results achieved together with the followed technological parameters formed the data basis in order to perform a detailed analysis about progressing of each technological stage itemized (apparition conditions, effects) setting the requirements for optimization of steel making-continuous casting flow sheet in Mittal Steel Galati ferrous metallurgy area. The recorded information corroborated by values of physical-chemical characteristics of slag investigated should allow the making and testing of several technological solutions for capitalization and recirculating of these materials.

KEYWORD: slag, recirculating, capitalization.

Introduction

The lasting development program of the Romanian ferrous metallurgy includes as major task the establishing of the intensive capitalization and recirculating technologies for steel melting shop slag.

The slag has to be suitable to conditions required by dynamic trials and/or matched with weather conditions (temperature variations) in order to be recycled in ferrous metallurgy or roads manufacturing.

This is caused by physical-mechanical characteristics like granularity, content of impurities, density, water uptake, shape of grains, impact crashing resistance, wear resistance, freezing-thawing resistance, polishing resistance, binders stickiness.

Steel melting shop slag is a dense material with rough density >3.2 g/cm^3, lasting stickiness and erosion resistance which allow it to be used in roads manufacturing for lifting layers or asphalt layers submitted to high requests.

The main performances of the steel melting shop slag characteristics against the products made of crushed stone and those from pit ballast, mostly used in roads manufacturing, are submitted in table no.1.

Magnetic separation of metallic inclusions and granularity screening are compulsory before use (chemical and mineralogical one at the same time) getting:

- a ferrous product, recyclable in ferrous metallurgy;
- 0.8 ÷ 0.16 type named disaggregated slag recyclable in both ferrous metallurgy and roads manufacturing;
- >16 mm type named non-disaggregated slag recyclable in roads manufacturing only. Slag fragments have heterogeneous texture varying from porous - alveolar up to compact, varying suitable from light to dark gray color, even brawn. Visual separation reveals a mass content with ~ 70% porous fragments and ~ 30% compact fragments.

Structural constituents were found out during laboratory tests for estimating the possibilities of using these slags.

Table 1. Characteristics of the steel melting shop slag

Characteristics	***Slag***	***Crushed ag.***	***Pit ballast ag.***
Apparent density, kg/mJ	3300-3500	2500-2700	2600
Water uptake, % from mass	0,7-1,0	<0,5	<0,5
Grain shape – shape coefficient, %	<10	<10	<10
Crushing degree, % from mass	13-17	17	21
Wear by Los Angeles machine, %	18-22	12	21
Compression strength, N/mm^2	320-350	260	250
Freezing-thawing resistance, % from mass – frost cleftness coefficient	<0,5	<0,5	<1
Bituminous earth stickiness, %	>90	>80	>80
Polishing coefficient (PSV), %	58-61	48	45

Experimental results

Four dust slag samples were exposed in CoKα radiation, sampled from the manufacturing flux of OLD1 Mittal Steel Galaţi, codified as it follows: D code - slag resulted after iron desulphuration; OLD code - slag tapped after elaboration in LD converter; LF code - slag resulted after treatment in LF plant; TC code - slag resulted after bubbling in ladle;

Phases identified by X ray difractometric analysis and their specific difractometric parameters (diffraction angles, distances between planes, Miller coefficients of crystallographic planes) are submitted in table no. 2. Phase quantitative ratio values are estimated for each sample. Graphical representation of structural constituents identified in samples (lines intensity depending on diffraction angles) may be seen in fig. 1÷4.

Table Difractometric parameters of analyzed samples

Sample code	Identified phases	Phase quantitative report [%]	Miller coefficients of crystallographic planes (hkl)	Crystallographic system
D	$Ca_3Si_2O_7$ rankinit	40,3	(202); (112); (221); (121); (320); (124); (115);	M
	CaC_2	7,7	(101); (110); (111);	T
	Fe_2O_3	18,7	(112); (101); (202); (123); (224); (202); (134); (231);	R
	Feα	21,0	(110); (200); (211); (220);	C.V.C.
	MgO	12,3	(111); (200); (220); (400);	C.C.
OLD	$2CaO\cdot Al_2O_3.SiO_2$ gehlenit	38,3	(111); (201); (211); (220); (311); (400); (323);	T
	Fe_2O_3	29,0	(101); (112); (101); (102); (202); (123); (103);(224);(134);(204); (235)	R
	CaO	22,5	(111); (200);(220); (222); (331); (400);(420);	C.F.C
	FeO	10,2	(111); (200); (220); (311); (222);	C.F.C
LF	$\beta CaO\cdot SiO_2$ wollastonit	38,0	(400); (310); (501); (203); (710); (313);(631);(322);(314);(223);(205)	Tr
	$CaO\cdot Al_2O_3.2SiO_2$ anortit	36,1	(220);(004);(204);(132); (130);(111)	Tr
	CaS	11,3	(111); (200); (220);	C.C.
	αAl_2O_3	14,6	(112); (102); (202); (123); (234); (202); (131); (134); (225);	H
TC	$2CaO\cdot Al_2O_3.SiO_2$ gehlenit	14,7	(111);(211);(212);(400);(410);(600)	T
	γCa_2SiO_4	33,9	(020); (103);(113);(121);(104);(311)	O
	αAl_2O_3	19,0	(112);(102);(202);(134); (231);(204)	H
	CaO	9,4	(200); (220); (332); (222); (400);	C.F.C
	$Al_2O_3\cdot SiO_2$	23,0	(122); (230); (042);	O

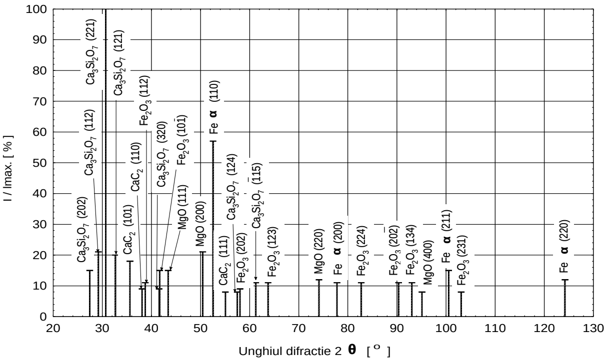

Fig.1. Diffraction lines intensity variation depending on diffraction angle. D code sample.

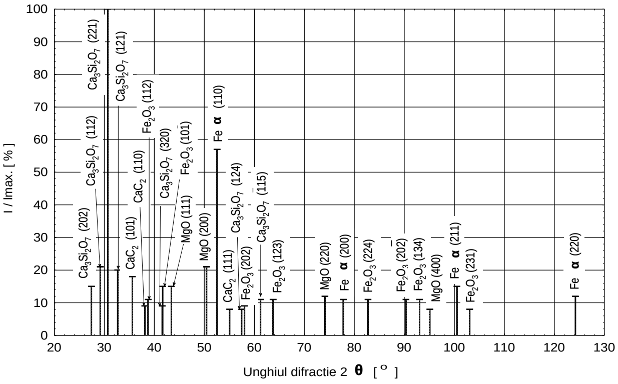

Fig.2. Diffraction lines intensity variation depending on diffraction angle. OLD code sample.

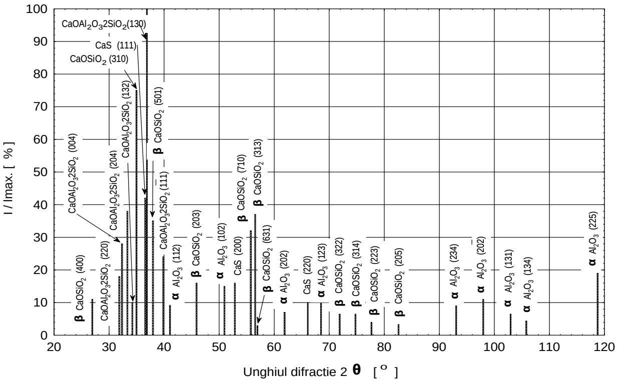

Fig.3. Diffraction lines intensity variation depending on diffraction angle. LF code sample.

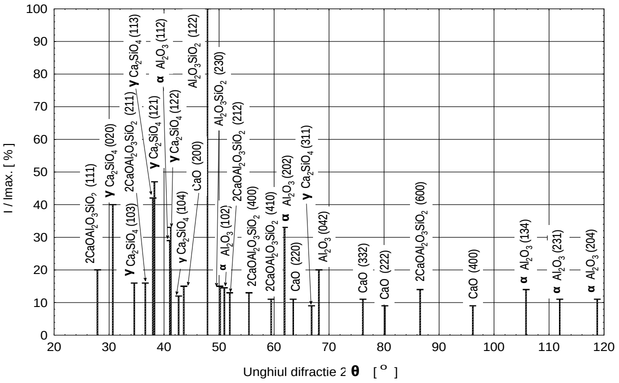

Fig. 4. Diffraction lines intensity variation depending on diffraction angle. TC code sample.

Difractometric analysis results enhanced the followings:

- **D** code slag beside the constituents specific for desulphuration plant reactions (calcium silicate $Ca_3Si_2O_7$, CaC_2, MgO) contain also ferrous as chemical element, in a non-allowed large quantitative ratio (**21,0%**) as well as Fe_2O_3 oxide in 18,7% quantitative ratio;
- **OLD** code slag has in composition, beside complex calcium silicate and calcium oxide, a significant ferrous content like FeO (10,2% quantitative ratio) and Fe_2O_3 in **29,0%** quantitative ratio;
- **LF** and **TC** code slag beside CaO, Al_2O_3 as well as simple or complex calcium and aluminum silicates **do not content ferrous oxides;**

Analyzing the results allowed characterisize the each technological stage running of the flow sheet in OLD1 Mittal Steel.

Iron presence in several of the investigated slags allowed finding out the deficiencies in the desulphuration process and converter steel making as well as stating the actions required in order to get rid of them.

Ladle iron desulphuration is considered to be an efficient process if it achieves the sulfur content decreasing up to the required values without increasing the iron content in slag. Several suitable desulphurating materials feeding in order to provide the making a slag with large sulfur absorption capacity and high flow ability to ensure the iron particles spreading in metallic bath may achieve this.

Shop steel making is achieved by combined blowing procedure (oxygen on the top side blown by lance and inert gases bubbling blown by nozzles located at the converter bottom side). This flow sheet performs as close as optimally possible when the slag is active and basic since the beginning of the oxygen blow providing the increase of iron quantity in the metallic bath.

Á Based on the information received it passed to improving the technological flows of iron desulphurating and converter steel making, in order to significantly decreasing the iron losses and experimenting the methods of exploitation the steel melting shop slag.

Conclusions

X ray difractometric analysis found out the structural constituents existing in the steel melting shop slag, bringing information required for complete featuring of these materials.

The results allowed enlarging the data basis regarding:

- The finding out of eventual deficiencies on the investigated flow sheet and stating the actions required in order to get rid of them;
- The delimitation areas of using the steel melting shop slag and testing the several receipts in order to reuse these materials;

The drawing up and testing of some technological solutions intended for valuating and recirculating the steel melting shop slag.

References

[1]. Tripşa I., Pumnea C-tin, 1981- “Steel doxidation”, Technical Publishing House, Bucureşti;
[2]. Skakov I, 1980 “Difractometric analisys methods”, Moscova;
[3]. Rău A., 1973 ”Non-metallic inclusions in steel” Technical Publishing House, Bucureşti.

THE ANNALS OF “DUNAREA DE JOS” UNIVERSITY OF GALATI.
FASCICLE IX. METALLURGY AND MATERIALS SCIENCE
N^{0}. 2 – 2007, ISSN 1453 – 083X

SEVERE PLASTIC DEFORMATION AN ADVANCED METHOD FOR NANOSTRUCTURING SHAPE MEMORY ALLOYS

Gheorghe GURAU, Carmela GURAU,
Dinel TANASE, Elena DRUGESCU
“Dunarea de Jos” University of Galati
email: gheorghe.gurau@ugal.ro

ABSTARCT

Severe plastic deformation (SPD) is an advanced plastic deformation. In this process nanostructuring metals and alloys may be produced. Nanostructured shape memory alloys are associate with a very high strength, toughness, fatigue life and wear resistance. In recent, bulk nanostructured SMA are used for medicine advanced applications and smart micro devices. In this paper we present the concept and principles SPD. There are two distinct methods: Equal Channel Angular Pressing ECAP or Equal Cannel Angular Extrusion –ECAE and High Pressure Torsion – HPT. Also we present some results about nanostructuring a hard deformable shape memory alloy using a original HPT, and a improved ECAE device.

KEYWORDS: severe plastic deformation, ECAP, HPT

1. Introduction

Herbert Gleiter presents in 1989 the concept of nano crystalline materials (ultrafine grained materials with a grain size under 100 nm) [1]. Since then this advanced material class has rapidly developed because technological and scientific importance.

Nanocrystalline materials contained extremely large fraction grains boundaries with a special atomic structure.

As a result, nanomaterials should have unusual properties. It is a very well known that grain refinement provides mechanical strength and thus can expect ultrafine grained materials to possess very high strength. Moreover, introduction of high density dislocations in SPD processed nonmetals may result in even greater hardening. In this case we have decreases ductility and can say that the strength and ductility are opposing characteristics.

Nanostructured metals show unique combination of exceptionally high strength and ductility.

Bulk nanostructured materials may be obtained in different ways: from nanopowders mixed in ball milling or mechanical alloying and compacting or by inert gas condensation.

The named methods have inconvenient like porosity or small dimensions (1 mm in thickness and 10nm in diameter).

A new approach in metallic nanomaterials processing is the plastic deformation using severe deformation degree. From the very beginning severe plastic deformation have been developed two techniques. Those techniques are – high pressure torsion (HPT) and equal channel angular pressing (ECAP) or equal chanell angular extrusion (ECAE)

1.1. Equal Channel Angular Extrusion

Equal channel angular extrusion was developed in 1980s in the former Soviet Union [2]. Method provides smallest grain size (1-10 ***μm***) with certain advantage in comparison with classic thermo-mechanical processes.

One advantage is that the method is applicable for all metallic material no mater chemicals composition, mono or polycrystalline without modification process parameters. ECAE provide de capability of produce in large bulk samples submicrometers or nanometers grain size that cannot be obtained using non conventional procedures. On the other hand ECAE may be integrated into a rolling line or wires line for log products. During the ECAE process metal billet is pressed through a die which present two channels equal in cross section and intersecting at an angle Φ (fig.1.)

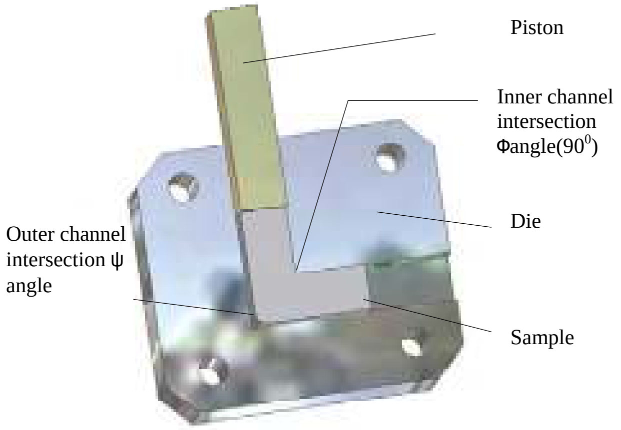

Fig.1 Equal channel extrusion dies

The billet undergoes essentially simple shear deformation but retains the same cross sectional geometry. The equal section in both channels makes possible multiple passes.

Repeated passes develop a very large deformation in bulk products. This process also leads to the formation of strong crystallographic texture in the material because a rotation of sample is possible [12](fig.2)

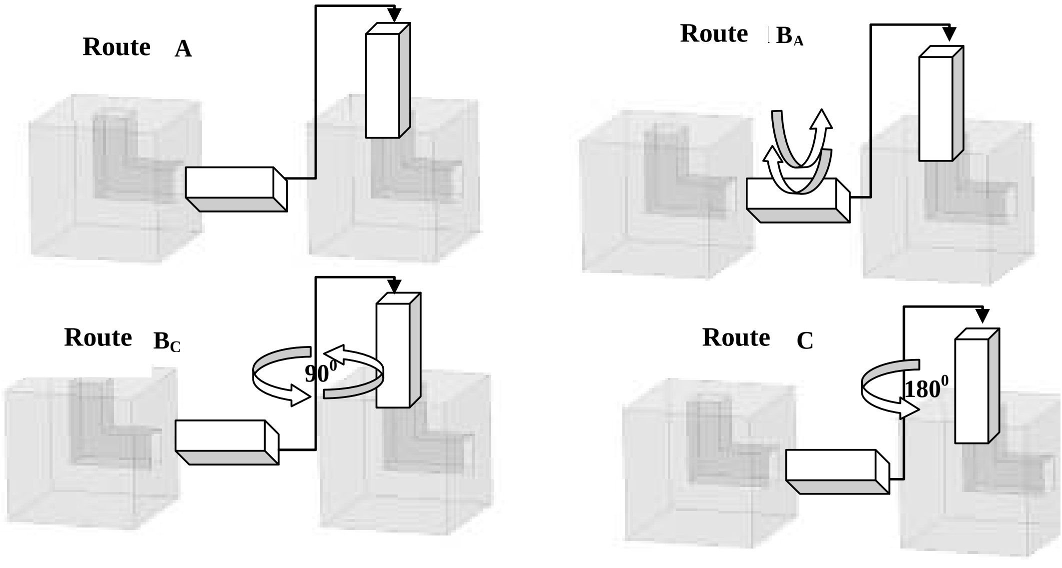

Fig.2 Different ECAE routes

The strain imposed on the sample in each deformation depend the angle Φ and also the angle Ψ, representing the outer arc of the curvature were two channels intersect (fig.3).

The corner angle Ψ is very important because the bigger the angle Ψ induce inhomogeneous metal [10] flow respectively inhomogeneous structure and properties (fig.4).

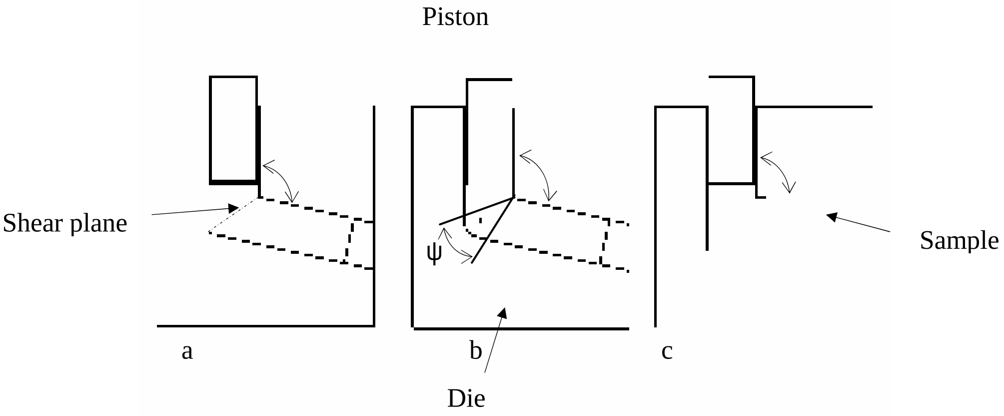

Fig.3. Schematic die with inner angle Φ > 90^0, and outer angle Ψ=0^0 (a), Φ > 90^0 and Ψ>0^0(b), Φ =90^0 and Ψ=0^0(c). [10]

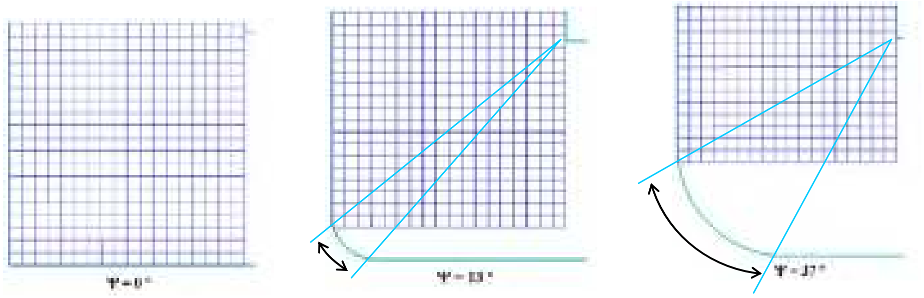

Fig.4. ECAE – various corner angles [10]

2. Experimental

2.1. A new conception ECAE device

In University of Galati, Plastic Deformation and Heat Treatment department a new ECAE device was developed. Based on scientific reports [9] these devices reduce significantly friction in the vertical channel. A Classic ECAE has four friction surfaces between device and sample. In the new method three friction surfaces was eliminated. The piston has a special form for supply the die with material without excessive friction force (fig. 5). Also in the section the piston has been eliminate the effort concentrators because a large radius was used.

Fig.5. The parts of the new ECAE die
a. piston, b. the die body, c. the die knife

2.2. A new method HPT

The HPT method involved a high pressure and a few rotations under this load. We developed a new HPT process for hard deformable materials. The news consist deformation at the high temperatures. This temperature is generated in system by friction at high piston rotations. All the process time pressure is action under piston. The HPT scheme is shown in figure 6.

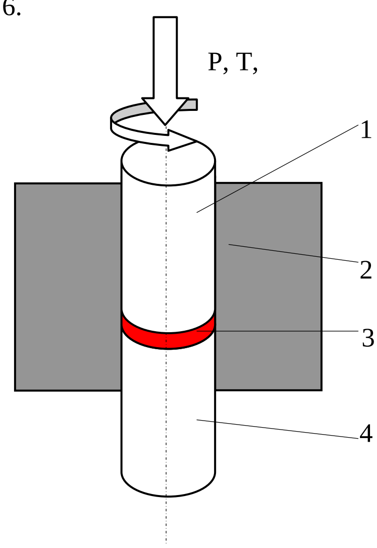

Fig. 6. HPT Scheme
1. revolving plunger, 2. container, 3. sample,
4. support plunger

3. Results and discussions

The new HPT method was applied on the shape memory alloy cooper based (Cu 12.88%wt Al 4%wt Ni). The samples used in severe deformation process were: hot extruded (Φ 4mm x 6 mm) and plates after ausforming (8mm x 8mm x 0.25mm). The structure of extruded samples was α, γ and pre martensitic forms with huge grains (fig. 7a.). The structure of plates after ausforming was typical γ' martensite (fig.7.b.).

After SPD HPT we obtained fine structures with nanometers grains size (fig.7.c)

4. Conclusions

- A new ECAE device was designed for reduce the processing force with reduce the friction between sample and die. Also the piston shape reduce the tensions concentrators.
- A new HPT method was developed and tested under hard deformable shape memory alloy.
- The nanostructure grain size was obtained.

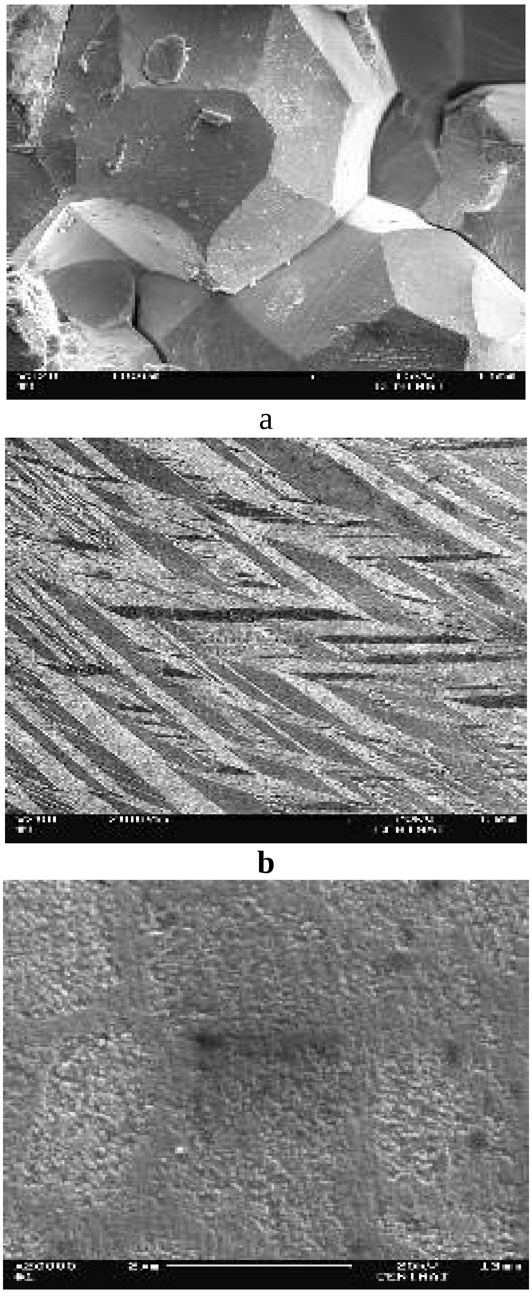
a

b

c

Fig.7. Shape memory alloy Cu 12.88%wt Al 4%wt Ni
a- hot extruded, b. quenched after hot rolling (asformed), c. nanostructured

5. References

[1]. K. Mueller a, S. Mueller b, ***Severe plastic deformation of the magnesium alloy AZ31*** Journal of Materials Processing Technology 187–188 (2007) 775–779

[2]. J.G. Li, M. Umemoto, Y. Todaka, K. Tsuchiya, ***Role of strain gradient on the formation of nanocrystalline structure produced by severe plastic deformation,*** Journal of Alloys and Compounds 434–435 (2007) 290–293

[3]. M. Hafoka, R. Pippana, ***Role of strain gradient on the formation of nanocrystalline structure produced by severe plastic deformation*** , Scripta Materialia 56 (2007) 757–760

[4]. B. Kockar a, I. Karaman a,*, A. Kulkarni a, Y. Chumlyakov b, I.V. Kireeva, ***Effect of severe ausforming via equal channel angular extrusion on the shape memory response of a NiTi alloy,*** Journal of Nuclear Materials 361 (2007) 298–305

[5]. S. Swaminathan,a T.L. Brown,b S. Chandrasekar,b T.R. McNelleya,* and W.D. Compton, ***Severe plastic deformation of copper by machining:Microstructure refinement and nanostructure evolution with strain,*** Scripta Materialia xxx (2007) xxx–xxx

[6]. M. Delince´ a, Y. Bre´chet b, J.D. Embury c, M.G.D. Geers d, P.J. Jacques a, T. Pardoen, ***Structure–property optimization of ultrafine-grained dual-phase steels using a microstructure-based strain hardening model,*** Acta Materialia 55 (2007) 2337–2350

[7]. A. Mishra , B.K. Kad , F. Gregori , M.A. Meyers ***,Microstructural evolution in copper subjected to severe plastic deformation: Experiments and analysis,*** Acta Mater 55 (2007) 13–28]

[8]. A. Concustell, J. Sort, S. Surinach, A. Gebert, J. Eckert, A.P. Zhilyaev, M.D. Baro´, ***Severe plastic deformation of a Ti-based nanocomposite alloy studied by nanoindentation,*** Intermetallics xx (2007) 1e8

[9]. J.-P. Mathieu, S. Suwas, A. Eberhardt, L.S. T´oth , P. Moll, ***A new design for equal channel angular extrusion,*** Journal of Materials Processing Technology 173 (2006) 29–33

[10]. S.C. Yoon, P. Quang, S.I. Hong, H.S. Kim, ***Die design for homogeneous plastic deformation during equal channel angular pressing,*** Journal of Materials Processing Technology 187–188 (2007) 46–50

[11]. L. Kommel, I. Hussainova, O. Volobueva, ***Microstructure and properties development of copper during severe plastic deformation,*** Materials and Design xxx (2006) xxx–xxx

[12]. Terence G. Langdon ***The principles of grain refinement in equal-channel angular pressing,*** Materials Science and Engineering A xxx (2006) xxx–xxx

THE ANNALS OF “DUNAREA DE JOS” UNIVERSITY OF GALATI.
FASCICLE IX. METALLURGY AND MATERIALS SCIENCE
N^{0}. 2 – 2007, ISSN 1453 – 083X

INTERMETALIC COPPER PHASE CHARACTERISTICS AND LINKS WITH THE GOLD SPHERE IN ALUMINA COVER SHEETS

Marius Dan BENTA, Petre Nicolae MOGAN, Georgiana DRAGUSIN
“Transilvania” University of Brasov, Romania
email: mariusbenta@yahoo.com

ABSTRACT

The time period in which the intermetalic sheet cover is developed into the gold sphere in alumina is fully known being relatively not much literature regarding the morphology ant intermetalic phases growth in the copper sphere related to the core with metal alumina. The optimisation and development of thicker copper wiring related in the linkage process(bonding process) for each application needs a intermetalic cover linkage bonding and the growth of intermetalic Au-Al phase which takes place after isothermic eldering.

This study describes the problems and aspects associated with detemining of the covering area and of the layer and a few characteristics of intermetalic Cu-Al and Au-Al compounds are brought in evidence by the difference between the growth the Au-Al intermetalic phases and Cu-Al intermetalic phases.

Positive aspects and the gold enheritage of gold and copper in this spherical bonds in are shortly discussed.

KEYWORDS: intermetalic, alumina, gold

1. Introduction

Wire-bonding is a main interconnection process in the packaging industry. Wires are bonded to Al pads using combined thermal and ultrasonic activation. Gold wires are the widely used and well characterized media for this process [1]. Recently, the use of copper wires is of interest to the industry due to its electrical and mechanical properties.

Since copper is relatively hard and readily oxidized, the use of copper wires in industrial interconnection processes requires special bonding procedures and equipment.

Moreover, due to the relatively slow formation of Al-Cu intermetallics, examination of the as-bonded Al-Cu interface by conventional characterization such as optical microscopy (OM) and scanning electron microscopy (SEM) with energy dispersive spectroscopy (EDS), provide almost no information related to the deterioration of the wire-bonds as a function of the bond life. Until today, the Al-Cu wire-bond interface was investigated by OM and SEM in samples which were mechanically polished, making it difficult to distinguish between the different Al-Cu intermetallics. Attempts were also made to resolve the intermetallic composition of the bonds via EDS incorporated in SEM [2]. In the present study, transmission electron microscopy (TEM), scanning transmission electron microscopy (STEM) and TEM-EDS were used for quantitative analysis of the intermetallic composition of as-bonded and heat-treated Al-Cu wire-bonds. A dual beam focused ion beam (FIB) was used to prepare sitespecific TEM samples. FIB was also used for preliminary analysis of cross-sections by ion-beam and high-resolution SEM. In order to understand the processes that occur at the Al-Cu interface, as-bonded samples and samples annealed in air and argon were prepared.

The channeling effect may occur for incident ions if a crystal in the sample is oriented in a low index zone-axis. In these conditions, the ion beam will penetrate deeper into the target before significant inelastic scattering occurs, resulting in a lower probability of secondary electrons escaping from the sample due to their limited mean-free-path. As a result, grains oriented in a low index zone-axis will have a darker contrast than randomly oriented grains (Figure 1).

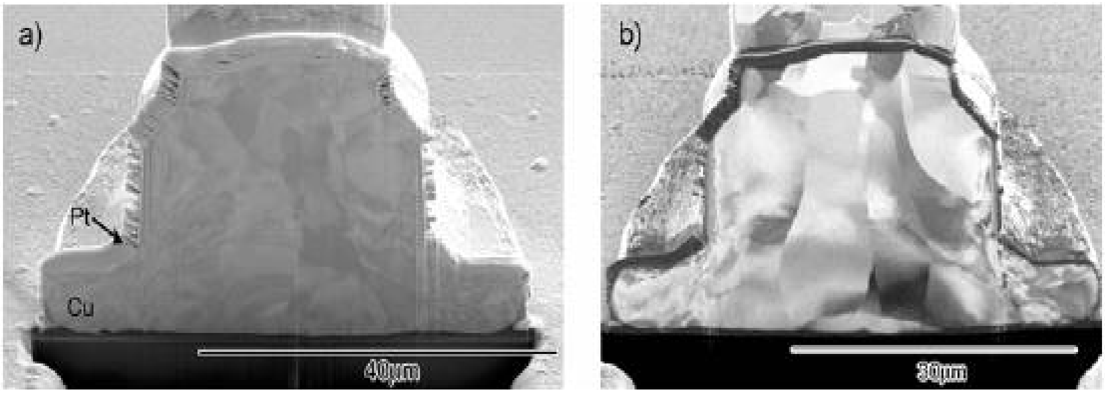

Figure 1. (a) Secondary electron SEM micrograph of the as-bonded Al-Cu interface and (b) ion induced secondary electron micrograph of the same specimen, showing the Cu grain morphology.

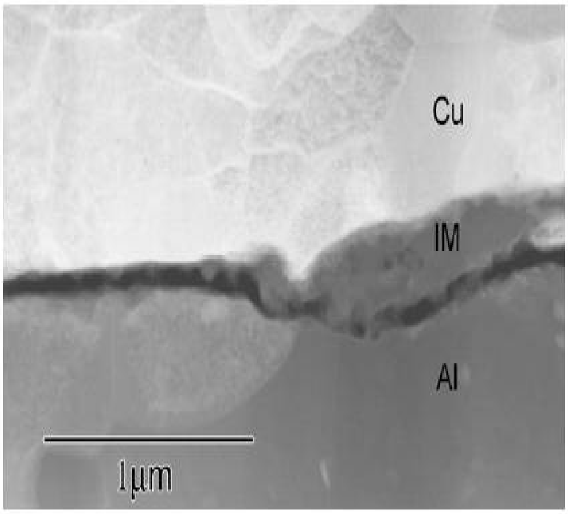

Figure 2. HAADF-STEM micrograph of the as-bonded Al-Cu wire-bond cross-section. A nonuniform intermetallic region is evident.

Figure 2 presents high angle annular dark field (HAADF) STEM micrograph of an area of the as-bonded Al-Cu wire-bond, indicating that intermetallic phases are formed in the as-bonded samples[3].

EDS analysis confirmed the presence of Al-Cu intermetallics, and that changes in the Cu concentration in the large intermetallic region was not monotonic as a function of a distance from the copper layer.

The composition of the intermetallic regions in heat-treated samples was evaluated by TEM-EDS and, wherever possible, confirmed by selected area electron diffraction patterns (Figure 3).

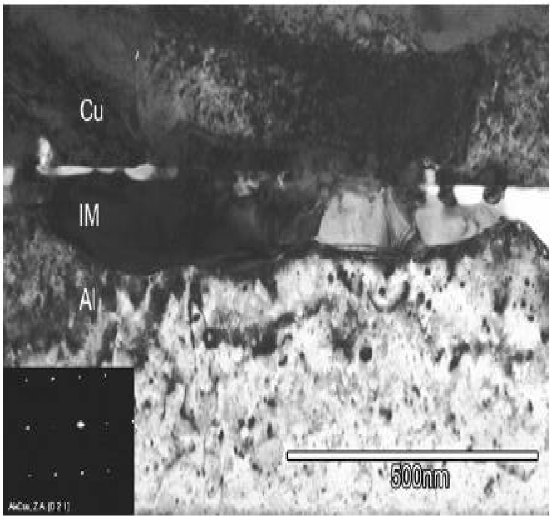

Figure 3. Bright field TEM micrograph of a central region of a Al-Cu wire-bond annealed for 24 hours in argon at 175°C. The inset diffraction pattern is of the dark intermetallic grain.

2. Tape Automated Bonding (TAB)

They will accommodate the flat TAB tape lead and provide the proper material for a reliable connection to the tape[4]. The bump fabrication process uses a metal deposition and plating process. First a series of barrier and seed layers of metal are deposited over the surface of the wafer. A layer of photoresist is deposited over these barrier and seed layers. A photomask is used to pattern the locations over each of the pads that will be bumped.

An etching process exposes the pads, and the open resist hole defines the shape and height of the bump. The bump, which is typically gold, is then electroplated over the pad and the deposited barrier metals. Once the plating is complete, a series of etching steps are used to remove the photoresist and the barrier metal layers that are covering the rest of the die. The gold bump protects the underlying materials from being etched.

While gold bumping is the most common, copper, tin-lead, as well as layered combinations of these materials are used for bumping. An alternative to die bumping is to create bumps on the tape. For high lead counts, wafer bumping is more common. Figure 4. illustrates a completed bump and a TAB tape lead.

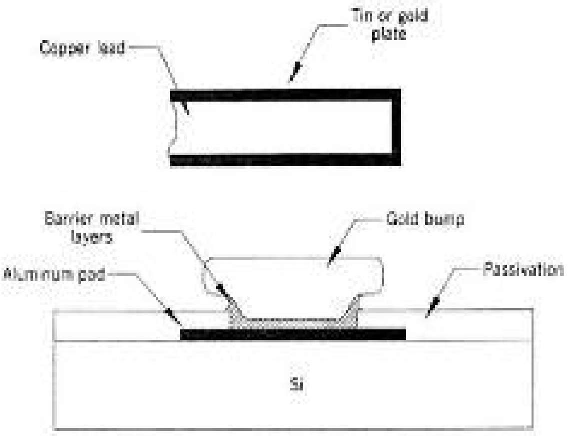

Figure 4. Tab with wafer bumping [5].

Gold top wafer metallurgy had been practiced in the past. With exception of GaAs and TAB, gold had been replaced by aluminum interconnects and then by advanced copper interconnects. Lower material cost plus ultra-fine line capabilities of both aluminum and copper were reasons for the displacement of gold as interconnect. However, to enter high temperature IC applications, to achieve superior reliability or to dissipate greater power, the resurrection of gold as the top metal is both practical and effective. This protective gold top is coined Power Au for the ability of gold to increase power capabilities of ICs, packages and systems.

Au wire bonded to aluminum forms many Au-Al intermetallics. This interdiffusion of Au atoms into Al bond pads is well studied. At higher temperature, diffusion and growth rate of intermetallics also accelerate. If the entire thickness of aluminum bond pad were converted into Au_4Al intermetallic, then the poor adhesion of Au_4Al to barrier metal between aluminum layers can result in wire bond separation and electrically open failure.

Even as Au_4Al intermetallic is growing, Kirkendall’s voids coalesce into hairline crack at intermetallics interface. These weakened interfaces are susceptible to stress failure and again result in electrically open failure.

The metal between Power Au and Al is not a perfect barrier however. Under higher temperature testing, barrier metal does eventually break down. Above 250°C plus self heating from 860mA current, gold atoms punch through the barrier metal and then gold diffuse into aluminum. Rapid diffusion of Au into Al forms visible ‘purple plague’ within aluminum. Scanning electron microscopy show a void in the Power Au line immediately above contact to aluminum. Missing gold has diffused down into the aluminum. Voiding in Power Au line leads eventually to electrically open failure. Both selection and thickness of barrier metal can be optimized for even higher temperature applications.

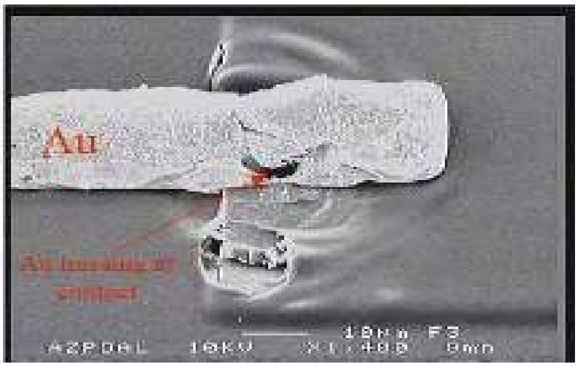

Figure 5. Power Au line with void above contact to aluminum after extremely high temperature testing and 860mA current. Gold diffused into aluminum and left a void.

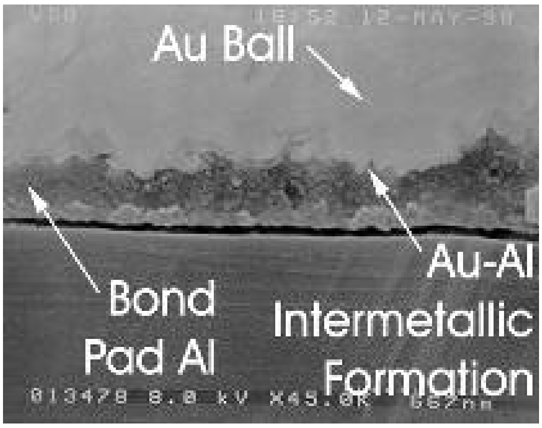

Figure 6. Shows a cross section of a Au-Al bond [6].

The wire pull test is used to measure the strength and failure mode of the wire bond. A small hook is attached to the wire loop and pulled. The hook is generally placed at the highest point close to the 1st bond to gauge the strength of the 1st bond or next to the wedge at the 2nd bond to ensure a reliable weld. Generally, if the hook is placed at the mid span of the wire, then the test will show the weakest link of the bond. This is typically either the neck of the ball bond (right above the ball) or at the heel of the wedge bond. The Pull test is basically a function of the wire diameter. Loop height and wire span are the most significant factors that determines the strength of a wire for a given wire diameter. Shorter span and a lower loop will result in a lower pull strength. As opposed to a longer span and a higher loop height which will result in higher pull strength.

Copper wire bonding is normally formed by a copper ball onto an aluminum based bond pad in microelectronic package. However, copper oxidation at the interface of Cu- Al bonding area causes the cracks, decreases the interfacial shear strength, and weakens the Cu-Al bonding.

Surface analysis of ball-peeled pad of Cu-Al bonding using XPS demonstrates the copper oxidation in the Cu-Al interface after autoclave test (at 121oC and 100% relative humidity). The binding energy scans for Cu 2p on the specimen after 0, 192, 384, and 576 hours in autoclave test chamber is carried out. After 576 hours corrosion, the chemical change of copper in a few atomic layers of surface from Cu to CuO. Furthermore, there are two major copper oxides peaks observed in the study, CuO and $Cu(OH)_2$. Cu_2O is not table in air and change to CuO immediately. Therefore, CuO_2 is not expected to be detected at the specimen [7].

Low cost, high thermal and electric conductivity, easy fabricating and joining, and wind rang of attainable mechanical properties have made copper widely used in electronic packaging, such as lead frames, interconnection wires, foils for flexible circuits, heat sinks, and WPB traces. However, unlike the aluminum oxide, the copper oxide layer is not self-protect.

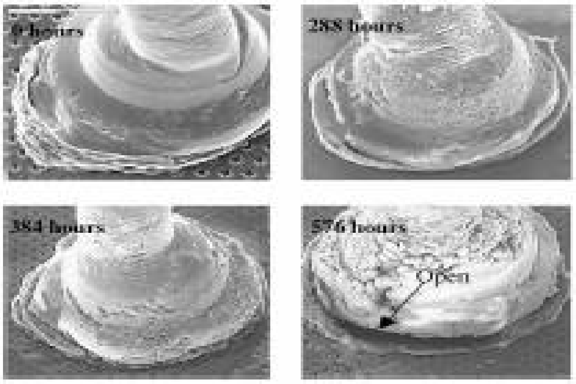

Figure 7. SEM pictures show corrosion and a crack after test hour increase (X1000).

Therefore, copper is readily oxidized, especially at elevated temperature. Copper oxidation is considered as a serious reliability problem in microelectronic package. The copper oxidation at the interface of Cu-Al bonding area causes the cracks, decreases the interfacial shear strength, and weakens the Cu-Al bonding. Also, Copper oxidation in the area of the lead frames die pad and mold compound causes the delamination of packages. Furthermore, the moisture penetrates through the crevices because copper oxidation induces poor adhesion in the area of the copper lead frames and molding compound, creating corrosion problem in the packages.

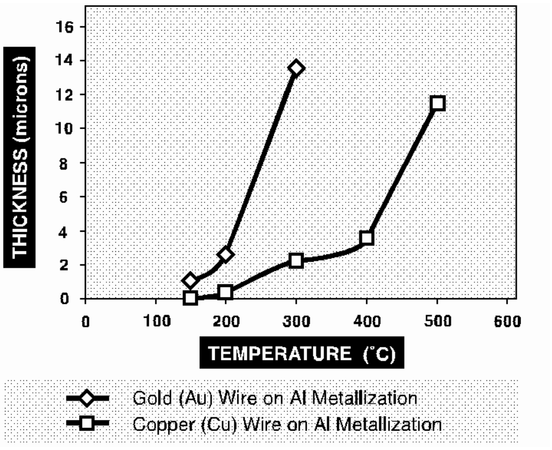

Tempered and annealed iCu copper wire exhibits higher tensile strength and elongation than gold wire, resulting in better ball neck strength, reduced wire sag and excellent loop stability during encapsulation. Because copper exhibits better conductivity than gold, DHF wire allows for increased device power ratings and also accounts for better heat dissipation in packages.

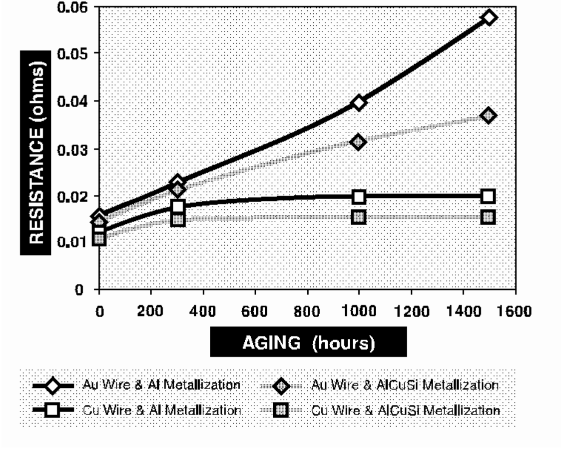

Figure 8.Intermetallic thickness vs. exposure for 6 hrs at respective temperature b) effect of wire material & substrate metallization on electrical resistance after aging.

Tests show that, after exposure at various temperatures, intermetallic growth is significantly slower in copper wire bonds than in gold wire bonds. This results in lower electrical resistance, lower heat generation and, ultimately, increased bond reliability. Tests also show that despite a lower amount of intermetallic penetration, pull force and shear testing show values that are equivalent to, or greater than, those obtained with gold wire.

Potential for maximum conductivity, device performance (tact frequencies of <500 MHz) and resistance to degradation in a mono-metallic system are the driving forces for the use of Cu wire in packages with Cu pads. DHF and iCu wire have been successfully ball-bonded to bare Cu lead frames and also AlSiCu metallized pads.[8]

3.Conclusions

Recent studies have shown that, in many applications, copper wire bonding can provide better performance and reliability than gold wire bonding. While copper wire and ribbon have been used in discrete and power devices for many years, these latest studies also show that successes in ball bonding thin copper wire to aluminum, silver-nickel plating and even bare copper, provide the potential for its use in high-end, fine- pitch packages with higher lead counts and smaller pad sizes. For these reasons, along with the lower inherent cost of copper material, Kulicke & Soffa Bonding Wire[8] has developed and optimised two copper wire products: DHF copper wire for ball and wedge bonds in power devices and discrete packages; and iCu for fine-pitch or high-end IC applications.

References

[1].M. Drozdov, G. Gur*, Z. Atzmon*, and W.D. Kaplan Microstructural Evaluation of Al-Cu Intermetallic Phases in Wire-Bonding;

[2]. G. Harman, "***Wire Bonding in Microelectronics Materials, Processes, Reliability and Yield***", 2 ed., Electronic Packaging and Interconnection, ed. C.A. Harper. 1997: McGraw-Hill.

[3]. F.W. Wulff, C.D. Breach, D. Stephan, Saraswati and K.J. Dittmer, ***Characterization of Intermetallic Growth in Copper and Gold Ball Bonds on Aluminum Metallization***, Proceedings of Electronics Packaging Technology Conference, 6th, Singapore, Dec. 8-10, 2004: 348-353, 2004.

[4]. *** Semiconductor Packaging Module II;

[5]. James J. Wang and Bob Baird Power gold for 175°c Tj-max;

[6].*** Semiconductor Packaging Assembly Technology 2000 National Semiconductor Corporation;

[7]. Ying Zheng ***Study Of Copper Applications And Effects Of Copper Oxidation*** In Microelectronic Package In Partial Fulfillment of MatE 234. 2003;

[8]. Kulicke & Soffa ***Complete Connection*** DHF &iCu Copper Bonding Wire for Power Devices and High-End ICs.

THE ANNALS OF “DUNAREA DE JOS” UNIVERSITY OF GALATI.
FASCICLE IX. METALLURGY AND MATERIALS SCIENCE
N^0. 2 – 2007, ISSN 1453 – 083X

SOME ASPECTS ABOUT THE REFRACTORY LINING WEAR IN FURNACES

Tibor BEDŐ
“Transilvania” University of Brasov
email: bedo.tibor@unitbv.ro

ABSTRACT

For melting cast iron, carbon steel, copper and copper alloys the quartzite is still one of the most used lining material and the most cost effective as well. The silica lining has to be replaced frequently due to the wear. In this paper there are present some aspects about the refractory lining wear in furnaces.

KEYWORDS: silica, quartzite, lining wear, furnace

1. General aspects

As is known to those skilled in the art, the handling of high temperature liquids, such as molten steel, requires special materials and techniques. The melting temperature of steel approaches 1600 °C, a level above that which most containment materials can withstand. Moreover, molten steel usually includes slag that can be fluid and corrosive which adds to the complexity and difficulty of efficient handling.

Ladles for handling such high temperature liquids typically have been constructed of steel outer shells lined with refractory brick that can withstand the extremely harsh conditions to which they are exposed. However, such brick wear and from time to time must be repaired or replaced. In addition, when high temperature liquids are poured into such ladles the impact forces (as, for example by a tap stream of molten steel) tend to markedly increase erosion in the lower sidewall and bottom regions of the ladle.

The silica lining normally used has to take the full burden of the chemical and mechanical wear that is imposed upon it during the melting. Chemical reactions will occur during the melting. The slag formed has several sources and the predominant source differs from furnace to furnace as will the slag composition.

The normal wear of a silica lining is the reaction of carbon with the silica $2C + SiO_2 \rightarrow Si + 2CO$. An increased reaction will take place when the carbon content goes up and silicon goes down. Increased temperature will speed up not only this reaction, but all chemical reactions between slag, oxides and lining material.

Typical refractory material life for the furnaces (i. e. total replacement as opposed to weekly repair of the pouring lip) lies between 320 and 490 runs [1]. The material could exceed 500 runs without problems as long as the pouring temperature does not exceed 1520 ^{o}C.

The so called “normal” slag has a very wide chemical composition as it is a result of several sources. This may come from [2]:

- scrap with rust which gives FeO;
- scrap with impurities such as sand and soil from scrap yard which gives SiO_2, Al_2O_3 etc.:
- slag binder not deslagged properly out of the furnace SiO_2, Al_2O_3, CaO, MgO, K_2O, Na_2O;
- alloying elements that are oxidized (MnO is the most severe);
- returns with adhering mould sand (sand, bentonite, sodium silicate etc.), SiO_2, Al_2O_3, Na_2O;
- cupola slag CaO;
- returns of ductile iron, Mg silicates.

The chemical composition of a slag can vary considerably but mostly fall inside the limits shown in table 1 [2].

Table 1. The chemical composition of a slag

Component	Variation limits
SiO_2	50 – 80 %
Al_2O_3	5 – 20 %
FeO	0 – 20 %
MnO	0 – 15 %
MgO	0 – 15 %
CaO	0 – 10 %
Alkali	0 – 5 %

The slag reacts with the lining material until it is saturated. If the temperature is increased a saturated slag formed at low temperature can dissolve more lining material. If an aggressive slag or oxide continuously is formed during the melting operation the slag attack will be unlimited.

The liquidus temperature of the slag should be as low as possible to diminish radiation heat losses but must also result in acceptable viscosities. Furthermore, low liqiudus temperatures will cause less refractory lining wear.

The variation of the slag infiltration in the refractory as a function of time and temperature is demonstrated, indicating that with an increase in holding time and temperature, slag infiltration increases substantially with a simultaneous decrease in the remaining refractory wall thickness.

The presence of residual moisture reduces the surface tension of the liquid metal, thereby augmenting its power of penetration into the refractory material. This results in a penetration depth of approximately 60 %, which already occurs during / after sintering. Too much residual moisture in the refractory material leads to significant metal penetration during the first days of operation.

The lining wear is directly influenced by the inside furnace space temperature. It is well-known the fact that the temperature is not evenly distributed on the entire lining thickness. The temperature decreases from the inside to outside of the lining, fact which make as well as the lining wear follow the same value effect.

The lining – melt metal separation surface is practical the most wear yielding zone of the entire lining weight. Being the zone in which both the maximum temperature of the lining and the medium aggressiveness from the furnace inside is at high level, this is practical the most affected zone. Following the wear distribution way on the refractory wall thickness it is apparent that the lining outside weight remains in good state even after a long usage standing.

2. Experimental data

The reaction with the melt metal and the slag is the most common reason for the inside furnace lining wear. The lining wear is promoting in time to the opposite side of the furnace lining getting on after a time to destroy them.

The wear distribution way analysis on the wall thickness was made using a Silica Mix melting crucible from a coreless induction furnace employed to iron melting process approximately 4 months. The furnace inside temperature was 1450 ^{o}C. After the melting crucible replacement, by this was taken samples which were analyzed. The analysis was made at the lining – melt metal surface (fig. 1); at 10 mm inside from this surface (fig. 2); at 30 mm inside from this surface (fig. 3); at a half of refractory wall thickness (fig 4) and at the outside lining surface (fig. 5).

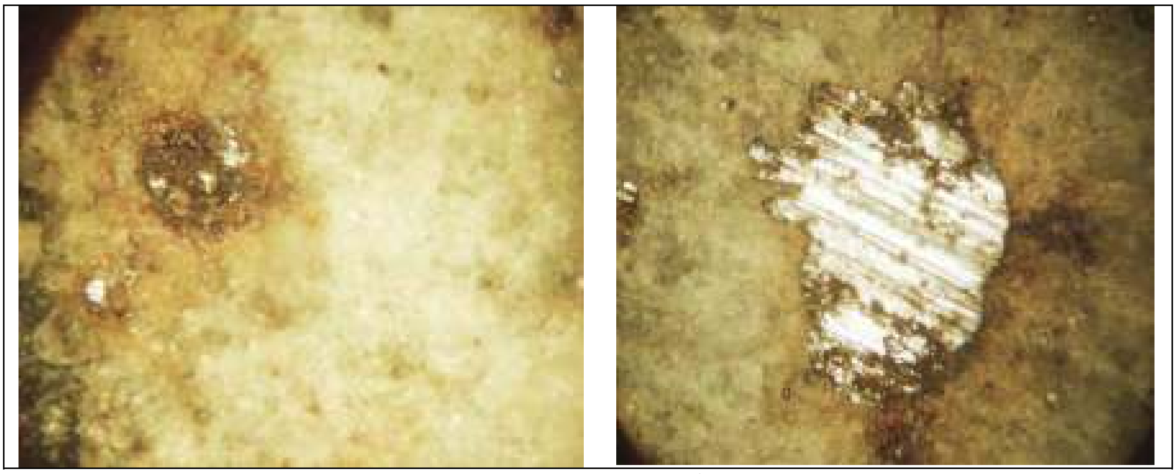

Fig. 1. Lining – melt metal interface (t = 1450 ^{o}C; time = approx. 4 months)

It is to notice the fact that the lining structure is almost destroyed at the internal surface (they are many metallic and slag inclusions) and become more and more uniform and homogeneous toward exterior. The fact that the lining wear is more increased at high temperatures is to understand concerning the pictures in fig. 6 and fig. 7.

There are presented samples from a melting crucible used at iron melting process (fig. 6) and samples from a melting crucible used at aluminum alloy melting process (fig. 7) (though it is to remark that in fig. 6 it is presented a Silica Mix furnace lining, while in fig. 7 it is presented an Orsova quartzite furnace lining).

Fig. 2. δ = 10 mm from the lining – melt metal interface
(t < 1450 ^{o}C; time = approx. 4 months)

Fig. 3. δ = 30 mm from the lining – melt metal interface
(t < 1200 ^{o}C; time = approx. 4 months)

Fig. 4. δ = 1 / 2 of refractory wall thickness
(t ≈ 700 ^{o}C; time = approx. 4 months)

The coreless induction furnace is presently the most used type of melting furnaces in the foundry industry. By careful handling of the slag together with a correct choice of lining material the increase of the lining life can be considerable.

Fig. 5. The exterior of the refractory wall
(t ≈ 100 ^{o}C; time = approx. 4 months)

Fig. 6. Macrostructure – Silica Mix lining
Crucible used to iron melting

Fig. 7. Macrostructure – Orsova quartzite lining
Crucible used to ATSi5Cu1 melting

3. Conclusions

Contrary to the case of the crucible furnace, in numerous metallurgical units, locally advanced but solidified metal penetration in the refractory material represents no risk. Even if metal fins extend through the refractory towards the vessel wall (steel shell) these are not dangerous as long as, on account of the cooling conditions, they are solidified or have a low temperature. Only when such or other wear phenomena lead to local overheating do these represent a potential hazard [3].

The premature failure of the refractory lining can result in the need for unplanned shutdowns to enable repairs to be made. Due to the need to cool, empty, repair and restart the furnace these "mini-shuts" can last for up to one week, with the resulting loss of production and disruption to normal operations. The unplanned nature of such shuts may result in them not being performed in the most efficient, cost effective or safe manner possible.

References

[1] ***, ***Rotary furnaces with oxyfuel combustion***, Casting Plant + Technology International 2 / 2002, p 44 - 45
[2] Torsten Bodelind, ***Minimising lining wear in induction furnaces***, Foundry International, march 1999, p 7 – 10
[3] Manfred Hopf, ***Monitoring of lining wear in crucible and channel induction furnaces***, Casting Plant + Technology International 2 / 2002, p 24 - 31

THE ANNALS OF “DUNAREA DE JOS” UNIVERSITY OF GALATI.
FASCICLE IX. METALLURGY AND MATERIALS SCIENCE
N^0. 2 – 2007, ISSN 1453 – 083X

STUDIES ABOUT ELECTROCHEMICAL PLATING WITH ZINC-NICKEL ALLOYS

Gheorghe GUTT[1], Violeta VASILACHE[1],
Maria POROCH-SERIŢAN[1], Traian VASILACHE[2]
[1]”Ştefan cel Mare” University of Suceava, [2] SC Daflog SRL-Madiaş
e-mail: violetaren@yahoo.com, mariap@usv.ro,

ABSTRACT

The electrochemical deposition of zinc and combinations with elements of the 8th group of the Periodic System (nickel, cobalt, iron) have good properties for anticorrosive protection, compare with pure zinc. For steel pieces, these films delay apparition and formation of white and red iron oxide. We used solutions with different concentrations of zinc chloride, nickel chloride and potassium chloride. For analyze the results we utilized the optic microscope and the X-ray diffraction.

KEYWORDS: Zn-Ni alloy, electrochemical deposition, corrosion

1. Preliminaries

In ordinary coating the zinc remains the principal metal for industrial applications, especially for coverage of steel products. Between the last two decades there were be applied alloys for the necessities of cover up the demand for products with high quality coatings. On the first place there are the machine buildings industry and the aerospace industry, also those for electrical components and for fixing devices.

In the European Union there are specially efforts and laws in the way to reduce the consumption of heavy metals like cadmium and mercury. Similar ways of action there are in the world community and organizations. The heavy metals are very toxic for human organism and for the animals, because they could produce hard diseases of the central nervous system. The heavy metals remain in earth and water for a very long period, so their effect it is dangerous after a great number of years.

In the domain of anticorrosion protection cadmium is much utilized together with zinc. Because of fact that consumption of heavy metals has to be reduced year by year, until the total elimination, there are searching for new technologies and one of the most promised of them is that of alloys electrochemical coatings with Zn-Ni, Zn-Co, Zn-Fe. [8], [9].

The greatest automobile companies are in a continuous course for prolonging the warranty period, so their products are better and better year by year. The majority of the European factories have been changed the specifications regard the improvement of the performances of the electrodeposited layer. Those new economic politics are based just on the using of alloys like Zn-Ni, Zn-Co and Zn-Fe.

Out of the machine building industry there are interesting in the using of electrodeposited alloys in the field of industry for defense.

The State Department of USA is asking for eliminate during the follow years of the old technologies with new technologies based on the zinc alloys.

2. Electrochemical processes on cathode

In the experiments we deposed zinc-nickel alloys on a gold substrate which was first deposed on a glass lamella through the sputtering method. We have chosen this method to realize the analysis of the deposed layers using the X-ray diffraction (XRD).

The electrochemical reactions which are produced on cathode could be considered effectuated in two steps, as Matlosz [6],[7] described them.

The zinc ions are deposed on their own substrate, on gold substrate used and on nickel substrate. Also, the nickel ions are deposed on their own substrate, on gold substrate and on the nickel substrate. In addition, we have to consider the secondary reactions, those where ions Zn^{2+} are combine with hydrogen to form ZnH^+, as well as ions Ni^{2+} will combine with hydrogen to form NiH^+. Those intermediary species, formed in the adsorption process, will decompose finally in metallic Zn, and metallic Ni respectively.

The electrochemical reactions could be written as follow:

$Ni^{2+} + e^- \rightarrow Ni^+_{ads}$
$Ni^+_{ads} + e^- \rightarrow Ni$
$Ni + H^+ + \rightarrow NiH^+_{ads}$
$NiH^+_{ads} + H^+ + 2e^- \rightarrow Ni + H_2$
$Zn^{2+} + e^- \rightarrow Zn^+_{ads}$
$Zn^+ + e^- \rightarrow Zn$
$Zn + H^+ \rightarrow ZnH^+_{ads}$
$ZnH^+_{ads} + H^+ + 2e^- \rightarrow Zn + H_2$

Ni^{2+} and Zn^{2+} are dissolved as metallic ions, hydrolyzed or not. Ni^+_{ads} and Zn^+_{ads} which could or couldn’t contain the hydroxyl group, are adsorbed univalent in intermediary reactions. Ni and Zn form the metallic layers of nickel and zinc respectively.

The kinetic of mass transfer is supposed respects the Butler-Volmer equation. In far away equilibrium conditions the anode reactions could be neglected. [2], [4].

3. The deposing of Zn-Ni alloys on a thin layer

3.1. Experimental details

The deposing of thin films of Zn-Ni was realized electrochemically. We worked a INCDFM-Bucharest-Măgurele institute. For obtaining films with desired properties it was necessary to investigate the influence of deposing conditions (like deposing potential, the bath composition, the temperature during the deposing process, ultrasonic treatment and mechanic agitation) against structure, morphology, composition and optical, transport and magnetic properties of the layers. We tried to obtain priory uniform layers. To realize this target it was necessary to find the interval of potentials to depose the stoichiometry composition of the alloy, searching to find the slowly as possible conditions.

We used the following compositions to prepare the electrolyte low acid for deposing of Zn-Ni alloys:

Solution I: zinc chloride 130g/l, nickel chloride 130 g/l, potassium chloride 230g/l, pH 5-6, t(°C) 24-30°C;

Solution II: zinc chloride 130g/l, nickel chloride 65 g/l, potassium chloride 230g/l, pH 5-6, t(°C) 24-30°C.

As working electrode we used a glass lamella having a gold thin layer deposed using sputtering method (using a Hummer 6 instalation). The pH level was maintained between 5 and 6 naturally without adding acids, because the salts were chlorides which produce after electrolytic dissociation have acid character (excepting KCl, salt of a strong acid and a strong base). The working temperature was between 24°C and 30°C.

To realize a good adhesion it was used the next method. The glass lamella was first polished, then gold plated in sputtering installation. We made some proves with bright glass, but the result was negative because all the gold was dissolved in solution.

As reference electrode it was used the calomel electrode immersed directly in the electrolytic cell.

3.2 .Methods and technique used, instruments, equipments and software

The electroplated layer of Zn-Ni alloy was made using a potentiostat-galvanostat Voltalab and software Voltamaster.

The measurement of structural and morphological properties of the films was realized using the optical microscope of the INCDFM institute and the XRD installation of Mechanics Faculty, University Ştefan cel Mare-Suceava.

3.3. Results and discussions regard the electroplating with Zn-Ni alloys

Figure 1 shows the polarization curves for electroplating with Zn-Ni alloys on Au substrate. At the beginning the current density grows insignificant with potential, due to the fact of electronic clouds around the electrodes and due to the thermal agitation which opposed to the ordinate movement of the ions in solution. Then is a passing portion followed by a linear portion when the current density grows with the potential. It is the time when the electrolytic cell is like an ohmic resistor, so the polarization curve shows clearly the constant ratio between potential and current density.

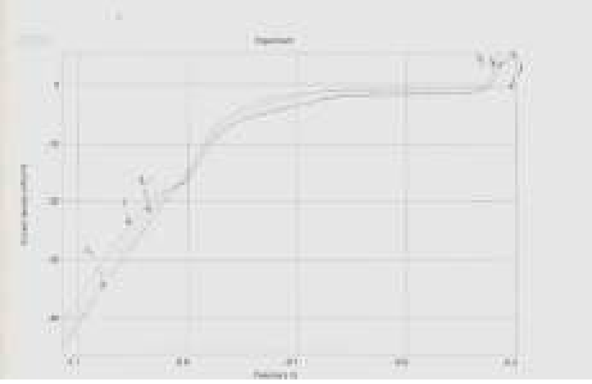

Fig.1. Polarization curves: 1- deposed on Au, 2- deposed on Zn-Ni alloy, 3- deposed on Zn-Ni alloy.

The figures 2 (a) and (b) shows the way of variation in time of current density in the case of those two solutions described above.

The decreased of the current density appears like a normal fact in electrochemical cover processes because in time the concentration of ions (and those of all components) in solution decrease and the number of charge transporters are smaller and smaller with time. There is also an initial period when the current density increase for a time. It is the period of advance of the electrochemical reactions, when the chaotic movement of the thermal agitation is progressively surpassed by the ordinate movement of the charge transporters in the electric field created by those two electrodes.

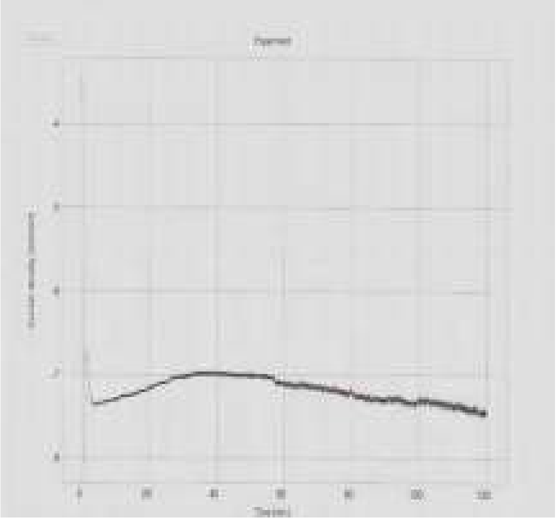

a) solution I

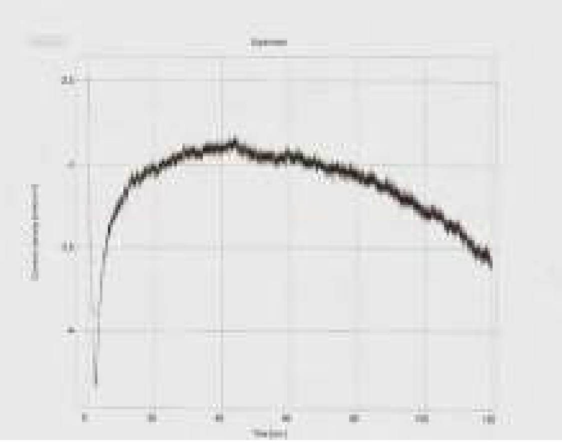

b***) solution II***

Fig.2. The current registered during the deposing of Zn-Ni alloy for 2 hours, at 30°C temperature.

The figures 3 and 4 represent photos of the surfaces covered with Zn-Ni alloys at 30°C temperature for two hours, but at different potentials. As it can see, in the first case (figure 3) the deposed has a better quality.

In figure 4 it could be observe micro-crashes in the deposed material. It was working at -1000mV potential. Micro-crashes could be explained through internal stress (mechanical) which appears and due to the fact that the increase of potential conduce to increasing also of the velocity of the ions in interaction with the cathode. Also the processes of dissolution of the electrode are much intense.

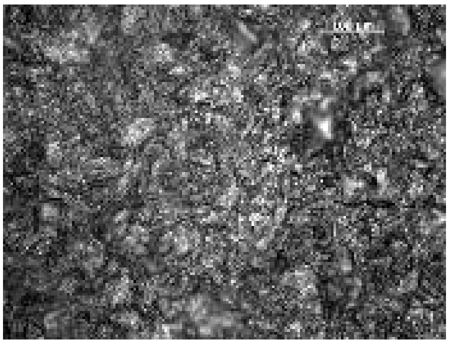

Fig.3. Microscopic photo of deposed Zn-Ni alloy at -850 mV, for 2 hours, at 30°C temperature.

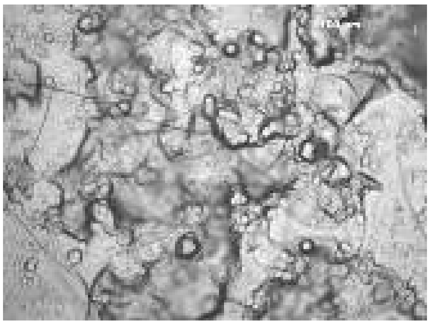

Fig.4. Microscopic photo of deposed Zn-Ni alloy at -1000mV, for 2 hours, at 30°C temperature.

4. The optimization of the process of electroplating with Zn-Ni alloy

On the way to optimize the process of electrochemical plating with Zn-Ni alloy, we shall use the results of the table and a method for optimization of Taguchi [1] type.

We shall take as factors which have to be controlled the next quantities:

- solution type: (1)solution I, (2) solution II
- discharge potential: (1) -850mV, (2) -900mV, (3) -1000mV, (4) -1100mV

The intensity of current will be measured and the efficiency of electroplating process will be calculated. We shall construct a matrix of the experiment, as it follows:

Table 1. The matrix of the experiment of electroplating with Zn-Ni alloy

No	Controlled factors		Measured values	
	Potential	Solution	Current	Efficiency
1	1	1	7	53
2	2	1	14	37.6
3	3	1	21	35.55
4	4	1	35	35.55 (**)
5	1	2	3	38.5
6	2	2	6	22.7
7	3	2	15	22.8
8	4	2	13	(**)
The average of the values				35.025

In the calculus of the average value of the efficiency we don’t take in consideration the values with (**) because these correspond with the cases when the alloy exfoliates. If it calculates the medium effect of every factor then it will obtain for the first solution:

(53+37.6+35.55)/3=42.05

and for the second solution:

(38.5+22.7+22.8)/3=28.

It could be observed that the first solution (those noted I) permit to obtain a greater efficiency compare to the second solution (those noted II).

Now we shall calculate the effect of the discharge potential and we shall find for the value of -850mV:

(53+38.5)/2=45.75.

For the value -900mV it will find immediately

(37.6+22.7)/2=30.15,

and for 1000mV we shall have

(35.55+22.8)=29.175.

As here it points to the problem of optimization in finding the better energy efficiency, and how it is seeing immediately that the efficiency decrease with the discharge of the potential, it is clearly that the most opportune value is that of -850mV, through the values chose for the experiment. As a matter of fact for this value it was obtain the better quality of the deposed.

Through those two solutions used for study, the solution I permitted to obtain the better efficiency and a good quality of deposed alloy.

5. The EDX analysis of deposed

In the University Ştefan cel Mare Suceava we analyzed the probes of Zn-Ni alloys with the apparatus Ray-ny Shimadzu EDX 720 in the material characterization laboratory. It could be observe that the Zn-Ni alloy it is co deposed in all the cases. The percents of zinc and nickel differs function of solution which was used in electroplating process and function of discharge potential used.

The results of analysis were written in table 2 and 3 and then we represent the graph of the composition of the alloy function of potential in the case of those two solutions with composition described above.

Together with zinc and nickel the analysis EDX found other chemical elements, but in reduced percent, as K, Ca and Fe.

Table 2. The composition of Zn-Ni alloys function of potential (solution I)

Potential (mV)	-850	-900	-1000	-1200
Zn (%)	53.206	56.717	64.321	66.423
Ni (%)	36.93	36.359	35.035	33.120

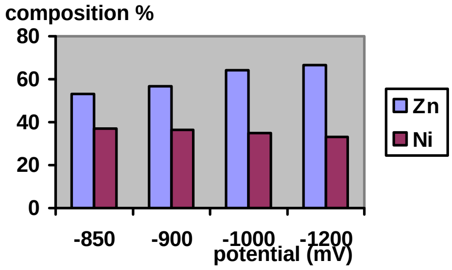

Fig. 5. The dependence of composition of Zn-Ni alloy co-deposed function of discharge potentials for the solution I; the deposed were effectuated at -850mV, -900mV, -1000mV and -1200mV

Table 3. The composition of Zn-Ni alloys function of potential (solution II)

Potential (mV)	-800	-900	-1000	-1200
Zn (%)	11.832	23.017	58.710	62.496
Ni (%)	29.949	33.338	31.127	27.818

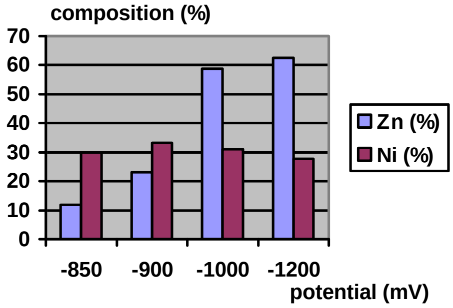

Fig. 6. The dependence of composition of Zn-Ni alloy co-deposed function of discharge potentials for the solution II; the deposed were effectuated at -850mV, -900mV, -1000mV and -1200mV

As it could be seen in all analysis effectuated, the Zn-Ni alloys were formed in all deposed layers. The ratio for those two metals differs function of work conditions (discharge potentials). Of course these conditions could be chosen after the criteria of using the final product, sorting the parameters in the way to obtain the desired alloy in the desired percents. It will modify the concentration of the solution in the electrolytic bath also in function of the scope.

6. Conclusions

The deposed of Zn-Ni alloys are important in technique. Following Brenner [3] definition, the electroplating of the system of Zn-Ni alloys is an anomalous co-deposition. So the co-deposition is possible only in particular experimental conditions.

To obtain the stoichiometric composition it has to follow carefully the values of the physics-chemic parameters.

The quality of the deposed could be controlled through the electrolyte concentration, discharge potential and the working temperature.

The surface for deposed also has to be finished with care because it is important.

The analyses XRD confirm that the zinc-nickel alloys were formed. Also it is confirmed that the percents of those two metals in the deposed alloy depend of working conditions.

References

[1] Alexis.J., ***Metoda Taguchi în practica industrială,*** Editura Tehnică, Bucureşti, 1999

[2]. Bajat,J.B., Maksimović,M.D., Radović, G.R., ***Electrochemical deposition and characterization of zinc-nickel alloys deposited by direct and pulse current,*** J. Serbian Chemical Society. 67(8-9)625-634(2002)

[3]. Brenner, A. ***Electrodeposition of Alloys***, vol.1, Academic Press, New York and London 1963

[4]. Di Bari,**G.A.,** ***Modern Electroplating, Fourth Edition,*** Edited by Mordechay Schlesinger and Milan Paunovic, John Wiley &Song, Inc., 2000

[5]. Grünwald,E., Mureşan,L., Vermeşan,G., Vermeşan,H., Culic,**A.,** ***Tratat de gtalvanotehnică***, Casa Cărţii de Ştiinţă, Cluj Napoca, 2005

[6]. Matlosz, M, ***Competitive effects in the electrodeposition of iron-nickel alloys,*** J. Electrochem. Soc., vol 140, Issue 8, aug. 1993, p2272-2279

[7]. Vallotton,P.M., Matlosz, M., Landolt,D., ***Experimental invstigation of the thermal effect in lead electrodeposition onto resistive substrates***, J. of Apllied Electrochemistry, vol.23, nr.9, sep.1993, p.927-932

[8]. Soares,M.E., Souza, C.A.C., Kuri, S.E., ***Corrosion resitence of Zn-Ni electrodeposited alloy obtained with a controlled electrolyte flow and gelatin additive,*** Science Direct, vol.201, Issue 6, dec.2006, p.2953-2959.

[9]. Wang Zha-Lun, Yang Yu-Xiang, Chen Ya-Ru, ***A Study on Electroplating of Zinc Nickel with HEDP***, The Journal of Corrosion, Science and Engineering, 2005

THE ANNALS OF “DUNAREA DE JOS” UNIVERSITY OF GALATI.
FASCICLE IX. METALLURGY AND MATERIALS SCIENCE
N^0. 2 – 2007, ISSN 1453 – 083X

MULTIFUNCTIONAL ZnO-BASED THIN FILMS BY SOL-GEL METHOD

Viorica MUSAT[1], **Elvira FORTUNATO**[2]
[1]”Dunărea de Jos” University of Galaţi,
[2]NOVA University of Lisbon-CENIMAT, Portugal
emails: viorica.musat@ugal.ro and emf@fct.unl.pt

ABSTRACT

The paper presents the crystalline structure, morphology, optical transmittance, electrical properties and room temperature photoreduction-ozone oxidation properties of some Al-doped ZnO thin films prepared by sol-gel method. The investigated films are high transparent (85-95% within the visible and near IR wavelength region), high conductive ($2.9\ 10^{-3}\ \Omega$ cm) and have a reversible photoreduction-oxidation response.

KEYWORDS: ZnO thin films, sol-gel, transparent electrode, ozone sensing properties.

1. Introduction

In recent years, the low-cost and no-toxic nanostructured ZnO-based semiconductive thin films have attracted much researchers attention to replace other very expensive materials in different transparent electronics application [1-7], such as indium thin oxide (ITO) in solar cells and flat DCL devices [1-2, 6], GaN in broadband UV photodetectors with high tunable wavelength [3]. Important applications of UV detector are research-missile warning systems, high temperature flame detection, air quality monitoring, gas sensing [4], accurate measurement of radiation for the treatment of UV irradiated skin.

High excitonic binding energy (aprox. 60 meV) of ZnO provides efficient excitonic emission at room temperature, which offers prospects of laser with low thresholds even at low temperature. In addition, the efficient blue–green emission at room temperature, makes ZnO very important for the fabrication of practical devices like light emission diodes, laser diodes, and solar cells [5].

ZnO transparent thin films transistors (TTFTs) are a very recent development. Among the possible applications of TTFTs are as transparent select-transistor in each pixel of an active-matrix liquid-crystal display (AMLCD), or as transparent alternative to amorphous silicon or organic thin-film transistors (OTFTs) [7].

This paper presents some results on the field of preparation and optical, electrical and UV/gas sensing characterization of semiconductive Al-doped ZnO thin films. Sol-gel method has been used for film preparation. This is one of the most efficient chemical method for the deposition of thin films, and represent a simple and low-cost processing alterna-tive to the vacuum deposition techniques [1-3, 5-8].

2. Experimental

2.1. Films preparation

Al:ZnO thin films were deposed using sols prepared with $Zn(CH_3COO)_2 \cdot 2H_2O$ 99,5%, $AlCl_3 \cdot 6H_2O$ 98% as precursors and ethanol as solvent. The thin films were deposed on Corning 1737 glass substrate by dip-coating technique. After each layer deposition, the gel films were dried and then pre-heated in air at 350 °C. The stabilized films were post-heat treated 1 hour in air at 600 °C for crystallization.

2.2. Films Characterization

The X-ray diffraction (XRD) patterns of the samples were recorded at room temperature using a Rigaku diffractometer (model RAD IIA), with CuKα radiation. The morphology on the surface and section of the films was analyzed using the atomic force microscopy (AFM). Tapping mode AFM experiments were performed in a Nanoscope IIIa Multimode AFM microscope (Digital Instruments, Veeco). Commercial etched silicon tips with typical resonance frequency of ca. 300 Hz (RTESP, Veeco) have been used as AFM probes.

The electrical resistivity of the films was measured in dark, using a KEITHLEY 617 Model Programmable Electrometer. The optical transmittance was measured using a UV-VIS-NIR double beam spectrophotometer (Shimadzu, UV-3100 PC) in the wavelength range 200 to 2500 nm. From the optical measurements, the optical energy gap, E_{gap}, was calculated assuming a direct transition between the edges of the valence and the conduction band, for which the variation in the absorption coefficient α with photon energy hν is given by the equation:

$$(\alpha h\nu)^2 = B(h\nu - E_{gap}) \qquad (1)$$

where B is 1/d and d is the film thickness. By plotting $(\alpha h\nu)^2$ versus hν, and extrapolating the linear region of the resulting curves, the E_{gap} value was obtained.

2.3. Sensing Test

The photoreduction - gas (ozone) reoxidation sensing behavior of thin films were investigated by electrical measurements at room temperature, which were carried out in a special chamber presented elsewhere [9]. The conductivity of the films decreases when are exposed in an ozone atmosphere. and increases by photoreduction, when the films were directly irradiated in vacuum by the UV light of a mercury pencil lamp with an average intensity of 4 mW/cm^2, at 254 nm for 20 min. First the films was exposed at UV light irradiation and after that, the chamber was backfilled with oxygen at a pressure of 600 Torr and an UV lamp was used to produce ozone (the films are shielded from the lamp). The films were maintained in this ozone atmosphere, when the re-oxidation of cobalt oxide crystallites results in a decrease of the film conductivity. An electric field of 50 V/cm was applied to the film sample and the electrical current was measured.

3. Results and Discussions

This paper presents some results obtained in the field of the preparation of transparent electrodes based on Al-doped ZnO thin films. The crystalline structure, morphology, optical, electrical and UV photodetection - ozone sensing behavior of these films are discussed.

The surface SEM micrographs (Fig. 1a) show a compact structure with quasi-regular grains, in both size and shape, with average grain size of about 60 nm. The cross-section SEM micrograph (Fig. 1b) show a very compact structure and a smooth surface.

Figure 2 show the XRD pattern of the film post-heated at 600^{o}C for the 2θ range where the three most important peaks of ZnO hexagonal (wurtzite type) structure are found. In contrast with the pattern of ZnO hexagonal structure with normal random orientation, this pattern shows a c-axis orientated structure where only the (002) peak is well developed. This preferential orientation of the grain growth, perpendicular to the surface substrate, favors the electrical conductivity of the film.

Tabel 1 presents the electrical properties of Al:ZnO thin film post-heated at 600^{o}C, obtained from Hall effect measurements. The high values of n-type carriers concentration and Hall mobility lead to high conductivity ($2.9\cdot10^{-3}$ Ω·cm) of the thin film.

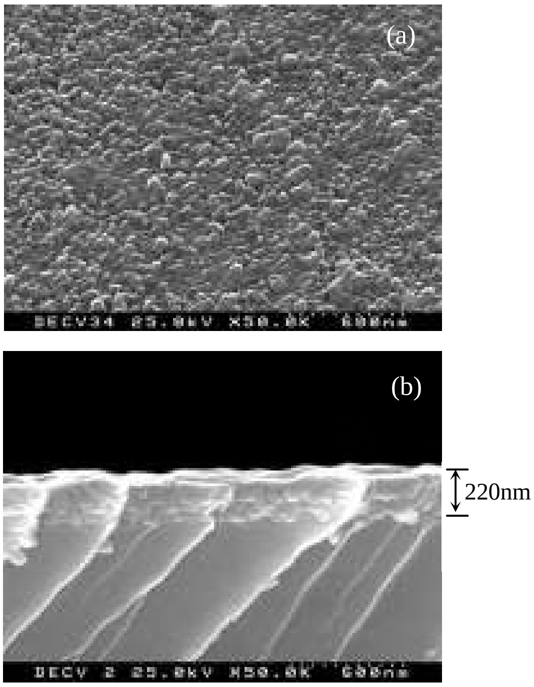

Fig. 1. SEM micrographs of the surface (a) and cross-section (b) of the Al-doped ZnO thin film.

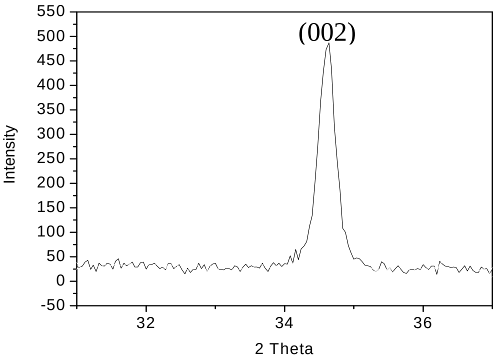

Fig. 2. XRD patterns of Al:ZnO thin film

Tabel 1. Electrical properties of Al:ZnO thin film

Film Type	Electrical properties		
	Resistivity ρ (Ω·cm)	Carriers concentration N (cm^{-3})	Hall mobility μH (cm^2/Vs)
Al: ZnO	$2.9\cdot10^{-3}$	$3.80\cdot10^{19}$	29.3

Figures 3 and 4 show the optical transmittance spectra and the calculation of the optical energy gap (E_{gap}), respectively. The optical transmittance spectra show a very good transmittance, between 85 and 95%, within the visible and near IR wavelength region.

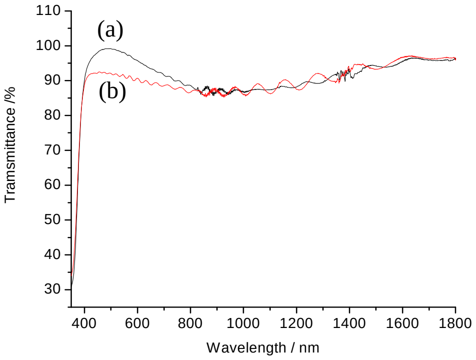

Fig. 3. Optical transmittance spectra of Al:ZnO thin films before (a) and after therma annealing.

The optical transmittance data presented in Fig. 3 curve (b) have been used for the calculation of direct optical energy gap (E_g), Fig. 4, according to the equation (1). The E_{gap} value of 3.48 eV has been obtained.

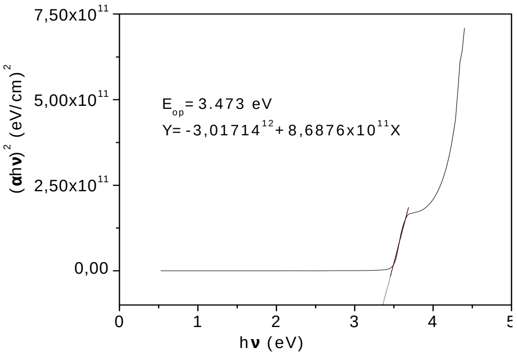

Fig. 4. The plot $(\alpha h\nu)^2$ vs. hν and the calculation of the optical energy gap (E_{gap}).

The photoreduction-oxidation cycles (Fig. 5) show a reversible change of two orders of magnitude in film resistivity during successive exposure to UV light and subsequent oxidative atmosphere of ozone.

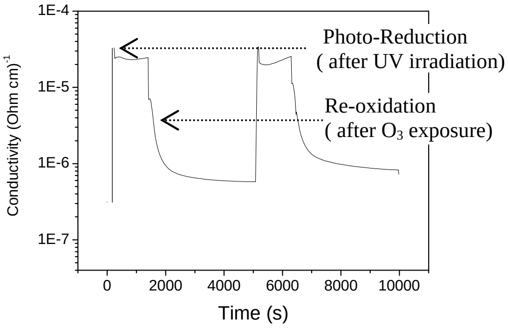

Fig. 5. Typical photoreduction - reoxidation cycles (room temperature)

4. Conclusions

Transparent conductive Al-doped ZnO thin film Corning 1737 glass substrate were prepared by sol-gel non-alkoxide route and the dip-coater technique for film deposition.

The Al-doped (2 wt.%) ZnO thin film with (002) direction oriented wurtzite type structure are high transparent (optical transmittance 80-95% within the visible and near IR wavelength region) and high conductive (resistivity of 2.9 10^{-3} Ω cm).

All the investigated films reveal reversible room temperature change in electrical resistance during UV irradiation followed by re-oxidation in ozone atmosphere.

References

[1] S. Bandyopadhyay, G.K. Paul and S.K. Sen, Solar Energy Materials & Solar Cells 71 (2002) 103.

[2] S. Fujihara, C. Sasaki and T. Kimura, Appl. Surf. Sci. 180 (2001) 341.

[3] Z.Q Xu, D. Deng, J.Xie, Y.Li, X.T. Zu, Appl. Surf. Sci., Appl. Phys. Lett. 90, 241918 (2007)

[4 W. Shen, Y.Zhao, C. Zhang, Thin Solid Films 483 (2005) 382-387.

[5] S. Chakrabarti, D. Das, D. Ganduli, S. Chaudhuri, Thin Solid Films 441 (2003) 228-237.

[6] E. Fortunato, P. Nunes, A. Marques, D. Costa, H. Aguas, I. Ferreira, M.E.V. da Costa, M.H. Godinho, P.L. Almeida, J. P. Borges and R. Martins, Surface & Coatings Technologies 151-152 (2002) 247.

[7]. B.J. So, Noris, J. Anderson, J.F. Wager, D.A. Keszler, J.Phys.D: Apply Phys. 36 (2003) L105-L107**.**

[8] M. Crisan, M. Zaharescu, D. Crisan, R. Ion and M. Manolache, J. Sol-Gel Science and Tech. 13 (1998) 775.

[9] A. Pimentel, E. Fortunato, A. Gonçalves, A. Marques, H. Águas, L. PereiraA, I. Ferreira, R. Martins, Thin Solid Films, 487 (2005) 212.

THE ANNALS OF "DUNAREA DE JOS" UNIVERSITY OF GALATI.
FASCICLE IX. METALLURGY AND MATERIALS SCIENCE
N^0. 2 – 2007, ISSN 1453 – 083X

STUDY OF THE THERMODYNAMIC REGIME AT THE CONTINUOUS CASTING OF STEEL

**Alexandru IVANESCU, Lilica IVANESCU,
Ciresica Cocindau, Viorel MUNTEANU**
"Dunarea de Jos" University of Galati
e-mail: ivanescu1944@yahoo.ca;

ABSTRACT

The paper presents the evolution of the heat exchange coefficient along the path of the continuous casting unit, as a function of the cooling water flow rate and the path length. The optimization of this thermodynamic regime assures the improvement of the quality of the continuous cast slabs and the increasing of the rate of obtaining the qualitatively corresponding slabs.

KEYWORDS: continuous casting, heat transfer

1. Introduction

- The secondary cooling in a continuous casting unit (**Figure 1**) represents the part of the machine in which the solidification, started in the crystallizer, ends.

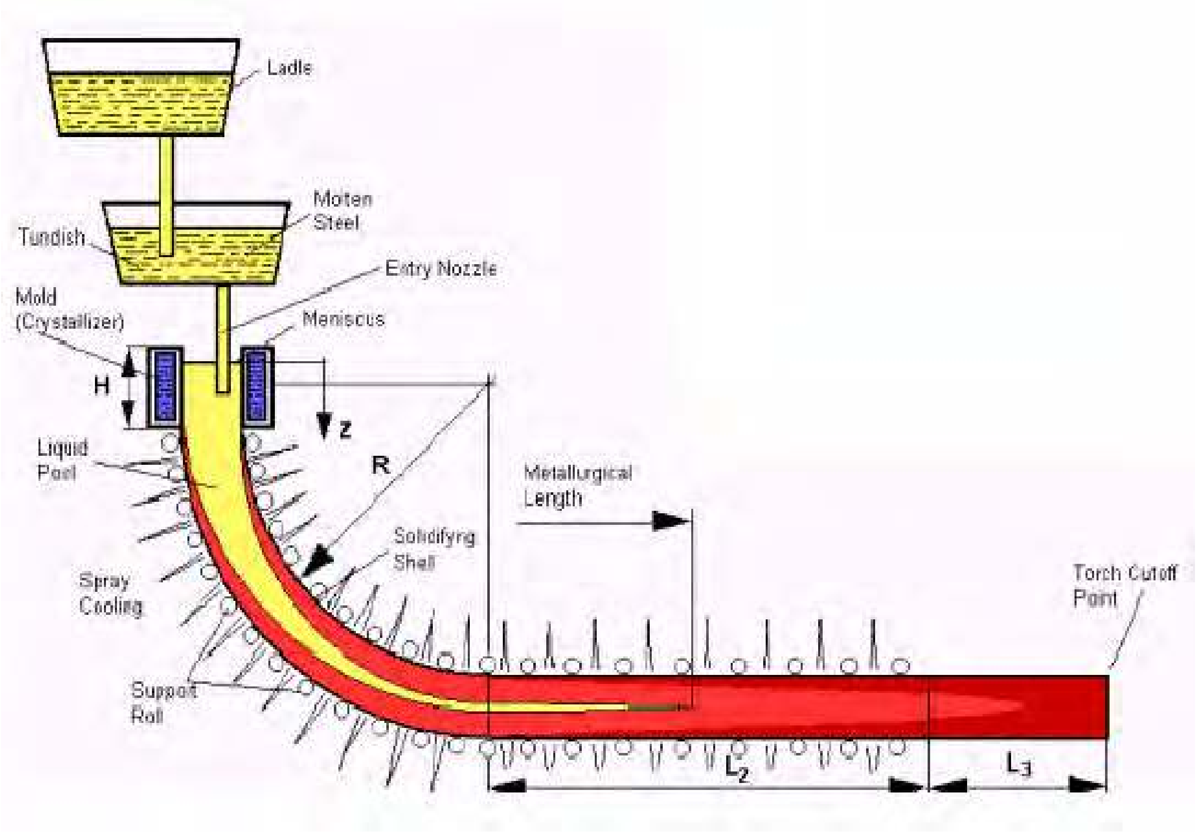

Fig. 1. Scheme of a continuous caster

In this zone there can be distinguished different elementary mechanisms of transfer which contribute to the evacuation of the heat from the slab surface:

- the radiation of the slab surface toward the environment;
- the convection of the environmental air, whose importance is smaller than the other heat transfer ways;
- the conduction at the direct contact of the slab surface with the rolls;
- the direct transfer to the pulverized water, the impact of the water droplets with the warm slab surface;
- the transfer by superficial boiling of water, which splashes along the surface or is accumulated by the supporting rolls. The heat repartition among these transfer ways depends on the machine type and the regulating conditions of the splashing and the approximated percentages of the evacuated heat in different ways are:
- radiation …….………….………28 %
- air convection………………...….0.5 %
- conductibility in rolls ……………17 %
- direct transfer at the rolls impact..16 %
- transfer at the cooling water….…38.5 %

The thickness of the solidified crust increases in the secondary cooling region as the removed heat quantity increases. The rate of the crust thickness increasing, is proportional to the removed heat quantity, which size depends on the heat exchange coefficient, α.

2. Experimental researches

The heat exchange coefficient, α, was determined using the relation [1-4]:

$$\alpha = Nu\,\frac{\lambda}{l}\ [\mathrm{W/m^2K}], \qquad (1)$$

where: λ is the thermal conductibility of the fluid, in [W/m.K]; l - the determinative length of the heat exchange (the dimension along the direction of the fluid flow), in [m]; Nu – the Nusselt criterion,

$$Nu = 0.151\ Re^{0.8}\ Pr^{0.75} \qquad (2)\ ;$$

$$Re = \frac{w\,d}{\upsilon} \qquad (3)\ ;$$

$$w = \frac{D_a}{A_d} \qquad (4)\ ,$$

with Re – Reynolds’ criterion, Pr – Prandtl criterion, w – is the cooling water rate of flow, in [m/s]; d – the nozzle diameter, in [m]; υ – the cinematic viscosity, in [m^2/s]; D_a - the cooling water flow rate, in [m^3/s]; A_d - the nozzle area, in [m^2]. In order to calculate the heat exchange coefficient the following characteristics of the cooling water have been used:

- the temperature …………15 ^{o}C ÷ 100 ^{o}C
- the thermal conductibility λ [W/m.K] ………………..0.588 ÷ 0.682
- the cinematic viscosity υ [m^2/s] ………………0.136 ·10^{-6} ÷ 0.29 ·10^{-6}
- Prandtl criterion 8.689 ÷ 1.716.

Table 1

Impact density [l/m^{2}min]	α [W/m^{2}K]	α [W/m^{2}K]
75	419.3	409.76
150	555.4	558.23
300	834.3	845.44
450	1108.6	1119.66
600	1398.3	1380.90
750	1626.3	1629.17
900	1872.6	1864.45
1050	2079.4	2086.75

3. Data processing

In Table 1 are presented the impact densities of the cooling water jets and the corresponding heat exchange coefficients.

From Figure 2 it can be seen that the heat exchange coefficient increases linearly with the increasing of the impact density.

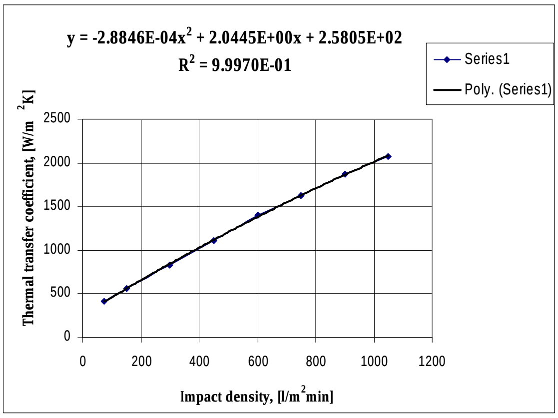

Fig. 2 The thermal transfer coefficient

Were determinate the steel temperatures in the distributor, the cooling water temperatures of the crystallizer at the entrance and at the exit, the temperatures of the crystallizer plates on the fixed part and on the mobile part. The data processing is presented in Figure 3.

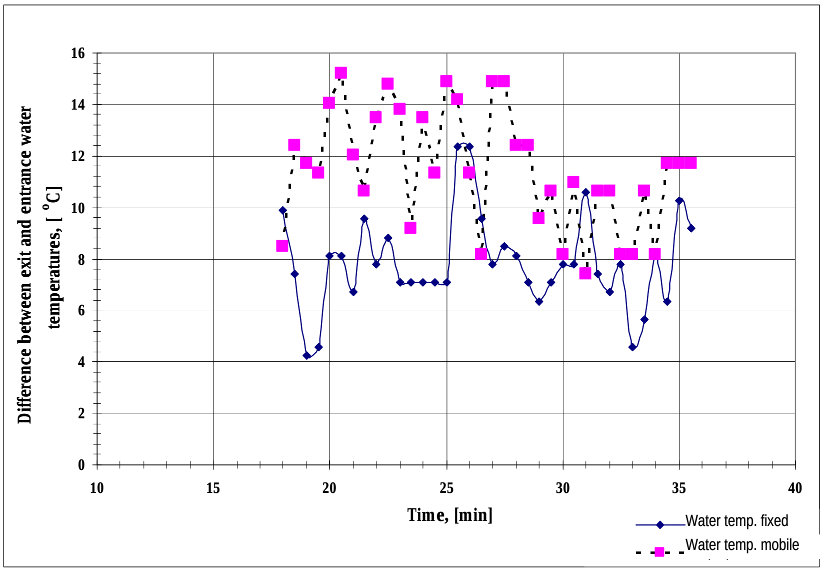

Fig. 3 Cooling water temperatures

In Table 3 are presented the secondary cooling zones with the nozzles types which run in these zones, the lengths of the zones, the splashing angles of the nozzles, their diameters and the technological flow rates on the nozzles, as well, for a pressure of 1 atm and 3 atm.

Table 3

Nozzle position	Nozzle type	Zone length	Splashing angle	Dimen sions	Equivalent diameter, d	Nozzle area, A_d	Distance, h	Flow length, l	Number of nozzles	Technological flow rate per nozzle, D		Technological flow rate per nozzle, D	
										1 atm	3 atm	1 atm	3 atm
		[m]	[°]	[mm]	[mm]	[mm^2]	[m]	[m]	[no.]	[l/min]		[m^3/h]	
Zone Ia fixed	**7680F**	**0.70**	120	1.6*10.77	3.38	17.23	0.115	0.398	8	6.66	11.53	0.400	0.692
	6065L		90	2.4	2.4	4.52	0.080	0.160	30	4.73	8.19	0.284	0.492
Zone Ia mobile	**7680F**	**0.69**	120	1.6*10.77	3.38	17.23	0.115	0.398	8	6.66	11.53	0.400	0.692
	6065L		90	2.4	2.4	4.52	0.080	0.160	30	4.73	8.19	0.284	0.492
Zone Ib fixed	**5580F**	**0.90**	120	1.3*11.29	3.12	14.68	0.110	0.381	25	6.15	10.64	0.369	0.639
Zone Ib mobile	**5580F**	**0.88**	120	1.3*11.29	3.12	14.68	0.110	0.381	25	6.15	10.64	0.369	0.639
Lateral left	**7680F**	**1.60**	120	1.6*10.77	3.38	17.23	0.080	0.277	2	6.66	11.53	0.400	0.692
	3565L		90	1.9	1.9	2.83	0.110	0.220	11	3.75	6.49	0.225	0.389
Lateral right	**7680F**	**1.57**	120	1.6*10.77	3.38	17.23	0.080	0.277	2	6.66	11.53	0.400	0.692
	3565L		90	1.9	1.9	2.83	0.110	0.220	11	3.75	6.49	0.225	0.389
Zone II fixed	**C200100**	**2.90**	120	1.3*27.5	4.87	35.75	0.395	1.368	10	9.59	16.61	0.576	0.997
Zone II mobile	**C200100**	**2.88**	120	1.3*27.5	4.87	35.75	0.395	1.368	10	9.59	16.61	0.576	0.997
Zone III fixed	**C120100**	**3.00**	120	1*27.5	4.27	27.50	0.395	1.368	8	8.41	14.57	0.505	0.874
Zone III mobile	**C110100**	**2.89**	120	1*27.5	4.27	27.50	0.395	1.368	8	8.41	14.57	0.505	0.874
Zone IV fixed	**664847**	**4.40**	120	1.45*20.94	4.48	30.36	0.425	1.472	12	8.84	15.31	0.530	0.919
Zone IV mobile	**664677**	**4.34**	120	1.05*20.94	3.82	21.99	0.425	1.472	12	7.52	13.03	0.451	0.782

On the basis of these data, using the relations 1÷4, there have been calculated the cooling water rates of flow, the ***Re*** and ***Nu*** criteria, and the heat exchange coefficient, $\boldsymbol{\alpha}$, at the cooling water pressure of 1 atm and 3 atm, respectively, which are presented in Table 4.

Table 4

Nozzle position	Nozzle type	*Re*	*Nu*	Rate of flow, *w*			
				1 atm	3 atm	1 atm	3 atm
				[m/s]		$[W/m^2K]$	
Zone Ia fixed	**7680F**	19157	33177	6.44	11.16	3007	4666
	6065L	36840	63802	17.44	30.20	12633	19603
Zone Ia mobile	**7680F**	19157	33177	6.44	11.16	3007	4666
	6065L	36840	63802	17.44	30.20	12633	19603
Zone Ib fixed	**5580F**	19157	33177	6.98	12.09	3144	4878
Zone Ib mobile	**5580F**	19157	33177	6.98	12.09	3144	4878
Lateral left	**7680F**	19157	33177	6.44	11.16	4323	6708
	3565L	36840	63802	22.03	38.15	9188	14257
Lateral right	**7680F**	19157	33177	6.44	11.16	4323	6708
	3565L	36840	63802	22.03	38.15	9188	14257
Zone II fixed	**C200100**	19157	33177	4.47	7.74	875	1359
Zone II mobile	**C200100**	19157	33177	4.47	7.74	875	1359
Zone III fixed	**C120100**	19157	33177	5.10	8.83	875	1359
Zone III mobile	**C110100**	19157	33177	5.10	8.83	875	1359
Zone IV fixed	**664847**	19157	33177	4.85	8.40	814	1263
Zone IV mobile	**664677**	19157	33177	5.70	9.88	814	1263

With the aid of the values presented in Table 3 and those calculated in Table 4, the following dependences have been represented: the variation of the cooling water flow rate along the path length on the fixed part, at the cooling water pressures of 1 atm and 3 atm (Figure 4); the variation of the heat exchange coefficient along the path length on the fixed part, at the cooling water pressures of 1 atm and 3 atm (Figure 5); the variation of the cooling water flow rate along the path length on the mobile part, at the cooling water pressures of 1 atm and 3 atm (Figure 6); the variation of the heat exchange coefficient along the path length on the mobile part, at the cooling water pressures of 1 atm and 3 atm (Figure 7).

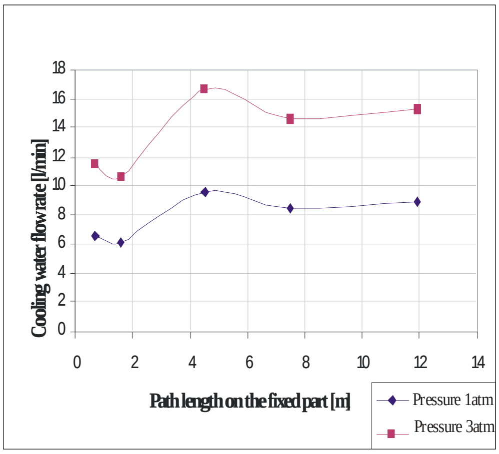

Fig.4. Variation of the cooling water flow rate along the curved path (fixed part).

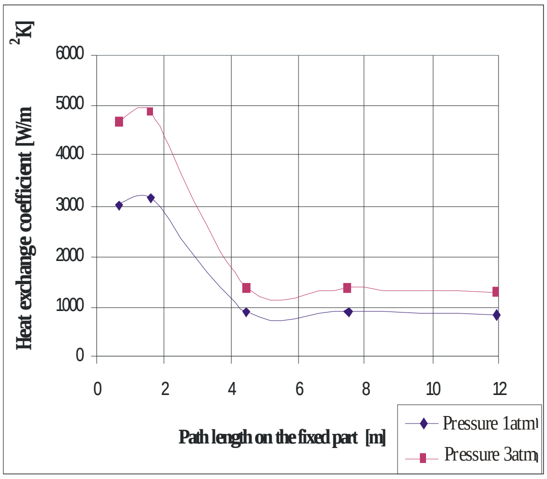

Fig.5. Variation of the heat exchange coefficient along the curved path (fixed part)

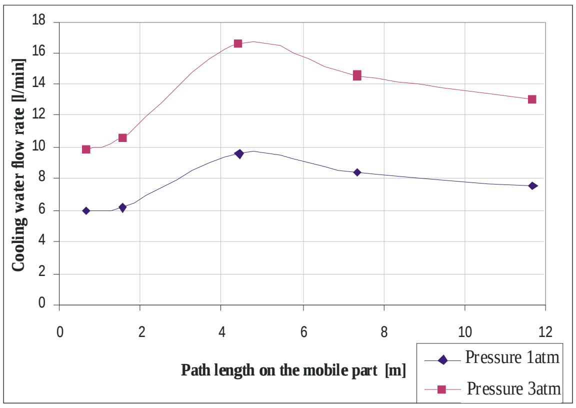

Fig.6. Variation of the cooling water flow rate along the curved path (mobile part)

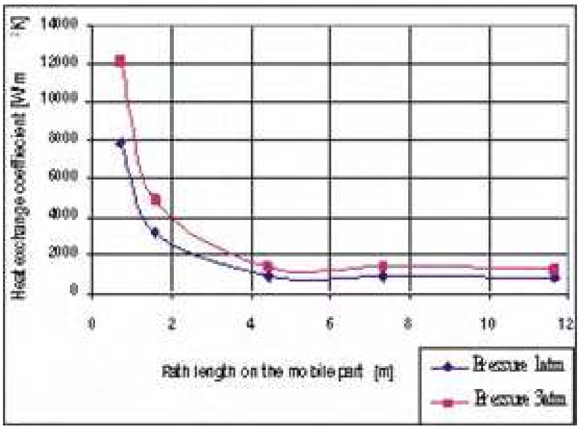

Fig.7. Variation of the heat exchange coefficient along the curved path (mobile part).

4. Conclusions

The heat exchange coefficient increases linearly with the increasing of the impact density of the cooling water jets. The difference between the cooling water temperature of the crystallizer at the exit and the temperature at the entrance is bigger at the cast beginning and is reducing as the cast duration increases. The variations of the cooling water flow rates along the path, both on the fixed part and on the mobile part, have similar curve rates, presenting a maximum at approximately 4 m from the crystallizer exit. On the mobile part, this maximum flow rate is achieved for a bigger value, as compared with the fixed part of the unit. The coefficient of heat exchange presents a minimum corresponding to the maximum in the diagram of cooling water flow rate, at approximately 4 m from the crystallizer exit. On the mobile part, the coefficient of heat exchange has bigger values than on the fixed part.

References

[1].Stefanescu, D., Leca, A., Luca, L., Badea, A., Marinescu, M., ***Heat and mass transfer. Theory and applications,*** Bucharest: Editura Didactica si Pedagogica, 1983.

[2].Ivanescu, A., ***Mass transfer at the metallic materials processing***, Bucharest: Editura Didactica si Pedagogica, 2004.

[3].Dragomir, I. ***Theory of the iron and steel processes***, Bucharest: Editura Didactica si Pedagogica, 1985.

[4].Munteanu, V., Geanta, M., *Casting of semi-products,* Bucharest: Editura Universitatii Politehnica, 2005.

MANUFACTURE OF STUD LINK CHAIN CABLE MADE OF GRADE U1 AND U2 STEEL

[1]Viorel DRAGAN, [1]Marian BORDEI, [2]Chris Mircea CHIS
[1]Dunarea de Jos” University“ of Galati
[2]Lead M&W Engineer LNG Chile
email: mbordei@ugal.ro

ABSTRACT

We have analyzed the fabrication technology of the link chain cable made of grade U1 and U2 steel from TREFO S.A. Galati and we had in view during the experiments several rolling programs. The main characteristics of a product quality, material or working process can be classified into the following groups: technological and contractual. Further on, we are going to present data regarding the link chain cable where samples were drawn, micro metallographic analysis referring to grade U1 and U2 steel and the characteristic obtained on the same areas where the metallographic analysis were made.

KEYWORDS: link chain cable, grade U1 and U2 steel

1. Introduction

Three grades of stud-link chain cable are covered, and are described in table 1.

All chain is to have a workmanlike finish and be free from injurious defects.

Table 1. The grades of stud- link chain cable

Strength Level	**Grade**	**Method of Manufacture**
Normal Strength	1	Flash Butt-welded
High Strength	2a 2b	Flash Butt-welded or Drop-forged Cast Steel
Extra-high Strength	3a 3b	Flash Butt-welded or Drop-forged Cast Steel

There is to be an odd number of links in each shot of anchor chain cable to insure shackles leading over the windlass in the same position. Steel chain made by processes or to requirements differing and certain types of drop-forged chain will be subject to special consideration. Manufacturers of Grades 1 and 2 chain and chain accessories are to submit their manufacturing process and material specifications for review. Data in support of mechanical properties, weld soundness (when applicable) and compliance with the Rules in all respects are also to be submitted for review and approval. Locking pins in detachable connecting links are to have taper contact at both top and bottom in the link halves.

Lead or other acceptable material is to be used for plugging the locking pin hole which is to contain an appropriate undercut recess or equivalent arrangement to secure the plug.

Studs are to be securely fastened by press fitting, or welding with an approved procedure. When the stud is welded in place, the weld is to be opposite the flash butt weld in the chain. The welding is to be carried out in the horizontal position at least on both faces of the link for a length sufficient to hold the stud securely in place. The grade U1 and U2 steel used for the ship and other structural applications, is in conformity with LR Rules. The chemical analysis prescribed for the grade U2 steel sheets was tested and the results are in table 2.

In order to realize a program for extended a fabrication authorization of the higher strength steels plates for ship or other structural applications Grades A, B, C, D and E, on effectuated an researches and experimental series which consists in: chemical analysis; Baumann sulphur print; metallographic analysis; non-destructive examination.

Table 2. The chemical composition for U2a grade

C	**Mn**	**Si**	**P**	**S**	**Cr**	**Ni**	**Cu**	**Mo**	**As**	**Al**
1.2 1.6	1.2 1.6	0.15 0.35	max 0.035	max 0.035	max 0.3	max 0.3	max 0.3	-	min 0.08	min 0.025

2. Experiments

2.1.Thermal treatment

Is realised according with the chain's grade: normalizing - for steel grade Ul and U2. The heat treatment is carried out in a deep furnace. The technical control - similar with the chains control.
The temperatures reached during the normalizing treatment are:
-normalizing temperature:

$T_{normalizing} = 735^0C$

-the furnace temperature is with 10 to 20 °C higher than the treatment temperature:

$T_{furnace} = 735 + 20 = 755\ °C.$

The air cooling follows this treatment.
-the tempering temperature is:

$T_{tempering} = 590^0C$

-the furnace temperature would be with 20 °C higher than the treatment temperature:

$T_{furnace} = 610\ °C.$

2.2. Test programme

Approval for Grade U2 chain cable also covers approval for the manufacture of lower grades up to the same maximum diameter provided that such cable is supplied in the normalized condition.

Separate approval tests are to be carried out where it is proposed to supply Grade Ul or U2 cable in the "as welded" condition (fig. 1).

Fig. 1. The common link.

The approval tests were carried out on the 64 mm diameter, U1 and U2 grade anchor stud link chain. In addition, a suitable length (about six times the diameter) of the bar material used for the manufacture of the cable is to be provided for the test purposes. This sample of bar material is to be heat treated in a manner simulating that used for the completed chain cable. The bar material is supplied by S.C. "C.O.S. TIRGOVISTE" S.A., having the ladle analysis in conformity with table 3.

Table 3. Chemical analysis of the ladle

C	**Mn**	**Si**	**S**	**P**	**Cr**	**Ni**	**Cu**	**Al**	**V**	**Nb**	**N_2**
[%]											
0.24	1.64	0.23	0.015	0.021	0.25	0.19	0.22	0.02	0.08	0.03	0.0090

The dimensions of the enlarged link and the end link before the proof load are given in table 4.

Table 4. The dimensions of the enlarged link and the end link before the proof load

Enlarged link				**End link**			
L	W	P	d	L	W	P	d
[mm]							
420	256	277	70.5/ 72.5	435	260.5	280	76.8/ 78.1

The common links were manufactured from 26SiMnl7 steel, 65 mm diam. bar material, charge 79611, having the chemical composition according to table 3. A careful visual examination was carried out, with specially reference to the uniformity of diameter, the shape of links. The links dimensions are shown in the table 4.

Magnetic particle inspection was carried out on 21 common links, 1pc. enlarged link and 1pc. end link. It was applied a load equal to 10% from 2190 kN and the chain cable's measured length was of 26810 m. Then, the chain length was submitted to a proof load of 2190 kN; after that the chain cable's length was submitted to 219 kN and there was measured the cable chain length: 26.94 m. The permanent elongation is of about 0.13 m. The length of chain cable was ultrasonic re-examined on a number of 10 common links, 64 mm diameter.

Table 5. The dimensions of the link

L (link's length)	**W (link's width)**	**P (pitch)**
[mm]		
383	230	254
384.5	234.5	256
388	231.5	260
383	235	254
386	234	258
385	234	258
387.5	236.5	261
385	235.5	259
388	234	261.5
386	235.5	258
387	234	261
386	235	261.2
383	234.5	255

There were dimensional checked 20 pcs common links; 5 pcs enlarged links and 5 pcs end links acc. There were checked all the cable's links at the outer surface and there were no objections (fig.2).

Fig.2. The macrostructure of the commom link, 500:1.

The specimen composed by 3 common links, lpc. enlarged link and 1 pc. end link was subjected at a tensile of 3130 kN and it wasn't destroyed.

The breaking test was continued until 3963 kN, when was broke a common link from the bend zone .

The values of the mechanical tests for the links cut from the chain cable subjected at the tensile test is according to the tables 6. The microstructure (fig. 3) and the Baumann‘s amprent (fig. 4) confirm the goods properties obtained by the mechnical te sts.

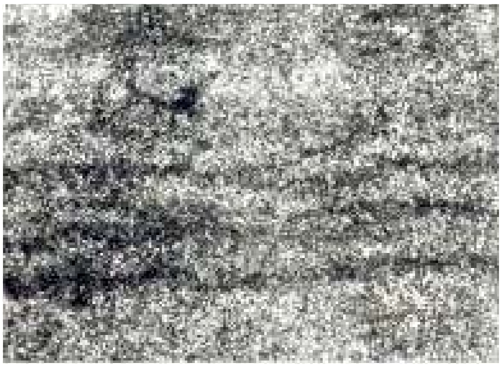

Fig.3. The microstructure of the common link, 500:1.

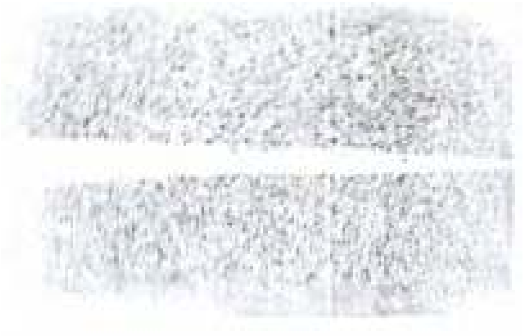

Fig.3. The Baumann amprent of the common link.

Table 6. Common links (The side opposite the weld)

Tensile strength	**Yield strength**	**Elongation**	**Red of area**	**Charpy V notch impact test Energy Joules**				**Cristalinity**
[N/mm^2]		[%]						
				Test temp	1	2	3	
813	701	21.4	63.2	0	194	184	234	80
				20	182	240	200	80
				-20	174	178	192	80
				-40	189	192	188	80

Conclusions

We have analyzed the fabrication technology of the link chain cable made of grade U1 and U2 steel from TREFO S.A. Galati and we had in view during the experiments several rolling programs. The main characteristics of a product quality, material or working process can be classified into the following groups: technological and contractual. Further on, we are going to present data regarding the link chain cable where samples were drawn, micro metallographic analysis referring to grade U1 and U2 steel and the characteristic obtained on the same areas where the metallographic analysis were made.

The manufacture program has been accepted in accordance with the requirements of Lloyd register.

References

[1]. Adrian,M., ***Tehnologia laminării***-Editura Tehnică, Bucureşti, 1977

[2]. Geru, N., ***Metalurgie fizică,*** Ed. didactică şi pedagogică, Bucureşti, 1981

[3]. Geru, N., ***Teoria structurală a proprietăţilor metalelor*****,** Ed. didactică şi pedagogică, Bucureşti, 1980

[4]. Geru,N., ***Materiale metalice. Structură, proprietăţi, utilizări***-Editura Tehnică, Bucureşti, 1985

[5]. Kaspar, R., The Influence of Thermo mechanical Treatment on the Transformation Behaviour of Steels, Steel Research, 6/1994, pag. 242-247

[6]. Slesar, M., ***Aspecte microstructurale ale proceselor de deformare şi de rupere***, Neue Hütte, 12/1989, pag. 450-453

[7]. Ursache,M., Chircă,D., Proprietăţile metalelor-Editura Didactică şi Pedagogică, Bucureşti, 1982.

[8]. http://www.sname.org/committees/design/SD-5/, ***Rule Requirements For Materials And Welding*****,** 2001.

AFFILIATED WITH:

- *ROMANIAN SOCIETY FOR METALLURGY*
- *ROMANIAN SOCIETY FOR CHEMISTRY*
- *ROMANIAN SOCIETY FOR BIOMATERIALS*
- *ROMANIAN TECHNICAL FOUNDRY SOCIETY*
- *THE MATERIALS INFORMATION SOCIETY (ASM INTERNATIONAL)*

ANALELE UNIVERSITĂŢII "DUNĂREA DE JOS" DIN GALAŢI.
FASCICULA IX. METALURGIE ŞI ŞTIINŢA MATERIALELOR
ISSN 1453 – 083X
Revistă bianuală acreditată CNCSIS
Categoría B+, Cod CNCSIS: 215
URL: http://www.fmet.ugal.ro

Editată sub egida
Facultăţii de
METALURGIE ŞI ŞTIINŢA MATERIALELOR
şi a Centrului de Cercetare
CALITATEA MATERIALELOR ŞI A MEDIULUI

Annual subscription (2 issues per year)

Edited under the care of
Faculty of
METALLURGY AND MATERIALS SCIENCE
and Research Center
QUALITY OF MATERIALS AND ENVIRONMENT

Data editării: 15.05.2007
Tiraj: 200 exemplare
Tiparul executat la
Galati University Press
editură acreditată CNCSIS
Str. Domnească nr. 47. Galati 800036 Romania

Edited date: 15.05.2007
Issues number: 200
Printed by
Galati University Press
accredited CNCSIS
47 Domnească Street, 800036 Galati, Romania

MANUSCRISELE, CĂRŢILE ŞI REVISTELE PENTRU SCHIMB, PRECUM ŞI ORICE CORESPONDENŢE SE VOR TRIMITE PE ADRESA:

MANUSCRIPTS, REVIEWS AND BOOKS FOR EXCHANGE COOPERATION, AS WELL AS ANY CORRESPONDANCE WILL BE MAILED TO:

LES MANUSCRIPTS, LES REVUES ET LES LIVRES POUR L'ECHANGE, TOUT AUSSI QUE LA CORRESPONDANCE SERONT ENVOYES A L'ADRESSE:

MANUSCKRIPTEN, ZIETSCHRITFTEN UND BUCHER FUR AUSTAUCH SOWIE DIE KORRESPONDENZ SID AN FOLGENDE ANSCHRIFT ZU SEDEN:

UNIVERSITATEA "DUNĂREA DE JOS" DIN GALAŢI
REDACŢIA ANALELOR
Str. Domnească nr. 47 – 800036 Galaţi, ROMÂNIA
E-mail: marian.bordei@ugal.ro

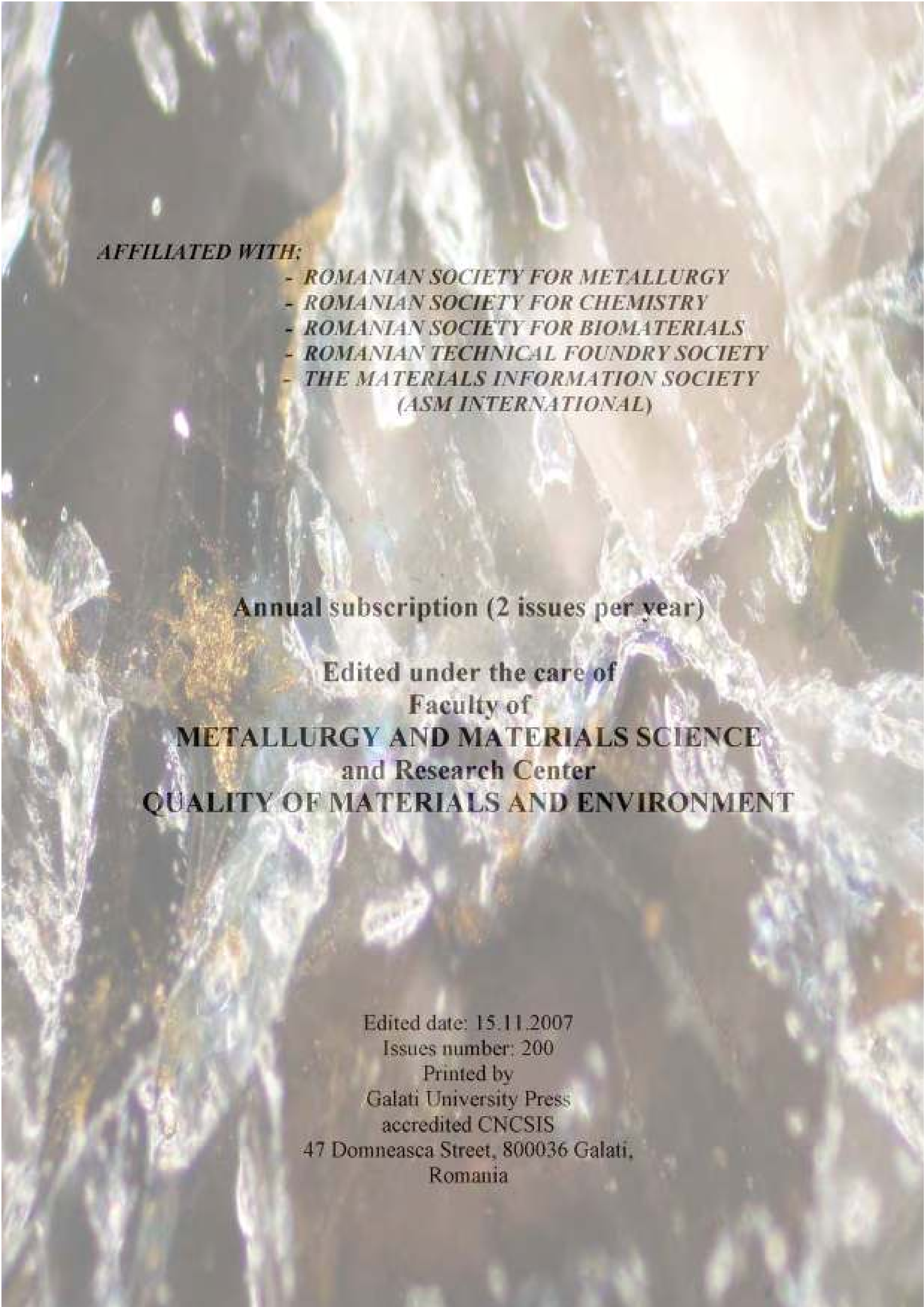

AFFILIATED WITH:

- *ROMANIAN SOCIETY FOR METALLURGY*
- *ROMANIAN SOCIETY FOR CHEMISTRY*
- *ROMANIAN SOCIETY FOR BIOMATERIALS*
- *ROMANIAN TECHNICAL FOUNDRY SOCIETY*
- *THE MATERIALS INFORMATION SOCIETY (ASM INTERNATIONAL)*

Annual subscription (2 issues per year)

Edited under the care of
Faculty of
METALLURGY AND MATERIALS SCIENCE
and Research Center
QUALITY OF MATERIALS AND ENVIRONMENT

Edited date: 15.11.2007
Issues number: 200
Printed by
Galati University Press
accredited CNCSIS
47 Domneasca Street, 800036 Galati,
Romania